Multiphysics Modeling and Statistical Process Optimization of the Scanning Laser Epitaxy Process Applied to Additive Manufacturing of Turbine Engine Hot-Section Superalloy Components

A Dissertation
Presented to
The Academic Faculty

by

Ranadip Acharya

In Partial Fulfillment
of the Requirements for the Degree
Doctor of Philosophy in the
George W. Woodruff School of Mechanical Engineering

Georgia Institute of Technology
December 2014

Multiphysics Modeling and Statistical Process Optimization of the Scanning Laser Epitaxy Process Applied to Additive Manufacturing of Turbine Engine Hot-Section Superalloy Components

Approved by:

Dr. Suman Das, Advisor
George W. Woodruff School of Mechanical Engineering
Georgia Institute of Technology

Dr. Yogendra K. Joshi
George W. Woodruff School of Mechanical Engineering
Georgia Institute of Technology

Dr. Jianjun Shi
School of Industrial and Systems Engineering
Georgia Institute of Technology

Dr. Arun Gokhale
School of Materials Science and Engineering
Georgia Institute of Technology

Date Approved: 10th September, 2014

Dr. Surya Kalidindi
George W. Woodruff School of Mechanical Engineering
Georgia Institute of Technology

Dedicated to my parents and to my dear wife for their constant support..

পুরাতন ভাষা মরে এল যবে মুখে,
নবগান হয়ে গুমরি উঠিল বুকে,
পুরাতন পথ শেষ হয়ে গেল যেথা,
সেথায় আমারে আনিলে নূতন দেশে ।।

When old words die out on the tongue, new melodies break forth from the heart; and where the old tracks are lost, new country is revealed with its wonders.

- **Rabindranath Tagore, Gitanjali**

ACKNOWLEDGEMENTS

I am thankful to my parents for giving me the privilege and support to be at the position I am in today, and particularly, to my mother for constantly supporting me during my graduate studies from a different continent. I am thankful to my dear wife, Sunipa for the emotional support she offered and also, for taking care of the daily necessities when I was busy in lab work.

I would like to express my deepest gratitude to Dr. Suman Das for his guidance and support as my advisor. He is an excellent researcher, an outstanding teacher, and above all, a very nice human being. I am indebted to him for all of the suggestions that he has provided me on interesting research topics and areas to pursue. He has been instrumental in my development on the academic and professional front. This body of work would not have taken shape without his advice, insight and encouragement.

The majority of this research work has been performed through grant N00014-11-1-0670 as part of the Cyber enabled Manufacturing Systems (CeMS) program by Office of Naval Research. In particular, I would like to acknowledge Dr. Khershed Cooper and Dr. Ralph Wachter, formerly in the ONR for their support.

I would also like to thank each of the members of my dissertation reading committee, Dr. Yogendra K. Joshi, Dr. Arun Gokhle, Dr. Jianjun Shi, and Dr. Surya Kalidindi for taking a significant amount of their valuable time to review my proposal and final dissertation. Their suggestions on how to make my work better and more scientifically valuable is greatly appreciated. I would like to thank Dr. Michael Middlemas for all of his guidance, advice and help during the time of need. I am thankful to Kysten Raleigh for her helpfulness in filling my

never-ending purchase requests and helping out with other administrative activities that make the research go smoothly. I am thankful to Steven Sheffield and Louis Boulanger of the ME machine shop for the quick support they provided even during the most difficult circumstances. I am thankful to Dr. Shreyes Melkote for letting me use the microindentation hardness tester in his lab. I would also like to offer my gratitude to Dr. Jeff Donnell for patiently proofreading my thesis and offering his valuable advice.

I would like to gratefully acknowledge my friends and lab mates at GT. I am fortunate to share lab space with them. In particular, I wish to thank Dr. Rohan Bansal, Justin Gambone, Shaun Eshraghi, Dr. Raphael Alabi, Dr. Anirudh Rudraraju, Dr. Dajun Yuan, Dr. Tao Wu, Andriy Dotsenko, and many others for their help and encouragement.

Finally I would like to thank my friends and extended family in Atlanta, Abhijeet Kumar, Ayan Chakraborty, Akash Chakroborty, Arkadeep Kumar, Archita Nath, Ananda Barua, Atiqur Rahman, Arindam Khan, Ashmita Bhattacharya, Brian and Joann Boham, Buddhika and Erandi Jayasena, Chandra Nath, Chuck and Debbie Emerson, Diya Sen, Debashish Banerjee, Moazzem Hossain, Nairwita Mazumdar, Neha Rahman, Payel Chtterjee, Ravi Pallantla, Rimi Hazra, Risha Ghosh, Rupan and Raka Saha, Sabyasachi Deyati, Samit Ghosh, Samrat Sen, Snigdha Pal, Sougata Sarkar, Suhas Madhusudana, Tarak Nandi, Zakir Khondkar, and many others for keeping my life enjoyable.

TABLE OF CONTENTS

LIST OF TABLES

LIST OF FIGURES

LIST OF SYMBOLS AND ABBREVIATIONS

SLE	Scanning laser epitaxy
PDAS/w	Primary dendrite arm spacing
CET	Columnar-to-equiaxed transition
OMT	Oriented-to-misoriented transition
SX	Single-crystal
DS	Directionally-solidified
EQ	Equiaxed
R.I.T	Rotor inlet temperature
HAZ	Heat-affected zone
DMLS	Direct metal laser sintering
ELMF	Epitaxial laser metal forming
SLS	Selective laser sintering
LMF	Laser metal forming
LENS	Laser engineered net shaping
OSAAC	One-step-ahead-adaptive-control
MHT	Microindentation hardness test
DoE	Design of experiments
EB	Electron beam welding
EBSD	Electron back scattering diffraction
SEM	Scanning electron microscopy
TEM	Transmission electron microscopy

OM	Optical microscopy
GTAW	Gas tungsten arc welding
DDM	Direct digital manufacturing
CFD	Computation fluid dynamics
FEM	Finite element modeling
CA	Cellular automata
LBM	Lattice-Boltzmann modeling
G	Temperature gradient
V	Solidification velocity
SG	Stray grain
FGM	Functionally graded material
E_d	Volumetric energy density
T_i	Turbine inlet temperature
T_e	Turbine exhaust temperature
PPM	Parts per million
λ	Wavelength
τ	Transmissivity
P	Laser power
S	Scan speed
H_v	Vickers microindentation hardness
σ_y	Yield stress
E_{snake}	Total energy of the snake line
F_{int}	Internal force of the spline

F_{image}	Image force
F_{con}	Constraints force
F_{line}	Intensity of the filtered Canny output
F_{term}	Termination force
F_{edge}	Edge force
f_i	Coefficient of the force terms
I	Image intensity
S	Displacement
N_0	Nucleation density
ΔT_{tip}	Tip undercooling
ΔT_n	Nucleation undercooling.
x,y	Coordinates
D	Diffusion coefficient in the liquid
Γ	Gibbs-Thomson coefficient
ρ_c	Correlation coefficient
COV	Covariance
T^2	Hotelling T^2-statistic
ΔT_0	liquidus-solidus range in initial alloy
K	equilibrium distribution coefficient
<ijk>	Direction
C	Polynomial fit constant
a, n	Material constant
Φ	Equiaxed fraction

G_{hkl}	Temperature gradient in <hkl> direction
P	Density
h	Enthalpy
T	Temperature
U	Velocity
K	Thermal conductivity
C_p	Specific heat
r	Volume fraction
Y	Mass fraction
μ	Viscosity
γ	Surface tension coefficient
α	Absorptance
ε	Emissivity of an object

SUMMARY

Scanning Laser Epitaxy (SLE) is a new laser-based layer-by-layer generative manufacturing technology being developed in the Direct Digital Manufacturing Laboratory at Georgia Tech. SLE allows creation of geometrically complex three-dimensional components with as-desired microstructure through controlled melting and solidification of stationary metal-alloy powder placed on top of like-chemistry substrates. The proposed research seeks to garner knowledge about the fundamental physics of SLE through simulation-based studies and apply this knowledge for hot section turbine component repair and ultimately extend the process capability to enable one-step manufacture of complex gas turbine components. Prior methods of repair specifically for hot-section Ni-base superalloys have shown limited success, failed to consistently maintain epitaxy in the repaired part and suffered from several mechanical and metallurgical defects. The use of a fine focused laser beam, close thermal control and overlapping raster scan pattern allows SLE to perform significantly better on a range of so-called "non-weldable" Ni-base superalloys. The process capability is expanded further through closed-loop feedback control of melt pool temperature using an infra-red thermal camera. The process produces dense, crack-free and epitaxial deposit for single-crystal (SX) (CMSX4), equiaxed (René-80, IN 100) and directionally solidified (DS) (René-142) Ni-based superalloys.

However, to enable consistent and repeatable production of defect-free parts and future commercial implementation of the technology several concerns related to process capabilities and fundamental physics need to be addressed. To explore the process capability, the fabricated components are characterized in terms of several geometrical, mechanical and metallurgical parameters. An active-contour based image analysis technique has been developed to obtain

several microstructural responses from the optical metallography of sample cross-sections and the process goes through continuous improvement through optimization of the process parameters through subsequent design of experiments. The simulation-based study is aimed at developing a multiphysics model that captures the fundamental physics of the fabrication process and allows the generation of constitutive equations for microstructural transitions and properties. For this purpose, a computational fluid dynamics (CFD) finite-volume solver is used to model the melting and solidification process. The development work also focuses on studying process response to different superalloy materials and implementing a multivariate statistical process control that allows efficient management and optimization of the design parameter space. In contrast to the prior work on single-bead laser scan, the model incorporates the raster scan pattern in SLE and the temperature dependent local property variations. The model is validated through thermal imaging data. The flow-thermal model is further tied to an empirical microstructural model through the active-contour based optical image analysis technique, which enables the identification of several microstructural transitions for laser beam describing a raster scan pattern.

The CFD model can effectively be coupled with finite element solver to assess the stress and deformation and can be coupled with meso-scale models (Cellular Automata) to predict different microstructural evolutions. The research thus allows extending the SLE process to different superalloy materials, performs statistical monitoring of the process, and studies the fundamental physics of the process to enable formulation of constitutive relations for use in closed-loop feedback control; thus imparting ground breaking capability to SLE to fabricate superalloy components with as-desired microstructures.

Chapter I

Introduction

1.1 Background of the SLE process

Additive Manufacturing is the most recently emerged concept in manufacturing that relies on 'material increase'. In these processes, the final object is obtained by either gradual addition of material or by gradual binding or solidification of materials. These developments are considered similar in importance to the advent of the numerical control machine tool in the fifties or the development of non-traditional machining processes in the sixties and the seventies. They also represent 'free-form' manufacturing since these are based on gradual generation of the overall shape without the need for tools, dies or molds. The process gradually evolved and the working material changed from polymer to metal, metal to metal-alloy and finally to superalloy components.

Superalloys are the nickel-, iron-nickel- and cobalt-based alloys that can withstand loading at temperatures close to melting temperature and are generally used for application with temperatures exceeding 540^{o}C (1000^{o}F)[1]. They are introduced to cope with the increasing demand for stronger and more corrosion-resistant materials for aircraft engines during World War II and have since then evolved to meet the increasing demand for more efficient gas turbines. The bulk share of responsibility for improved properties can be attributed to the presence of the intermetallic compound (γ' phase) which resists the propagation of dislocation movements and allows increased strength at elevated temperatures for longer durations. The superalloys also evolved from equiaxed (EQ) to directionally-solidified (DS), and finally to single-crystal (SX)

microstructure to reduce the grain boundary void formation and to improve the creep strength. All these development also resulted in huge expenditures to manufacture increasingly sophisticated gas turbine blades.

Gas turbines are commonly used in aircraft propulsion systems and in industrial power generation. They represent the most aggressive application of structural materials. Modern day turbine engines typically operate under a Brayton cycle in which the inlet air is first compressed, and then mixed with fuel that is combusted and finally exhausted through an expansion turbine to generate power. The efficiency (η) of the cycle is given by equation 1 as,

$$\eta = 1 - \frac{T_e}{T_i} \tag{1}$$

Here, T_e = exhaust temperature and T_i= Inlet temperature. Since, the exhaust temperature cannot be lowered than the ambient temperature, the focus of the design has always been on increasing the inlet temperature, which in effect increases the operating temperature of the turbine. This also requires increasing the pressure ratio across the turbine stages, thus creating a very aggressive environment for the hot gas flow components. Typically, an increase of 10^{o}C (50^{o}F) in the operating temperature increases the efficiency by 1%. In the last 30 years the peak operating temperature of the gas turbine hot-section components has increased from 982^{o}C (1800^{o}F) to 1427^{o}C (2600^{o}F). This development has posed serious design challenges from the thermal cooling and fatigue strength aspects. Hence, to increase the efficiency of a gas turbine, three complimentary approaches have been adopted. The first is to improve the creep strength and fatigue resistance of the material that allows operation of the turbine at higher temperatures. This approach is used in the aviation industry requiring use of novel and improved superalloys, and

also drove the research of DS/SX superalloys. The DS/SX microstructure prevents grain boundary sliding, thus causing enhanced creep strength. The industrial gas turbine is also catching up with this trend and using similar materials as the aircraft engine [2]. The second approach to solve the thermal cooling problem is to use metallic coatings in the hot gas path and combustion hardware to improve the oxidation and corrosion resistance. Additionally, ceramic coatings are used to improve thermal protection. The third approach is to use elaborate and complex film cooling schemes to keep the metal temperature within design limits. The recent industrial gas turbines are benefitted in this aspect since they can use steam cooling that is superior compared to the air cooling in aircraft engines [2].

High gradient casting (investment casting with high and well controlled thermal gradient) is typically used to develop customized and fine structured superalloys. Due to the complexity and sensitivity of casting DS and SX parts, there are relatively few foundries in the world capable of producing them, resulting in high costs and long lead times for these components. However, the operational life of the gas turbine hot-section components decreases due to several reasons. Firstly, increased cooling effectiveness achieved with the advanced air cooling and steam cooling schemes produces higher thermal gradients in hot-section turbine components. This significantly increases the thermal strain associated with these parts and the thermal cycle associated with the strain causes severe fatigue loading. Secondly, the turbine blades are increasingly cast with DS/SX microstructures that can provide higher yield strength as the operating temperature is increased. This is partly due to the presence of secondary γ' phases that form an anti-phase boundary and lock the disassociated or partial dislocation movement [3, 4]. However, the secondary phases also increase the susceptibility to cracking. Additionally, despite being cast with these advanced single-crystal microstructures, the turbine blades still have a

limited operating life due to material loss at the blade tip resulting from the abrasion between the blade and the engine shroud. Once a blade has experienced a certain amount of material loss (typically on the order of 0.5-1mm on an 8 cm tall blade), it cannot be used any further and has to be scrapped since the superalloys involved are 'non-weldable'.

Due to the high cost of producing SX cast turbine blades, the cost of replacing each blade is several thousand dollars. With each engine containing several hundred airfoils (blades and vanes), the total cost of replacing all airfoils can reach hundreds of thousands of dollars. Hence, it is of great interest to develop a process which can restore the single-crystal microstructure at the damaged location and allow for the airfoils to be reused rather than be scrapped and replaced. Thus, various OEMs and spare parts manufacturers in the aerospace industry are interested in a process capable of repairing and reconditioning these blades such that they can be re-inserted in an engine. Currently, there is no effective way of repairing turbine blades that have been cast with a directionally solidified or single-crystal morphology due to the fact that many of these alloys are considered 'non-weldable' and there is difficulty in retaining the underlying microstructure of the substrate or to maintain epitaxy in the newly deposited material. As an example, a gas turbine blade made of a superalloy as shown in Figure 1(a), has to be scrapped if the total abrasion wear at the blade tip exceeds 0.5 mm. The cost of a typical blade ranges from US$ 500 to 2000 and if the total number of blades in a gas turbine engine is considered, the estimated replacement cost is in the ranges of hundreds of thousands to millions of dollars for each gas turbine. Similarly, fatigue cracks and other forms of damage limit the life of platform components shown in Figure 1(b). The primary goal of SLE process development is to address this problem. The aim of ongoing research on SLE is to demonstrate that it is possible to repair the damaged and worn-out components and place them back into operating service. The

secondary objective of SLE process development is to build complex gas turbine engine components from the ground up, using layer-by-layer fusion of superalloy powders.

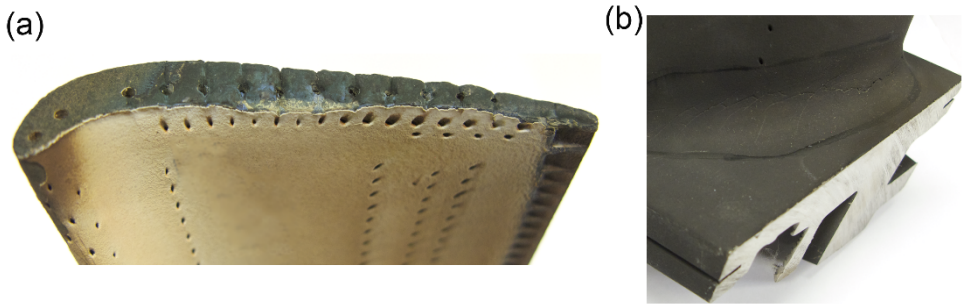

Figure 1. (a) Turbine airfoil with worn out blade tip and (b) cracking in the platform section.

In the proposed research, Scanning Laser Epitaxy (SLE) is a new laser based additive manufacturing process that is capable of fulfilling both the aforementioned requirements i.e. it can deposit superalloys of the same composition as the repaired substrate at the damaged location, and it can grow the deposit epitaxially from the base material.

1.2 How is SLE different?

Figure 2(a) and (b) shows a schematic diagram elaborating the two modes of operation for SLE. Figure 2(a) elucidates the repair process that can create an epitaxial deposit upto 2.5 mm thickness atop a like-chemistry base substrate. A stationary powder bed of desired thickness is utilized and a single-pass of the rastering movement of the laser beam is required to perform the repair process. Figure 2(b) shows the multi-layer mode that enables building of component from ground up. Here the desired thickness of the component is divided into several layers and after each pass the created layer has to be lowered by the layer thickness value. A sationary powder bed of desired thickness is swept over the previous deposit and the rastering movement

of the laser is repeated based on the geometry requirement of the subsequent layer. A certain portion of the underlying layer is melted to create adequate metallurgical bond with the subsequent layer and to induce epitaxy. This is repeated until desired dimension of the component is achieved.

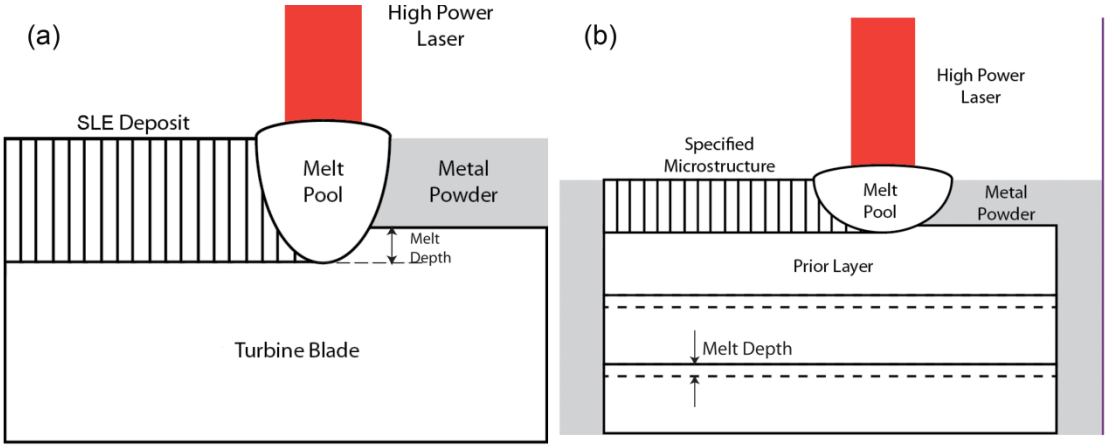

Figure 2. Schematic of SLE (a) for single layer deposition (b) for multi-layer deposition.

Figure 3 shows typical SLE workpiece coupons used in the experimental setup used for this dissertation's research. SLE involves the use of a pre-placed powder bed as shown for positions 1 and 2. In SLE, a tightly focused laser beam is guided by high-speed galvanometer scanners, allowing for tight control over the amount of energy being applied to the top of the pre-placed powder bed, as well over as the speed at which the melt pool moves across the substrate. This allows a proper metallurgical bonding between the newly created deposit and the substrate material as shown in Figure 4. Under the proper operating conditions and with a sufficient substrate meltback, the melted powder undergoes epitaxial solidification from this partially remelted surface of the substrate. The solidification microstructure in the new deposit thus follows the microstructural morphology of the underlying substrate, allowing for equiaxed (EQ), directionally-solidified (DS) and even single-crystal (SX) growth.

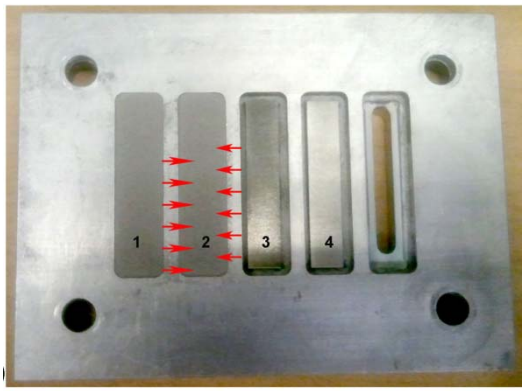

Figure 3. Placement of superalloy coupons in the SLE process. The rightmost position shows the blank base to simulate the cooling holes in turbine blades. Positions 4 and 3 show bare coupons and positions 1 and 2 show a coupon with powder placed on top it. The rastering movement of the scan is shown for the coupon in position 2.

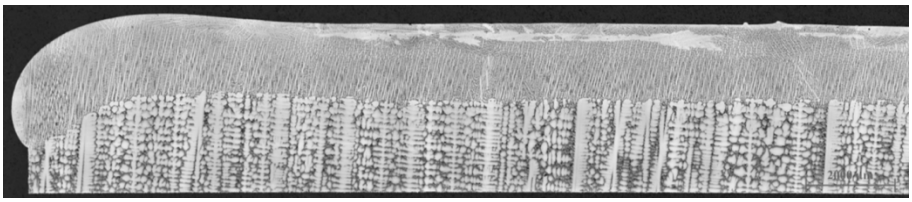

Figure 4. Representative SLE deposition for SX CMSX-4 showing an excellent metallurgical bond between the substrate and the deposit region.

The key differences between SLE and laser cladding-based processes such as laser engineered net shaping (LENS) [5-7] are twofold. A schematic of the LENS process is shown in Figure 5. In SLE, the powder bed is stationary, while in LENS, the powder is fed via a deposition head. This powder feeding causes additional turbulence and unwanted convection in the melt pool, thus breaking the dendrites of the solidified region and inhibiting SX growth. Thus, the powder blowing mechanism in the LENS process makes it unsuitable for the superalloys with the SX morphology. Another difference concerns the speed of the substrate's mechanical movement in

the LENS process. Here, the scan speed is limited to a certain range and hence for 'non-weldable' superalloys, the combination of lower scan speed and high scan power results in parts that have lower quality in terms of crack propensity and fatigue strength. In SLE, the galvanometer-driven movement of the laser beam allows precise motion and faster scan speed, thus potentially improving the quality of the fabricated component.

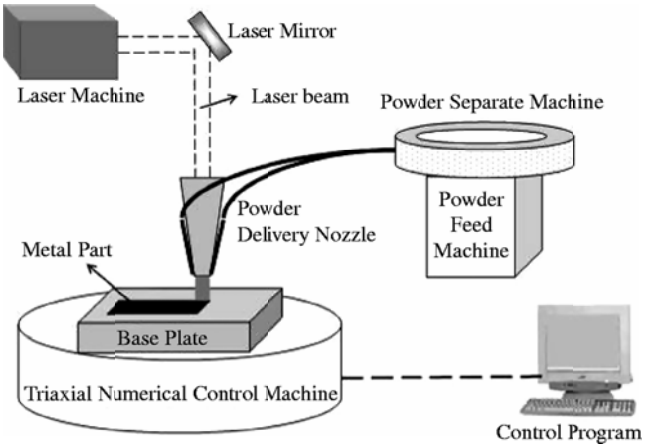

Figure 5. Schematic of LENS process [8].

Multiple control parameters can be introduced to determine the quality of the parts created by SLE. The melt depth, the uniformity of the deposit or surface waviness and the formation of cracks should be controlled to obtain a part with higher reliability. Similarly, from the microstructural point of view, the morphological transitions such as the columnar-to-equiaxed transition (CET) and the oriented-to-misoriented transition (OMT) should be minimized to obtain a better quality deposit. All these can be achievable using a physics-based model that allows concurrent modeling of thermal phenomena and microstructural transformation. Since SLE does not involve blowing powder into the melt pool, the process excludes the possibility of the deposit being spoiled by the severe forced convection; hence, it is more responsive to feedback control. However, a physics-based model can provide better understanding and reliable

constitutive relations for different materials that can be used, with a control law. In contrast, a, design-of-experiments based model will lack the generalization present in the physics-based model and must be repeated for all the materials because of the widely varying properties of Ni-based superalloys. A coupled-flow-thermal-microstructural model is necessary to reduce the experimental cost and to obtain a deeper understanding of the entire manufacturing process.

1.3 Statement of the problem

In the last 30 years the peak operating temperature of gas turbine engines has increased from 982^{o}C (1800^{o}F) to 1427^{o}C (2600^{o}F). This poses serious design challenge from the thermal cooling and fatigue strength aspect. To increase the efficiency of gas turbines, considerable research was done on the material aspects primarily to improve the creep strength and fatigue resistance of the material, in order to allow operation of the turbine at higher temperatures. This drove designers in the aircraft industry to use novel and improved superalloys, and drove research into DS/SX superalloys. The DS/SX microstructure prevents grain boundary sliding, thus causing enhanced creep strength [9]. The primary strengthening phase in Ni-based superalloys is Ni_3(Al, Ti), which is called gamma prime (γ′). It is a coherently precipitating phase (i.e., the crystal planes of the precipitate are in registry with the gamma matrix) with an ordered $L1_2$ (fcc) crystal structure. The close match in matrix/precipitate lattice parameters (~0-1%), combined with chemical compatibility allows the γ′ to precipitate homogeneously throughout the matrix and to have long-term stability. The presence of the γ′ particles in the microstructure prevents dislocation movements. In the γ′ morphology, Al or Ti replaces the Ni atoms at the corner of the fcc cell However, this γ′ incorporation also causes increased brittleness during heat treatment and is the primary reason for the non-weldability of the superalloy

components. Figure 6 shows the tendency for solidification cracking as a function of Al+Ti contents [10]. The alloy is considered 'Difficult-to-weld if the total Al+Ti content exceed 4wt%, and the welding difficulty increases as the total Al+Ti content increases. The present research seeks to investigate 'non-weldable' alloys with Ti+Al content exceeding 5 wt%.

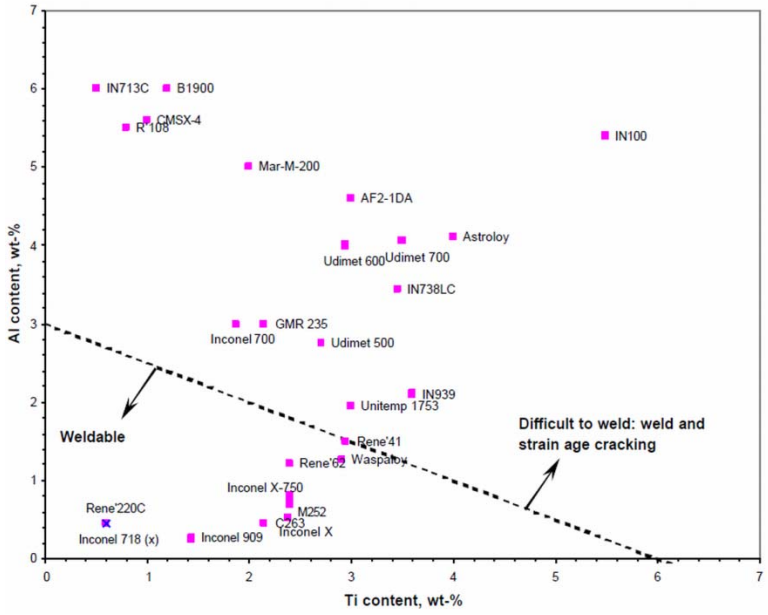

Figure 6. Cracking susceptibility as function of Al+Ti content in superalloys. The superalloys above the dotted are considered 'non-weldable' [10].

Any additive processing technique involving superalloys involves melting of the component and the addition of material to obtain a proper metallurgical bond and to maintain epitaxy between the deposit and the substrate superalloy, unless filler material is used for a brazing like procedure and epitaxy is not desired. However, the severity of the application at high temperature and pressure conditions necessitates epitaxy and cannot accommodate a foreign material as done in brazing. The processing challenges start with the incorporation of melting. The wide solidification range of superalloys promotes solidification cracking; the local dissolution of

different phases causes liquation cracking, and the incorporated gas results in porosity within the deposit region.

The difficulty level increases as we move from EQ alloys to DS or SX alloys. In addition to restricting the cracks and porosity, epitaxy also becomes a deciding factor and either the columnar orientation has to be maintained (for DS alloys) or the nucleation of new grains has to be prevented (for SX alloys). The processing of SX alloys is particularly difficult, since the operational parameters need to be optimized to minimize constitutional undercooling. Otherwise, new grains will start to nucleate at the dendrite tips. This phenomenon always remains a possibility while processing an undercooled melt, and proper control of operational parameters is required in order to eliminate or reduce the creation of new grains.

Since the processing of superalloys is quite difficult, it is essential to understand the fundamental aspects from a physics perspective. To model the laser processing, an effective thermal model must be built; it must account for the spatially variable moving heat source, and it must predict the resultant temperature distribution. The variable properties of the material must be incorporated to predict the onset of melting and re-solidification once the heat source moves over a given position. Additionally, the fluid flow problem inside the melt pool, which comes in whenever the liquid state is found within a domain, needs to be tackled. Solidification analysis requires close attention to the mushy region that restricts the fluid flow. The temperature driven surface tension gradient expands the melt pool laterally and brings Marangoni convection into the problem. The treatment of the laser scan pattern as a raster scan, the boundary physics and free boundary, and the conjugate heat transfer at domain interfaces, all complicate the physics. The governing physics so far detailed are based on immediate consolidation, which does not

consider the problems of differential absorption and scattering of incident laser light due to the powder bed.

This complex thermal and fluid dynamics problem needs to be coupled with some tool to predict the microstructure and morphology of the deposit. Cellular automata is an effective tool that can be coupled with the thermal solution to predict the grain structure [11]. Additionally, an empirical model can be built from the experimentally obtained microstructures, which provides precise locations of transformations for SX deposits. These branches of the problem are closely related to the image analysis problem and to identification of different characteristics in the deposit. Finally all the modeling efforts must concur with the experimentally obtained results to validate the model developed. The different branches involved in this complex problem are highlighted in Figure 7, and some important aspects of the processing physics are dealt with in the present research.

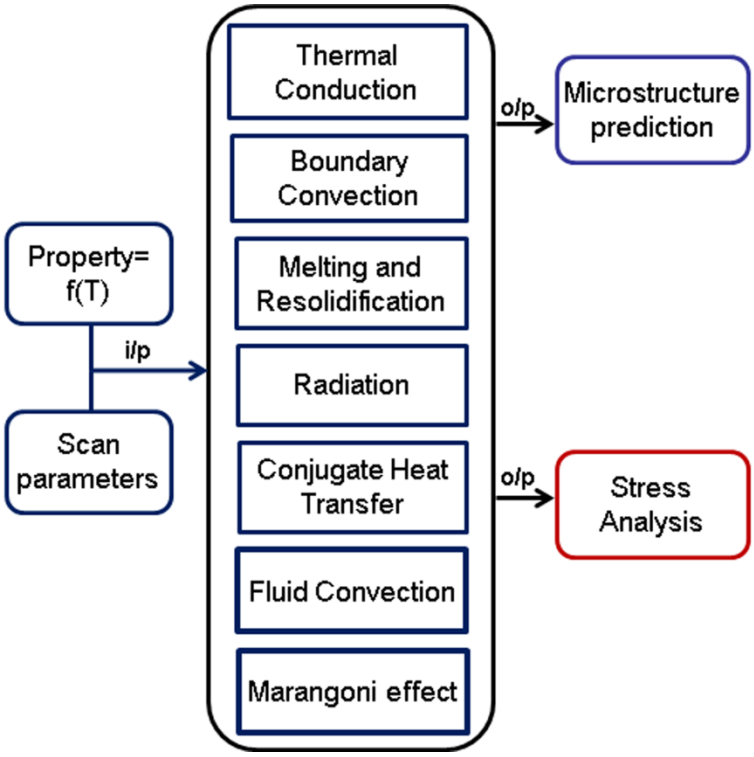

Figure 7. Coupling of essential physics in SLE process.

1.4 Significance of the work

Examples of SLE deposited on SX (CMSX-4) and EQ (René 80) superalloys are shown in Figure 4 and Figure 8. As known from prior literature, the existing state-of-the-art methods of repair fail to maintain the epitaxy in the SX deposit, and deposits are plagued by crack formation for EQ deposits. For example, selective laser melting (SLM) is not capable of creating structures with defined microstructure, and often has issues with warping and porosity in underlying layers. Direct metal laser sintering (DMLS) has issues with regulating the melt depth of each layer. In LENS the powder is blown into the melt pool, thus creating additional convection and unwanted turbulence, which may result in grain multiplication and formation of stray grains. This limits the

use of LENS for SX superalloys. Additionally, processes such as SLM, DMLS, and LENS operate using open-loop control schemes and under improper atmospheric conditions, limiting the quality of the produced deposits. In contrast, for SLE, feedback control is attempted and is found to consistently produce dense, uniform deposits for both SX and EQ superalloys [12].

Figure 8. Representative René 80 deposit produced by SLE.

However, applying feedback control for any given superalloy requires closer investigation of the operational parameter set. An important criterion is the determination of energy density that allows a good metallurgical bond between the newly created deposit and its substrate. The metallurgical bond is primarily important at the starting edge of the sample. A number of preheat scans (to-and-fro movements of the laser beam in one direction without moving forward) are required to ensure a proper fusion at the starting edge. Otherwise, there will not be a good metallurgical bond at the starting edge of the deposit as shown in Figure 9. However, too many repeat scans can cause balling at the starting edge, and sometimes excessive meltback near the starting edge as shown in Figure 10. Similarly if the scan speed is too high, the deposit will melt, and there will be a thermal lag in the substrate region, resulting in warping of the sample as shown in Figure 11. Use of higher power expands the melt pool, resulting in a lower temperature gradient in the vertical direction and significantly reduced SX height, as shown in Figure 12.

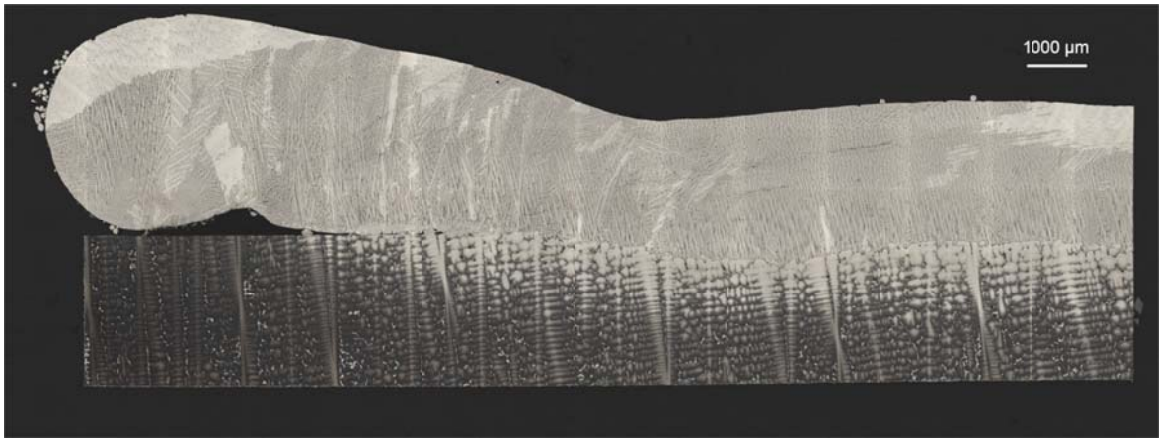

Figure 9. Lack of fusion at the starting edge for SLE deposit due to reduced number of preheat scans.

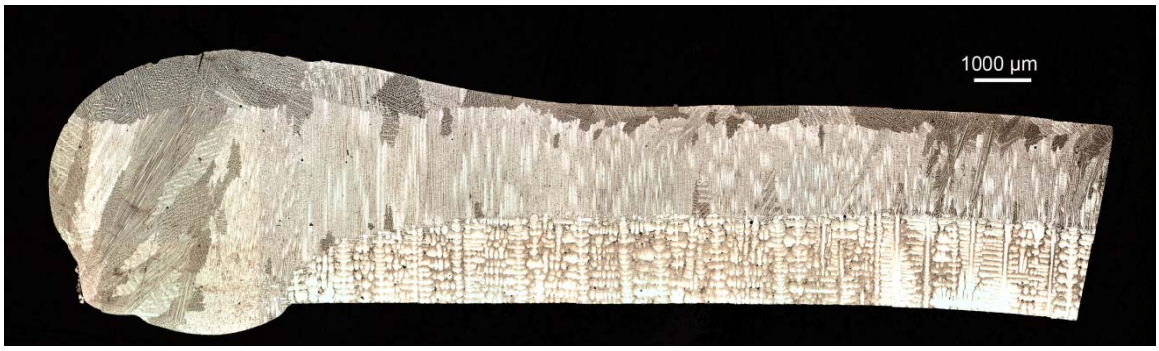

Figure 10. Excessive meltback due to excessively large number of preheat scans.

Figure 11. Warping of SLE deposit due to higher scanning speed.

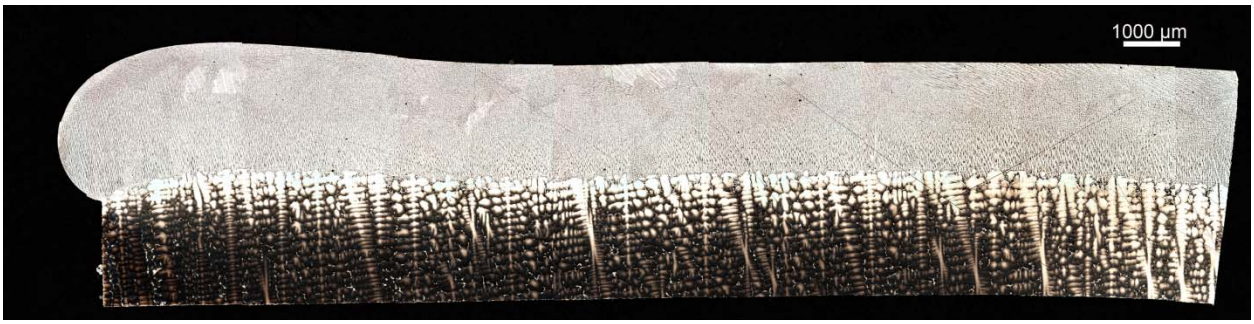

Figure 12. Smaller SX height due to inadequate vertical temperature gradient generated by operational parameters.

As highlighted in the last paragraphs, the critical experimental effort in SLE is to investigate the effect of operational parameters on each individual material and to determine the optimal set of parameters that can create a deposit with a reasonable meltback of substrate, yet that does not allow ripples at the top surface or balling near the starting edge. From the microstructural aspect the deposit should be epitaxial; so, for an SX deposit the SX height should be maximized. The number of cracks and the amount of porosity should be minimized in the resultant deposit. Consequently, for each set of parameters, the responses need to be recorded and the parameter set has to be refined to find the optimal operational range for scan speed, scan power, scan spacing and number of preheat scans. These experiments can be judiciously performed by applying design of experiments (DoE) based on the input parameters and output responses, and is of utmost significance.

Since, the number of output responses is large; a control chart based on individual variables will eventually lead to an inflated out of control error (α-error) or a false signal (β-error). Also, individual monitoring of the parameters does not provide any indication about the change in covariance matrix. So, multivariate statistics will be more adequate to better understand the

process. This will also allow generation of control limits for the superalloy and continuous refinement or improvement of the operational regime.

The materials studied in this dissertation represent a wide range of Ni-based superalloys. René 80 and IN 100 are considered 'non-weldable' by the presently available repair methods [10]. No repair attempts are made on IN 100 because of the higher propensity of crack formation in this EQ superalloy. CMSX-4 is a SX superalloy that has been previously studied, and limited success has been obtained in maintaining the epitaxy [5, 13-15]. René 142 is one of the most oxidation resistant superalloys developed [16], and limited data is available on the attempt to coat René N5 by depositing René 142 [17, 18]. All these alloys are significantly different in thermo-physical properties, emissivity and mechanical properties [19]. Hence the DoE approach highlighted in the last paragraph needs to be repeated for each superalloy in order to establish the differential responses of the individual materials.

The requirements of a physical model that can provide insight into the SLE process for individual superalloys are described in last section. The existing coupled thermal-fluid flow solution for laser heat treatment lacks generalization for a raster scan approach and does not consider the local property variation as a function of temperature [20]. More importantly, the coupling of computational fluid dynamics solutions and microstructural evolution is attempted in the present research through cellular automata and empirical models by using a robust image analysis tool based on active contouring.

1.5 Research questions

The primary endeavor of the present research can be summarized by the following questions.

1. Can SLE successfully create dense, crack-free deposits for different 'non-weldable' superalloys? We can divide this problem into different material types.

    a. Can SLE create an epitaxial SX deposit without harming the parent material and deteriorating the properties by introducing cracks and porosity?

    b. Can SLE create a crack-free, dense and uniform René 80 deposit with EQ morphology?

    c. Can SLE repair a 'non-weldable' alloy such as IN 100, which is impossible to repair by any given state-of-the-art methods?

    d. How will SLE perform with different superalloys for the substrates and the deposit, and what will be the microstructural characteristics of the deposit?

2. Is it possible to obtain an optimal parameter range for individual superalloys, and how can the multivariate statistics improve the optimization process?

3. Is the coupled thermo-fluid model adequate to simulate the SLE process and predict the melt depth correctly? How should the findings of the model be validated?

4. Is the microstructural model adequate to describe the microstructural transition and morphology?

If different materials are shown to be repaired using SLE, then this technology can work as an effective tool in creating engine-ready components with functionally graded materials (FGM). It is hypothesized that proper control of process parameters in the SLE process will allow for the joining of previously non-joinable nickel-base superalloys as well as the creation of deposits

with spatially tailored microstructures. The insights available from the models will allow determination of an empirical microstructural model based on operational parameters. The use of feedback control coupled with microstructural simulation is hypothesized to be capable of creating as-desired deposits with functionally graded materials and microstructures.

1.6 Outline of the dissertation

Chapter 2 of this dissertation will outline the prior repair efforts for hot gas flow components in gas turbines. The challenges and prior efforts in modeling the complex physics are highlighted. The emphasis is on understanding the process-property relationship and resultant mechanical problems associated with cracks, porosity etc.

Chapter 3 will present details about all of the hardware and software implemented as part of this dissertation that enables the SLE process. This will also serve as the validation tool for the model developed.

Chapter 4 will focus on details of a feasibility study of depositing individual materials by SLE and will closely look at the microstructural responses for each individual superalloy.

Chapter 5 will cover the implementation of a coupled flow-thermal model that can take into account the input parameters, material properties and governing physics and can predict the flow physics. The flow-thermal model is coupled to a robust empirical microstructural model via an image analysis tool based on an active contouring model. Additionally the model validation is performed via real time thermal imaging data, and a cellular automata model is developed to predict the microstructure.

Chapter 6 will cover the design of experiments study on selected superalloys and identify the output parameters for the multivariate statistics study. A Hotelling T^2 method will be applied to develop a control chart for each individual superalloy.

Chapter 7 will provide a summary of the research conducted as part of this dissertation, address the novel contributions, and outline some potential avenues for further research in this area.

Chapter II

Background

2.1 Introduction

The growth of solid freeform fabrication (SFF) technology has been enormous in the last few decades. Several complimentary technologies simultaneously evolved to meet new challenges in the manufacturing domain. Transfer methods of SFF (Selective laser sintering, Computer aided pattern modeling) focused on generating patterns that are used to generate the final component. Indirect methods (RapidTool, Laminated object manufacturing) successfully created intermediate density parts and required post-processing operation to achieve final density. In contrast, direct methods (LENS, ELMF) implies additive consolidation of feedstock to complex shapes having full or near full density without the use of additional densification step [21]. The features of the direct method potentially mark it as the ideal candidate for the one step manufacture and repair of gas turbine hot-section components.

This chapter focuses on the development of gas turbine materials technology, on understanding the processing challenges faced due to material complexities of superalloys and, on the role of additive manufacturing and multi-physics models in resolving some of these problems.

2.2 Gas turbine application

As highlighted in chapter I, the gas turbine hot-section components represent the use of the strength of material at its extreme limits. The goal of increasing efficiency pushes the operating temperature and pressure ratio to increasingly higher values and consequently, only the most

advanced superalloys can be used in order to meet the high temperature specific strength requirements. Hence, research has been undertaken to improve superalloy properties to make them more durable and less crack susceptible. In this endeavor, the rupture strength, creep strength, oxidation resistance, and impact toughness of the superalloy are considered the governing properties to identify suitable candidate compositions for hot-section components in gas turbine. The hot-section combustion components are typically equipped with Ni-based superalloys while Ti or Co-based alloys are still used for other sections. The same trend is observed for industrial gas turbines. Figure 13 shows the cutaway of a commercial jet engine where the hot-section components are highlighted in red color.

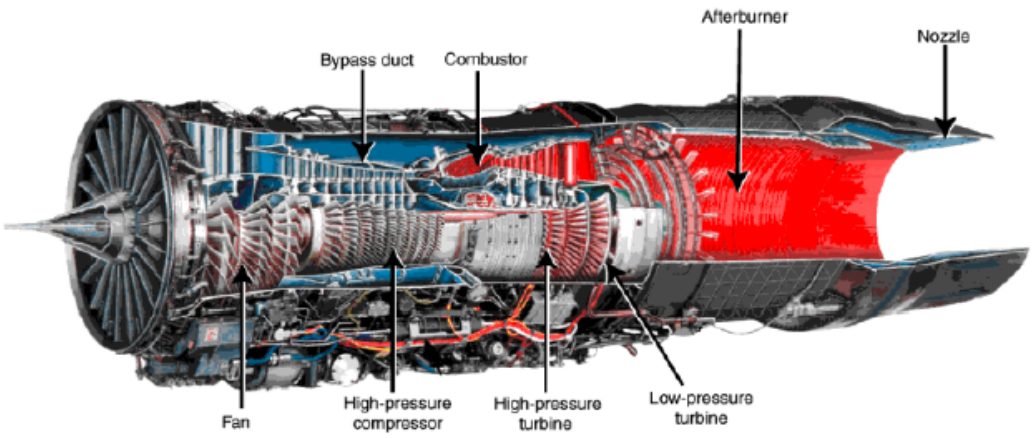

Figure 13. Cutaway of a commercial jet engine.

2.3 Superalloys

Superalloys were introduced to cope with the increasing demand for stronger and more corrosion-resistant materials for aircraft engines during World War II and since then evolved to meet the increasing demand for more efficient gas turbines. As mentioned in the last section,

turbine engine manufactures strive to increase the operating temperature as well as pressure ratio of the exhaust turbines operating in their engines. Figure 14 shows the progression in turbine operating temperature over the past 70 years as the material evolved from EQ to DS and finally to SX [22]. The temperature capability here corresponds to 1000 hrs. of creep life that results in 1% strain at that temperature.

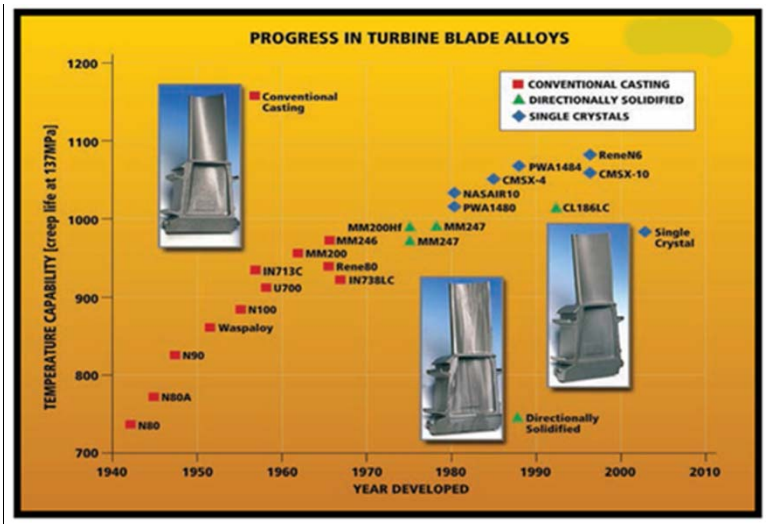

Figure 14. Progress in turbine blade alloys over 1940-2010 [23].

Superalloys typically contain close to ten different alloying elements to reach the desired property level for the hot rupture strength, fatigue resistance, creep strength etc. Typically high gradient casting (investment casting with high and well controlled thermal gradient) is used to develop customized and fine structured superalloys, although some wrought superalloys are also in use. The characteristics of a cast component is the segregation of constitutional elements, and the superalloys are characterized by different morphological phases in their composition such as different geometrically close packed phases (γ', γ'', η etc.), multiple types of carbides (MC, M_6C, $M_{23}C_6$, M being the metal) etc. It can be said that the grain size and morphology along with the production and control (manipulation) of the various phases provide unique characteristics to the superalloys.

The following paragraphs will highlight the benefits of Ni-based superalloys in extreme temperature and pressure conditions, explain the compositional and microstructural aspects of superalloys and describe the processing difficulties encountered in repairing superalloys.

2.3.1 Advantages

Figure 15 shows the increase in efficiency of the utility gas turbine (UGT) sector after World War II. This increase can be attributed to the increase in rotor inlet temperature (RIT). RIT increased from 500^{o}C to 1600^{o}C during this time [24]. This demand for high temperature systems was met by increasing the use of superalloys in gas turbine components. Figure 16 shows how the relative weight of superalloy components nearly doubled in 20 years for UGTs. To improve the efficiency, weight must be shed from the engine components for aero-engines, which requires selection of high specific strength materials that can retain strength near melting temperature. Figure 17 shows the comparison of specific strength for different superalloys [23]. The set of specific strength curves with temperature takes account of the material's density, and indicates that even though nickel is practically twice as dense as titanium, it is the only material that retains sufficient integrity at high temperature. Ti-based superalloys are also avoided because in addition to being unstable above 600^{o}C, they can ignite and cover the rearward stages with molten metal when used in hot-section components [23]. Figure 18 (a) is a general arrangement of a state-of-the-art engine that depicts the range of materials employed to use the potential of each material to the maximum and Figure 18(b) shows a 3D arrangement of the materials and specific alloys for a turbine [25].

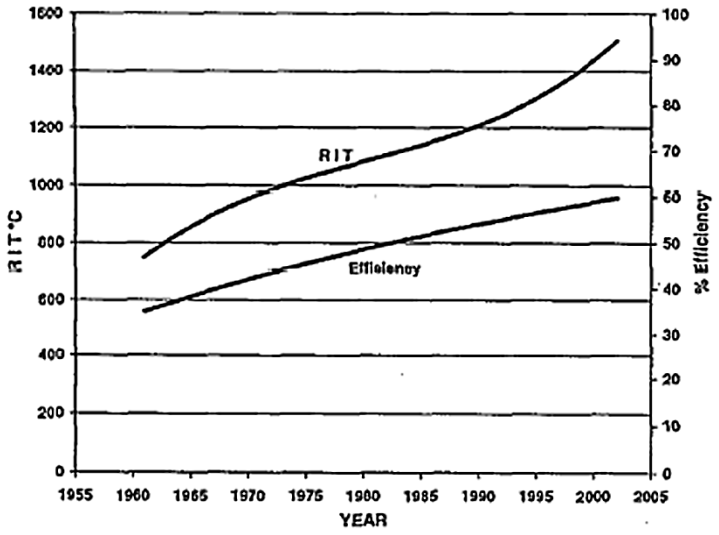

Figure 15. Improvement in R.I.T and efficiency over the year 1960-2005 [24].

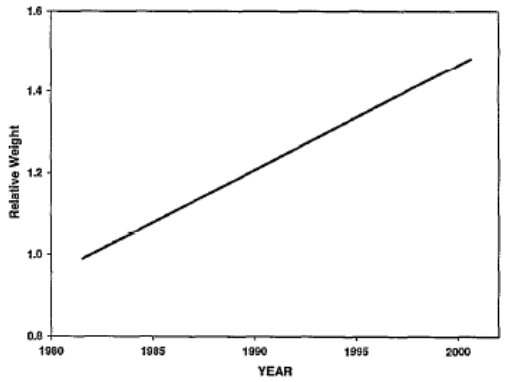

Figure 16. Increase in relative weight of superalloys in UGT over time.

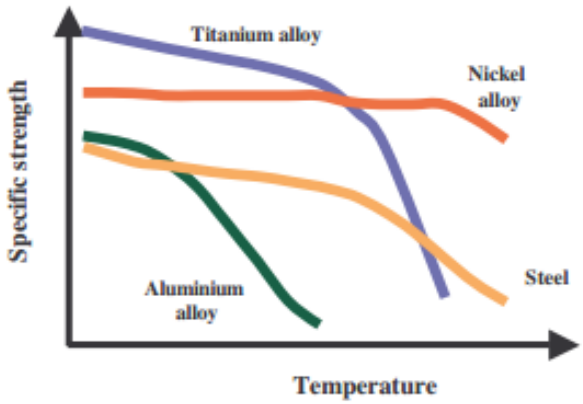

Figure 17. Specific strength behavior with temperature for different superalloys [23].

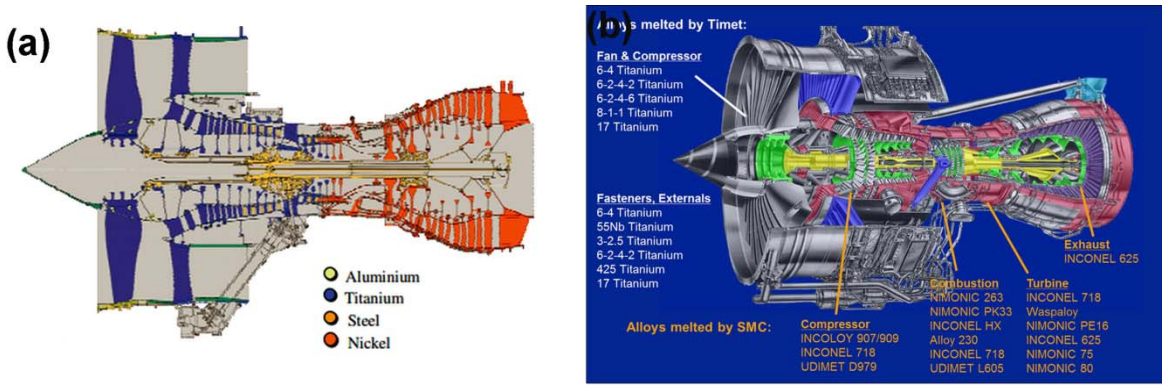

Figure 18. General arrangement of turbine materials [23, 25].

Ni-based superalloys exhibit high rupture strength at high temperature primarily due to precipitation strengthening of the ordered γ′ phase in the fcc γ matrix [26, 27]. The fraction of the γ′ phase is found to be the major factor influencing flow strength in Ni-based superalloys. The increased additions of Al and Ti to the fcc γ matrix increase the volume fraction of the γ′ phase. The γ′ phase, which is normally observed in cubic or spherical shape, coherently precipitates in the γ phase, remains stable till a very high homologous temperature, impedes the movement of dislocations and thus improves the mechanical properties, especially at high temperatures [28]. The addition of Ti is found to reduce the fault energy in the γ′ phase [29]. The Ti/Al ratio has great influence on the high temperature corrosion resistance and mechanical properties of Ni-based superalloys [30]. The precipitate of β-NiAl in the γ matrix for alloys with low Ti/Al ratios leads to the propagation of cracking into the grain interior. In contrast, a high Ti/Al ratio leads to the precipitation of η-Ni_3Ti at grain boundaries, which weakens the strength of the grain boundaries. The precipitates of both the β-NiAl and the η-Ni_3Ti phases are harmful to the stress-rupture life, and a peak stress-rupture life appears at intermediate values of the Ti/Al ratio, as shown in Figure 19. The rupture strength also depends on the heat treatment procedure

involved. The goal of the engine manufacturer is to obtain a high enough longitudinal rupture strength while maintaining an adequate transverse rupture strength. Figure 20 shows variations in the longitudinal rupture strength for different heat treatment procedures applied to the alloy René 142 [31]. This method of determining the heat treatment steps to optimize the rupture strength is an essential step in the development of any given superalloy.

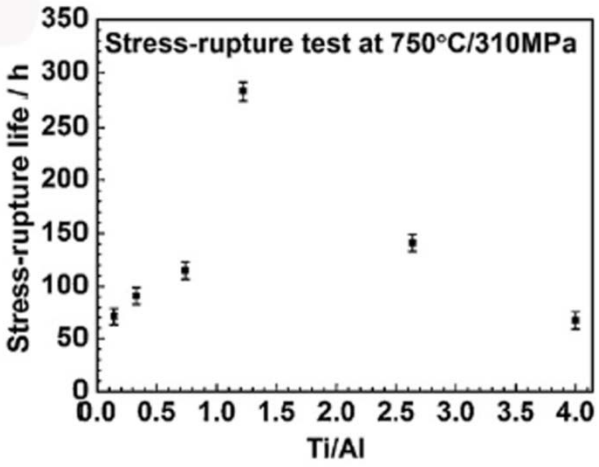

Figure 19. Variation of stress-rupture life (in hours) as a function of Ti/Al ratio [30].

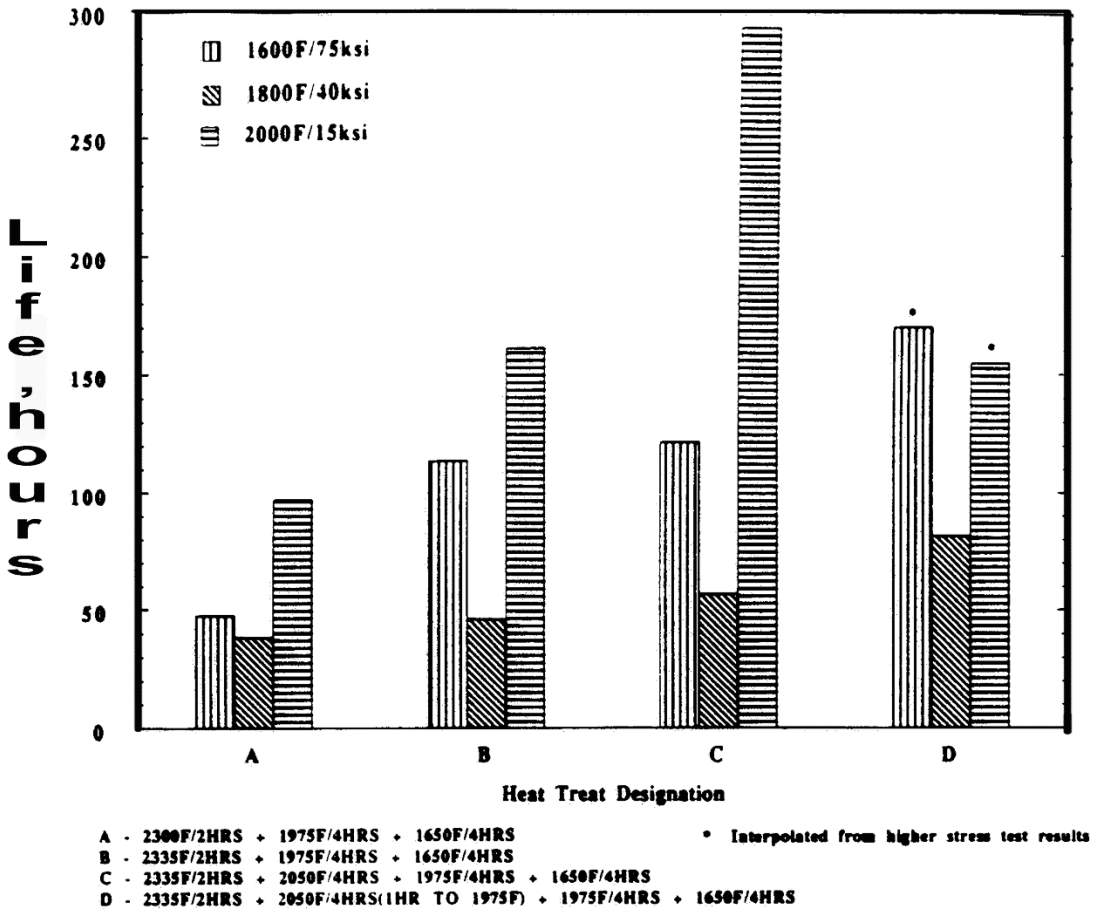

Figure 20. longitudinal rupture strength variations for different heat treatment procedures applied to the alloy René 142 [31].

High velocity oxidation resistance is another desirable characteristic in present day superalloys. Pursuit of this goal has led to the development of DS René 142 from the René 150 alloy; DS René 142 also contains 3% Rhenium for solid solution strengthening. The presence of 2.2% Vanadium is the primary reason for poor oxidation resistance in René 150. Optimization of Ti, Al and Cr content and elimination of V provided the exceptional oxidation resistance in René 142. The oxidation test verified only 1 mil of metal surface loss at 2150°F with velocity at Mach 1 [31]. Figure 21 compares the oxidation resistance of different superalloys. The surface loss in René 142 is clearly 5-25 times smaller than those of different 'second-generation' superalloys.

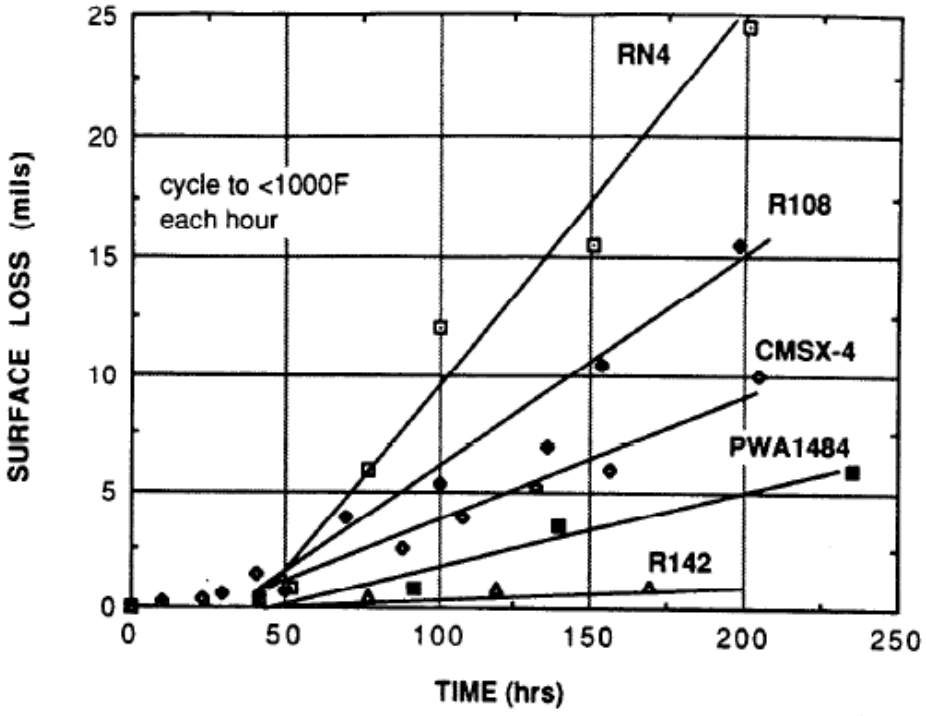

Figure 21. Comparison of oxidation resistance for different superalloys at 2150^{o}F and at Mach 1 velocity [31].

Superalloy components also need to endure impact loadings against foreign objects during their service at high temperatures; thus high impact toughness is also required to prevent catastrophic failure. A study of M951 alloy based on Charpy test concluded that MC carbides are the crack initiation sites [32]. The nucleation, growth and coalescence of dimples formed at the fracture surface are found to be the major fracture feature at elevated temperature.

Superalloys in hot-section turbine components are subjected to prolonged loading at high temperature, so high creep resistance is a very important criterion for the selection of a superalloy. As shown in Figure 22, Ni-superalloys last longer at elevated stress and temperature

levels compared to Fe-Ni and Co-based alloys. The grain structure of the superalloy also contributes to the creep properties. SX morphology provides higher stress rupture strength.

The Larson-Miller parameter is a means of predicting the lifetime of material with respect to time and temperature; this is done by using a correlative approach based on the Arrhenius rate equation. The value of the parameter is usually expressed as shown in equation 2,

$$LMP=T(C + \log t) \tag{2}$$

where C is a material specific constant often approximated as 20, t is the stress-rupture time in hours and T is the temperature in Kelvin scale [33]. The Garofalo sine–hyperbolic expression suitably correlates stress dependence for the entire stress regime, as it reduces to a power–law relationship at low stresses and becomes exponential at higher stress limits [34]. Scholz et al. studied the creep behavior of SX CMSX-4 in the temperature range 850^{o}C to 1050^{o}C [35]. Figure 23 shows the Larson-Miller plot obtained for <001> crystallographic orientation and demonstrates the creep response for CMSX-4. Similarly, Egly et al. [36] also investigated the fatigue and lifetime effects for CMSX-4 resulting from thermo-mechanical loadings tests that used different strain paths and different phase shifts between temperature and mechanical strain.

2.3.2 Fabrication

Investment casting is the traditional method of creating superalloy parts for the hot-section components of gas turbines. However, the complexity of the casting process increases as we move from EQ to DS and to SX casting.

For the EQ components, the molten metal is poured into a ceramic mold at a pressure below 10^{-2} torr. The entire process is conducted in vacuum to prevent the highly reactive elements in the

superalloys from reacting with oxygen and nitrogen in the air [37]. With proper control of metal and mold thermal conditions, the molten metal solidifies from the surface toward the center of the mold, creating an EQ structure. To prevent shrinkage porosity, care is taken to allow proper feeding of molten metal to the casting while it solidifies.

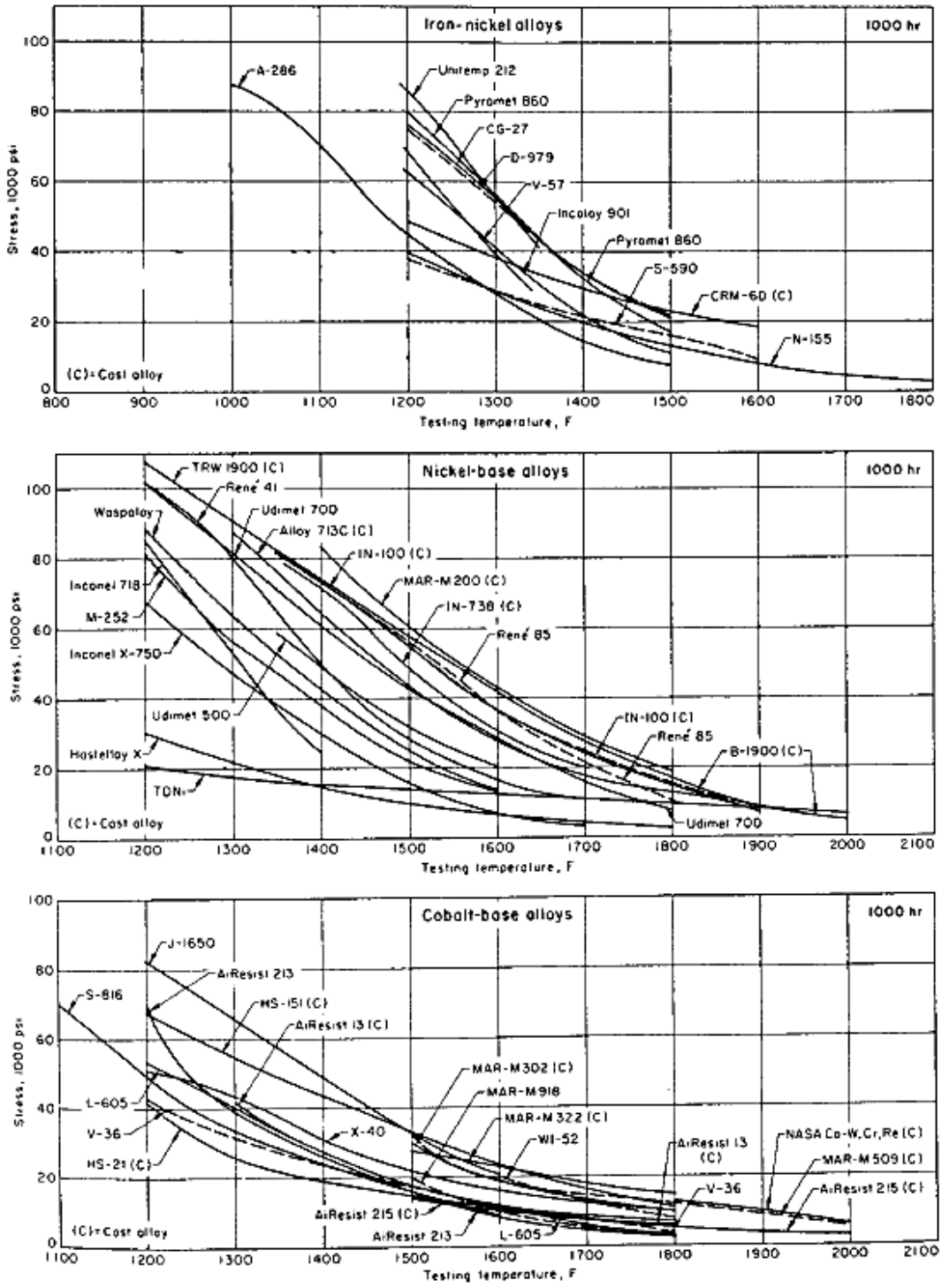

Figure 22. Effect of temperature on 1000 h stress-rupture strength of a variety of superalloys plotted by alloy type [9].

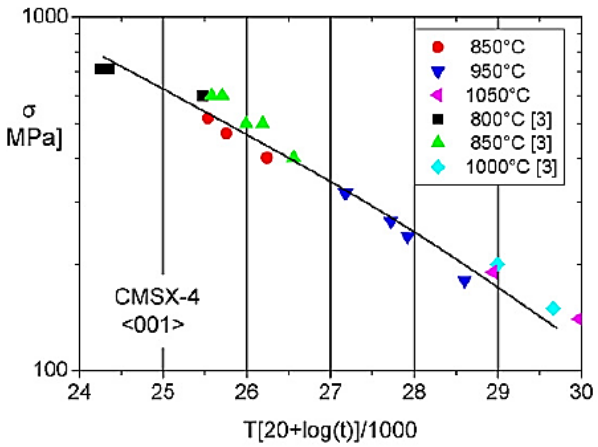

Figure 23. Larson-Miller plot for CMSX-4 with <001> orientation at different temperatures [35].

DS and SX components are typically investment cast using either a Bridgman or Stockbarger technique. In these techniques, the mold is slowly vertically withdrawn from a casting furnace or induction heater at a controlled rate (on the order of several centimeters per hour), thus slowly propagating the solid-liquid interface and elongating the grains in the direction of withdrawal. Normally, this results in a DS structure, but if a seed crystal or seed selector is placed at the bottom of the casting mold, these techniques can produce an SX structure [38]. Figure 24(a) shows a Bridgman casing process where the crucible is drawn downwards at a constant temperature gradient and uniform rate. The cooling rate is a product of temperature gradient and the crucible velocity here, and thus the microstructure uniformity is maintained. The other process shown in Figure 24(b) is for DS components, and the microstructure is no longer uniform. Here the growth rate and the temperature gradient decrease as the distance from chill increases.

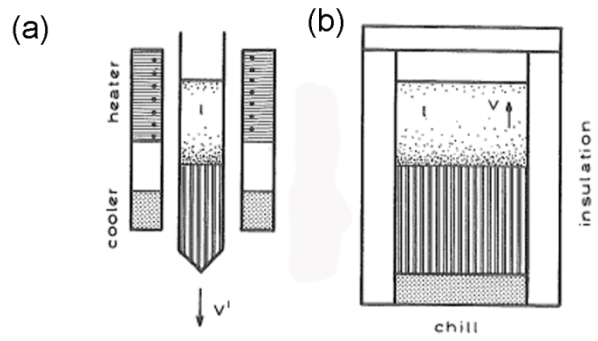

Figure 24. (a) Bridgman casting for SX superalloy (b) for DS superalloy [37].

To improve the productivity of SX casting, liquid metal cooling-assisted casting (LMC) has been adopted. Low thermal gradient, slow growth rate and long solidification time restrict the use of the Bridgman technique in the industrial environment. In LMC, a liquid metal such as Al/Sn is used as cooling medium. The main advantage of LMC is the increased thermal transfer due to the conductive cooling as compared to the radiative cooling in the Bridgman process. The liquid metal is in equal contact with every individual mold, which enables greater part to part consistency. The increased withdrawal rate due to the higher thermal gradient decreases the time for mold-metal reaction and increases the rate of production. Figure 25 shows the details of the LMC process.

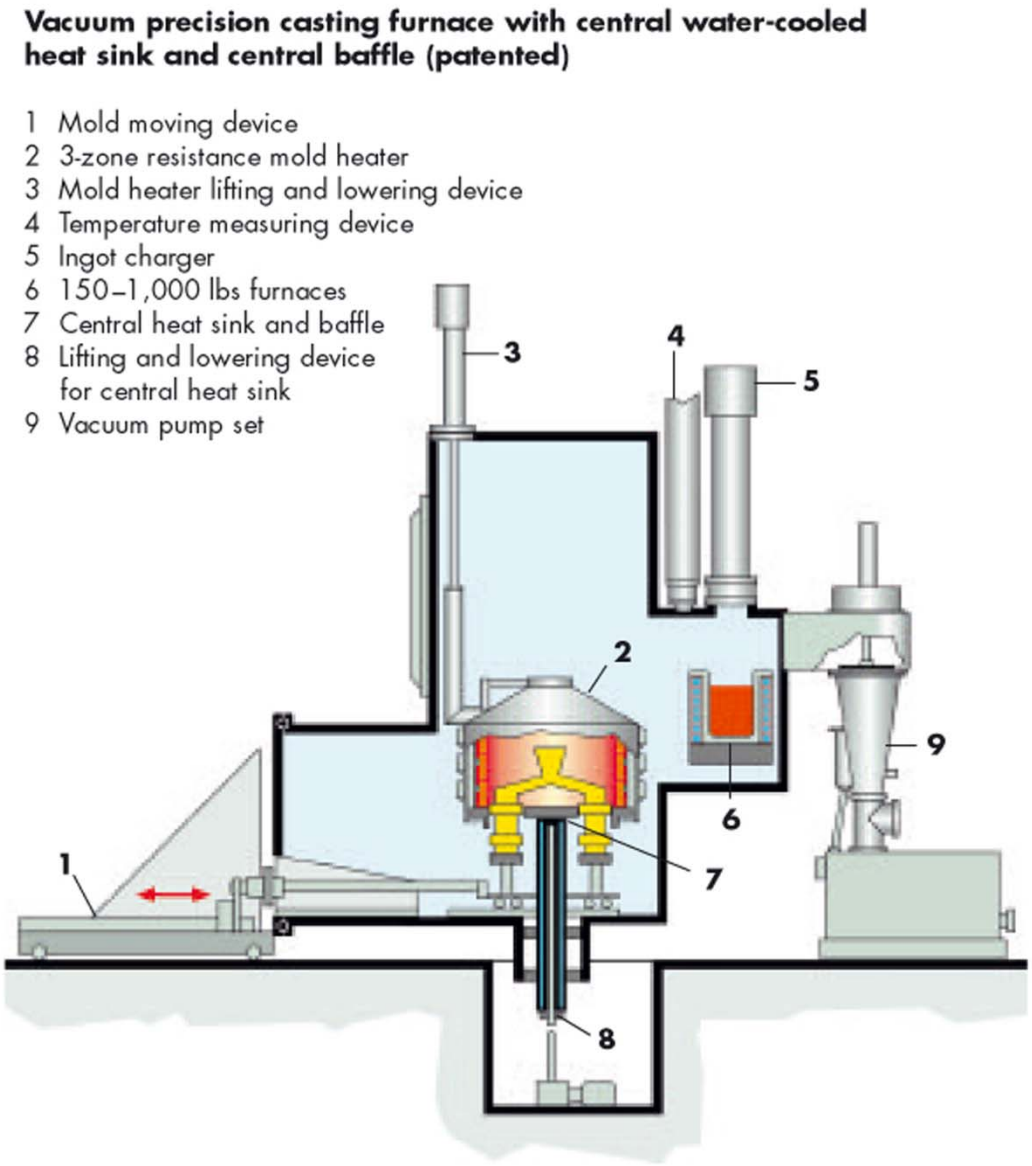

Figure 25. Schematic of the LMC process [39].

2.3.3 Composition and Microstructure

Ni-based superalloys primarily consist of intermetallic precipitates in a solid solution of fcc-Ni matrix or γ matrix. The intermetallic precipitates are known as γ′, and a high volume

fraction of γ′ (up to 70%) is typically added to improve the strength of the γ-matrix. The γ′ is chemically represented as $Ni_3(Al, Ti)$, with Al and Ti replacing the corner Ni atoms in an fcc structure and forming a coherent phase with fcc-$L1_2$ phase. The secondary phase precipitate provides substantial dislocation motion retardation at high temperatures by forming an anti-phase boundary and locking the disassociated dislocations at high temperatures [4, 40, 41]. This translates to various types of improved strength, including high temperature tensile strength. Figure 26 shows the crystal structure and arrangement of γ and γ′ phase in Ni-superalloy. The main purpose for γ′ strengthening in superalloys is to retain the stability and the coherency of the γ′ precipitate with the γ matrix up to a very high homologous temperature.

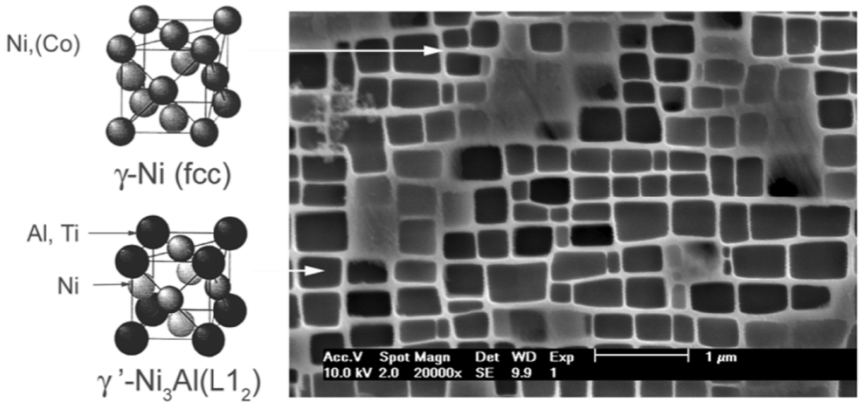

Figure 26. γ matrix and γ' precipitate in CMSX-4 superalloy [13].

A typical Ni-base superalloy used in gas turbine applications contains more than ten elements to optimize the material for best possible performance in an aggressive loading scenario. The optimized alloy should meet increased mechanical and thermal strength demands and should be metallurgically stable at elevated temperatures during service life. Generally, aluminum, titanium and tantalum are used as precipitation-strengthening or gamma-prime forming elements. Among other elements, chromium is added to improve corrosion resistance, whereas molybdenum and tungsten are used to increase the melting temperature of the alloy [9]. Al can also build a protective Al_2O_3 layer and add to the corrosion and oxidation resistance. Tungsten, niobium,

tantalum and molybdenum also help improve the creep strength of the alloy, as they diffuse slowly because of their higher atomic weight, thus imparting more microstructural stability. Some of these elements partition to the γ matrix while others partition to the γ′ precipitate [42]. Rhenium is added to retard the coarsening of γ′ precipitate. It generally partitions to the γ matrix. Carbon and boron are used as grain boundary strengthening elements; however, they also reduce the melting temperature of the alloy. Careful element addition is necessary in superalloys, since some elements facilitate formation of brittle plate-like μ, sigma or Laves phases. The μ phase is typically of rhombohedral crystal structure and is found in alloys with excess percentage of Mo or W. The sigma phase is a tetragonal phase that forms after prolonged exposure to a temperature between 540^{o}C and 980^{o}C. The Laves phase is hexagonal and also forms due to high temperature exposure. These phases are topologically close-packed (TCP) phases and cause reduction in rupture strength and ductility [9]. Cr is a potential brittle sigma phase former. Hence it is increasingly being put in the coating material rather than the superalloy for the blade itself [42]. This unfortunately results in both a loss of solid solution strengthening and oxidation resistance. The addition of molybdenum for solid solution strengthening and aluminum for oxidation resistance initially compensated for the reduced chromium, but it was found that chromium levels around 1.5% were needed to avoid the onset of hot corrosion [43]. Molybdenum levels above approximately 3.5% were also found to be harmful to hot corrosion resistance, leading to the substitution of some molybdenum by other refractory metals such as tungsten, tantalum and niobium [44]. Grain boundary carbides play a major role in the control of creep and fracture behavior and can be modified by heat treatment and by the addition of minor constituents such as boron and zirconium [24]. Hafnium is also a strong carbide former and is added to

polycrystalline alloys to improve grain-boundary ductility [45]. Table 1 shows the role of elements on the property modification of superalloys.

Table 1. Role of elements in nickel-based superalloys [42].

Elements	Effect on microstructure and properties
Co, Cr, Fe, Mo, W, Ta, Re	Solid-solution strengthening
Ti, W, Mo, Ta, Nb, Hf, Cr	Carbide former
C,N	Carbonitride former
Al, Ti	Forms γ′ phase
Co	Raises solvus temperature of γ′ phase
Re	Retard γ′ phase coarsening
Nb, Ta	Forms γ″ phase $Ni_3(Nb,Ta)$
Al, Ti, N	Form hardening precipitates and/or intermetallics
Al, Cr, Y, La, Ce	Increase oxidation resistance
La, Th	Improve hot corrosion resistance
Cr, Co, Si	Increase sulphidation resistance
B, Ta	Improve creep properties
B	Improves rupture strength
B, C, Zr, Hf	Grain refiners
Hf	Improve ductility at intermediate temperatures

Despite the superior properties attained by optimizing the alloying elements, Ni-based superalloys are still tested in the extreme limit when it comes to gas turbine applications. The presence of carbon and boron reduces the melting point and the high temperature microstructural stability of the alloy. However, these are important elements for equiaxed or polycrystalline superalloys. Turbine components cast with a polycrystalline morphology are also prone to failure because they contain some grain boundaries that are transverse to the longitudinal direction of the blades or to the main axis of stress when a blade is rotating around in an engine. EQ grains are prone to form voids at the grain boundary that are transverse to the longitudinal direction. Hence to reduce this problem, DS superalloys were introduced around 1960 [46]. The resultant oriented grain structure runs parallel to the major axis of the part and contains no transverse grain boundaries. The elimination of these transverse grain boundaries imparts additional creep and

rupture strength to the alloy by reducing the creep void formation, and the orientation of the grain structure provides a favorable modulus of elasticity in the longitudinal direction to enhance fatigue life. By directionally solidifying the alloy GTD-111, an increase of approximately 23ºC (40ºF) in creep strength and an increase of approximately 10X in fatigue life could be realized [47]. The increase in creep strength and fracture toughness can be further enhanced by casting the blade with SX morphology that does not contain any grain boundary at all. This SX morphology also allows removal of carbon and boron that would otherwise reduce the melting temperature and the fatigue life of the alloy. As an example, the use of Rene´N5 can produce an increase of more than 35ºC (~60ºF) in creep strength and 2X to 3X increase in fatigue life when compared to DS GTD-111. Figure 27 shows the grain morphology of EQ, DS and SX turbine blades and Figure 28 shows the temperature ranges that can be attained by changing the morphology from EQ to DS and finally to SX.

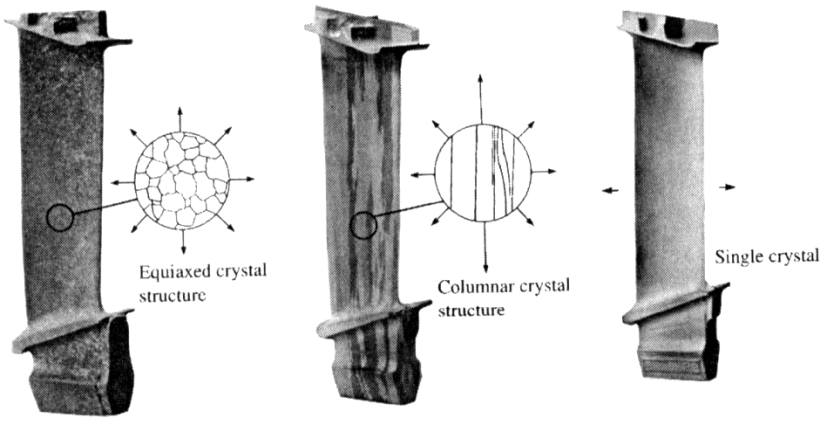

Figure 27. EQ, DS and SX morphology in turbine blade [38].

SX morphology can be further improved by adding Rhenium (Re). The 'first-generation' SX superalloys (e.g. PWA 1480) did not contain Re and offered 25-50^{o}C improvement over R.I.T and 1% improvement in creep life. The 'second-generation' SX superalloys (e.g. CMSX-4)

contained 3% Re and offered 30-35^{o}C improvement in R.I.T. The 'third-generation' SX superalloys (e.g. CMSX-10) contain more than 5% Re and a higher amount of refractory metals (W,Al). This further enhanced the creep-rupture strength and improved the R.I.T by 30^{o}C, enabling use of un-cooled blades at 1200^{o}C, thus causing increased efficiency by reducing amount of cold air requirement [47]. Figure 29 shows the gradual improvement in the low-cycle-fatigue (LCF) life of the turbine buckets by introducing SX morphology and increasing Re content.

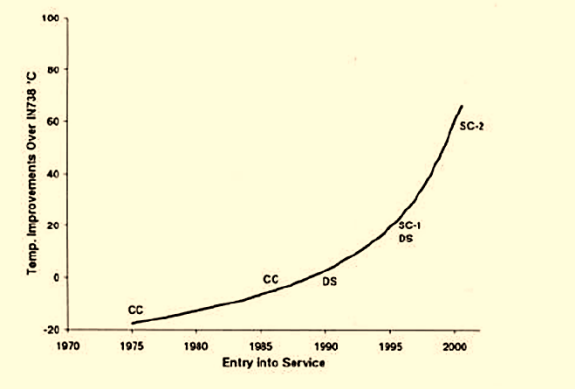

Figure 28. Increase in R.I.T over IN738 due to introduction of DS, SX (1st generation) and SX (2nd generation) superalloy [24].

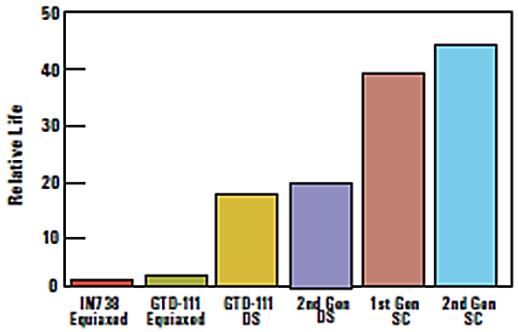

Figure 29. Increase in bucket life due to change in morphology and Re content.

2.3.4 Processing challenges

Most Ni-based superalloys are cast, and it is very important to consider the castability of alloys and subsequent cracking tendency after heat treatments. The castability test [48] for Ni-based superalloys is graded as shown in Table 2.

Table 2. GE DS castability test rating [31]

Rating	Criteria
A	No Cracks
B	Minor crack at tip, less than l/2" long or in starter zone.
C	One major crack, greater than l/2" long
D	Two or three cracks
E	Several cracks, more than 3 and less than 8
F	Many cracks - most grain boundaries

The superalloys investigated in this dissertation are all precipitation-hardened alloys or gamma-prime formers. The improvement in the property comes at the cost of processing difficulty, primarily evidenced by crack formation. Strain age cracking is caused as a consequence of the precipitation of γ' phases, hardening of the alloy during thermal exposure and transfer of solidification strains onto the grain boundaries. The susceptibility to strain-age cracking and the alloy weldabilty is often qualitatively described for Ni-based superalloys by plotting Al vs. Ti content in the alloys [10]. The alloy is considered 'non-weldable' if the total Al+Ti content exceeds 4wt%, and the welding difficulty increases as the total Al+Ti content increases. The superalloys investigated in the present research all fall in the "Difficult to weld" category as shown in Figure 6.

i) Types of crack formation

Different forms of cracking act as obstacles in the repair or processing of Ni-base superalloy components. The crack mechanism can be primarily distinguished as solidification cracking,

grain boundary liquation cracking/hot tearing, strain-age cracking (cold cracking) and ductility dip cracking. A brief description of the mechanisms of crack initiation and propagation is given below.

Solidification cracking occurs within the newly formed weld bead when the mushy, two-phase liquid-solid region experiences tensile stresses, and the high fraction of solid present (typically solid fraction>0.9) restricts the flow of liquid metal to backfill the interdendritic regions [10, 49]. The interdendritic regions are torn apart by tensile thermal stresses generated behind the weld bead as it progresses. Formation of solidification cracking is promoted by a wide solidification range for the alloy and by low welding traverse speeds. This form of welding defect in Ni-based superalloys can be avoided by optimizing the welding procedures used. Figure 30(a) shows one example of such cracking along the centerline of a weld bead in IN718.

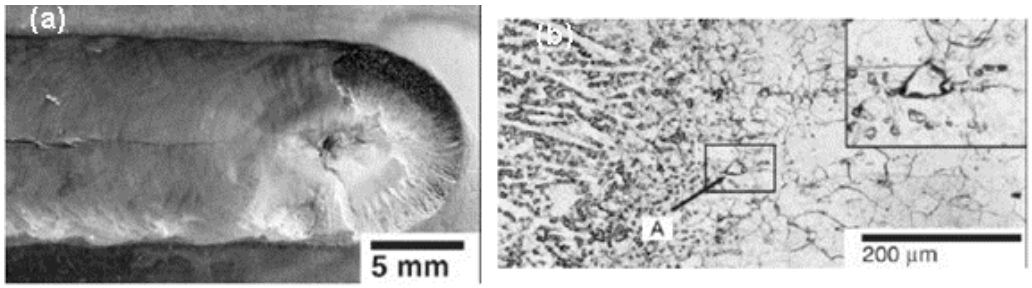

Figure 30. (a) Example of solidification cracking in IN718 during gas tungsten arc welding (GTAW) and (b) Example of hot tearing in IN718 during GTAW.

Local or partial dissolution of grain boundary phases leads to the formation of a low melting point eutectic and to melting of grain boundary regions, thus leading to grain boundary liquation cracking or hot tearing when the liquid film in the heat-affected zone (HAZ) fails under the tensile stress [50]. Typically the intermetallic carbide compounds (MC and M_6C) and different

secondary phases (Laves- and σ-phases) contribute to partial dissolution, and hence to the lowering of melting point. Different impurities such as sulfur, boron and phosphorus act to suppress the eutectic melting temperature and consequently to increase the HAZ fissuring susceptibility [10, 51]. A second mechanism known as constitutional liquation is particular to precipitation-hardened materials and occurs when a constituent particle such as TiC reacts with the surrounding matrix, causing localized melting. Creation of smaller grains exposes more boundary area and lowers the strain value, resulting in reduction of hot tearing. It is also verified that welding conditions such as heating rate affect the formation of this kind of crack. Increasing welding power results in more area being liquated, and the tendency of HAZ cracking thus increases. Figure 30(b) shows an example of hot tearing in IN718 in the HAZ.

Strain-age or cold cracking is a characteristic of the γ′-Ni_3(Al, Ti) precipitate strengthened alloys during the post-weld heat treatment or during subsequent high temperature service. Such cracking arises due to the presence of either residual stresses developed during manufacture, or applied stresses arising from service exposure. Often, the carbides act as the crack initiation sites. Intergranular micro-cracking in either the HAZ or in the weld bead forms as a consequence of the precipitation-hardening of the alloy during thermal exposure and transfer of solidification strains onto the grain boundaries [52].

The presence of chromium-rich boride particles often results in a different form of crack growth known as ductility dip cracking [53]. Ni-base superalloys lose their ductility on heating at the nil ductility temperature (NDT) and recover their ductility on cooling at the ductility recovery temperature (DRT). The difference between these two temperatures is known as the brittle temperature range (BTR); this is the temperature range where the alloy is susceptible to microfissuring at the HAZ. Boron and chromium lower the melting point and the DRT, thus

increasing the BTR and increasing the probability of cracking. However, the alloys investigated in the present research do not contain the high amount of Cr (more than 25%) required to initiate this process.

ii) Grain size

For EQ alloys, the grain size is a very important parameter that governs the mechanical properties. The increase in grain size, while modifying the grain morphology from polycrystalline to SX, normally would have resulted in a reduction of yield strength as indicated by the Hall-Petch relationship as:

$$\sigma_y = \sigma_0 + \frac{K_y}{\sqrt{d}} \tag{3}$$

Here, σ_o is the starting stress for the dislocation movement, K_y is the strengthening coefficient, d is the characteristic grain size and σ_y is the yield stress. The additional advantage of utilizing secondary phase precipitates is attributable to very high yield strengths for Ni-based precipitation hardened superalloys. However, EQ alloys are also more prone to creep void formations, since the grain boundaries are oriented in random direction and more grain boundary area is susceptible to the transverse loading than DS or SX alloys. Larger grain sizes in EQ alloys are beneficial from a creep strength perspective, since that reduces the grain boundary area. However, EQ alloys with larger grain sizes are also more prone to liquation cracking, since the grain boundary always acts as a potential site of segregation. Under rapid heating, the grain boundary phases are unable to dissolve fully into the surrounding matrix, and their partial dissolution leads to the formation of a low melting point eutectic and to melting of the grain boundary region [53]. Rush et al. showed that an increase in grain size lowers the ductility and

causes more segregations of melting point depressing elements at the grain boundary, resulting in an increase in average crack length [52, 54]. This can be also related to laser power, since application of higher laser power results in more area being liquated causing the temperature gradient to be reduced and larger grains to start forming. However, this might also result in re-solidification at lower temperature and change of the stress nature from tensile to compressive. Hence, the constitutional liquation, i.e. grain boundary γ′ dissolution and formation of γ/γ′ eutectic, is more detrimental and results in more liquation cracking [55]. Ideally, from an application point of view, the core of the hot-section components should be of fine grain structure thus establishing higher strength. However, near the boundary region the grain size should be larger to improve the creep strength.

iii) Porosity

In a typical laser repair of Ni-based superalloy components, two different classes of porosity can be observed. The first class arises as a casting defect. During the solidification of castings, a third gas phase forms and causes porosity. Pores form due to inadequate feeding of the volumetric change from liquid to solid and to the partitioning of solutes such as hydrogen, nitrogen, and oxygen [56].

On the other hand, in a laser repair process the cast part shows porous structure due to gas entrapment. However, even during the laser repair, pores can form due to inadequate compensation of solidification shrinkage by liquid flow. The interdendritic region sometimes gets starved due to the mushy region surrounding it, thus causing pores and often leading to cracks [57].

iv) SX characteristics

A SX deposit can further be characterized by three different microstructural parameters, which are of importance in determining the properties of the deposit. These parameters are primary dendrite arm spacing (PDAS), the columnar-to-equiaxed transition (CET) and the oriented-to-misoriented transition (OMT).

a) Primary dendrite arm spacing (PDAS)

Theoretically, it can be shown that for constrained growth, the tip undercooling is determined by the solute flux at the tip [37]. Assuming the fully developed dendrite as an ellipsoid of revolution [58], and assuming conditions of marginal stability [59], the PDAS follows the proportional relation $w \sim G^{-0.5}V_{sl}^{-0.25}$ (w = PDAS, G = temperature gradient and V_{sl} = solidification velocity). Pollock et al. reported the effect of the cooling rate on PDAS for different Ni-based superalloys in the investment casting process [60]. The proportional relation is employed to estimate the temperature gradient in the liquid metal cooling-assisted casting process for René N4 [61].

b) Microstructural transition

An important phenomenon in the solidification of SX superalloys is the columnar-to-equiaxed transition (CET) near the top surface of the deposit. In this process, the heat flow direction is in the negative z-direction, while the dendrite grows in the positive z-direction. The solidified region acts as a heat sink, and the temperature gradient ahead of the solidification front decreases. The CET is known to occur due to an increase in the isotherm velocity near the surface and a decrease in the temperature gradient which causes the formation of a

constitutionally undercooled zone [13, 14]. This transition parameter was correlated in prior literature to the temperature gradient and the solidification velocity.

A second solidification phenomenon known as a oriented-to-misoriented transition (OMT) [7] occurs in the SX deposit. The OMT is caused by a change in the direction of the temperature gradient in the solidifying metal deposit. This occurs as the substrate becomes increasingly hot toward the end of the scan, resulting in a growth competition between the columnar grains.

c) Stray grains

Constitutional undercooling results in the generation of EQ grains near the top surface of the laser-deposited part. However, due to local inhomogeneity in the temperature gradient and the solidification velocity, grains within the SX region nucleate with high and tilted boundary. These are known as stray grains. One reason for such stray grain formation is the breaking of secondary dendrite arms and convection of those broken pieces to a new location. The broken dendrite arms act as sources of nucleation in the new site [13]. This is the biggest drawback of the laser-based processes that rely on blowing powder onto the melt pool, since the excess convection allows easier breaking and convection of dendrites.

Stray grains are detrimental for mechanical properties. Because there are only a few stray grains, the high angle grain boundary area is fairly small. Due to segregation of γ/γ' eutectics around the grain boundary, a liquid film forms around the stray grains. Since the total grain boundary area is small, this will result in higher grain boundary wetting. Thus the material becomes more prone to cracking [42]. An increase in the number of stray grains will reduce the wetting but will further compromise the material property due to loss of SX nature.

2.4 Repair techniques

Repair attempts on modern superalloys started in the late sixties. Different welding techniques such as activated diffusion bonding involving vacuum furnace brazing, and diffusion and aging heat treatments were attempted [62]. In the present context, weldability is defined as "the capacity of a material to be joined under the imposed fabrication conditions into a specific, suitably designed structure and to perform satisfactorily in the intended service providing fitness for purpose with minimal distortion and a controlled/limited numbers of defects"[10]. The state-of-the-art processes for repair of turbine blades are still based either on the welding or the additive manufacturing based approaches.

2.4.1 Welding-based methods

Welding processes have been applied to the repair of Ni-base superalloys. The most commonly used processes are gas tungsten arc (GTA) welding or tungsten inert gas (TIG) welding, electron beam (EB) welding, and laser welding. Milidantri et al. tried to minimize the crack formation by heating the weld adjacent zone above the ageing temperature and maintaining it below the incipient melting temperature [63]. Each of these processes is typically subjected to the same limitations in producing specified microstructures such as DS or SX and crack formation [10, 64, 65]. United Technologies attempted a two-step process for the welding and the resultant crack generation. The first step deposits filler metal into the repair, and in the second a broad and shallow melt pool is created by using a defocused beam to obtain epitaxial morphology from the substrate to the top of the deposit [66]. Hence this method is typically suited for local repair on simple contours. Different methods have since then been tried in order to better suit complex contours [67-69]. Laser welding and EB welding of superalloys like

CMSX-4 have been shown to be less susceptible to cracking and stray grain formation than GTA welding.

2.4.2 Additive manufacturing-based methods

With the advent of the laser cladding processes, repair of components made of the "Difficult to weld" category of superalloys has been attempted [13, 14, 70, 71]. The first such attempt was made in United Technologies Research Center [72]. In this method, a continuous melt pool is first created using a high-power laser, and then powder is blown from a feeder assembly to create the deposit. The movement of the X-Y table in the scan direction helps move the scan in a desired-direction. Laser Engineered Net Shaping (LENS) [73, 74], Laser Metal Forming [75] and Epitaxial Laser Metal Forming (ELMF) [7, 13] evolved from this methodology. The schematic of the laser cladding process is shown in Figure 31.

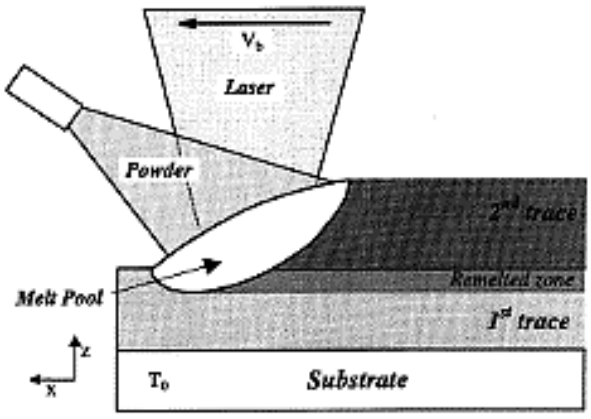

Figure 31. Schematic of a laser cladding process [5].

Attempts to repair cracks that form on the platform of a turbine blade were made using laser cladding. The work has since been expanded to many different alloys including CMSX-4, [20, 76, 77] but the SX growth is limited to a height of between 100-200μm. Although these methods

have seen some success, this method of repair has typically been plagued by crack formation as well as grain multiplication that occurred when dendrite arms were separated from their main dendrites due to remelting [13, 65, 78]. This grain multiplication results in a high-angle grain boundary and increased wetting at the grain boundary, resulting in more number of cracks. The powder blowing mechanism used for cladding processes leads to two significant problems. The first problem is in the disturbance of convective currents in the melt pool caused by the high velocity powder particles entering the melt, adversely impacting DS and SX microstructure formation and causing stray grain formation. The second problem is the limitation that having a mechanical powder feed assembly causes on the speed at which the energy source can scan across the substrate. It has typically been found that higher scan speeds lead to reduced cracking and stray grain formation, but the speed at which the energy source can move is significantly limited by the X-Y stage on which the substrate is mounted in typical cladding operations.

2.4.3 Processing parameters

Prior research showed the strong influence that the process parameters exert on the mechanical properties and microstructural transitions of the weld bead/deposited superalloy. Rush et al. studied the effect of process parameters on the cracking behavior of René 80 deposit using cold metal transfer with IN625 as filler alloy [54]. Welding power is shown to have high significance on the level of cracking, whereas welding speed has little effect. When welding using the laser, it is shown that the power and spot size are more crucial to the material cracking than the travel speed. It is indicated that the weld bead geometry has high significance over the occurrence of cracking, with a relationship between welding power, weld bead geometry, and stresses controlling the occurrence and magnitude of cracking. Lippold et al. studied SX CMSX-4 and analyzed the susceptibility to cracking as function of process parameters for electron beam

welding, and they compared the results with those obtained for GTAW. It was shown that electron beam processes are less prone to cracking [79]. Anderson et al. studied the formation of stray grains for GTAW, laser beam and electron beam welding processes and concluded that with the use of localized heat in the laser beam and in the electron beam processes, stray grain formations are reduced [80]. This is elaborated in Figure 32.

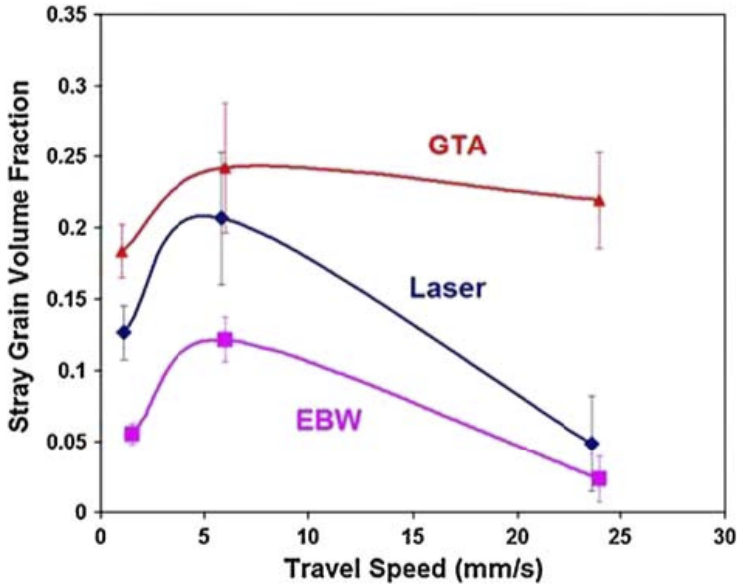

Figure 32. Comparison of stray grain volume fraction for different welding schemes as a function of travel speed [80].

Gäumann [5] studied the CET phenomenon in SX deposit produced using the ELMF process and developed a process map based on the operational parameters. The process parameters work together to affect different derived variables, such as temperature gradient (G) and solidification velocity (V). The CET is shown to occur below a critical value of the ratio, $\frac{G^n}{V}$, with n=3.4 and the SX morphology criterion can be expressed as,

$$\frac{G^n}{V} > K \tag{4}$$

Where, K is material dependent parameter and is experimentally determined to be 2.7×10^{24}.

Figure 33 shows the effect of process parameters such as laser power, scan speed, laser beam diameter and preheating temperature on the simulated $\frac{G^n}{V}$ ratio. This clearly illustrates that increasing the laser power reduces the $\frac{G^n}{V}$ ratio in the vertical direction. Increasing the preheating temperature produces a similar effect on the $\frac{G^n}{V}$ ratio. The laser beam diameter was shown to have a minor effect on this ratio. In contrast, low and high scan speeds both increases the $\frac{G^n}{V}$ ratio compared to the intermediate values of the scan speed.

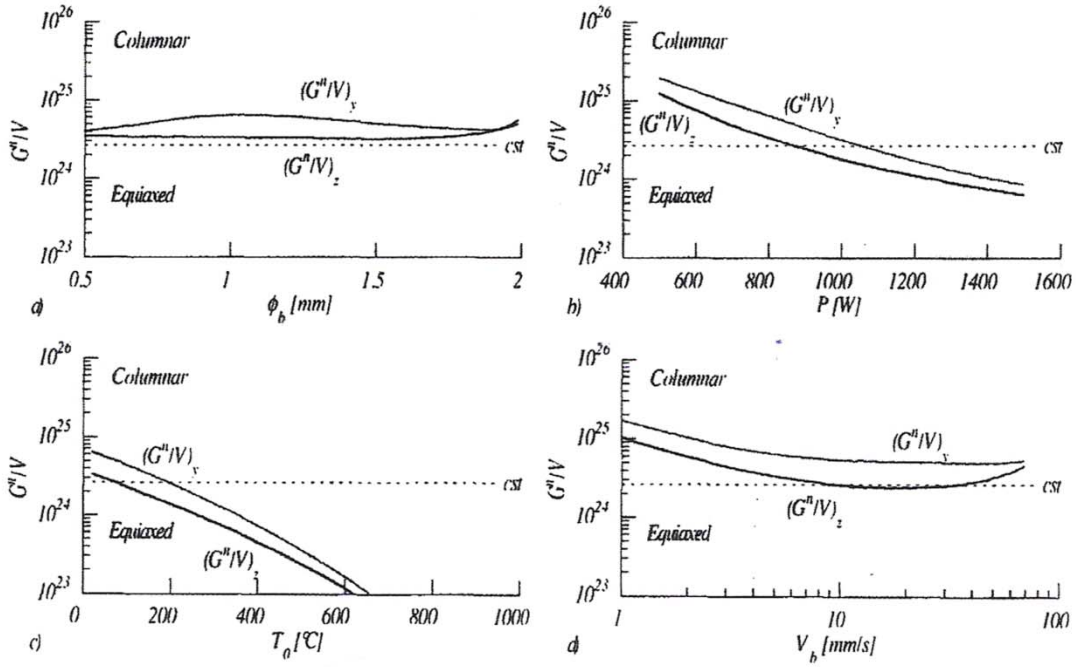

Figure 33. Effect of process parameters on $\frac{G^n}{V}$ ratio [13].

Later, Mokadem [13] coupled the effect of substrate orientation in order to characterize the dendrite growth geometry and then correlated the OMT phenomenon with the process parameters. Anderson et al. correlated the formation of stray grains with the process parameters in a more recent attempt [20].

2.5 Modeling schemes

The modeling approach involved in solving the laser-material interaction started with the analytical modeling of temperature distribution due to a localized heat source. Recent simulations tried to solve the detailed physics numerically. However to reduce the computational burden, the analysis is restricted to a small subset of the detailed physics problems, such as agglomeration of powder, tracking of melt pool or modeling a single bead scan with constant property material. These are studied using an advanced numerical scheme.

2.5.1 Analytical modeling

Rosenthal [81] first proposed a solution of the temperature field due to a moving point heat source over a solid body. The temperature field can be represented as,

$$T(x,y,z) = T_0 + \frac{\beta P}{2\pi K r}\exp\left\{\frac{-V_b(r+x)}{2\alpha}\right\} \tag{5}$$

Figure 34 shows the movement of the point source in the x-direction over the semi-infinite solid body with constant thermo-physical properties and the xyz co-ordinate system tied to the source. P and V_b are the power and the velocity of the source, r is distance of an arbitrary point given as $=\sqrt{(x^2+y^2+z^2)}$, K is the thermal conductivity of the solid body, α is the thermal diffusivity and β is the absorptivity of the solid body relative to the source.

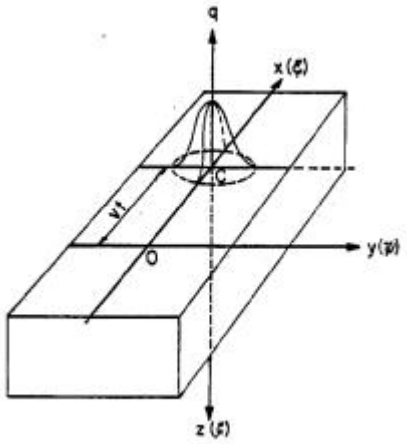

Figure 34. Movement of a Gaussian heat source over a semi-infinite solid body and the co-ordinate direction tied with the source [82].

The point source assumption prevents the use of equation 5 for a laser beam with finite size. Cline [83] modified the Rosenthal solution for a Gaussian beam intensity profile with intensity distribution given by,

$$I(x,y) = \frac{2\beta P}{\pi \phi_b^2} \exp\left[\frac{-2\left(x^2+y^2\right)}{\phi_b^2}\right] \tag{6}$$

The temperature distribution due to heat source with a Gaussian beam diameter = Φ_b can now be written as,

$$T = T_0 + \frac{2\alpha\varepsilon P}{K\pi^{1/2}} \int_0^{\infty} \frac{\exp\left\{-2\dfrac{\left(x+V_b t\right)^2+y^2}{\varphi_b^2+8\alpha t} - \dfrac{z^2}{4\alpha t}\right\}}{\sqrt{(\alpha t)}\left(\varphi_b^2+8\alpha t\right)} dt \tag{7}$$

Equation 6 computes the temperature field over the solid body and enables the temperature gradient to be computed in different directions. Gäumann used this methodology to obtain the liquid isotherm [5] and used that to obtain a circular melt pool.

Since the experimentally observed melt pool is ellipsoidal, Christensen et al. [84] tried to match it. Their results suggested an elliptic melt pool in the beam travel direction and a transverse semi-circular cross section. Goldak et al. [85] in their research assumed a double-ellipsoid weld pool shape that consisted of the front and rear ellipsoid quadrants. The angle between the workpiece surface and the tangent to the melt pool contour was assumed to be a right angle in their study. Liu et al. [77] rectified this approach and formulated the 3D melt pool shape by assuming a non-right angle value of these angles (α, β in Figure 35).

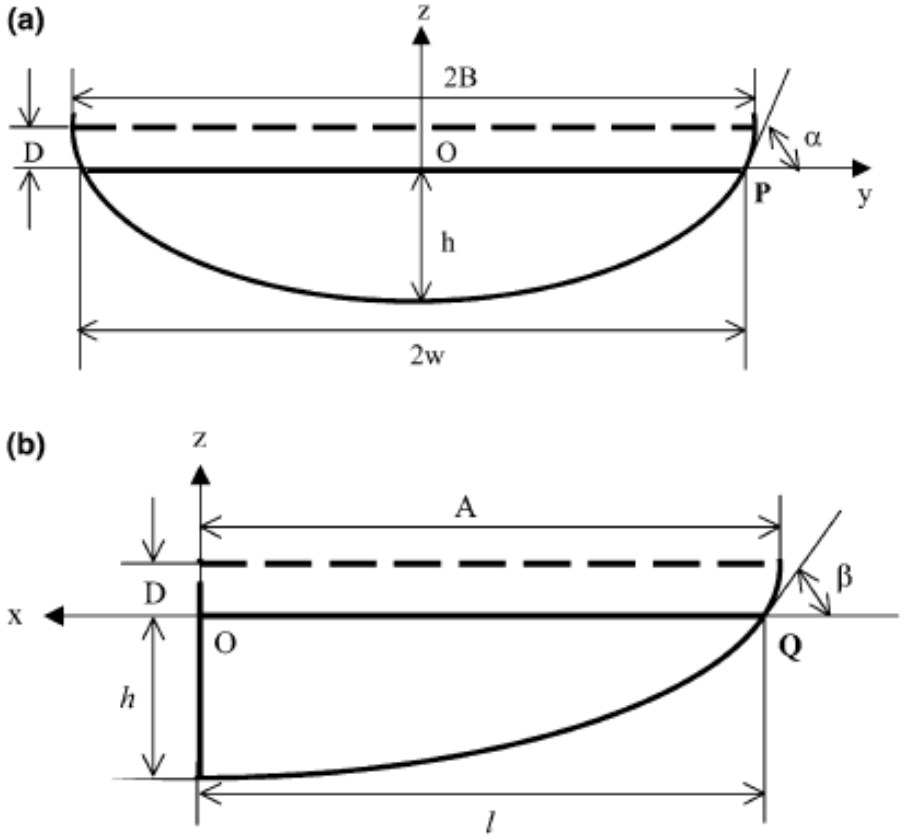

Figure 35.(a) Sections of the melt pool in (a) y-z plane and (b) x-z plane [77].

2.5.2 Numerical schemes

There are several drawbacks in the analytical schemes presented. They cannot take into account the melting and solidification of a superalloy, accurate representation of laser heat source is difficult, and local variation of thermo-physical properties cannot be accommodated. Different numerical schemes are attempted to solve particular subsets of the problem.

i) Fluid dynamics modeling:

Approaches based on finite element methods (FEM) and finite volume methods (FVM) have been employed for the thermal modeling of the laser-material interactions [20, 86-90]. Investigation of the effect of fluid convection in the laser melt pool started in mid-1950s [91]. A CFD-based model allowed modeling of convection inside the melt pool [92]. A coupled flow-thermal model was developed in order to simulate the conditions inside the laser melt pool while considering surface tension driven flow known as Marangoni convection (or Bernard-Marangoni convection). Since a liquid with a high surface tension pulls more strongly on the surrounding liquid than one with a low surface tension, the presence of a gradient in surface tension (due to temperature gradient) will naturally cause the liquid to flow away from regions of low surface tension. This extends the melt pool laterally and makes it shallower [93, 94]. Marangoni convection was found to have a major influence on surface rippling [83, 95]. Oreper et al. [96] developed a two-dimensional convection model in which buoyancy, electromagnetic and surface tension gradient forces were considered. The surface tension gradient was shown to have the dominant effect on determining the flow pattern. Different flow-zones in a weld pool are identified in Figure 36, which shows the flow vortices and the stagnant region [97].

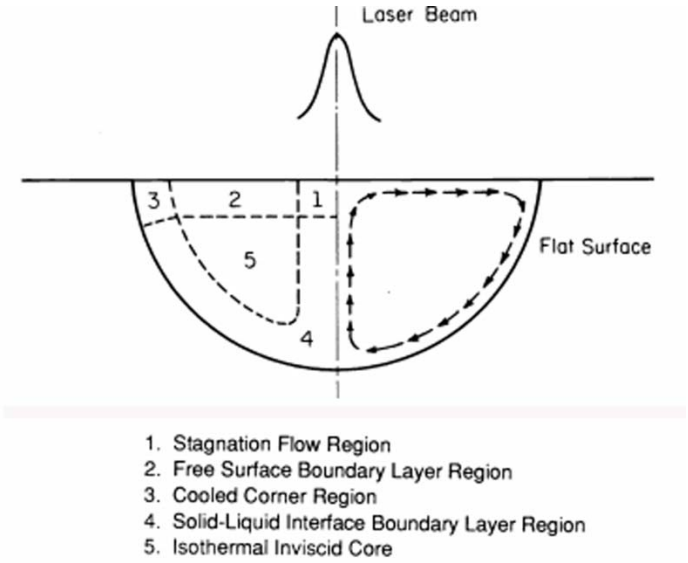

Figure 36. Different flow zones in a laser melt pool [97].

Figure 37 shows the simulated fluid flow, demonstrating flow vortices for different power and welding speed that were obtained by Paul et al. [98]. In this study, a portion of the vaporized material was allowed to condense in the interior surface of a hollow quartz tube. The composition of the condensate was used to determine the relative rates of vaporization of the individual elements and the effective weld pool temperature for vaporization. Figure 38 shows the temperature profile obtained for laser power at 500 W, where the peak temperature was experimentally verified.

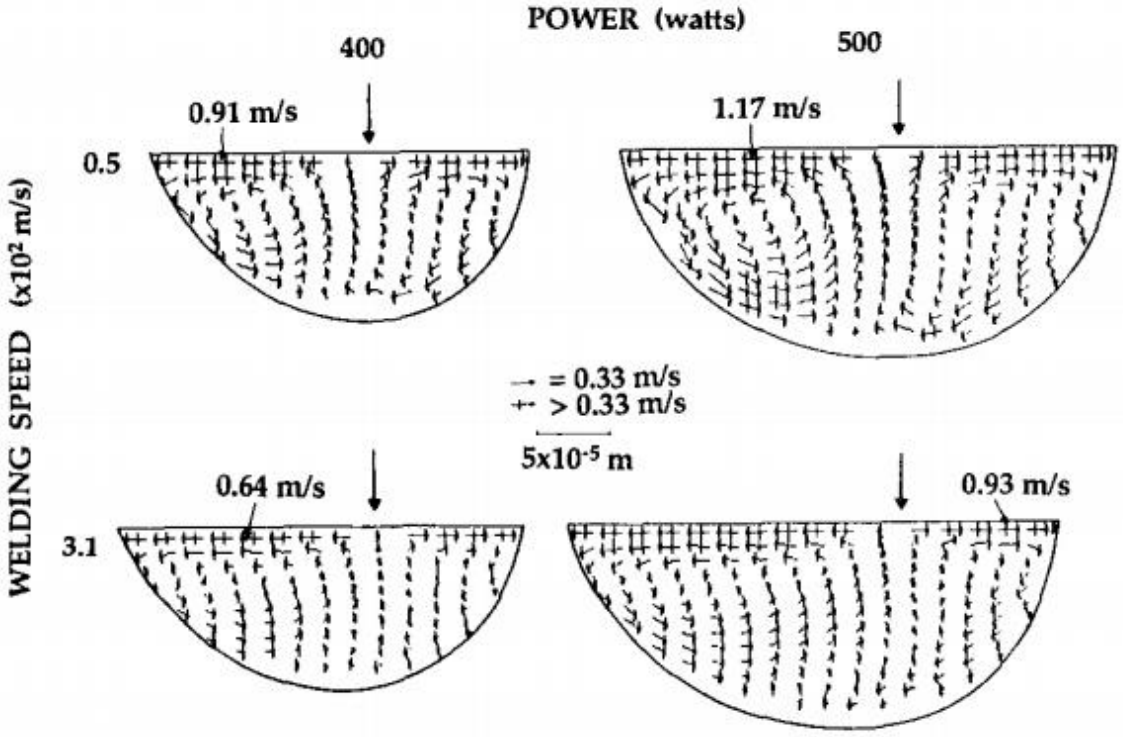

Figure 37. Flow vortices as a function of laser power and welding speed [98].

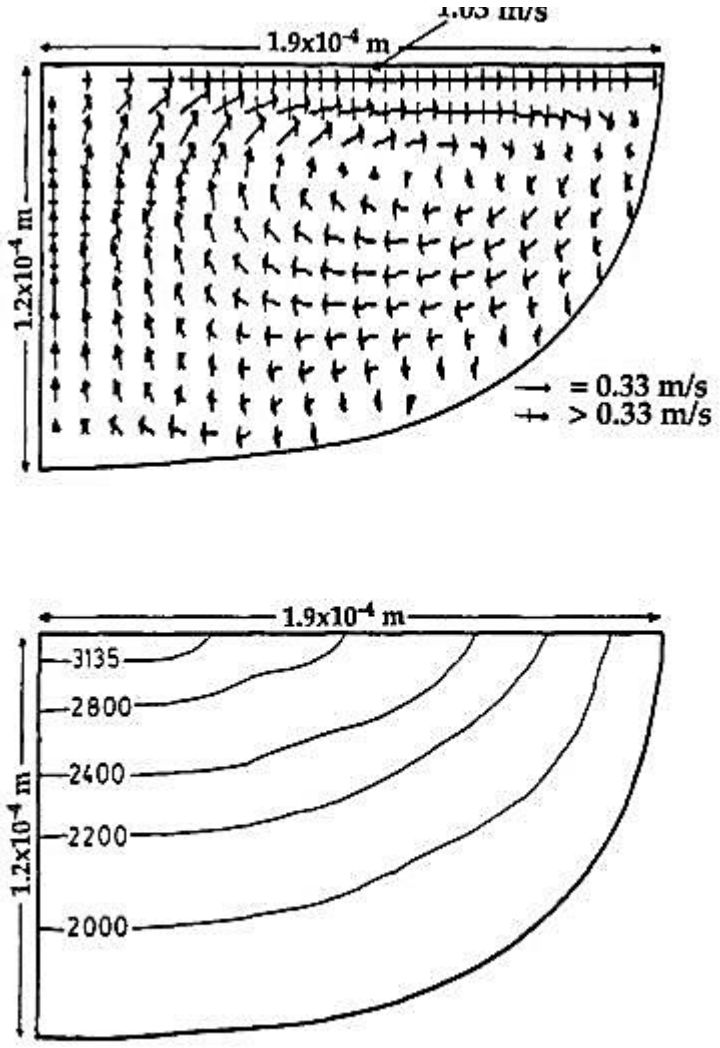

Figure 38. Calculated velocity and temperature profile in the transverse plane for P=500W [98].

Recently, the shape of the deposited layers was predicted by using a modified immersed boundary method with a finite difference scheme [99]. A level-set method has also been attempted to track the free surface motion of the molten pool with the powder material feeding and scanning of the laser beam for multilayer cladding for processing of SX superalloy [100].

ii) Sintering modeling:

Advanced physics associated with laser processing, such as the powder consolidation during sintering and radiation in-coupling, have also been attempted. The sintering phenomenon is a complex process where cohesive necks grow at particle contact and the atomic motions eliminate the high surface energy associated with powder. The structural changes that thus occur are dependent upon several transport mechanisms, which are mostly diffusion based processes. At each contact a grain boundary grows to replace the solid vapor interface. Sintering can be distinctly classified into 3 stages [101]. The initial stage sintering equation can be written as (for $X/D < 0.3$)

$$X / D = Bt / D^{m} \quad \textbf{(8)}$$

where X is the neck diameter, D is the particle diameter, t is the isothermal sintering time and n, m and B depends on the mechanism of mass transport (viscous flow, plastic flow, evaporation-condensation, lattice diffusion, grain boundary diffusion and surface diffusion). The intermediate stage of sintering is characterized by pre-rounding, densification and grain growth and in the final stage, isolated, spherical pores shrink by bulk diffusion. Hence, the complete sintering model involves modeling of a very complicated physics and is simplified by many researchers to predict the property changes due to sintering. A model has been developed to find effective contact thermal conductivity based on relative density and mean coordination number of crystal [102].

iii) Radiation modeling:

Modeling of the radiation phenomena in the opaque powder bed is also important, as the laser beam undergoes multiple reflections that result in deeper penetration. This phenomenon has

been modeled using a ray tracing model to find the total energy in-coupling [103]. Recently, the coupled radiation and heat transfer equation has been used to model the interaction of laser radiation with the powder bed [104]. This allows the effective thermal conductivity to be modeled by considering the temperature dependent phase function model. The radiation model provides a volumetric heat flux in the governing equation.

iv) Finite element modeling of residual stress:

FEM simulations are also attempted to predict the residual stress in molten metal. The localized high temperature gradient results in a severe residual stress and, as a consequence, hot tearing and cold cracking defects are generated [53]. These types of defects must be avoided to maintain high fatigue strength. Hot tearing typically occurs during solidification at high solid fractions, since the solidification shrinkage may not be compensated by the surrounding liquid and hence, tensile stress results in a partially coherent solid [57]. Hot tearing is also shown to be a function of tilt boundary misorientation, with higher values of misorientation causing more hot tearing [105]. Cold cracking is linked to the rapid cooling process, which results in a higher amount of residual stress [13]. FEM simulations enabled thermal stresses to be predicted at any location and point of time [106].

The mechanical model is essential for equiaxed alloys such as René 80 and IN 100, since they are known to be prone to grain boundary liquation/HAZ cracking and solidification cracking [107]. Hunziker et al. modeled solidification cracking using FEM, while HAZ cracking requires involvement of the element concentration at grain boundaries [49].

2.5.3 Microstructural models

The correlation of process parameters and microstructure has provoked a lot of interest since the advent of advanced numerical methods. The emphasis on solidification microstructure started in the seventies, and theoretical understanding was established [37]. Microstructure modeling for Ni-based superalloys in additive manufacturing was done comprehensively by Gäumann using DendM and TCalc [5]. The microstructural aspects of interest are briefly highlighted in the following section, which is followed by a discussion of cellular automata (CA) methods and their prior usage in microstructure prediction.

a) Microstructural aspects

The microstructural aspects of interest in the present study are the PDAS, the CET and the OMT.

i) PDAS

In a constrained growth process like SLE, the dendrites are constrained to adapt to the corresponding tip undercooling, and the tip undercooling is determined by the solute flux at the tip [37, 58]. The assumption of marginal stability yields the following relation for the PDAS [37],

$$w = 4.3\left(\frac{D\Gamma\Delta T_0}{k}\right)V^{-0.25}G^{-0.5} \tag{9}$$

where, w is PDAS, D is diffusion coefficient in liquid, Γ is the Gibbs-Thomson coefficient, ΔT_0 is the liquidus-solidus range in the initial alloy concentration, k is the equilibrium distribution coefficient, V is the solidification velocity and G is the temperature gradient. A similar relationship can be developed for low Péclet numbers and can be written as [108],

$$\boldsymbol{w = 6(\Delta T_0 k D \Gamma)^{0.25} V^{-0.25} G^{-0.5} \left[1 - \left(\frac{DG}{V \Delta T_0 k}\right)\right]^{0.5}} \quad (10)$$

Hence, the PDAS essentially follows the proportional relation as given by equation 9. However, it has been established that the above models cannot provide a precise prediction for PDAS and are only useful in obtaining a qualitative estimate for PDAS [109].

ii) CET

The theoretical basis of the CET was first proposed in the eighties. Hunt was the first to propose the instability criterion of the columnar front and the initiation of the CET as [110]:

$$G < \left(\frac{-4\pi}{3\ln(1-\phi)}\right)^{1/3} \sqrt{\frac{N_0}{n+1}}\left(1 - \frac{\Delta T_n^{n+1}}{\Delta T_{tip}^{n+1}}\right)\Delta T_{tip} \quad (11)$$

$$\text{and , } V = \Delta T_{tip}{}^{n} / a \quad (12)$$

Here a, n are material constants (n=2 [110]), φ is the equiaxed fraction (critical value = 0.066%), N_0 is the nucleation density, ΔT_{tip} is the tip undercooling, and ΔT_n is the nucleation undercooling.

Hunt simplified the solution by assuming a pseudo-binary alloy composition. Later on, the accuracy was improved by taking into account the composition and associated liquidus temperature profile for the growth of multicomponent dendrites [15, 111]. The Rappaz modification, [11] which takes into account the multi-component dendrites instead of pseudo-binary alloy composition and the dependence on dendrite orientation, is applied to predict the CET as follows:

$$G_{hkl}^{n} / V_{hkl} \geq a.\left\{\left(\frac{-4\pi}{3\ln(1-\phi)}\right)^{1/3} \sqrt{\frac{N_0}{n+1}}\left(1-\frac{\Delta T_n^{n+1}}{\Delta T_{tip}^{n+1}}\right)^{n}\right\} \quad (13)$$

Where, <hkl> refers to direction, (a, *n)* are material constants (*n*=3.4 for CMSX-4 [13]), and φ is the equiaxed fraction (critical value = 0.066%). Hence, the higher the value of G_{hkl}^{n} / V_{hkl}, the lower the value of φ and hence the lower the possibility of the CET. Previous literature suggested a critical value of this CET criterion (G_{hkl}^{n} / V_{hkl}value at the SX termination point) that can be applied to predict the CET. Gäumann et al. [5, 14] used a depth-weighted average of G^{n} / V to characterize a single weld pool. Later, Vitek et al. avoided this simplification in the computation of G by applying the Rosenthal solution to compute G and the melt pool shape [112]. Recent simulations [20] used a complete CFD-based 3D model for a single-bead scan pattern, allowing the variation of G and V over the melt pool co-ordinates. The critical value of this parameter that governs the CET was shown to be 2.7×10^{24} (in S.I. unit) [5, 13, 14, 20]. However, these efforts did not consider the effect of the trailing edge of the melt pool exclusively in evaluating G and V. Previous literature also suggested different values for the CET criterion between 5.9×10^{21} to 4.7×10^{25} based on operating conditions such as laser power, scan speed and preheating temperature [5].

iii) OMT

The OMT is caused by a change in the direction of the temperature gradient in the solidifying metal deposit. This occurs as the substrate becomes increasingly hot toward the end of the laser scan, resulting in a growth competition between the columnar grains. The present methodology to predict the OMT is developed for a laser beam describing a single bead scan.

Thus, the OMT phenomenon is predicted based upon finding the minimum dendrite growth velocity [7, 76, 113]. This leads to minimum undercooling at the dendrite tip [113]. Hence, this process essentially relies on finding the direction that is most closely aligned to the heat flux direction. For a single bead scan pattern the direction cosine can be found analytically as shown in Figure 39 [77].

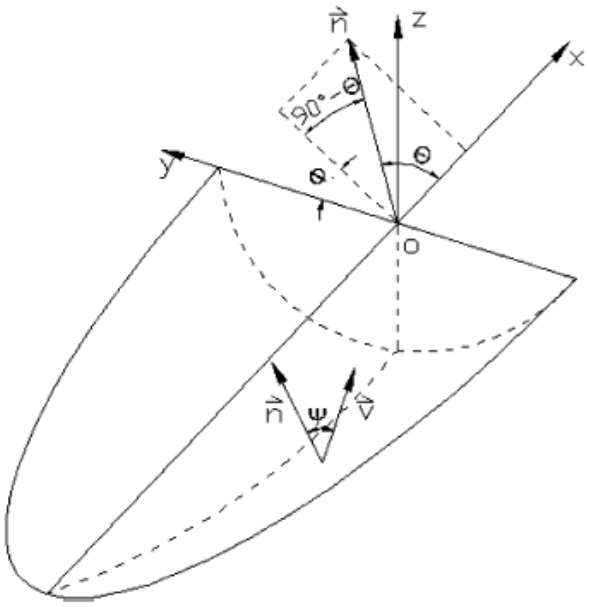

Figure 39. Analytical evaluation of direction cosines for dendrite growth directions[77]

b) Cellular automata

Cellular automata (CA) are an idealization of a physical system in which space, time and the physical quantities (or state of the automaton) take only a finite set of values. Since they were invented by von Neumann in the late 1940s, CAs have been applied to a large range of scientific problems [114]. Rappaz et al. used the CA approach to provide a probabilistic model of solidification that works on the principle of minimization of interfacial energy, and then coupled it to a macroscopic heat flow model [115]. They used a two-dimensional CA technique to

include the mechanisms of heterogeneous nucleation and of grain growth. Their CA model used two distributions of nucleation sites to treat nucleation occurring at the mold wall and in the liquid metal. The model was then applied to small specimens at uniform temperature. The CET, the selection and extension of columnar grains which occur in the columnar zone and the impingement of equiaxed grains were demonstrated. Chen et al. [116] simulated single linear passes for various processing conditions for GTAW. They applied a coupled cellular automata-finite element (CAFE) model to partial melting of an initial grain structure and epitaxial growth in the undercooled zone of a liquid pool, thus simulating the formation of a solidification structure. CA models are also coupled with free surface models (Level-set model) and phase field (PF) models. Tan et al. [117] simulated and validated a series of laser cladding processes by a multiscale model, where the two submodels are implemented in a decoupled manner. The three-dimensional thermal model is first used in conjunction with level-set method to investigate the macroscale heat/mass transport phenomena and to generate the thermal history of the entire process. The predicted thermal history was then applied to the two dimensional CAPF model, which simulates the microscale dendritic growth and associated solute redistribution on a cross section of the clad track. Recently Wang et al. [117] simulated the grain selection process during single crystal casting of a Ni-base superalloy DD403 in spiral grain selector by a macro-scale ProCAST coupled with a mesoscale CAFE model.

2.6 Summary

The discussion presented here highlights the essential requirements of gas turbine hot-section components and the material selection for the hot gas flow path components. The economic benefit of the repair technique motivated the research in welding and additive

manufacturing-based repair of blades and turbine platforms. The existing state-of-the-art repair technology demonstrated limited capability in restoring stationary components made from superalloys containing less than 4 wt% (Ti+Al). Maintaining epitaxy for SX superalloys and reducing mechanical defects for any Ni-based superalloys are the biggest challenges encountered. Thus, fluid dynamics simulation of the laser melt pool is conducted and microstructural models are developed to gain fundamental insight and to transfer some of those insights into the processing technique. The key challenges in development of the process and multi-physics model are as follows:

1. Ni-based superalloys are prone to solidification cracking and liquation cracking. It is of immense interest to develop a process that can reduce the residual stress buildup and produce crack free deposits.

2. SX superalloys also suffer from loss of epitaxy and stray grain formation. Without SX morphology, maintaining the creep strength of the original component will not be possible. Hence, an epitaxial growth is desired without disrupting the SX morphology.

3. The superalloy deposit also needs to be dense and continuous across the deposit-substrate interface.

4. The simulation should take into account a raster scan scenario instead of a laser beam scenario in describing a single bead pattern. The realistic property data of the superalloy also need to be incorporated.

5. The multi-physics model needs to be coupled with a microstructural model and needs to be experimentally validated.

6. It is important to develop microstructure-process map correlations that provide an optimum range of process parameters for SX, DS and EQ deposits. Currently, the state-of-the-art techniques provide limited success in developing the process maps for 'non-weldable' epitaxial superalloy components.

7. Techniques for qualification, verification and validation are required, as parts built through additive manufacturing exhibit microstructures and properties that are often different from those of parts processed through conventional deformation processing, solidification, powder metallurgy or other approaches. Hence, a multivariate statistical control approach demonstrating a control chart for a process and microhardness measurement to demonstrate the properties of the created component is essential.

Chapter III

Experimental setup

3.1 Introduction

The work on Scanning Laser Epitaxy (SLE) presented in this dissertation, is a direct descendant of a powder bed-based process referred to as direct selective laser sintering (SLS) developed in the late 1990s at the University of Texas at Austin [21]. SLS starts with a CAD model of the part to be built. The CAD file is sliced at discrete intervals in the build direction and the resulting cross-sections are stored sequentially in a "build file". Scanning algorithms are devised to plan the path of the laser beam. The powder bed is sintered conforming to the geometry requirement for the layer. Next, the power bed is lowered by a distance equal to the layer thickness and a fresh layer of powder is deposited by a roller mechanism. The next cross-section is then laser-sintered deeply enough to fuse it to the underlying layer and thus, by sintering layer upon layer, the entire part is fabricated. The schematic of the process is shown below in Figure 40. The components created through direct SLS processes are fully dense or nearly fully dense, and can be post-processed through the use of hot isostatic pressing (HIP) to achieve full density through the colure of any residual porosity. In contrast, SLE extends the work on Direct SLS by allowing for the direct construction of net-shape engine-ready components that have specified EQ, DS or SX microstructure and do not require HIP for densification.

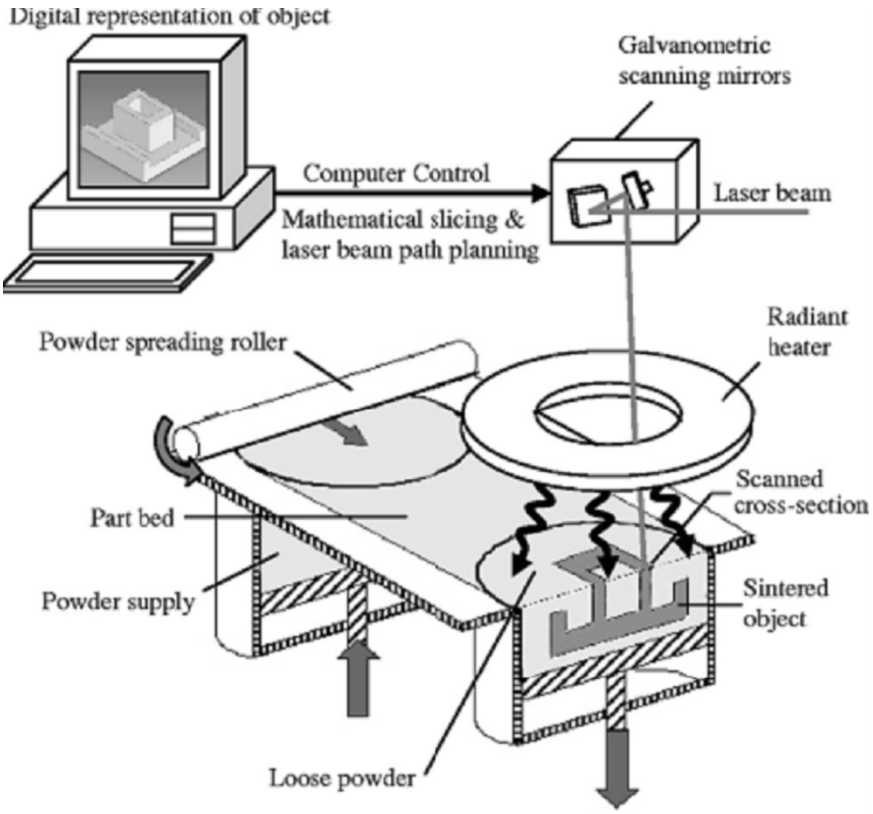

Figure 40. Schematic of the SLS process [118].

This chapter provides an overview of the hardware and software implemented for the SLE process to successfully fabricate components. It also describes the experimental procedure followed to verify, validate and qualify the created components. Instead of using a commercially available machine, a custom designed and built machine is utilized to enable easier access and broader level of control to process parameters. Figure 41 explains the SLE working principle through a schematic. A control computer is responsible for the pre-set scan path generation and process parameter input, which is transmitted via a DAQ card to the laser and scanner. A video microscope enables visualization of the SLE process in real time while a thermal imaging camera allows determination of melt pool and records its average temperature. This response signal,

when coupled with the feedback control allows real-time on-the-fly regulation of melt pool temperature by computer control of the laser power.

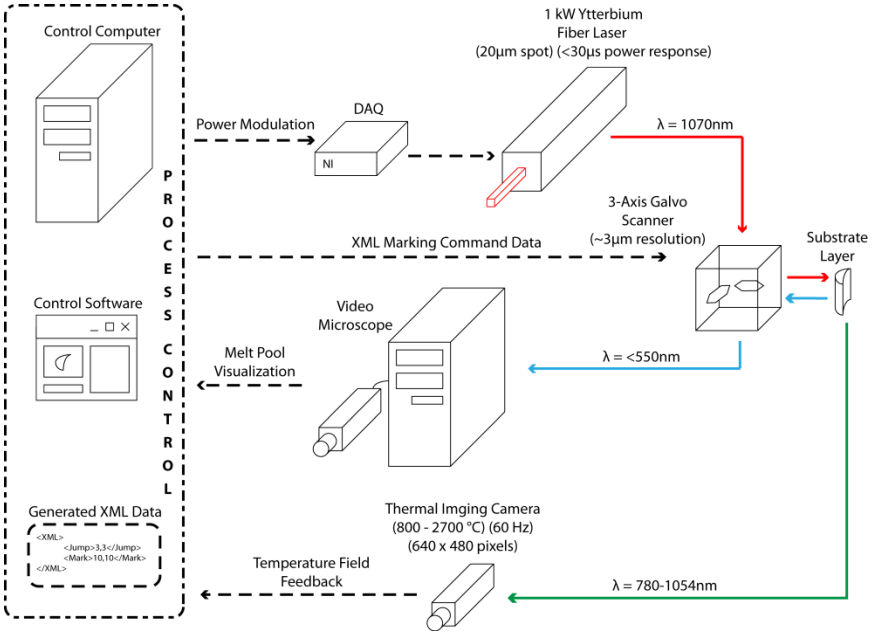

Figure 41. Overview of the SLE process [12].

3.2 Laser setup

The key pieces of hardware involved in the SLE process are a high power 1.1kW Ytterbium fiber laser, a 3-axis galvanometer scanning system, a controlled atmosphere processing chamber, a thermal imaging camera, and a melt pool video microscope.

3.2.1 ND:YAG Laser setup

During initial development of the process a ND:YAG laser was used. The powder was deposited in thicknesses ranging from 1 to 2 mm, to find the ideal deposit height. The powder was held in place above the substrate using wells cut into a Cotronics foam ceramic board that is

resistant to thermal shock. A continuous wave 1064nm 2.4kW Nd:YAG laser (Model: MM2400, Make: Hobart Laser products, Inc.) beam was used in conjunction with a galvanometer scanner (Model: EC1000, Cambridge Technologies) to focus the beam to 1.5mm diameter at the top of the substrate. A raster scan pattern across the width of the sample was used to propagate a linear melt pool across each substrate. The scanner was capable of moving the laser at several m/s scan speed, and the low response time of 700 μs potentially enabled high bandwidth feedback control. Three variables were altered between experimental runs: laser power, scan speed, and the number of repeated scans at the start of the raster pattern. A 95-5 beam splitter in the path of the laser was placed between the laser and the scanner unit. This beam splitter caused 5% of the beam power to be split off and fed to a coherent FieldMaxII^{TM} laser power meter. This allowed for measurement of 5% of the laser beam power during processing and gave an indication of the actual apparent power during each experimental trial. Figure 42 shows the ND:YAG laser setup and the arrangement of the galvo scanner and the controlled atmosphere glovebox.

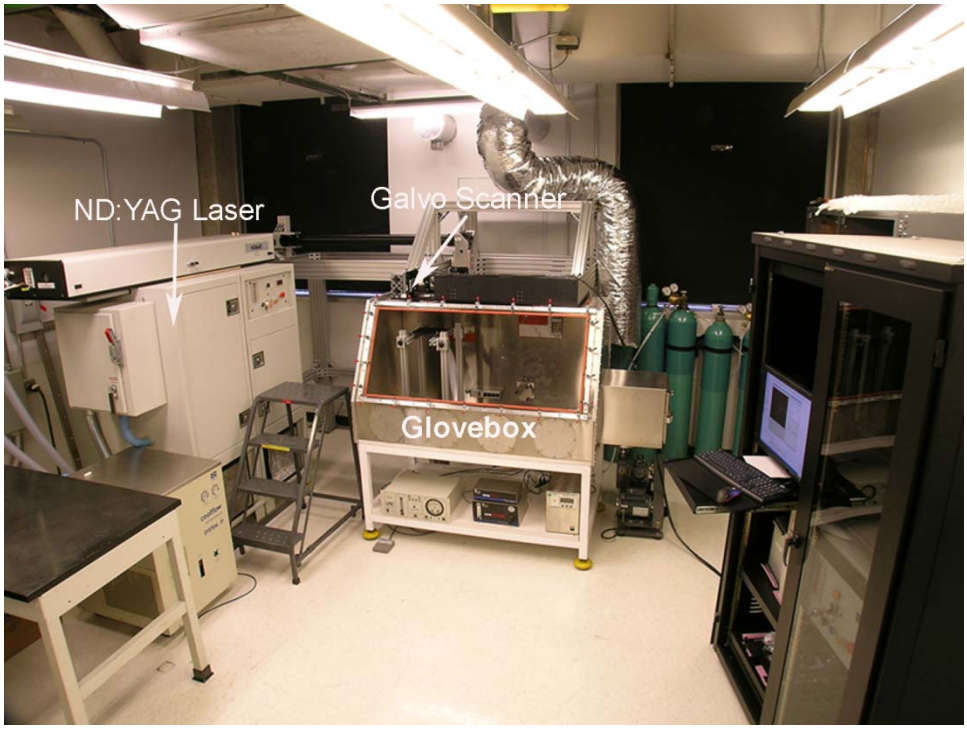

Figure 42. ND:YAG laser setup with the galvo-scanner and the controlled atmosphere glovebox.

3.2.2 YLS-1000 Laser

The laser currently being used for SLE processing is an IPG Photonics YLS-1000 continuous wave (CW) diode-pumped single mode Ytterbium fiber laser with a wavelength of approximately 1075nm. The 0-10V analog voltage provided to the YLS-1000 to control the laser power is supplied by a National Instruments PCIe-6321 data acquisition (DAQ) card with a maximum modulation rate of 900 kS/s and a 16-bit resolution. The DAQ card converts the computer's digital control signal into the analog voltage required by the laser during both open loop and closed loop control. The laser power was correlated with the analog input voltage by using the laser power meter built into the YLS-1000. The selected YLS-1000 laser can shutter the laser beam on and off within 100 μs and adjust its power in response to an external analog

voltage signal at a rate of 5 kHz, allowing for high bandwidth control of the amount of energy being applied to the substrate. Figure 43 shows the fiber laser, which is more compact than the previously used ND:YAG laser.

Figure 43. YLS-1000 fiber laser

3.2.3 Scanner

The scanner currently being used with the YLS-1000 fiber laser is a 3-axis galvanometer scanner (HP/GSS-Frauno, Cambridge Technology, Bedford, MA, USA). The optical head of the laser is fitted to the scanner using a custom designed collimator by Cambridge technology. The fiber laser is focused by the scanner to a spot of 20 μm in diameter, enabling both tight control of the local temperature conditions surrounding the melt pool and post-process cleanup operations via laser cutting. The laser scanner has the capability to move the incident laser beam across a 185mm by 185mm X-Y scan field at speeds of up to several m/s. Prior to entering the scan head the incoming laser beam is collimated by a 50mm diameter IPG-1070 collimator with a focal length of 160mm and an output beam $1/e^2$ value of 16mm. The optics internal to the Cambridge scanner then focuses this beam down to a minimum spot size of 20 μm. The third axis of the scanner, the z-axis, is a prescanning objective dynamic focusing module (DFM), illustrated in

Figure 44, that can adjust the beam focus during a scanning operation. The beam focus adjustment corrects for the focus lost due to changes in working distance as a scan moves across the scan field. Additionally, it can adjust the focus to enable scanning on curved surfaces. Figure 45 shows the scanner unit arrangement on top of the controlled atmosphere glovebox.

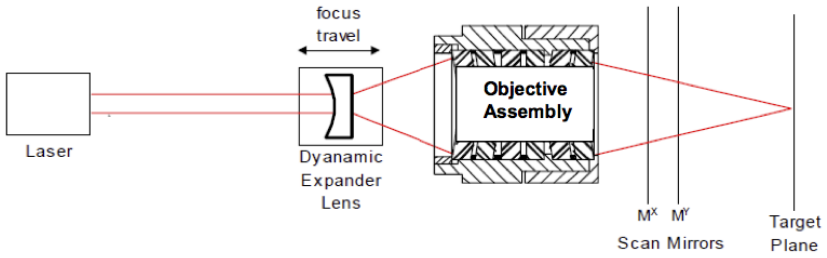

Figure 44. Optical path inside the 3-axis scanner and the arrangement of the dynamic expander lens in the DFM unit.

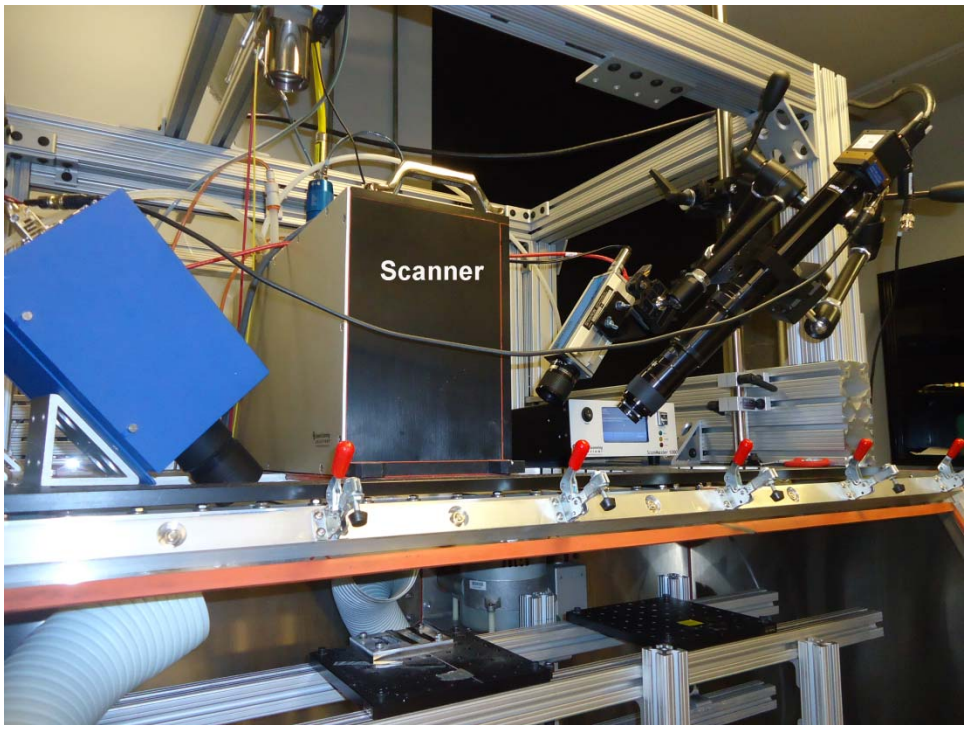

Figure 45. Scanner arrangement on top of glovebox.

3.2.4 Scanner Controller and software

The 3-axis galvanometer controlled scanner is controlled by a ScanMaster^{TM} (Maker: Cambridge Technology, Bedford, MA, USA) EC1000 unit via custom code written in visual C#. The scanner controller unit is shown in Figure 46. The board-level API for the EC1000 makes extensive use of XML to pass parameters between a client application and the DLLs.

The control software enables coupling of all the hardware components, such as the laser, scanner, DAQ, thermal camera etc. in a customized package specifically written for the SLE by Bansal [12]. The software is capable of importing XML job data, producing rectangular raster scan patterns of specified parameters, streaming marking commands to the scanner on the y, controlling the laser power, and measuring and analyzing temperature field data acquired by the thermal imaging camera at a rate of 60 Hz. An overview of the C# software is shown in Figure 48.

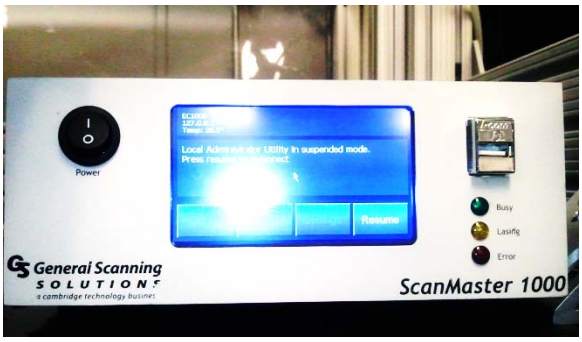

Figure 46. ScanMaster module for scanner control

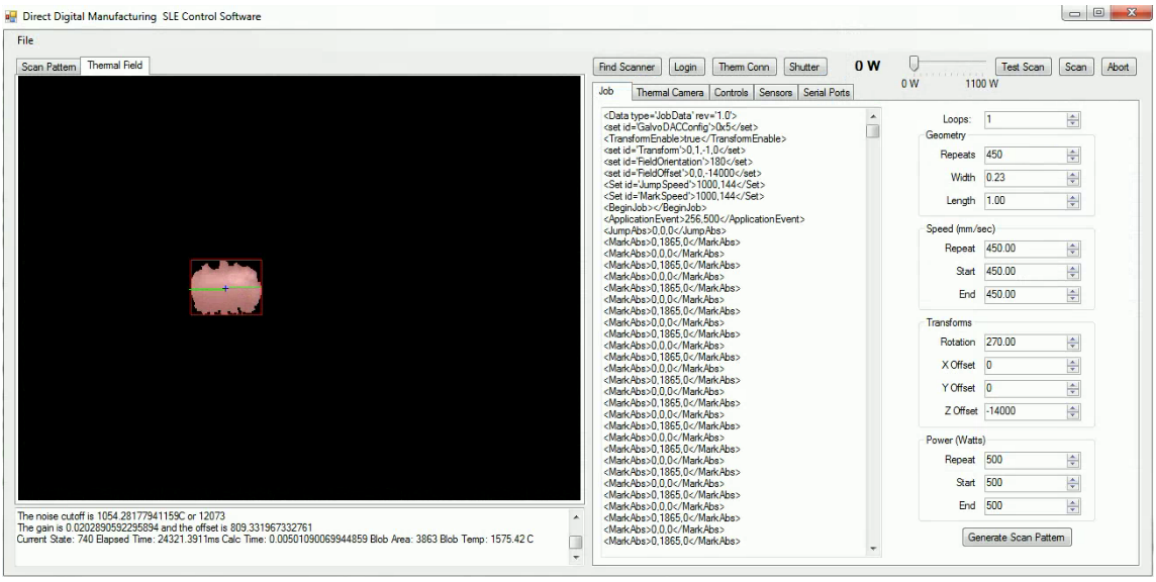

Figure 47. Overview of the custom C# software to control the SLE process showing job generation and thermal image processing/melt pool detection via thermal imaging camera [12].

The software allows control over four primary input parameters. They are: laser power (P), raster scan speed (V), repeat scan number (N) and scan path. Most of the input parameters are self-explanatory. The scan path depends on the geometry of the sample and can be varied. Different sample geometries are shown in Figure 49. During the scan, the starting edge of a geometry is scanned repeatedly (N times) to initiate a melt pool at the starting edge and to allow some pre-heating of the coupon. However, a high number of repeat scans can be detrimental and might produce too large a melt pool or reduce the vertical temperature gradient by increasing substrate temperature. Once the melt pool is established, smooth propagation of the melt pool is obtained by choosing a proper value of repeat scan speed.

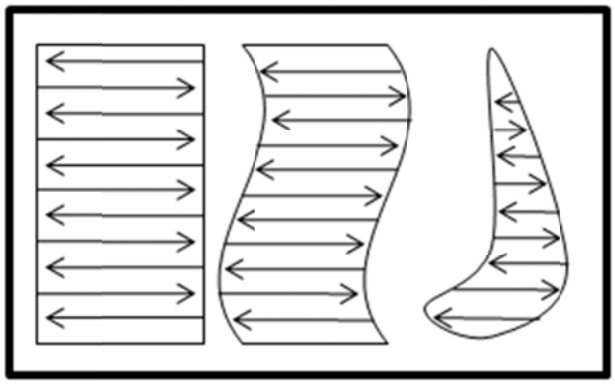

Figure 48. Different possible scan paths in SLE.

3.2.5 Controlled atmosphere processing unit

The SLE process is carried out inside a controlled-atmosphere customized glove box (Terra Universal, Fullerton, CA, USA). During processing, the chamber is backfilled with argon until the chamber atmosphere contains less than 50 parts-per-million (PPM) oxygen at atmospheric pressure. The oxygen level is measured by an Ntron Model 3100 oxygen analyzer that has been calibrated at atmospheric and 99.999% pure argon oxygen levels. An Inconel plate is used to hold the sample coupons in place during processing, as shown in Figure 3. The plate acts as a heat sink comparable to a turbine blade, and the through holes allow for heat distribution comparable to the tip cap of a turbine blade.

The chamber contains a conveyor belt-like assembly that can hold up to five carrier plates that hold the samples during processing as shown in Figure 49. A smoke exhauster unit (Model:S-981-2B Extract-All, Air Impurities Removal Systems, Wauwatosa, Wisconsin, USA) is installed inside the glovebox to protect the scanner mirrors from the smoke generated during processing. After all of the samples on one carrier plate are processed, another carrier plate can be moved into place under the scan field, allowing for higher throughput during experimentation. The

processing chamber can also be equipped with the layering system shown in Figure 50 for processing of multi-layer deposits.

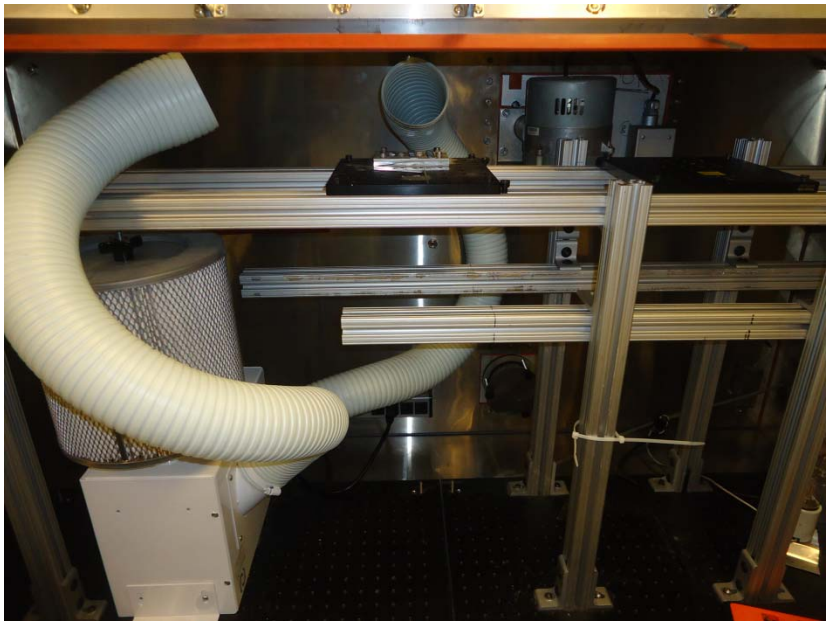

Figure 49. Conveyor belt assembly in glovebox with the fume extractor unit.

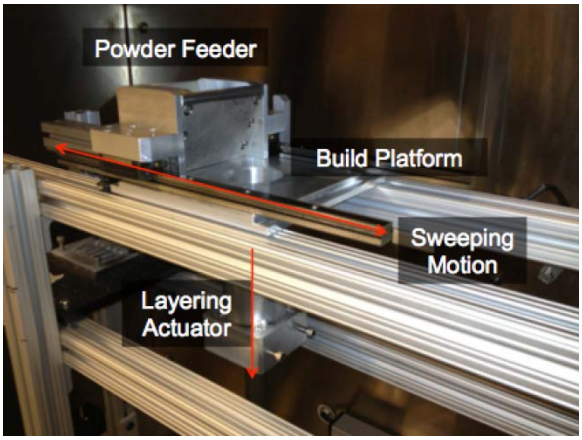

Figure 50. Proposed multi-layer deposition system [12].

3.2.6 Thermal imaging camera

A Mikron MCS640 thermal imaging camera (shown in Figure 51) is the main instrument providing data to be used in closed-loop feedback control of the SLE process. The thermal

camera captures the temperature field for the whole processing zone at a rate of up to 60Hz, which is the limiting rate on the real-time control scheme. The thermal imaging camera utilizes a microbolometer array to measure the infrared energy emitted by an object and turn it into an electrical signal. The normal operating frequency range of the camera is 780nm to 1080nm, but a notch blocking filter has been added to the camera to additionally block the 1060nm to 1080nm range such that reflected energy from the incoming laser beam is rejected. There are a significant number of spectral emission lines within the 780nm to 1060nm band for the main alloying element (e.g. Ni, Cr); and thus if the emissivity is properly calibrated, the thermal camera will be able to measure the temperature of these alloys [12].

Figure 51. Mikron IR camera mounted on top of glovebox.

The radiant energy emitted by a real non-ideal 'gray body' object can be related to the ideal emittance by equation 14 as,

$$\varepsilon = \frac{W_o}{W_{bb}} \tag{14}$$

Where, ε is the emissivity of the object, W_o is total radiant energy emitted by the object at a given temperature T, and W_{bb} is the total radiant energy emitted by a blackbody at a given temperature T. For a black body, the emissivity and absorptivity are equivalently 1. In an actual object, some of the radiation is transmitted through the object and some is reflected back, resulting in the following relation:

$$\alpha + \tau + \rho = 1 \tag{15}$$

where, α is the absorptivity or equivalently the emissivity of the object, τ is the transmissivity, and ρ is the reflectivity. The total radiant energy emitted by the object is found by integrating Planck's Law from 0 to infinity, resulting in the Stefan-Boltzmann law shown in Equation 16:

$$W = \varepsilon\sigma \mathrm{T}^4 \tag{16}$$

where, W is the total radiant energy emitted by the body, ε is the emissivity of the object, σ is the Stefan's constant (=5.670373×10^{-8} W m^{-2} K^{-4}), and T is the temperature of the object. Assuming a constant emissivity with respect to optical frequency, this equation can also relate the amount of energy emitted by a particular frequency range to a unique temperature. Internally to the camera, the total radiant energy measured by each pixel is represented as a 16-bit energy unit. These energy units are converted to a temperature using a factory-calibrated function. The conversion between energy units and temperature can be requested via the camera's API. The camera has been calibrated to measure temperatures with an accuracy of 0.5%± 1°C.

An accurate emissivity value is required as an input setting for the thermal camera in order to obtain reliable temperature measurements. The emissivities of different superalloys were measured using a method similar to that described in the work of Ghaemi [119]. In this work, the emissivity was approximated for a temperature between the solidus and liquidus temperatures by defocusing the laser beam and using a low power to slowly heat up and melt a sample of the cast

substrate while the thermal camera measured the average temperature of the laser spot location [12]. For instance, the emissivity value for René 80 was found to be 0.52 at the solidus temperature, which is near the emissivity value of 0.4-0.5 reported for partially oxidized molten Ni-base superalloys in the literature [120].

3.2.7 *Video microscope*

The PyrocamLP video microscope (Control Vision, Inc., Sahuarita, AZ, USA) allows a real-time view of the operation at a maximum frame rate of 60 frames per second. The minimum exposure of the video microscope is 3.3µs, and it can provide up to 20µm resolution. The images can be saved as a sequence of images or as a compressed or uncompressed .avi file to enable post-process diagnostics and inspection. A high power, pulsed xenon strobe illumination (X-strobe, Model:X-1200, Excelitus technologies, Waltham, MA, USA) synchronized with high-speed shuttering, illuminates the processing zone while suppressing the ambient light associated with the SLE, allowing the process details to be observed in real time. The xenon strobe produces intense pulses of radiant energy covering the ultraviolet (UV), visible (VIS) and near infrared (NIR). Additionally, an external triggering feature allows the PyroCamLP system to be synchronized with the SLE process, making it possible to view specific events in the process. Figure 52 shows the strobe and the PyroCam video microscope.

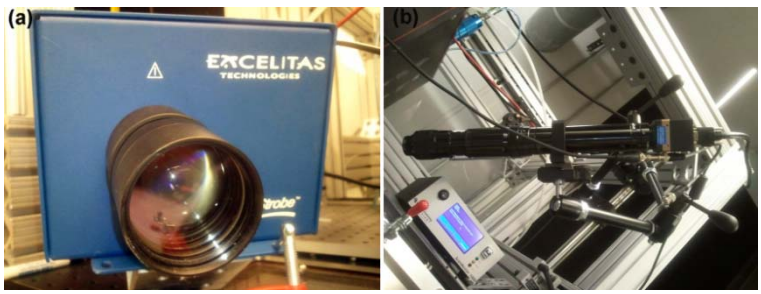

Figure 52. (a) Xenon strobe and (b) Pyrocam video recording microscope.

3.2.8 Arrangement

The arrangement of the hardware and the control computer along with the purging lines is shown in figure 54. This arrangement allows simultaneous operation of the thermal imaging camera and video microscope while running the SLE process via the control computer that integrates the laser, scanner controller and IR camera.

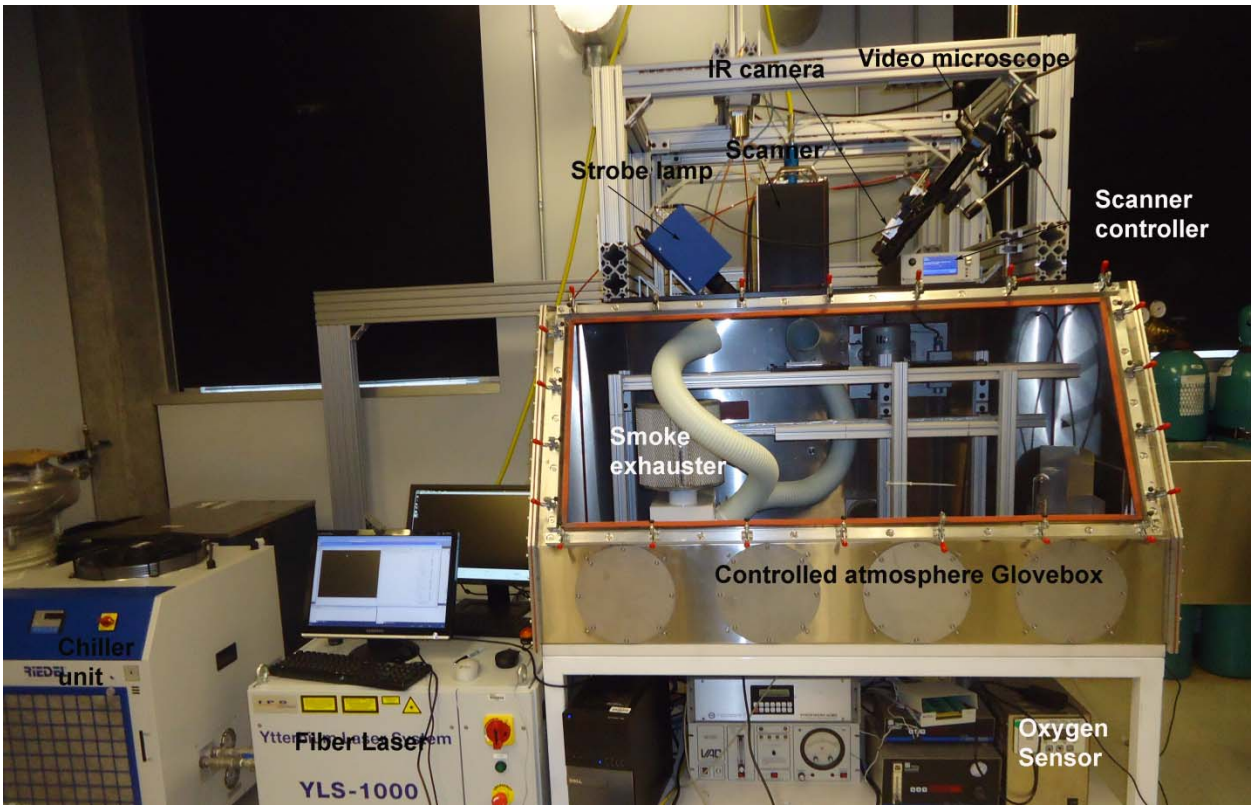

Figure 53. Arrangement of SLE equipments.

3.3 Metallurgical examinations

Detailed metallurgical investigations were undertaken to obtain optical microstructural images of the etched samples. Each specimen was later analyzed to determine the height of the deposited material, the uniformity of the deposit height, the amount of melt back along the

substrate and the locations of cracks or porosity. A customized image analysis code was written in MATLAB^{TM}(Mathworks, Inc.) to extract all the metrics that are essential for the design of experiments (DoE)-based process parameter optimization [121]. Defects found with high circularity values are labeled as pores and those found with low circularity values are labeled as cracks. Advanced microstructural investigations such as scanning electron microscopy (SEM), transmission electron microscopy (TEM), electron back-scatter diffraction (EBSD), and microhardness indentations were also carried out on a small subset of the samples to identify the microstructural characteristics and the mechanical properties

3.3.1 Sectioning operation

Each sample was sectioned using an IsoMet 4000 linear precision sectioning saw (Buehler, Lake Bluff, Illinois, USA) along the length and width to allow for views of the microstructure. The sectioning saw allows a rotational speed of 3600 rpm and a feed rate up to 0.25 in/min while cutting the samples. Cool 2^{TM} (Buehler) coolant was used during the cutting operation. The samples were first cut lengthwise, and then sectioned by widthwise cut, as shown in Figure 54.

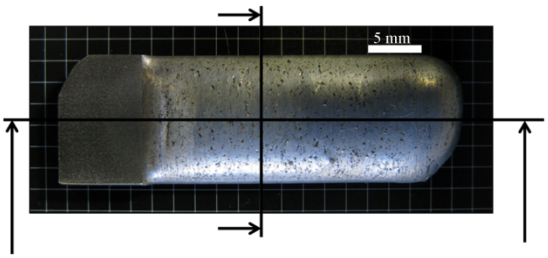

Figure 54. Lengthwise and widthwise cut for the SLE samples.

3.3.2 Sample mounting

Each section of the sample was mounted in Bakelite using a Buehler SimpliMet 3000 compression mounting press (shown in Figure 55). The mounting cycle comprises an automated heating and cooling cycle at 4200 psi. Epomet^{TM} molding compound (Buehler) was used as the mounting medium.

Figure 55. Buehler SimpliMet 300 mounting press.

3.3.3 Sample polishing

The mounted samples were then ground to a smooth finish using a EcoMet 250 (Buehler) automated polisher. The polishing unit is illustrated in figure 57. The rough polishing was conducted by 240 grit paper. The samples then underwent a fine polishing operation with diamond solutions. Finally, the samples were smoothed to a mirror finish using a 0.5µm silica suspension. The detailed procedure is established in the work of VanderVoort et al. [122] and provided in Table 3.

Figure 56. Buehler Ecomet 250 polisher.

Table 3. Polishing procedure adopted for Ni-based superalloy [122].

Surface	Abrasive/Size	Load(Lb) / Specimen	Platen Speed (rpm)/Direction	Time (minutes)
Carbimet® waterproof discs (psa)	220-240 (P240-P280) grit SiC water cooled	6	240-300/Comp	Until Plane
Ultra-Pol Silk Cloth (psa)	9-µm Metadi® Supreme Diamond Suspension	6	100-150/Comp	5
Trident cloth (psa)	3-µm Metadi® Supreme Diamond Suspension	6	100-150/Comp	4
Trident cloth (psa)	1-µm Metadi® Supreme Diamond Suspension	6	100-150/Comp	3
Microcloth pad (psa)	0.05-µm Masterprep™ alumina slurry	6	80-150/Contra	2

3.3.4 Sample etching

The polished samples were exposed to Kalling's No. 2 etchant (50ml Ethanol, 50ml HCl and 2.5gm $CuCl_2$) to reveal the microstructure for optical microscopy. Some other etchant compositions frequently used for SEM and optical microscopy are listed in Table 4.

Table 4. Etchant for Ni-based superalloys [12].

Etchant Composition	General use
15 ml HCl, 10 ml glycerol, 5 ml HNO3	Glyceregia. Mix fresh; do not store. Good for about 20 minutes. Use by swabbing. General purpose etch.
5 g $CuCl_2$, 100 ml HCl, 100 ml ethanol	Waterless Kalling's reagent (number 2). This reagent can be made as a stock solution. Good grain boundary etch.
5 ml H_2SO_4, 3 ml HNO_3, 92 ml HCl	Add sulfuric to HCl, stir, allow to cool; add nitric. Discard when etch turns orange. Use under hood. Do not store.
50 ml HCl, 1 -2 ml H_2O_2, (30%)	Attacks in Ni-base alloys. Immerse for 10 -15 seconds.
100 ml water, 100 ml HCl, 100 ml HNO_3, 3 g molybdic acid	Mix and allow the solution to age for at least 1 h before use. Immerse specimen for a few seconds to reveal as-cast structure. Reagent can be made as a stock solution.

3.3.5 Optical Microscopy

Imaging was conducted using a Leica DM6000 optical microscope at 100x magnification. This microscope is capable of stitching images obtained through an X-Y scan and is capable of predictive focusing accounting for surface unevenness. One representative widthwise cross-section for CMSX-4 is shown in Figure 57. The optical micrograph clearly indicates microstructural refinement in the SLE deposit region and SX growth till a reasonable height from the top of the substrate.

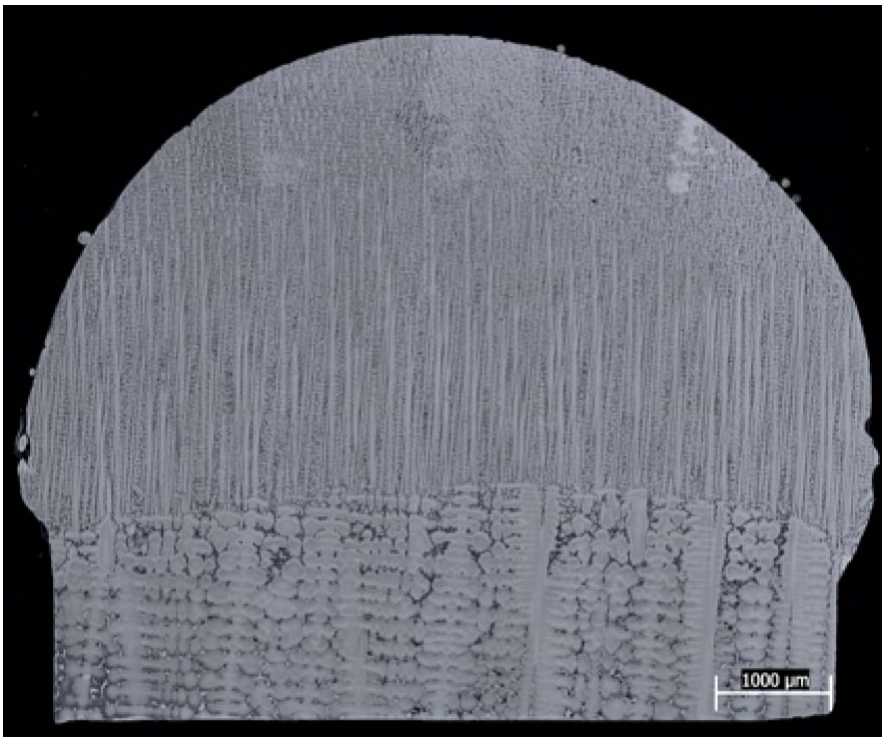

Figure 57. Representative widthwise etched optical micrograph for CMSX-4.

3.3.6 Microindentation hardness test (MHT)

MHT was carried out using a microindentation hardness indenter (Wilson Tukon^{TM} 1102, Buehler) with load fixed at 500 gf. The Tukon 1102 Tester is equipped with a three position turret which includes one indenter position as well as a 10x and 50x objective lenses. The hardness values are reported in Vicker's microindentation hardness scale (HV_{500}). The force is applied smoothly, without impact, and held in contact for 10 to 15 s. The instrument is shown in Figure 58.

Vickers microhardness measurement uses the average value of the diagonal of the indentation in calculating the HV value as expressed in equation 17.

$$HV = \frac{1854.4P}{d^2} \tag{17}$$

A spacing of 2.5 times the average diagonal of the indentation was maintained between different indentations. This was done to avoid the effect of the strain field from the previous indentation [123].

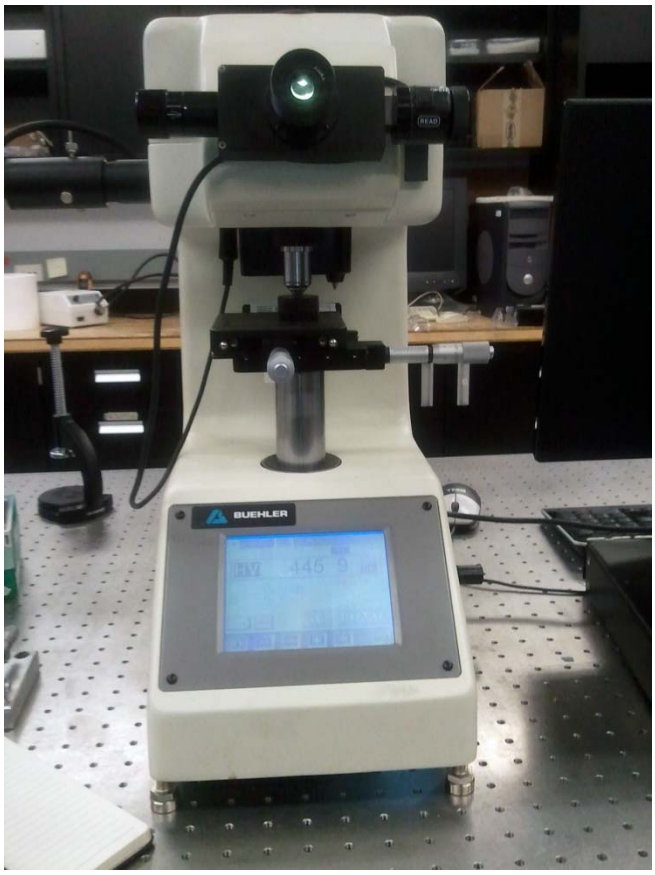

Figure 58. Buehler microhardness instrument.

3.3.7 Scanning electron microscopy

To understand the microstructural composition and to characterize the newly formed superalloy deposits, SEM investigation was carried out on LEO-1530 and LEO-1550 SEM. Energy dispersive X-ray spectroscopy (EDX) was carried out and reported. For further

investigation, γ′ etchant (Pratt & Whitney #17, composition: 100 mL H_20 + 100 mL HCl + 100 mL HNO_3 + 3 g MoO_3) was utilized. This etchant preferentially attacks the γ′ precipitate phase, leaving the residual gamma channels and former location of precipitates visible upon metallographic inspection.

3.3.8 Transmission electron microscopy

FIB was performed with an FEI Strata DB 235 dual beam FIB/SEM equipped with a liquid metallorganic ion source (LIMS) for protective Pt layer deposition. Bulk samples were extracted from the deposit and substrate regions of samples, and were sufficiently far from the deposit/substrate interface so as not to remove material from the HAZ. The sample was thinned with the ion beam to a maximum of 100 nm thickness, and then removed from the SEM chamber for TEM analysis. TEM analysis was performed using a JEOL 2010F high resolution TEM (HR-TEM). Bright field TEM (BF-TEM) was performed for general microstructural characterization and secondary γ′ precipitate size analysis.

3.4 Summary

This chapter explains the fundamental working principles of SLE and elaborates upon the key components involved. The technology involved in SLE makes it an ideal candidate for the repair of Ni-based superalloy and promises to deliver more. There are several reasons to believe that the SLE process will be able to address all of the challenges involved in repair of Ni-base superalloys and will be capable of producing Ni-superalloy based monolithic structures of specified microstructure directly from powders. The reasons are elaborated in the following paragraphs.

3.4.1 Crack susceptibility

The SLE process is able to operate at a much higher scan velocity because the laser is scanned using a set of high speed galvanometer scanners and is not mechanically attached to and impeded by any powder blowing mechanism. Thus, it offers more flexibility on the scan speed and can reduce the crack formation that is due to low scan speed [49]. The high resolution scan spacing used in the SLE process causes each subsequent raster scan to overlap a portion of both the prior and the subsequent raster scans, resulting in a pre-heat and post-heat treatment during the scanning operation, eliminating any hot tearing as seen in other processes. The high resolution scan spacing also results in the development of considerably finer grain structures in the deposits made via SLE as compared to investment casting and cladding; this exposes a large boundary area and limits the stresses that would otherwise cause liquation cracking [52, 54]. These features have made it possible to use SLE to work with materials such as René 80 or IN 100, which are highly susceptible to liquation and strain-age cracking and are considered unsuitable for processing by previously existing systems. Further control of the temperature gradients present in the process in real-time can only serve to further improve the SLE process and limit the surface tension-driven instabilities that contribute to many of these hot tearing and other cracking phenomenon [12].

3.4.4 Complex geometry

The use of a very finely focused and localized heat source, capable of delivering immense energy density (of order 10^{10} J/m^3), together with the real-time feedback control enables repair of a complex geometry and potentially makes this process suitable for repairing complex blade contours in gas turbines. The fast bandwidth of the real time feedback control

enables accommodation of sharp change in 2-D cross-section, thus adding to the existing capabilities of the SLE process.

3.4.2 Stray grains

The use of a pre-placed powder bed in the SLE process eliminates any melt pool disturbance that would be caused by the powder blowing mechanism used in cladding processes, removing another potential cause of poor microstructure formation. Real-time control of the melt pool temperature allows the proper range of temperatures to be maintained, to restrict the growth of stray grains while reducing surface rippling due to Marangoni effect.

3.4.3 Functionally graded microstructure

Another key characteristic of the SLE process is its ability to create functionally graded microstructures. SLE shows the potential to repair DS, SX and EQ superalloys. Hence, these morphological features can be incorporated in a single layer or into multi-layer technology. A number of applications for turbine components with functionally graded microstructures have been identified. One example is that of a turbine disc made of a superalloy composition with equiaxed structures of radially increasing grain size. The smaller grains at the inside of the disc offer better tensile capabilities, while grains towards the outside offer superior resistance to fatigue and creep [124]. Typically components like these require numerous long processing steps and lengthy thermal treatment times to produce functionally graded microstructures. SLE potentially offers the ability to produce components like these in a single processing step while also enabling creation of complex internal features due to the layer-by-layer processing.

3.4.4 Qualification, verification and validation

The metallurgical investigation techniques adopted for the current project enabled the development of a quantitative tool that can extract microstructural information and provide the optimized operational parameter ranges to be used for future trials [121]. This methodology can be further used to develop a quality control chart based on multivariate statistics. This investigation is also further used in the validation of a CFD-based multi-physics model. The coupling of the multi-physics model with the quantitative metallography enabled verification of the stochastic models for microstructural parameters and transitions [125]. The advanced microstructural study and microhardness measurements provide scientific insights into the laser-material interactions in the SLE process. The real-time thermal feedback and melt pool video microscope enables tracking of processing data and can further be used to identify defects during processing.

Chapter IV

SLE Process Development

This chapter studies the feasibility of repairing the 'non-weldable' superalloys by SLE. As part of the study, detailed microstructural results and characterization details are presented to demonstrate the ability of SLE to produce fully-dense crack-free deposits of specified microstructure.

The following chapter presents the microstructural results and mechanical properties for two EQ alloys (IN 100, René 80), one SX alloy (CMSX-4) and one DS alloy (René 142).

4.1 Materials

René 80 and CMSX-4 superalloy powders were produced by Praxair Surface Technologies through an atomization process. René 142 superalloy powder was obtained from General Electric and IN 100 superalloy powder was obtained from Pratt & Whitney-HMI Metal Powders. The compositions of these superalloys are listed in Table 5.

Table 5. Compositions of the superalloy powders investigated [38].

Name	Cr	Co	Mo	Re	W	Al	Ti	Ta	Hf	B	C	Zr	Ni
René 80	14	9	4	-	4	3	4.7	-	0.8	0.015	0.16	0.01	Bal
CMSX-4	6.5	9.6	0.6	3	6.4	5.6	1	6.5	0.1	-	-	-	Bal
René 142	6.8	12.0	1.5	2.8	4.9	6.15	-	6.35	1.5	0.015	0.12	0.02	Bal
IN-100	10	15	3	-		4.7	5.5	-	-	0.014	0.18	0.06	Bal

As the compositions show, all of the superalloys investigated in this dissertation contain more than 4wt% of (Al+Ti) and are deemed to be non-weldable by state-of-the-art repair techniques. Although the processing challenges associated with these superalloys are extreme, it did not deter the researchers to find the use of these superalloys in the gas turbine components. René 80 was one of the first gamma-prime strengthened nickel based superalloys used to provide strength and oxidation resistance in the late sixties [126]. The low cycle fatigue behavior of René 80 made it a suitable blade material in the temperature regime 871^{o}C to 982^{o}C. After observing the higher propensity for crack formation in René 80 alloy due to the dissolution of grain boundary phases such as carbides and borides, later efforts mostly sought to optimize the heat treatment that can minimize the segregation of melting point suppressing elements at grain boundaries [55, 127, 128]. With the introduction of DS and SX superalloys, the allowable turbine R.I.T has increased to 1427^{o}C (2600^{o}F) over the last 30 years. However, the methods of casting precision components are expensive and René 80 is still a suitable candidate for various hot-section components in aircraft gas turbines and industrial gas turbines. Attempts to repair René 80 started in the late sixties. Different welding techniques such as activated diffusion bonding involving vacuum furnace brazing, and diffusion and aging heat treatments were attempted [62]. Since the brazing alloys are of different composition, epitaxy cannot be maintained and the joint strength is poor.

IN 100 is one of the most heavily alloyed Ni-based superalloys, containing more than 60 vol% of precipitation hardening phases [129]. The properties are not only a function of the composition but are also found to be dependent on the morphology of the carbides [130]. Three distinct populations of precipitates in IN 100 are reported, and it is verified that the size and precipitation temperature of the precipitates control the yield strength [60]. IN 100 is a major turbine disk

alloy [131]. However, Ni–Zr intermetallic compounds are reported to form below the γ′-solvus temperature and to cause incipient melting [132, 133]. The application of fusion welding processes to precipitation hardened nickel base superalloys containing high Al or Ti has been severely limited due to their high susceptibility to (HAZ), cracking during welding and postweld heat treatment [10, 134, 135]. There is no report on any attempt to repair IN 100 by traditional or additive manufacturing. In the present research, the processing of EQ René 80 and IN 100 superalloys is investigated to determine whether SLE can effectively produce crack-free, dense deposits of these so-called 'non-weldable' superalloys.

CMSX-4, another alloy commonly used in jet turbine components, is typically cast with SX microstructure. It is a second generation SX alloy developed by the Cannon Muskegon Corporation that contains Rhenium to retard coarsening of γ′ at high temperature and assist in creep resistance at high temperatures. CMSX-4 is one of the SX alloys that is processed using ELMF [5, 7, 13, 14], electron beam and laser beam welding [20, 80]. Limited success has been obtained in maintaining the SX morphology, since the height of the SX region is limited to a low value of around 200 μm. The present research includes CMSX-4 to evaluate the ability of SLE to produce SX deposits of this alloy.

René 142 is typically cast in DS morphology and is known for high velocity oxidation resistance and reasonable longitudinal rupture strength [16]. A reported effort involving laser cladding was not able to produce crack free DS René 142 deposit on René 125 [17]. Electron beam melting reported successful fabrication of DS René 142 with 59 vol% γ′ and yield strength comparable to the commercially available alloy [136]. In the present research René 142 is deposited on SX René N5 cast substrates, and the microstructure and mechanical properties are studied to understand the feasibility of SLE for DS deposition.

4.2 Feasibility study on René 80

4.2.1 Powder processing

Processing the powder before using it in the stationary powder bed is of paramount importance in SLE. Any adsorbed contaminants in the metal powder, such as gases or moisture, could volatilize during processing and would result in either oxidation at the free surface of the melt pool or creation of gas porosity or voids near the top of the deposited material, as will be shown later in this chapter. The oxidized particles get carried by melt pool convection and can be trapped near the interface as well..

It is also essential for the powder to have a spherical or near spherical morphology to attain good flow characteristics in the melt pool. The size distributions and the morphology of the powder were studied with both optical microscopy and SEM. The René 80 powders were found to be mostly of spherical morphology with a normal size distribution ranging from 60 to 120 μm, as seen in Figure 59. In addition, to investigate the issue with porosity, the powders were mounted in epoxy and polished to reveal the cross-section. Several cross-sections were imaged, and no major internal porosities were detected for René 80, as seen in Figure 60.

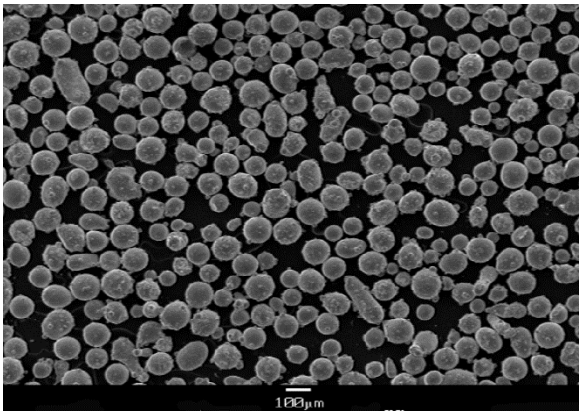

Figure 59. SEM image of René 80 powder

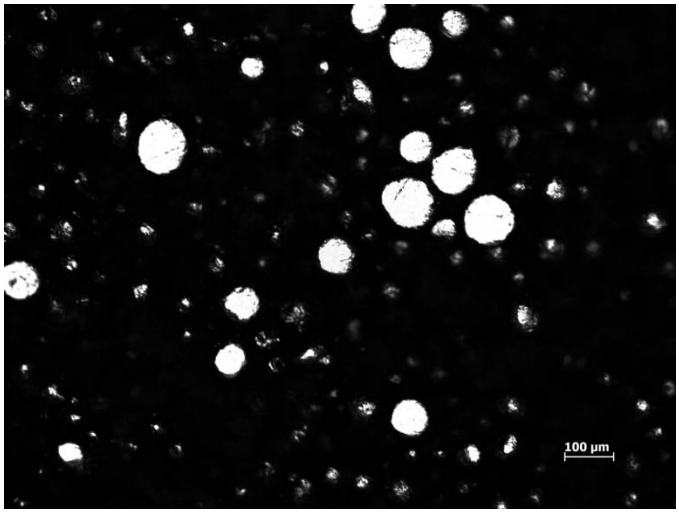

Figure 60. Optical microscopy of the René 80 powder cross-section after polishing.

4.2.2 Optical microscopy

Figure 61 shows the transverse microstructure of the René 80 sample. As can be seen from Figure 61(a), there is an excellent metallurgical bond between the substrate and the deposit region, and the deposit is crack-free and dense. Although there is no indication of cracking in the deposited material, several of the René 80 samples showed evidence of spherical porosity, especially towards the top of the sample. The deposit region also shows a finer microstructure

compared to the substrate region, as shown in Figure 61(b). The microstructural refinement might be attributed to the localized heating and fast cooling due to laser heat source application. The microstructure of the deposited region consists of the dendrite segregation patterns (Figure 61(c)). Due to the segregation of heavy elements, such as W and Mo, at the core of the dendrite, while Al and Ti elements are enriched in the inter-dendrite region, the etching made the dendrite region bright and the inter-dendritic region gray [128].

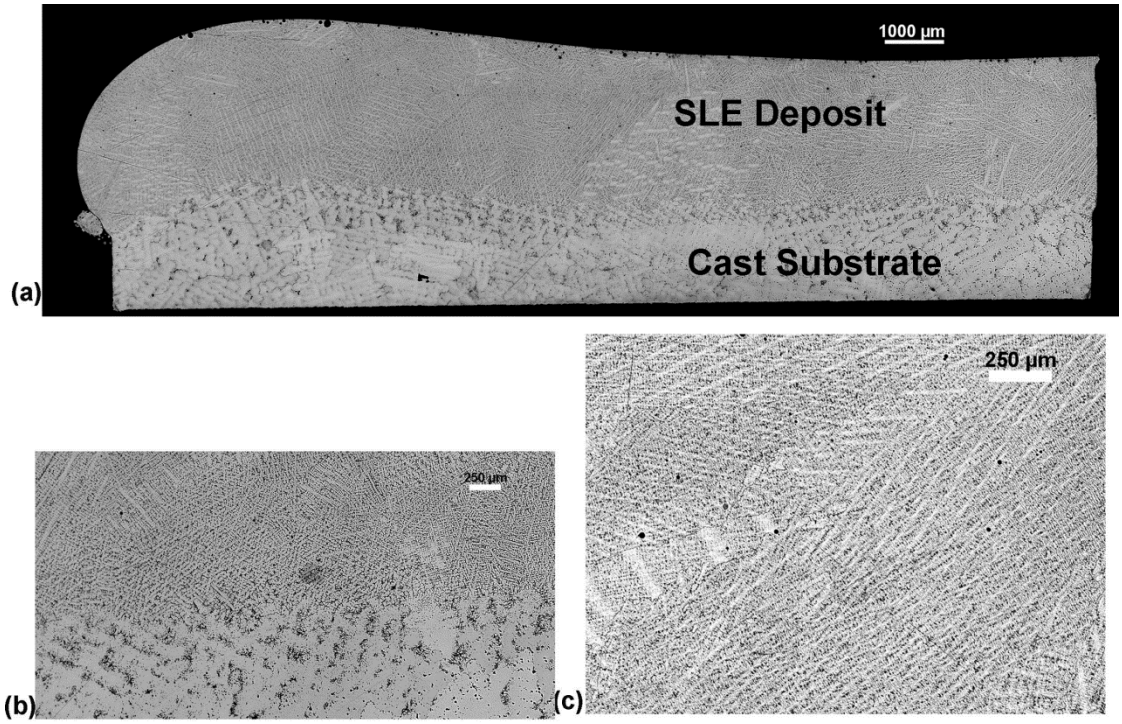

Figure 61. Representative transverse optical micrograph of René 80 sample showing (a) crack-free and dense deposit, (b) Metallurgical bond between the substrate and the deposit and (c) dendrite segregation pattern in the deposit region.

4.2.3 Scanning electron microscopy

The major constituents of the microstructure of René 80 are the γ matrix; the γ′ phase precipitates in the γ matrix, and the carbides. Figure 62(a) shows a SEM image of the

morphology of the deposit region with the presence of blocky carbides. The carbides are found to be rich in Co, Ni, Mo and Cr from the EDS profile, as shown in Figure 62(b); this is characteristic of MC carbides [127, 128]. Figure 62(c) shows the morphology of inter-dendritic and dendritic regions and Figure 62(d) shows the γ′ morphology in the dendritic region. The carbide phases are mostly present in the inter-dendritic region as seen in Figure 62(a).

SEM analysis using γ′ etchant exhibited a bimodal size distribution of γ′, but did not exhibit the typical primary and secondary precipitate structures. Fine γ′ precipitates formed large clusters that exhibited irregularly shaped morphologies as shown in Figure 63(a). Homogeneously precipitated γ′ varied in size depending on location. It was observed that these γ′ precipitates exhibited a size gradient in which larger precipitates were found in the vicinity of clustered fine γ′ and smaller precipitates were observed in locations away from fine γ′ clusters as shown in the inset of Figure 63(a), and in detail in Figure 63(b). This larger homogeneously precipitated γ′ appeared to be on the order of 25 to 50 nm, whereas smaller homogeneously precipitated γ′ appear to be approximately 10 nm in size.

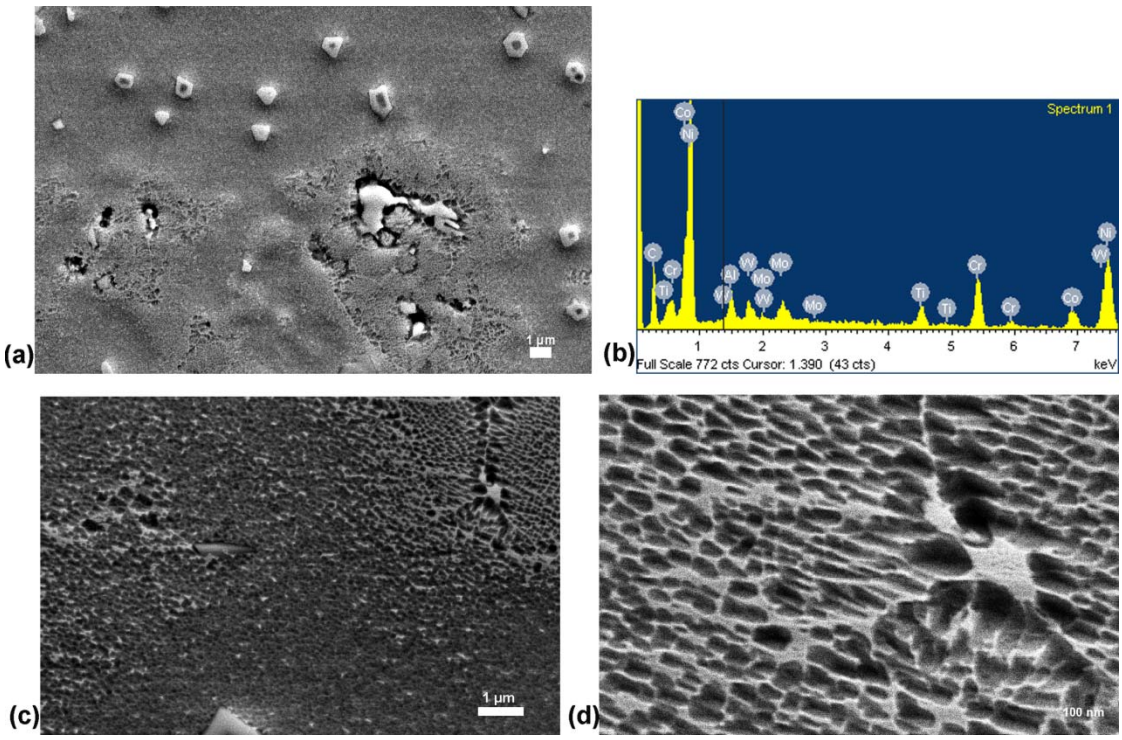

Figure 62. (a) SEM image showing the presence of carbides in the deposit region and (b) the SEM-EDS profile of blocky carbides, (c) The morphology of γ′ in the dendrite core and interdendritic region and (d) γ′ morphology in the dendritic region.

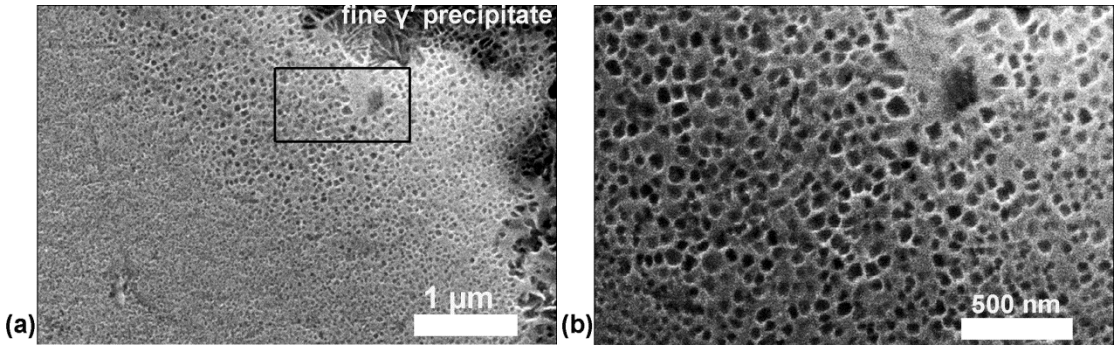

Figure 63. (a) Formation of irregularly shaped clusters by fine γ′ precipitates and (b) size gradient of homogeneous precipitate near fine γ′ cluster.

4.2.4 *Transmission electron microscopy*

SEM and TEM investigations were carried out on a smaller subset of samples in order to understand the microstructural difference between the substrate and the deposit region. As seen in Figure 64(a) and (b), in the substrate region, the carbide particles are larger than the carbide particles in the deposit region. According to Figure 64(c), the secondary γ′ particles showed a characteristic dimension in the range of 50 nm in the substrate region. The particles are finer in the deposit region, with characteristic dimensions in the range of 10 nm as seen in Figure 64(d).

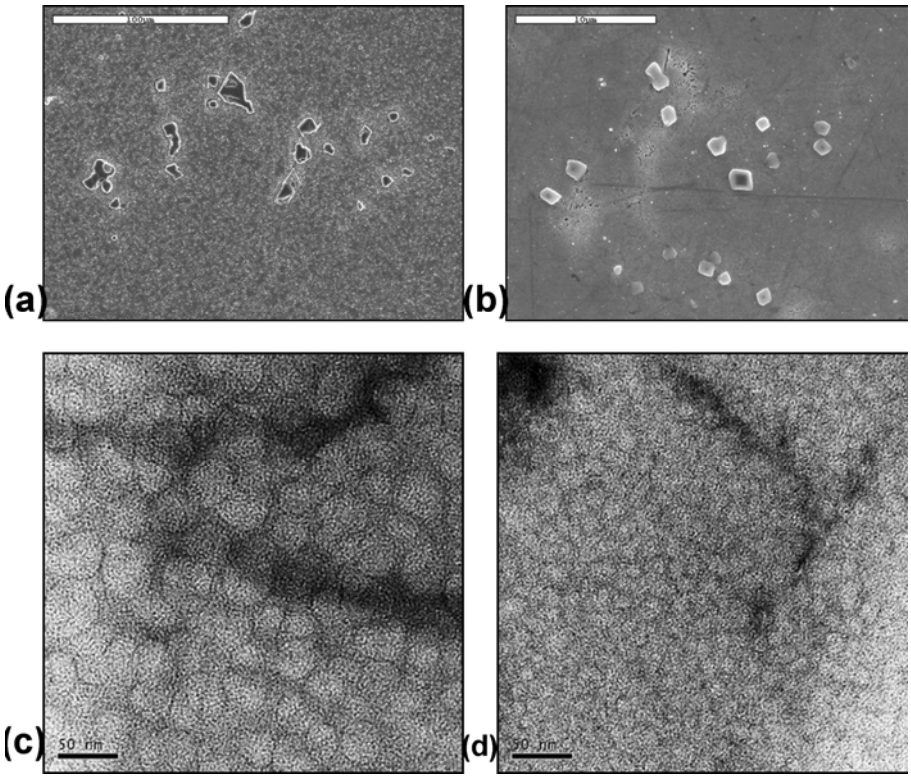

Figure 64. SEM image of the carbide particle in the (a) substrate region, and (b) the deposit region, TEM image of the secondary γ′ particle in the (c) substrate region and (d) deposit region.

4.2.5 Microindentation Hardness Test (MHT)

MHT results indicated higher values of the Vickers microindentation hardness in the deposit region than the substrate. The bulk substrate region shows a microindentation hardness value in the range of 400 HV. However, the hardness increases significantly as the HAZ is approached and can reach 460 HV near the interface. The deposit region has HV_{500} within a range of 465-515 HV, depending on the energy density used. Figure 65 reports the variation of the average HV_{500} with the volumetric energy density. The energy density is calculated as,

$$E_d = \frac{P}{S.S * V_S * t_p} \qquad \textbf{(18)}$$

where, E_d is energy density, P is the scan power, S.S is the raster scan spacing, V_s is the raster scan speed and t_p is the powder thickness. The error band for each sample suggests a wide variation in hardness in the deposit region.

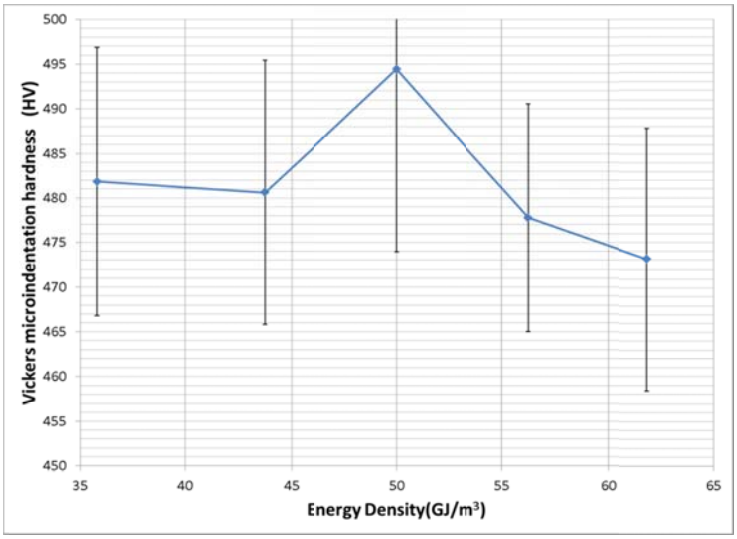

Figure 65. Variation of microindentation hardness with energy density

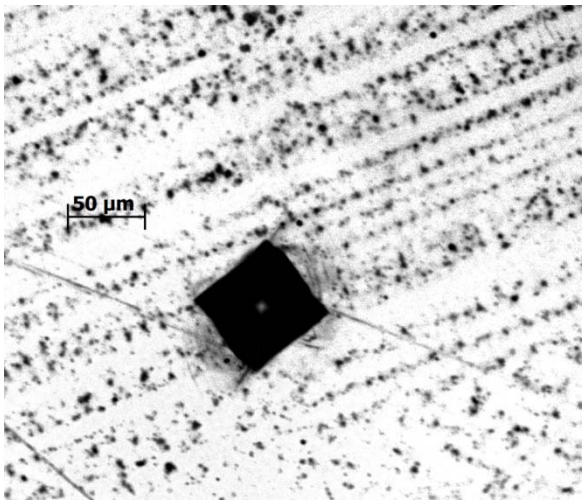

Figure 66. Representative microindentation on René 80 deposit.

Figure 66 shows one representative optical image of the indentation, and table 6 summarizes the measurement results. The yield stress was approximated as, $\sigma_y \approx HV/3$ (HV measured in GPa) [136]. Vickers microindentation hardness values around 450 were reported for René 80 away from the bonding zone in transient liquid phase diffusion bonding[137]. Osoba et al. reported microhardness values at different heat treatment conditions and correlated them with microfissuring tendency. The highest value obtained was near 420 HV [53]. DS René 80 has a higher concentration of Al + Ti, the major elements of the hardening phase, which results in its higher hardness (440±5 HV) [138]. Hence, it can be safely stated that the microindentation hardness of SLE deposited René 80 is comparable to the commercially available alloy and is likely to possess even higher hardness.

Table 6. Summary of microindentation hardness results for René 80.

Region	HV_{500}	HV (GPa)	H_{RC}	σ_y (GPa)
Deposit	490	4.805	49.0	1.602
Substrate	400	3.923	40.8	1.308

4.3 Feasibility study on CMSX-4

4.3.1 Powder processing

CMSX-4 powder was treated by the same procedure as René 80. The morphology, size distribution and cross sections of powders are analyzed using optical microscopy and SEM. The CMSX-4 powders are mostly spherical, with powder diameter normally distributed within 90-150 μm as evidenced by

Figure 67. Several cross-sections of CMSX-4 are imaged, and no major internal porosities are detected as seen in the representative image in Figure 68.

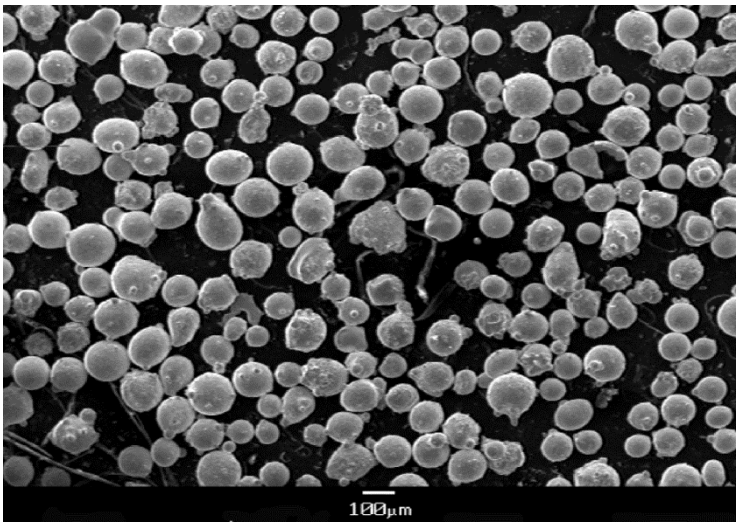

Figure 67. SEM image of CMSX-4 powder.

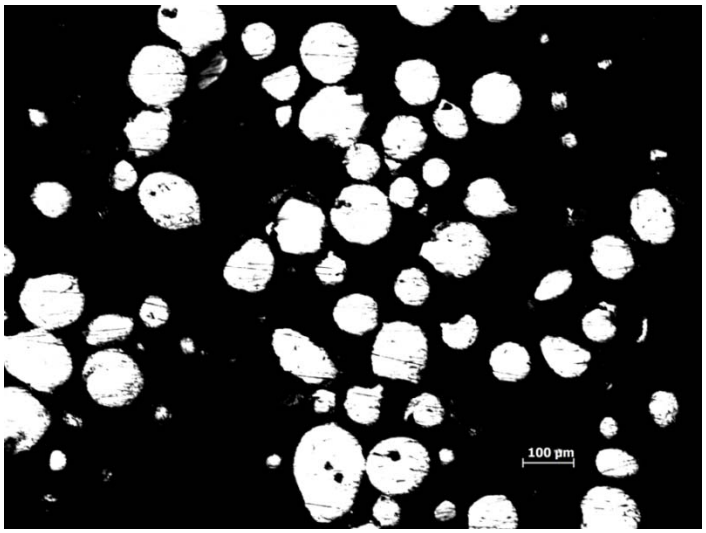

Figure 68. Optical microscopy of the CMSX-4 powder cross-section after polishing.

4.3.2 Optical microscopy

As demonstrated by the sample in Figure 69, many sections showed a full metallurgical bond along the entire length of the sample and also across the entire width. The transition from the cast CMSX-4 substrate to the laser processed material is indicated by the sharp change in dendrite spacing. The characteristic primary dendrite arm spacing (PDAS) in the substrate region is around 300-500 µm. The deposit region shows PDAS in the range of 15-30 µm as revealed from optical microscopy, which is in a range similar to that reported in other powder-based laser-repair processes [13, 20]. The higher cooling rate in the SLE process, (which is the product of the solidification velocity and the temperature gradient at the solid-liquid interface) in the range of 3.25 to 9.5 K/s, is responsible for the fine microstructure in the deposit region compared to the cast substrate and can lead to superior mechanical properties like tensile strength and ductility [139]. Also of note is the fully dense, porosity-free deposit. These traits are consistently found in samples manufactured using the SLE process and are necessary for their implementation on any commercial engine. In ELMF, powder blowing may break the dendrites and the convection of

the broken dendrites leads to undesired nucleation at different locations leading to stray grain formation [13]. The use of a stationary powder bed in SLE thus prevented stray grain formation to a significant extent, as shown in representative lengthwise cross-section in Figure 69(a) and in a widthwise cross-section in Figure 69(b).

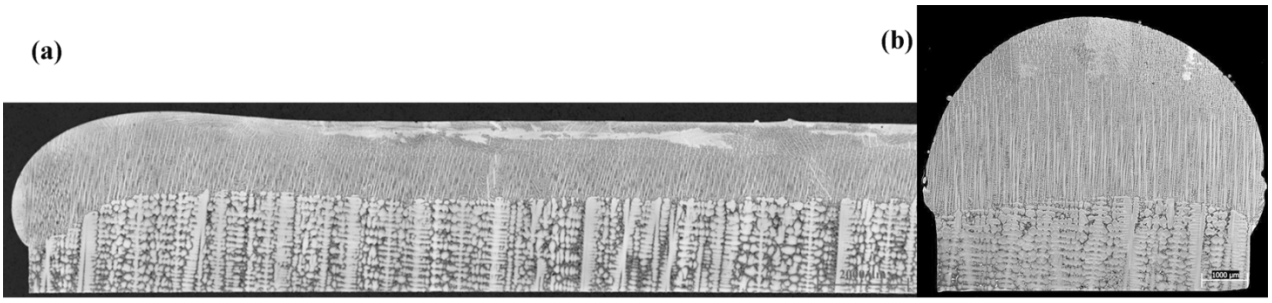

Figure 69. Representative (a) lengthwise section of the first half of a CMSX-4 sample with the starting edge on the left side of the image and (b) widthwise section at the middle of a CMSX-4 Sample.

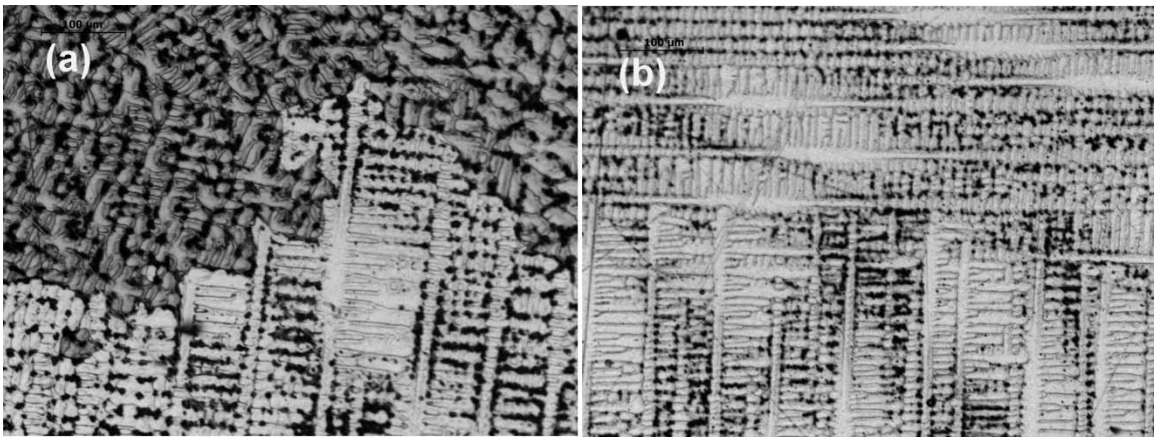

Figure 70. (a) Columnar-to-equiaxed transition (CET) and (b) Oriented-to-misoriented transition (OMT).

Figure 70(a) provides a detailed view of the transition from the columnar to equiaxed/polycrystalline morphology, known as the columnar-to-equiaxed transition (CET). The CET is due to the increase in isotherm velocity near the surface and a decrease in the temperature

gradient, which causes the formation of a constitutionally undercooled zone [13, 37, 58]. Figure 70(b) provides a detailed view of the transition from single-crystal growth in the <001> direction to the <100> direction, which coincides with the direction of travel of the line source. This change is known as the oriented-to-misoriented transition (OMT) [13] and is caused by a change in direction of the dominant temperature gradient as the substrate becomes increasingly hot toward the end of the scan, resulting in growth competition between columnar grains.

Despite these regions of misoriented dendrites and equiaxed grains, most samples showed an SX deposit height close to 1000 μm, as seen in Figure 71. The deposits are dense and crack-free; they show less bending and lower surface rippling at the top edge. In production parts, the misoriented and equiaxed microstructure formations would be removed via machining and grinding operations or via a re-melt operation if multiple layers were to be built.

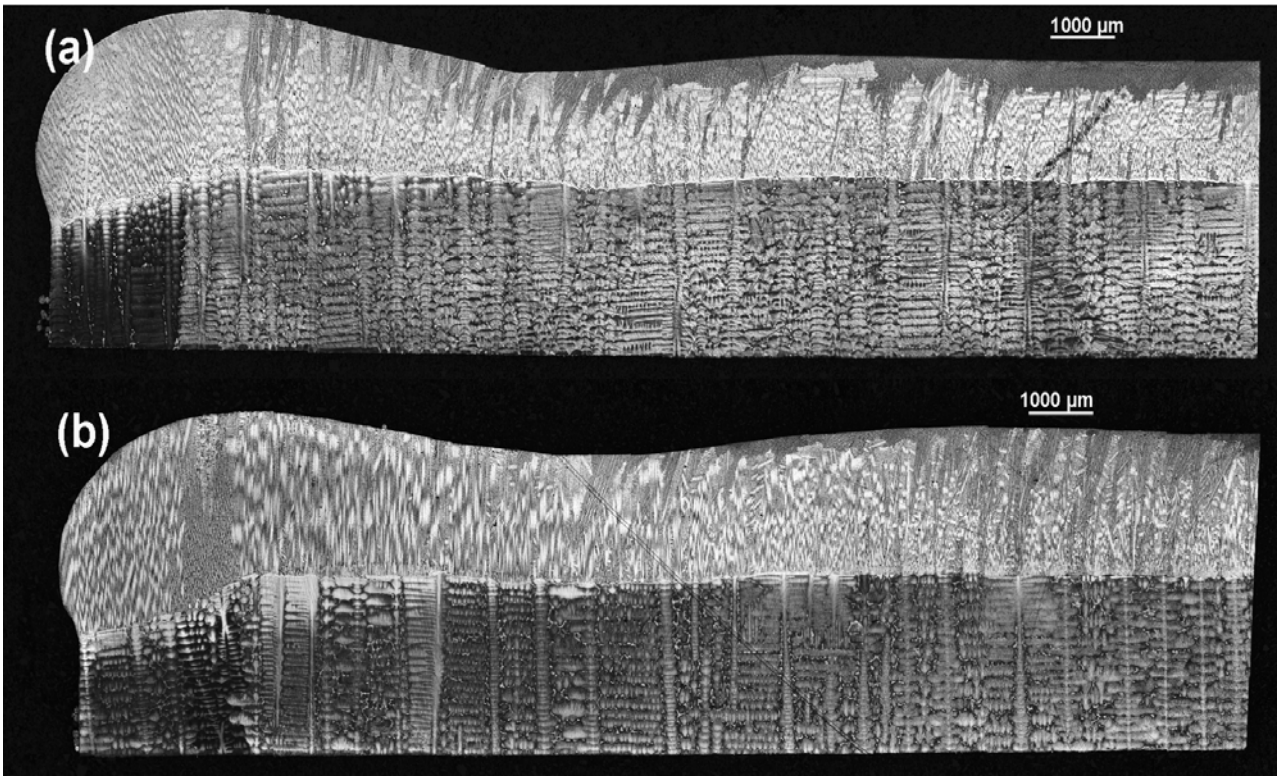

Figure 71. Example of CMSX-4 deposits.

4.3.3 Scanning electron microscopy

SEM was conducted on the substrate, the deposit and near the interface region after etching the sample with γ′ etchant (100 mL H_20 + 100 mL HCl + 100 mL HNO_3 + 3 g MoO_3). The substrate region showed the regular γ/γ′ matrix in Figure 72(a). The average channel width is 100 nm in size and the size distribution is uniform in nature. In contrast, the deposit region shows variation in the size of the γ′ precipitate, as evidenced by Figure 72(b) and (d). The γ′ becomes finer as we move away from the interface. Figure 72(c) and (d) shows the structure of the interface region. The metallurgical bond is continuous; however, the morphology is different at the interface. The features are very similar to the TCP phases described in the existing literature [140]. Similar interface TCP structures were also observed for CMSX-4 thermal barrier coatings [141].

4.3.4 EBSD

Another tool essential for the characterization of SX deposits is electron back scattered diffraction (EBSD) analysis. For SX CMSX-4 deposits, the dendrite orientation is an important criterion, and an industry standard acceptable range of the misorientation angle is $\pm 15^0$ degrees from the nominal vertical direction. EBSD can provide this information from the transverse cross-section as shown in Figure 73. The image also shows a small EQ region at the top and few stray grains in the deposit. Hence, this technique is also useful in providing nucleation site information.

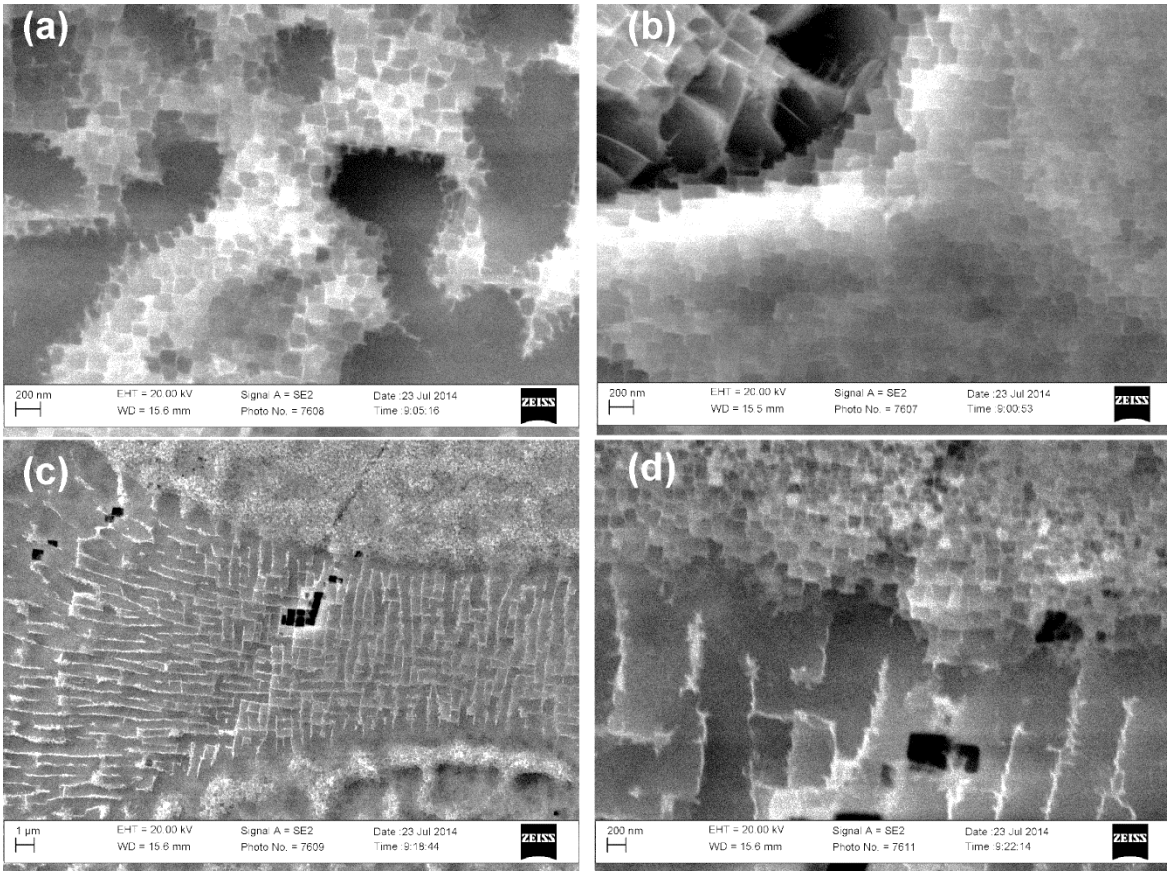

Figure 72. SEM image showing (a) γ/γ´ structure in the substrate region (b) size gradient of γ´structure in deposit region, (c) features near the interface region, and (d) close-up view of the deposit region near interface.

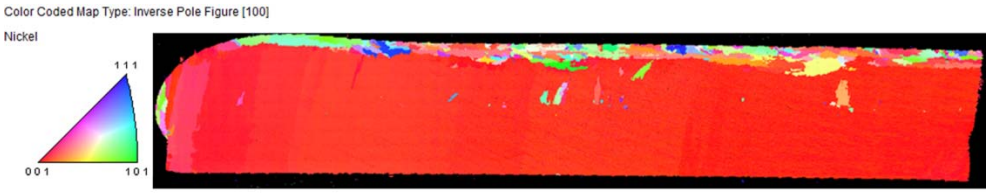

Figure 73. Representative EBSD map of CMSX-4 sample.

4.3.5 Microindentation Hardness Test (MHT)

Figure 74 shows a representative Vickers microindentation on CMSX-4 deposit region. The CMSX-4 samples contain different morphological zones. Typically there is a microstructural refinement near the interface between the substrate and the deposit. This is followed by a columnar zone that is oriented in <001> direction. In some deposits, OMT is observed and the dendrites change their growth direction to <100>. In addition, CET is observed at the very top due to constitutional undercooling and the nucleation of equiaxed grains is observed.

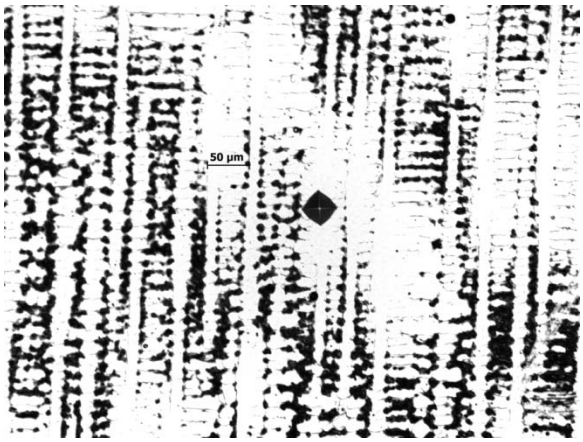

Figure 74. Representative microindentation on CMSX-4 deposit.

Figure 75 shows two examples for line profiling of the microindentation hardness at different regions of CMSX-4 deposit. The indentations were made near the bottom edge of the substrate, (S1) and then the indenter progressively moved upwards to S2, followed by interface (I/F), columnar region (C1, C2), transition region (CET or OMT), and finally misoriented (F1, F2) or EQ region (EQ1, EQ2). Table 7 describes two typical sets of line profile data obtained for the CMSX-4 samples. The substrate region progressively gets harder as the interface zone is approached from the bottom. The <001> columnar region typically showed higher hardness than either the <100> columnar zone or the EQ region.

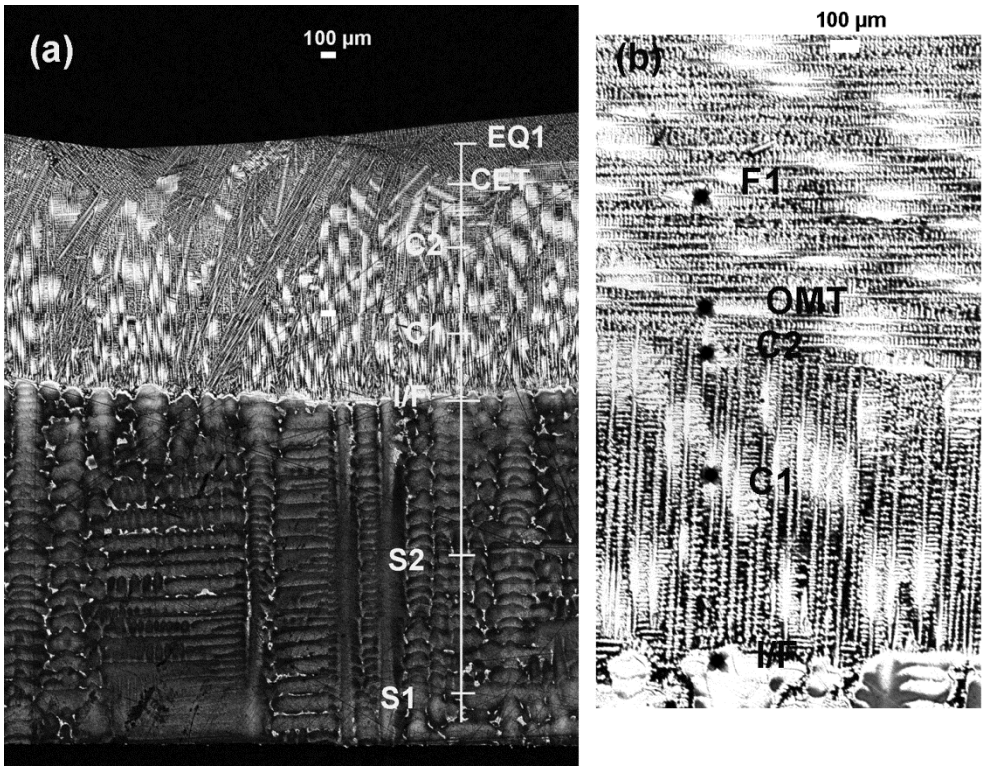

Figure 75. Microindentation at different region of CMSX-4 deposit to obtain line profiling of HV for (a) Deposit with EQ region and (b) deposit with flipped columnar growth.

Table 7. Line profile representative data for CMSX-4 deposit.

Line profile with EQ region		**Line profile with misoriented region**	
Location	HV500	Location	HV500
S1	360.7	S1	396.8
S2	376.1	S2	403.9
I/F	461.9	I/F	423.3
C1	475.6	C1	446.9
C2	481.1	C2	444.9
C3	458.8	OMT	436.2
CET location	426	F1	416.1
EQ1	422.4	F2	445.9
EQ2	442	F3	450.8

Figure 76 shows the variation of HV values for SX and EQ regions. The SX region displayed higher hardness values consistently across the energy density range, with HV values ranging

from 432 to 490. The substrate region showed a hardness value of 402 HV on average. Table 8 summarizes the MHT results for the substrate and the different regions in the deposit. The average value of hardness for the SX region is 15% higher than that for the cast CMSX-4 substrate.

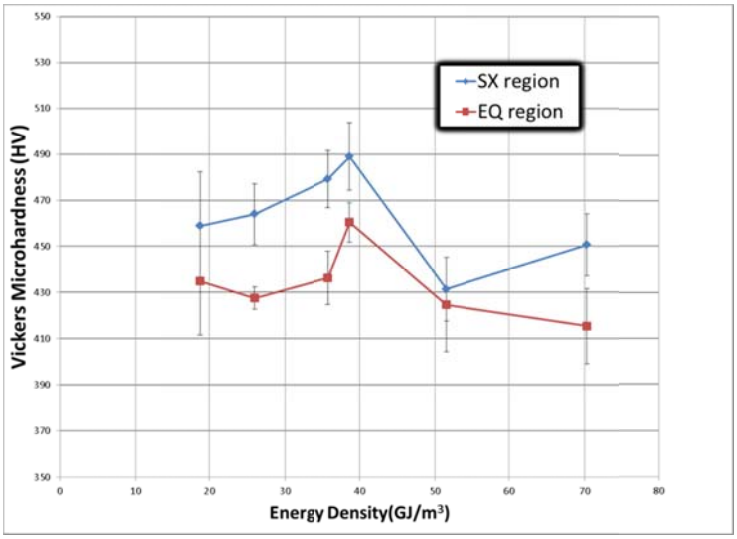

Figure 76. Vickers microhardness variation with energy density for CMSX-4 deposit.

Table 8. Summary of microindentation hardness test results for CMSX-4.

Region	HV_{500}	HV (GPa)	H_{RC}	σ_y (GPa)
Columnar	462	4.531	46.2	1.510
Equiaxed	433	4.246	45.7	1.415
Substrate	402	3.942	41.0	1.314

The MHT results obtained in the present study for CMSX-4 are significantly higher than the values obtained from existing literature. Aluru et al. [142] conducted a microhardness study for CMSX-4 processed through transient liquid phase bonding with other EQ superalloys. They obtained a value of 420 for HV. Lapin et al. [143] investigated the microindentation hardness as a function of volume fraction and size of primary γ′ precipitate in Bridgman casting. It was

shown that the hardness value increased with increase of volume fraction and decrease with the size of primary γ′ precipitate. The maximum hardness value obtained for 70 vol% and 147 nm size of primary γ′ precipitate was close to 430 HV, which is still lower than the hardness obtained for <001> region in the present study. This result can be linked to the microstructural refinement in SLE, since the primary γ′ precipitates produced in this process are typically smaller than 100 nm in size.

4.4 Feasibility study on IN 100

4.4.1 Powder processing

IN 100 powder was treated through the same procedure as René 80. IN 100 showed evidence of oxidized particles and porosity in the deposit. The morphology, size distribution and cross sections of powders were analyzed using optical microscopy and SEM. The IN 100 powders are mostly spherical with powder diameter showing a bimodal distribution with means of 20 and 60 μm as evidenced by Figure 77. Several cross-sections of IN 100 were imaged, and internal porosities were detected in most cases as seen in the representative image in Figure 78.

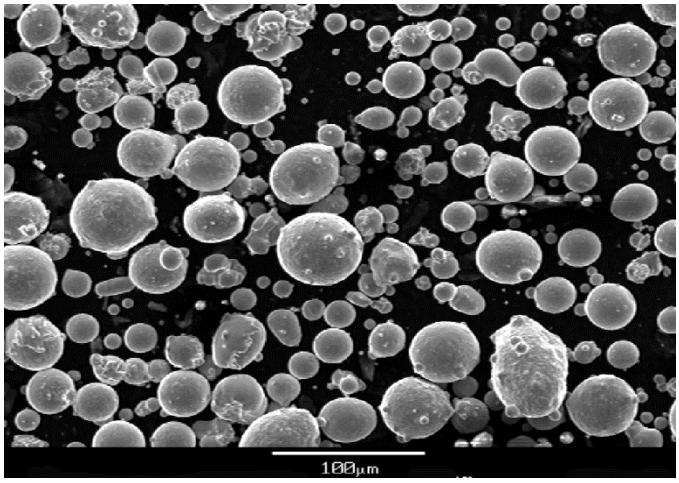

Figure 77. SEM image of the IN 100 powders.

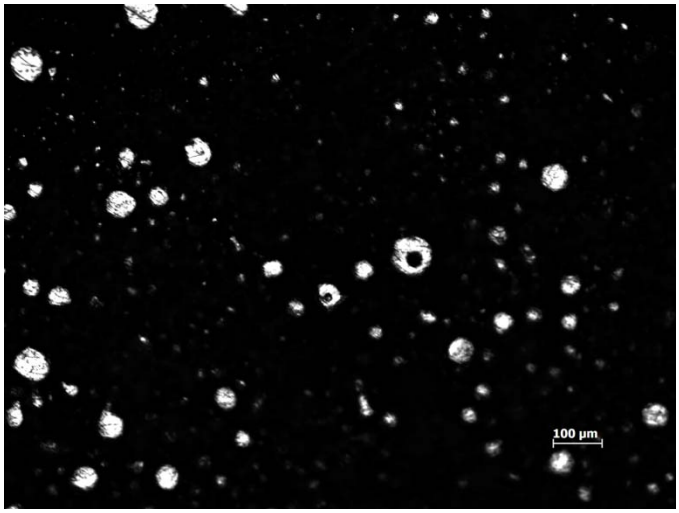

Figure 78. Optical microscopy of the IN 100 powder cross-section after polishing.

4.4.2 Optical microscopy

The longitudinal micrographs of two representative unetched IN 100 deposits are shown in Figure 79. The IN 100 samples are crack-free and near-fully dense. However, the oxidization of the IN 100 powder and the smaller gas porosity appearing in the powder remained a problem. As shown in the last paragraph, the IN 100 powders had internal porosity, and the particle diameters followed a bimodal distribution. The use of a coarse scan spacing often leaves the

powder partially melted, and the internal porosity contributes to a significant amount of smoke evolution during processing. Hence, the baking cycle was made longer as a remedy. Further to that, the scan spacing was adjusted in later trials to completely melt the powder. However, this may result in excessive melting of the substrate and a higher melt depth as shown in Figure 80(a) and (b). Hence a careful optimization of the scan parameters and scan spacing was used to optimize the parameter space. Figure 80(c) shows a deposit with reasonable melt depth and significantly less porosity.

The etched samples shown in Figure 80 also revealed a very fine microstructure in the deposit region compared to the substrate region. The characteristic dendritic segregation pattern is observed, with dendrite spacing ranging 20-30 microns in the deposit region.

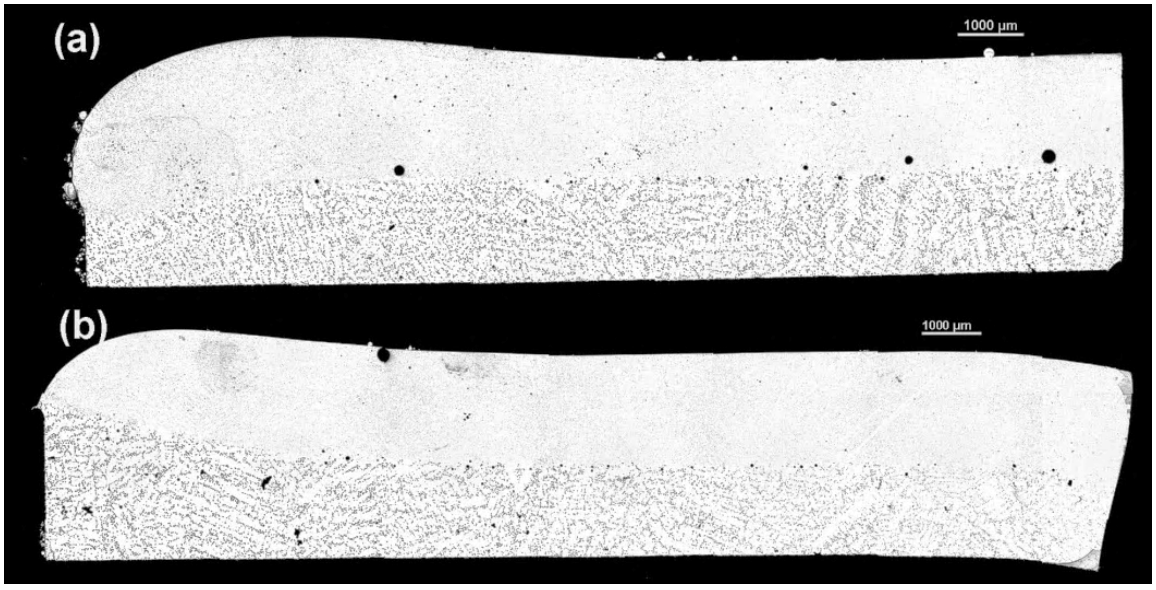

Figure 79. Representative optical micrograph of unetched IN 100 samples.

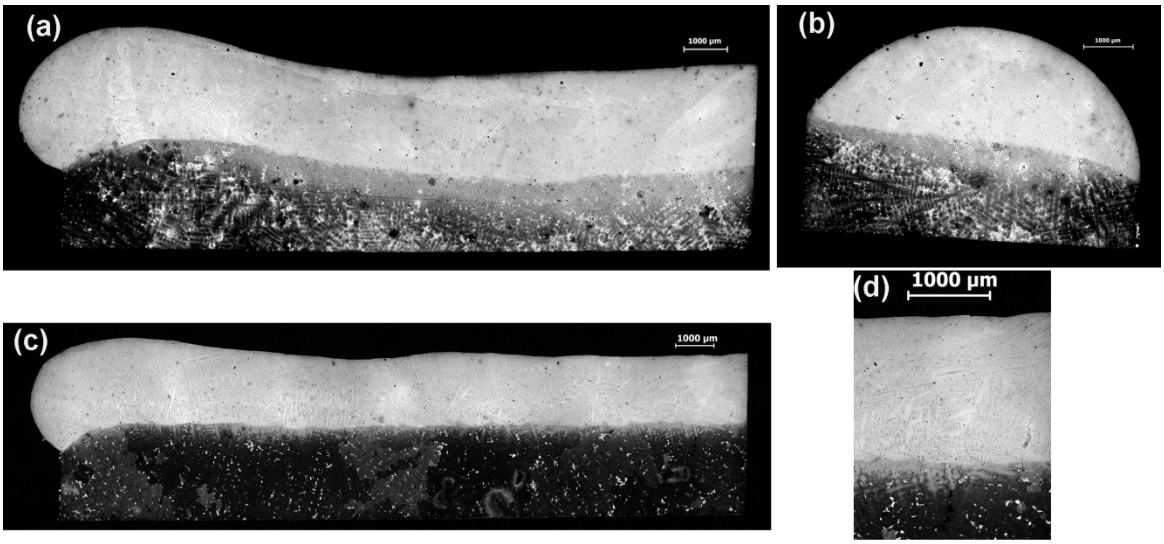

Figure 80. Optical micrograph of etched IN 100 samples showing (a) Sample with higher melt depth, (b) higher melt depth in widthwise cross-section, (c) sample with reasonable melt depth and (d) Microstructure refinement in the deposit region.

4.4.3 Scanning electron microscopy

SEM conducted over the substrate and the deposit region clearly indicated refinement of microstructure as shown in Figure 81. The regular γ/γ′ structure is present in both the substrate and the deposit regions. However, the substrate region shows a channel width of γ/γ′ in the micron scale. In contrast, the deposit region shows a very fine γ/γ′ structure, with channel width ranging from 100 nm to much lower size. The primary γ′ precipitates showed variation in size in the deposit region, while the substrate region is uniform on this aspect.

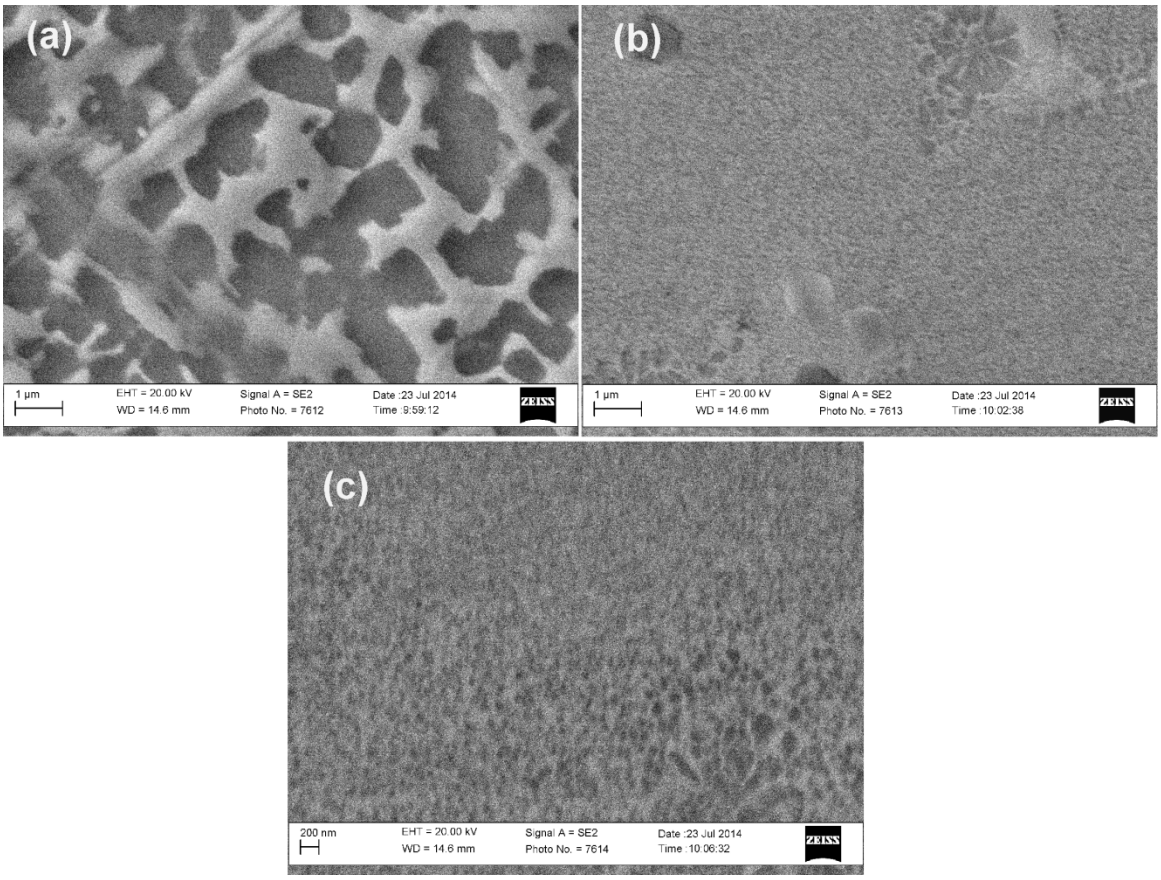

Figure 81. SEM image showing (a) coarse γ/γ′ channel width in substrate, (b) finer microstructure in deposit and (c) close-up image revealing γ/γ′ structure in deposit.

4.4.4 Microindentation Hardness Test (MHT)

MHT conducted over the substrate and the deposit regions of various samples revealed an increase in the hardness in the deposit region by 10% or more when compared with the substrate. A representative indentation in the deposit region is illustrated in Figure 82. The variation of microhardness with energy density is plotted in Figure 83. The samples processed using lower energy densities were found to possess slightly higher hardness. The higher energy density due to lower scan spacing extends the melt pool and reduces the temperature gradient, which might have caused a lower solidification rate and slightly coarser microstructure, resulting in lower

hardness. However, detailed SEM investigations for different samples are required to conclusively verify this reasoning.

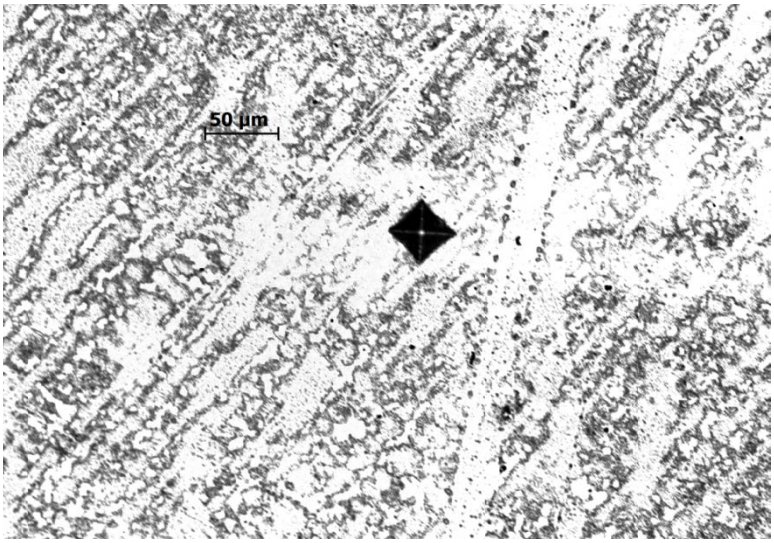

Figure 82. Representative microindentation on IN 100 deposit.

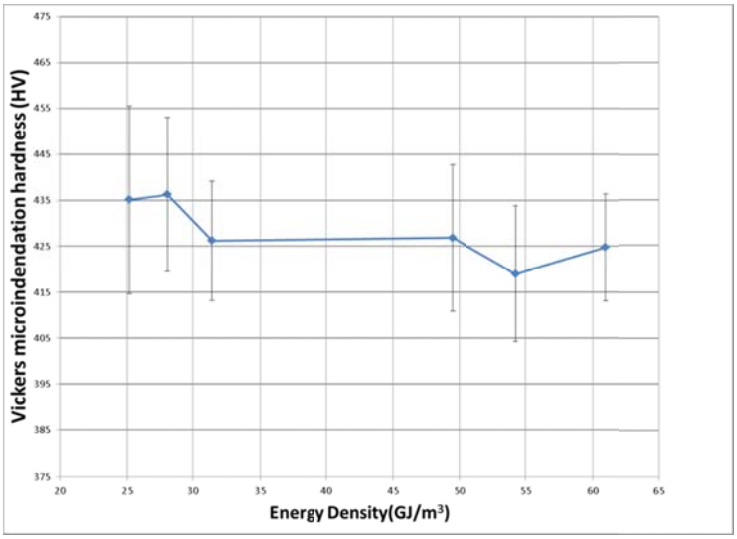

Figure 83. Variation of microindentation hardness with energy density for IN 100 deposit.

Table 9 summarizes the results of MHT. The deposit region showed an average HV_{500} value of 427 across all energy density, which is an increment of around 10% relative to the cast IN 100 samples.

Table 9. Summary of microindentation hardness test results for IN 100.

Region	HV_{500}	HV (GPa)	H_{RC}	σ_y (GPa)
Deposit	427	4.188	43.3	1.396
Substrate	390	3.825	39.8	1.275

4.5 Feasibility study on René 142 on SX René N5

4.5.1 Powder processing

René 142 powder was treated through the same procedure as CMSX-4. The morphology, size distribution and cross-sections of the powders were analyzed using optical microscopy and SEM. The René 142 powders are mostly spherical, although some irregularity in shape is found. The powder diameter is normally distributed within 90-150 μm, as evidenced by Figure 84. Several cross-sections of René 142 were imaged, and few or no major internal porosities were detected, as seen in the representative image shown in Figure 85.

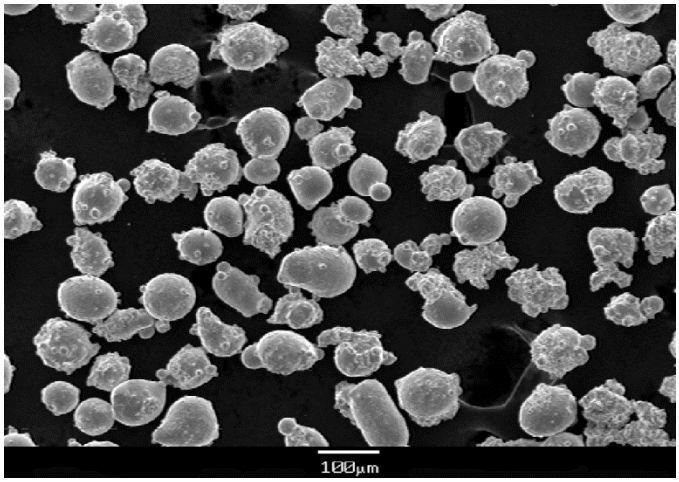

Figure 84. SEM image of the René 142 powder.

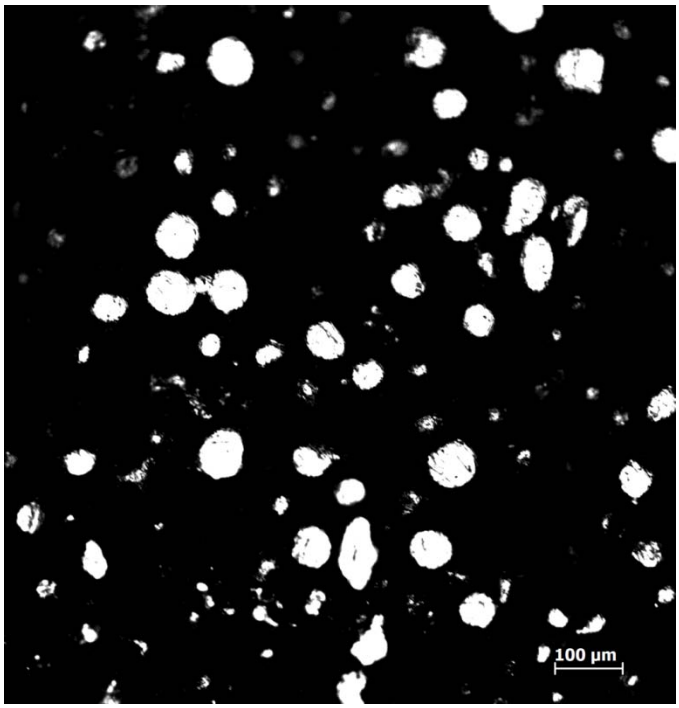

Figure 85. Optical microscopy of the René 142 powder cross-section after polishing.

4.5.2 Optical microscopy

The René 142 superalloy powders were deposited on SX René N5. The trials involved two different columnar orientations (<001> and <100>) for the René N5 deposits. Figure 86 shows an optical micrograph for two representative samples with differently oriented substrate regions. All of the samples revealed dense, crack-free deposits and microstructure refinement. The deposit region showed <001> columnar growth, flip of columnar orientation to <100> at variable heights and nucleation of equiaxed grains at the very top. The melt depths and deposit heights were also uniform across the length of the samples.

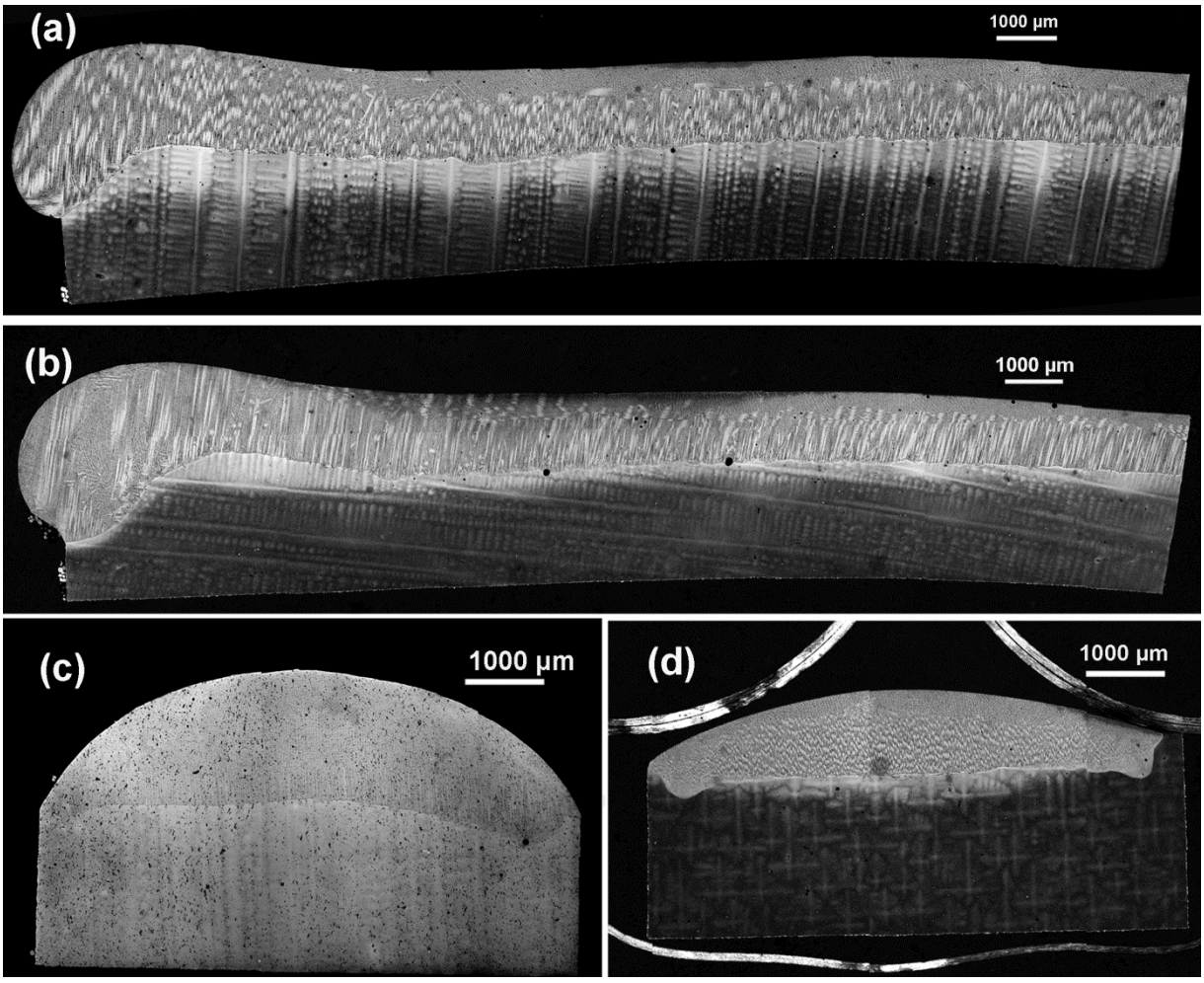

Figure 86. Optical micrograph of René 142 deposit on SX René N5 (a) longitudinal cross-section with substrate columnar orientation <001>, (b) with substrate columnar orientation <100>, (c) widthwise cross-section with substrate columnar orientation <001> and (d) widthwise cross-section with substrate columnar orientation <100>.

Figure 87 (a) shows the flip of columnar orientation from <001> to <100>, or OMT, and Figure 87 (b) shows the nucleation of equiaxed grains near the top region. The deposit region always showed finer dendrites in the etched optical micrographs, as shown in Figure 86 and Figure 87. The average PDAS in the substrate is close to 400 µm and the average PDAS in the deposit region ranges from 30 to 40 µm.

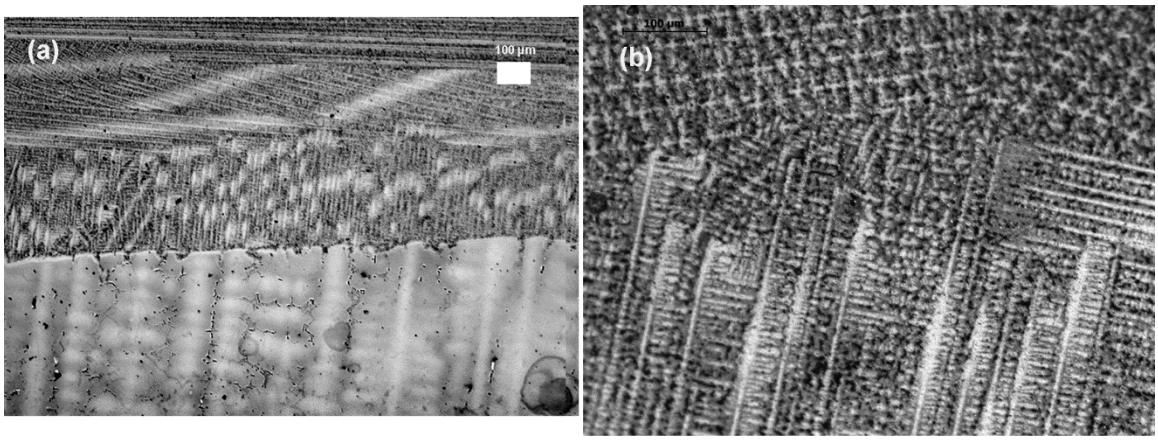

Figure 87. Optical micrograph showing (a) columnar flip and (b) equiaxed grain formation at the top region of René 142 deposit.

4.5.3 EBSD analysis

In order to understand the grain orientation and crystallographic texture EBSD analysis is carried out on two representative René 142 deposit. As revealed in Figure 88, apart from some stray grains at the top, it is hard to decipher any contrast and most of the deposit appears to be a single grain. Even the substrate orientation of <100> did not prohibit dendritic growth in <001> direction in the deposit region as seen in Figure 88(a). The starting edge showed some stray grains in Figure 88(b). The pole figure maps and inverse pole figure maps provide orientations with highest probability and orientation with respect to normal direction in Figure 89 and Figure 90.

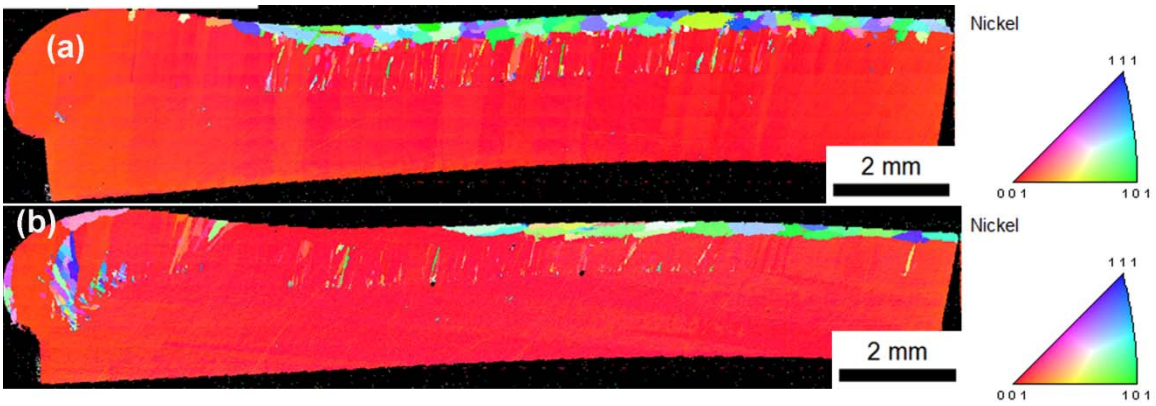

Figure 88. Large area orientation map obtained by EBSD of René 142 deposit on SX René N5 (a) with substrate columnar orientation <100>, and (b) substrate columnar orientation <001>

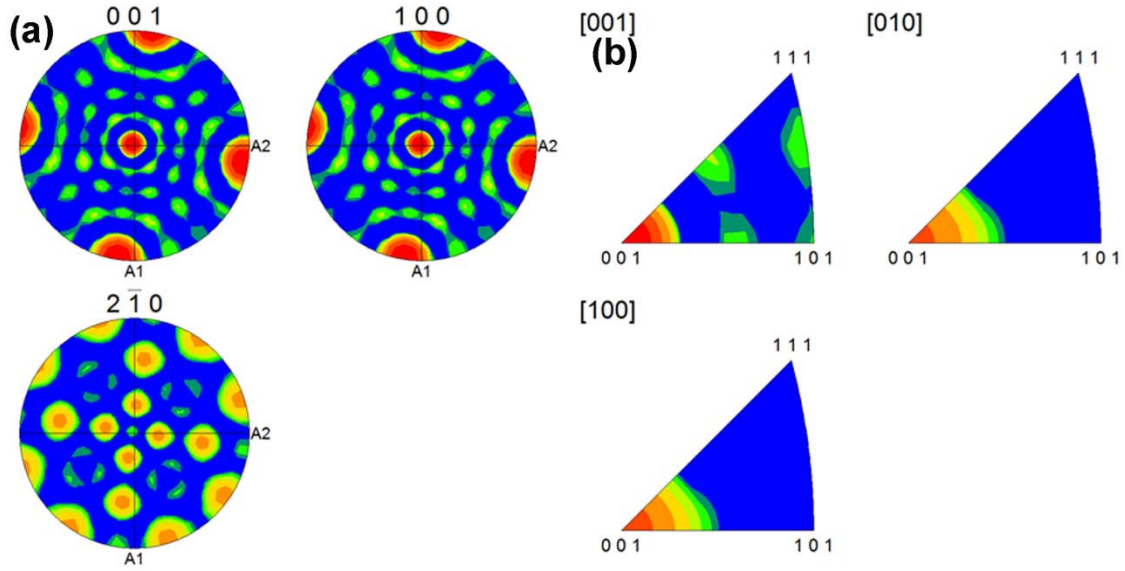

Figure 89. (a) Pole figure map and (b) inverse pole figure map obtained by EBSD of René 142 deposit on SX René N5 with substrate columnar orientation <100>.

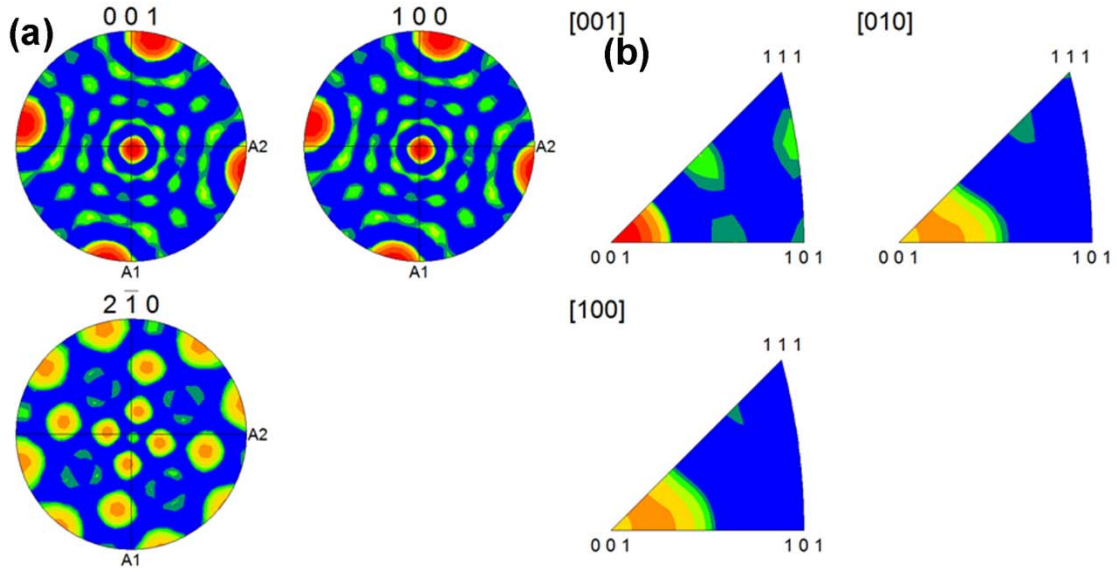

Figure 90. (a) Pole figure map and (b) inverse pole figure map obtained by EBSD of René 142 deposit on SX René N5 with substrate columnar orientation <001>.

Figure 91(a) and (b) shows the grain size map as estimated from the EBSD analysis. Essentially most of the deposit region is a single grain with equivalent diameter exceeding 7000 µm and the substrate orientation did not change the trends of the size distribution.

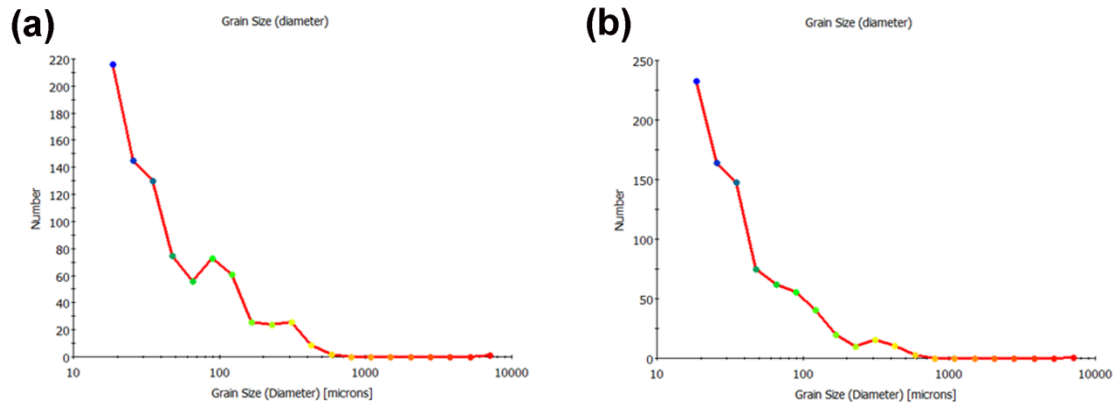

Figure 91. Grain size map of the deposit region for (a) substrate columnar orientation <100> and (b) substrate columnar orientation <001>.

4.5.4 Microindentation Hardness Test (MHT)

MHT conducted over the substrate region did not show any significant change of hardness due to changes in columnar orientation. The average value of the cast substrate hardness ranges from 400 to 420 HV. However, variations in hardness value were observed in different regions of the deposit. Figure 92 shows a representative microindentation near the interface and the columnar region.

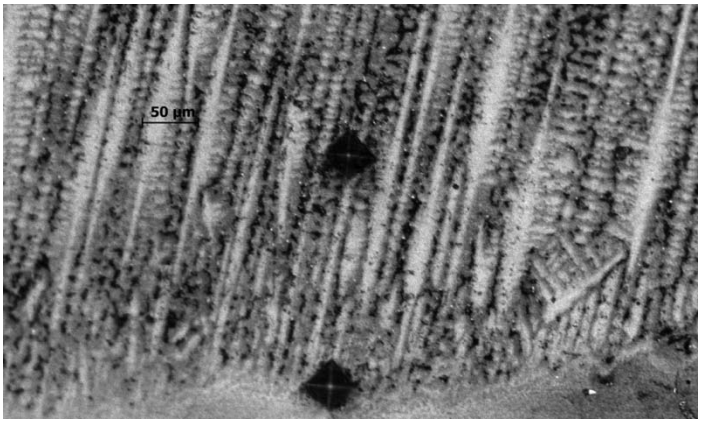

Figure 92. Representative microindentation on René 142 deposit near the interface and at the columnar region.

Figure 93 shows microindentations at different regions of the deposit and near the interface. The variations of HV values with energy density for different regions are plotted in Figure 94. The <001> columnar region consistently showed higher HV values ranging from 465 to 482. The <100> columnar and EQ regions showed hardness values in the range of 430-450 HV.

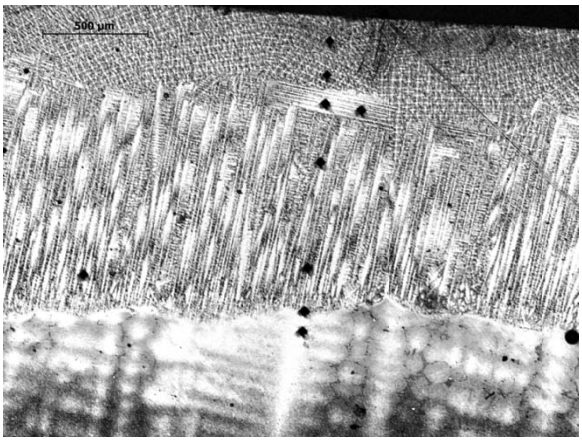

Figure 93. Microindentations at different regions of the René 142 deposit.

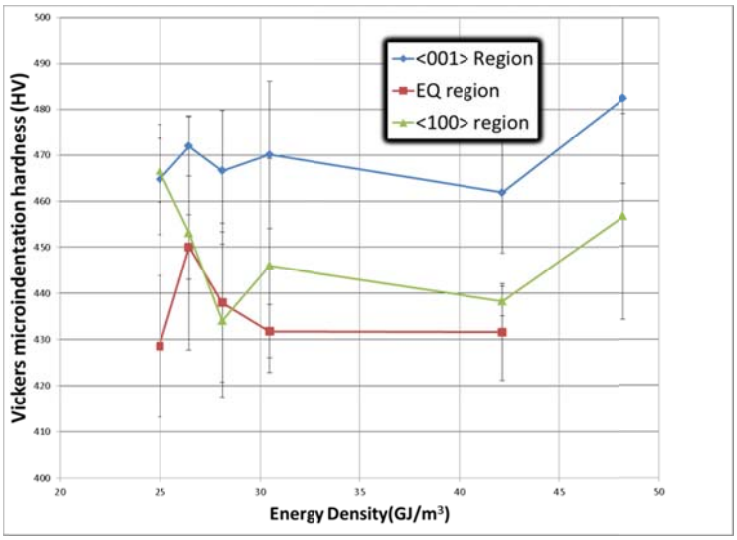

Figure 94. Variation of microindentation hardness for different region of René 142 deposit.

Table 10 summarizes the results obtained for MHT across the different regions. The prior literature on EBM-processed René 142 deposit reported an HV value of 4.2 GPa for DS René 142 [136]. The hardness values observed in the present investigation are higher for both the <001> and the <100> columnar regions. The <001> region showed an HV value of 4.6 GPa and the <100> region showed an HV value of 4.4 GPa. The EQ region displayed a lower hardness of 4.28 GPa.

Table 10. Summary of microindentation hardness test results for René 142 deposit on SX René N5 Substrate.

Region	HV_{500}	HV (GPa)	H_{RC}	σ_y (GPa)
<001> region	469.6	4.605	46.9	1.535
<100> region	449.2	4.405	45.3	1.468
EQ region	436	4.276	44.1	1.425
Substrate	410	4.021	41.8	1.340

4.6 Summary

This chapter describes a SLE processing feasibility study conducted on four different 'non-weldable' superalloys, EQ René 80, EQ IN 100, SX CMSX-4 and René 142. The results prove that SLE can be used successfully and consistently in the creation of depositions and the production of components with desired microstructure. Hence, the hypothesis that SLE can overcome the challenges associated with the non-weldability of different hot-section superalloys is clearly validated. The key conclusions are summarized in the paragraph below.

4.6.1 Weldability

Figure 95 illustrates the effect of four major alloying elements (Ti, Al, Cr and Co) on the weldability of superalloys [144]. The alloys investigated in the present research are marked on the weldability assessment chart, and, as can be seen, all of them are susceptible to HAZ cracking. The alloys CMSX-4, René 142 and IN 100 can all be considered as 'difficult-to-weld'. However, the present study conducted on processing of these alloys through SLE clearly shows that these alloys can be repaired without producing any macro-cracks. Additionally, the desired microstructure (EQ/DS/SX) can be maintained in the deposit region for a considerable height (on

the order of 1000 μm and higher). The locations of microstructural transitions depend on the thermal gradient and solidification velocity and will be further elaborated on in chapter V. However, the ability to produce the dense, crack-free deposit eliminates or nearly eliminates any post-processing operation such as HIP. However, different types of heat treatment cycles might be mandated depending on microstructural and property requirements in the final product prior to insertion into service.

The optimization of process parameters yields a continuous, dense deposit without any major cracks or porosity. The porosity and oxidation of IN 100 is still a challenge, but it is more due to the bimodal distribution and internal porosity of the specific powder used rather due to any process limitations of SLE. The ability to consistently produce these deposits with epitaxial microstructure extends the utility of SLE for FGM. The absence of powder blowing into the melt pool, pre-and post-heat treatment of the melt pool by the scanning laser, the precise and fast movement of the heat source and the baking of powder prior to SLE can be cited as the reasons of improvement over the existing state-of-the-art techniques. Together, these features impart significant added capability to the SLE process as illustrated in this feasibility study.

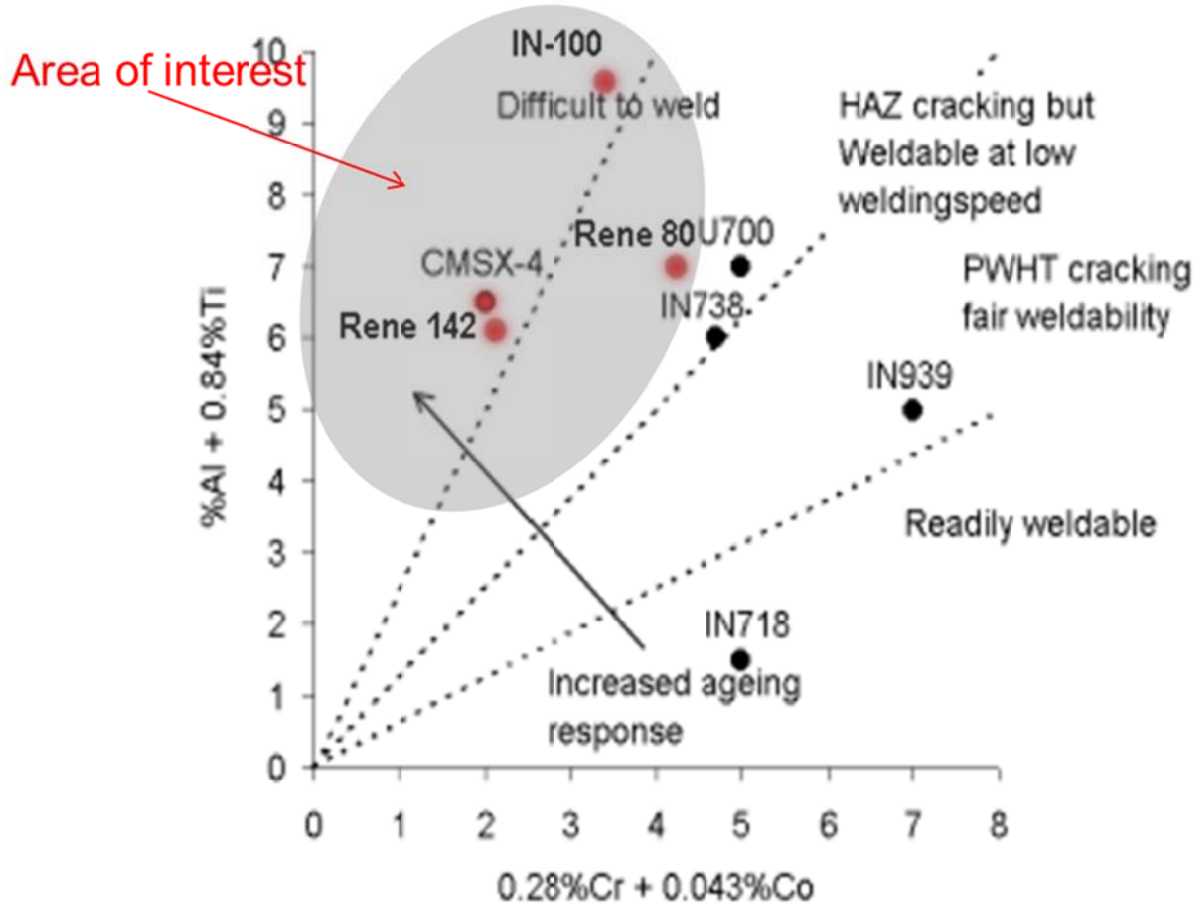

Figure 95. Modified weldabilty assessment chart after considering the effect of Cr and Co [42, 144]. The superalloys marked with red dots are investigated in the present research and mapped into the weldability assessment chart.

4.6.2 Microstructure refinement

The refinement of the microstructure in the deposit region as compared to the microstructure in the cast substrate is another notable feature of SLE. A detailed microstructural study conducted on René 80 confirms refinement of the primary and secondary γ′ precipitates and microstructural refinement as a whole. Similar results are obtained for SX CMSX-4 as well. The PDAS in the deposit region is 10 to 20 times finer than that of the cast substrate. The EQ IN

100 deposit also showed refinement of the dendritic structure and reduction in the size of the primary γ′ precipitates. The René 142 deposit also showed refinement in PDAS over the cast SX René N5. Refinement in microstructure can theoretically impart more strength to the deposit region.

4.6.3 Mechanical properties

A summary of the MHT tests conducted in the present investigation is highlighted in Table 11. The data clearly explains the superiority of the deposit region in terms of Vickers microindentation hardness value and confirms the theory that the microstructure refinement can potentially impart more strength in the deposit region. In addition to that, the hardness values obtained are in a similar range as or are higher than the available hardness data of different superalloys, as explained in Table 11. For the SX or DS alloys, the comparison is made on the basis of the <001> columnar region, since this is the desired morphology in the application area. However the data presented is averaged over the entire energy density spectrum. Thus, SLE can produce deposits with higher hardness by optimizing the process parameters. As a result, the actual increments in hardness values over those of the cast substrates or published in existing literatures are higher in practice.

Table 11. Comparison of hardness value with cast substrate material and maximum value obtained from literatures.

Name	$HV_{Deposit}$ (GPa)	$HV_{Substrate}$ (GPa)	Increase over substrate (%)	HV(GPa) (Lit.)	% increment from available literature
René 80	4.805±0.6	3.923±0.3	22.483	4.315 [138]	11.36
CMSX-4	4.531 ±0.4	3.942±0.35	14.942	4.250 [143]	6.61
IN 100	4.188±0.7	3.825±0.8	9.490	NA	NA
René142	4.600±0.5	4.021±0.45	14.399	4.200 [136]	9.52

4.6.4 Retention of morphology

The retention of SX or DS morphology in the deposit region is of paramount importance for gas turbine components. The elimination of the grain boundary transverse to the stress direction imparts improved creep resistance. The microstructural investigations, namely the optical micrographs and EBSD results for CMSX-4 and René 142, clearly elucidate that SLE is able to retain the morphology of the cast substrate. It is possible to obtain a higher SX height or <001> columnar height through careful optimization of the process parameters. This allows the SLE process to be applied to various SX or DS superalloys.

Chapter V

Process Modeling

5.1 Introduction

The output responses required to characterize SLE-produced parts are numerous and varied. The melt depth, uniformity of deposit or surface waviness and crack formation should be controlled to obtain parts with higher quality and reliability. Similarly, from a microstructural point of view, the CET and OMT should be minimized or controlled to obtain better quality deposits. Thus, a multiphysics approach that allows the coupling of flow-thermal phenomena and microstructural transformations can provide a better understanding and reliable initial processing parameter ranges (scan speed, laser power etc.) for different materials. In contrast, a design-of-experiments (DoE) based model will lack the generalization present in the physics-based model and will need to be repeated for each new material because of the widely varying properties of Ni-based superalloys. Hence, a coupled flow-thermal-microstructural model is necessary to reduce the experimental cost and to obtain a deeper understanding of the entire manufacturing process.

This chapter studies the fundamental aspects of SLE without sacrificing the intricate details of scan parameters and complex material properties. A CFD-based multiphysics model was developed and coupled with stochastic microstructural models that enabled predictive capabilities to be developed for laser-material interactions in SLE.

5.2 3D domain Computational fluid dynamics (CFD) modeling

The CFD-based multphysics model requirements are elaborated in Chapter I. Figure 7 depicts the physical phenomena involved in SLE. Consideration of the detailed scan geometry and variation of thermo-physical properties makes the solution more accurate. However, tracking the melt pool in the 3D domain requires a huge number of mesh elements and makes the solution computationally expensive. The ND:YAG laser used with SLE allowed a 3D model to be used due to its comparatively large Gaussian beam diameter (1.5 mm). Hence, the initial model used the set of scan parameters associated with the ND:YAG laser, and the validation study was based on the microstructural features, namely the melt depth data.

In the current work, the laser beam was scanned at high speeds in the y-direction while stepping over in the x-direction, and this behavior was modeled as a line source scanning in the x-direction. The power profile in the y-direction was formulated from the transient averaged intensity data for a single scan and fitted with a 10^{th} degree polynomial. The complete scan pattern was formulated in this manner. The associated melting and re-solidification of the CMSX-4 powder bed and the substrate were taken into account by using the equilibrium phase change model. Heat transfer to the base plate was also modeled using the heat conduction equation. The complete simulation, along with post-processing to predict the microstructure, was performed in the ANSYS CFX modeling environment. Additional physics were incorporated into the model using CFX Expression Language (CEL), and additional post-processing in CFD-Post was carried out using a Perl script. This enabled the integration of thermal-fluid modeling with microstructure prediction. Reasonable agreement was obtained between the simulation and the experimental results in terms of melt depth, flow phenomena and microstructural changes.

5.2.1 Material properties

A transient, multi-domain model with temperature-dependent property values was developed to simulate the thermal aspects of the model and to predict the melt depth. Thermo-physical property data for liquid and solid CMSX-4 was accurately modeled using tabular data [145]. The Inconel 625 property data was also modeled using tabular data [9]. The following thermo-physical properties were modeled as temperature-dependent for the liquid and solid phases: specific heat, viscosity and thermal conductivity. An example of the variation of specific heat with temperature for the liquid phase is presented in Table 12. The change in density was modeled using the Boussinesq approximation to avoid solver instability in a closed domain. In the commercial code, a 'multicomponent model' was used, and the mixture of solid and liquid CMSX-4 was treated as a 'variable composition mixture' with the reference enthalpy of the liquid phase set as 231 kJ/kg or latent heat value. The phase change was determined through the algebraic relation for the solid fraction as a function of local temperature. No additional consideration was provided for the presence of powder instead of solid CMSX-4.

Table 12. Variation of specific heat of liquid CMSX-4 with temperature [145]

Temperature (K)	Specific heat (J/gK)
1653	0.69
1703	0.74
1723	0.78
1753	0.78
1773	0.77
1793	0.76
1813	0.75
2000	0.75

5.2.2 Geometry, mesh generation and boundary conditions

The process was tested on rectangular SX cast CMSX-4 coupons having dimensions of 35.56mm x 10.16mm x 2.54mm. Each substrate was placed into a 35.56mm x 10.16mm recession cut into an Inconel 625 base plate. The multi-domain model consists of a deposit domain (consisting of the substrate as well as the powder bed), the excess powder surrounding the melt pool, and the Inconel 625 base plate. Figure 96 shows the different domains involved. The mesh for the given problem was generated in ANSYS Mesher. The deposit domains were modeled using a finer mesh, and the mesh was gradually refined near the top surface. The node count for the given case was around 250k, with skewness not exceeding 0.5.

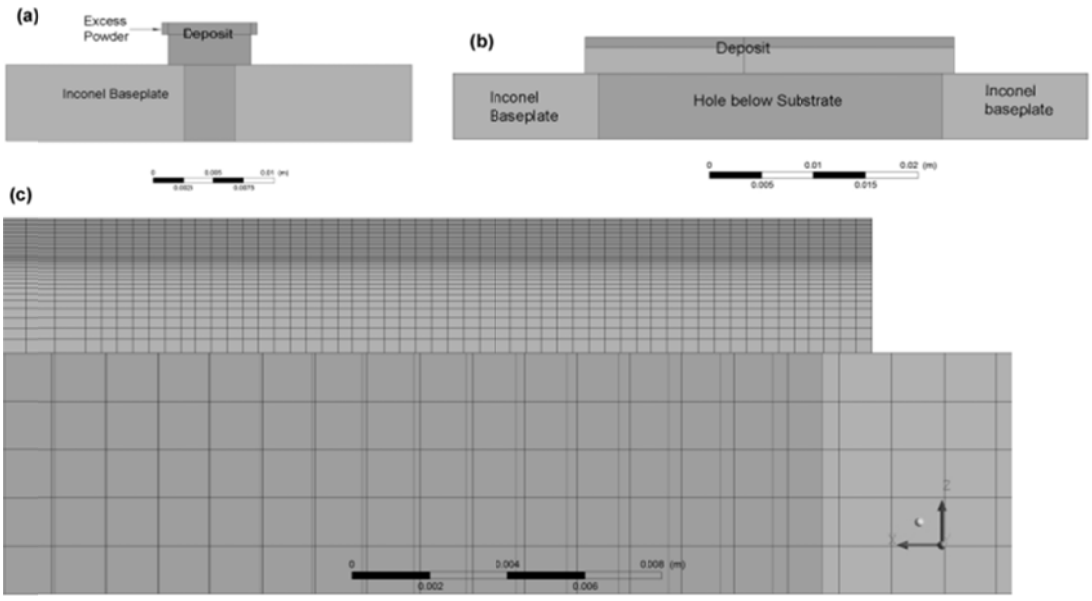

Figure 96. (a), (b) CFX multi-domain model showing different domains in CFD model and (c) Finer mesh in the Deposit domain.

All the boundary surfaces of the connected solid domains not interfaced with deposit were treated as an adiabatic wall. The top surface of the deposit domain was modeled as a wall with a

specified shear value determined by the Marangoni effect. The side surfaces of the deposit domain were modeled as openings that allow both inflow and outflow and provide solver stability. SLE starts from ambient conditions; hence, 300K was used as the initial temperature.

5.2.3 Physics definition

a) Heat source

The actual laser heat source has a Gaussian beam radius of 0.75 mm. The spatial intensity profile of the laser beam completing upon one scan in the y-direction was averaged for a single scan length over the sample width and was fitted with a 10^{th} degree polynomial. This particular profile was then used as a line source with Gaussian distribution applied in the x-direction. The particular form of intensity profile used was,

$$I(y_n) = \sum_{i=0}^{10} \left(P_i y_n^i \right) \tag{19}$$

with, y_n=(y-mu)/sigma (mu, sigma are laser beam parameters)

The coefficients were determined from a simulation of a laser beam rastering in the y-direction and by averaging the power profile in the y-direction. The width of the coupon was used in calculating the residence time of a line heat source in any given position, and after that time the line heat source was moved forward by the scan spacing.

b) Energy equation

The solid and liquid component enthalpy equations, expressed in terms of volume fraction, r, are:

$$\frac{\partial(\rho_S r_S h_S)}{\partial t} + \nabla \bullet (\rho_S r_S U_S h_S) = \nabla \bullet (r_S k_S \nabla T_S) + I \tag{20}$$

$$\frac{\partial(\rho_L r_L h_L)}{\partial t} + \nabla \bullet (\rho_L r_L U_L h_L) = \nabla \bullet (r_L k_L \nabla T_L) - I \tag{21}$$

Here ρ is the density, h is the enthalpy (including the latent heat), T is temperature, U is velocity and I is the interphase heat transfer. The subscripts S and L refer to the solid and liquid components respectively.

Equations 20 and 21 can be expressed more compactly as:

$$\frac{\partial(\bar{\rho}h)}{\partial t} + \nabla \bullet (\bar{\rho}Uh) = \nabla \bullet (\bar{k}\nabla T) + S - \nabla \bullet (\bar{\rho}Y_S(U - U_S)(h_L - h_S)) \tag{22}$$

where $\bar{\rho}$ is mixture density, h is the mixture enthalpy, $\bar{k}$ is mixture conductivity, Y_S is the mass fraction of solid, and S is the source term due to laser heat source [146].

The final term of Equation 22 represents an additional source due to the difference in velocity between the solid and liquid components. This term is finite only in the mushy region of the flow ($0 < Y_S, Y_L < 1$). In regions of pure liquid or pure solid, the mixture enthalpy equation is identical to the appropriate component enthalpy equation.

For the other two domains (Baseplate and Excess Powder), the solid conduction equation was solved as:

$$\frac{\partial(\rho H)}{\partial t} = \nabla \bullet (K \nabla T) + S_0 \tag{23}$$

where, ρ=Density, H=Enthalpy, K=Thermal conductivity, S_0=Source/sink.

Since there was no flow into or out of the domain, the chosen model prevented the use of an explicitly varying density for liquid CMSX-4. Therefore the volumetric changes were accounted for by using the Boussinesq approximation to artificially include a buoyancy-induced source term.

c) Melting and solidification

In order to consider the resistance to flow in the mushy region, a Darcy-like source term was incorporated in the momentum equation. The permeability source term S_M was modelled using the Kozeny-Carman equation [147].

$$S_M = \min\left(C, \frac{\mu_L}{K_0}\frac{(1-r_L)^2}{r_L^3}\right)(U - U_S) \tag{24}$$

Here, μ_L is the viscosity and K_0 is the proportionality constant in Kozeny-Carman equation.

To prevent division by zero, the term is bounded by a user-specified maximum, C.

In the turbulence equations, sink terms similar to the Darcy terms in the momentum equation were applied to damp the turbulence in solid regions. For the k-ε model, these sink terms took the form [146]:

$$S_k = -\frac{\mu_L}{K_0}\frac{(1-r_L)^2}{r_L^3}k \quad , \quad S_\varepsilon = -\frac{\mu_L}{K_0}\frac{(1-r_L)^2}{r_L^3}\varepsilon \tag{25}$$

Here k is the turbulence kinetic energy and ε is the turbulence eddy dissipation.

d) Marangoni convection

A liquid with a high surface tension pulls more strongly on the surrounding liquid than one with a low surface tension. Hence, the presence of a gradient in surface tension (due to a

temperature gradient) will naturally cause the liquid to flow away from regions of low surface tension. This extends the melt pool laterally and makes it shallower [93].

The effects of Marangoni convection were studied by imposing surface tension driven shear force at the free surface [148] through the following relations:

$$\mu \frac{\partial U_x}{\partial x} = r_L \frac{\partial \gamma}{\partial T} \frac{\partial T}{\partial x}, \quad \mu \frac{\partial U_y}{\partial y} = r_L \frac{\partial \gamma}{\partial T} \frac{\partial T}{\partial y} \tag{26}$$

Here, $\frac{\partial \gamma}{\partial T}$ represents the temperature coefficient of surface tension after neglecting the concentration of surface active species such as Sulfur or Oxygen, and subscripts x and y denote components in the x- and y-directions respectively.

e) Solution and post-processing

The conservation of H-energy was assured at all connecting interfaces. The convection heat loss was modeled using Newton's law of cooling as a surface sink term applied at all boundaries open to the surroundings. Radiation loss was also modeled from open surfaces using a sink term. The transient model was solved using a time step value equal to 0.00215 s. The inclusion of convection, the phase change model, and the Darcy sink term together necessitated the use of a lower time step value in order to ensure solver stability. The imbalance in the system was kept within 1% and the convergence ensured the RMS value of the residuals to a value below 1×10^{-4}.

Once solved, the results were post-processed in CFD-post to analyze the melt pool nature, the melt depth profile and the temperature distribution. Including the convection allowed the velocity field to be visualized. For comparison purposes, pure conduction modes were also run with the same set of parameters, and the results were compared to distinguish the effects of

convection and surface tension on the melt depth and the microstructure.

f) Process parameters

Table 13 lists the process parameter ranges used to simulate the laser-material interaction for CMSX-4. Different powder heights of 1 mm, 1.5 mm and, 2 mm were simulated

Table 13. Process parameter ranges used for simulation.

Process Parameter	Range/Value
Powder Thickness	1 mm, 1.5 mm, 2 mm
Laser Power	400 – 600 W
Scan Speed	150 – 250 mm/sec
Initial Repeat Scans	50 – 150

5.2.4 Results and discussion

The melt depth profile is of particular importance for the present application, and hence it was compared with the actual micrograph. Reasonable quantitative agreement was achieved in the simulated profile and observed data as shown in Figure 97(a) and (b) for two different powder thicknesses and operating parameter sets.

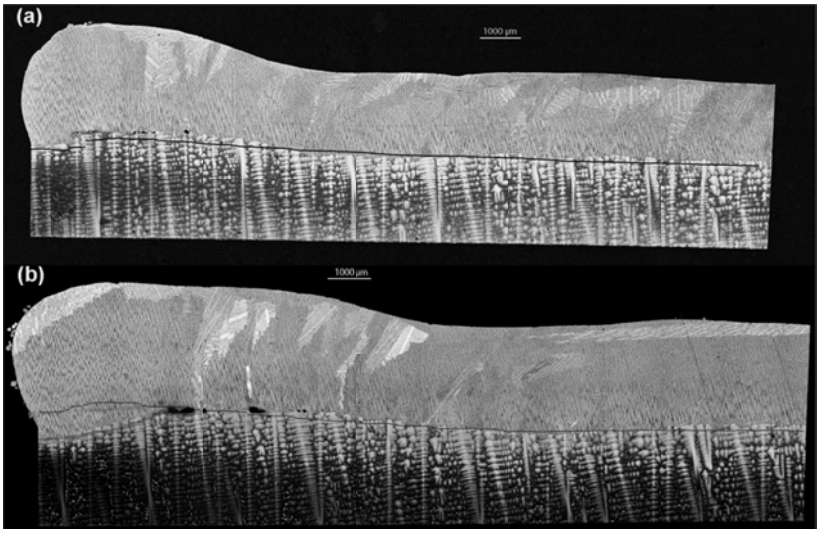

Figure 97. Comparisons of the simulated melt depth (Dark gray line) with actual micrograph for (a) powder thickness = 1 mm and (b) powder thickness = 1.5 mm

In order to understand the effect of convection on the estimated melt depth, simulations that did not incorporate fluid convection were carried out and comparisons were drawn with the actual melt depth profile. As seen in Figure 98, the discrepancy is centered at the starting edge and begins to dissipate as the scan progresses. However, at any position of the heat source, incorporating convection into the simulation resulted in a decrease of melt pool depth by around 10% over the results obtained with the pure conduction model. Incorporation of Marangoni convection makes the melt pool even shallower.

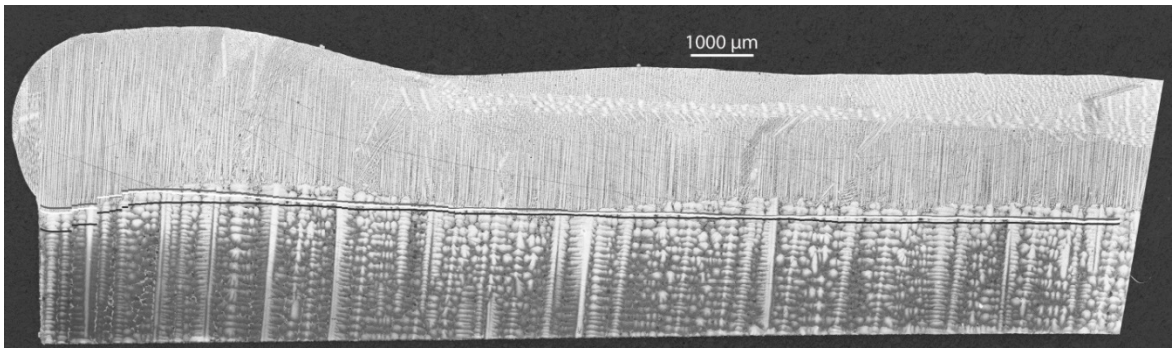

Figure 98. Comparisons of the melt depth with actual micrograph for models with pure conduction (black line), pure convection (white) and Marangoni effect with convection (dark gray)

The effect of convection on the mushy zone is studied in Figure 99. The mushy zone volume increases with time and does not attain a steady state value. As shown, the extent of the mushy zone decreases by around 30% when convection is included, and it further decreases after incorporating the effect of surface tension, as shown in Figure 99(b). Within the mushy zone, the high volume fraction of the solid restricts the flow of the liquid and causes tensile stresses that might result in solidification cracking [49]; hence accurate estimation of the mushy zone is required to predict crack growth.

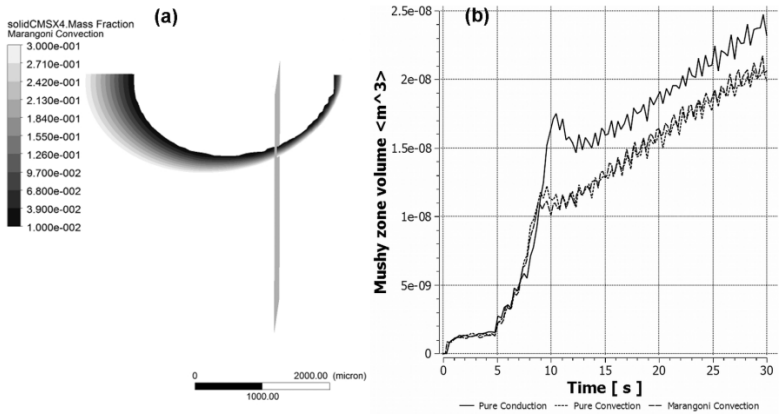

Figure 99. Representative contour plots showing (a) Extent of the mushy zone and (b) comparison of mushy zone volume with time for pure conduction, natural convection and Marangoni convection.

As seen in Figure 100(a), in the representative case, all the models attain a steady periodic melt pool width between 2.1-2.4 mm. The pure conduction model shows the largest width and depth, since the heat is primarily confined within the melt pool. When only natural convection is incorporated, the melt pool width decreases to 2.1 mm. However, after inclusion of Marangoni convection, the melt pool width increases and shows traits similar to those of pure conduction. The melt pool becomes shallower with incorporation of convection, as seen in Figure 100(b), and it shows an asymptotic nature with time for all models. The pure conduction model reaches a melt depth value of 1.4 mm in the representative case, while Marangoni and natural convection models indicate a slightly lower value.

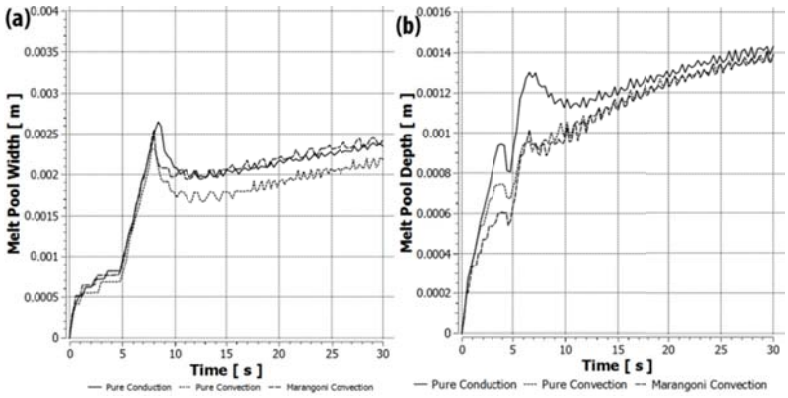

Figure 100. Representative Plots showing comparison between different models for (a) Melt pool width and (b) Melt pool depth.

The most significant effect of convection is observed on the temperature gradient profile at the solid-liquid interface. As shown in Figure 101, the melt pool takes a convex hull shape in the raster scan scenario instead of an ellipsoidal profile, as has been observed by others in single bead scans of laser cladding [77]. When convection is included, a decreased range of temperature gradients is found over the melt pool. As a result, the maximum temperature gradient decreases while the minimum observed value increases. However, the maximum value is always observed ahead of the heat source, in a region which will undergo remelting as the scan progresses. The region that lies behind the heat source is important, and this region experiences increased temperature gradients because convection is included in the calculation. However, the inclusion of Marangoni convection provides a more accurate representation due to the surface convection, which lowers the temperature gradient at the back surface.

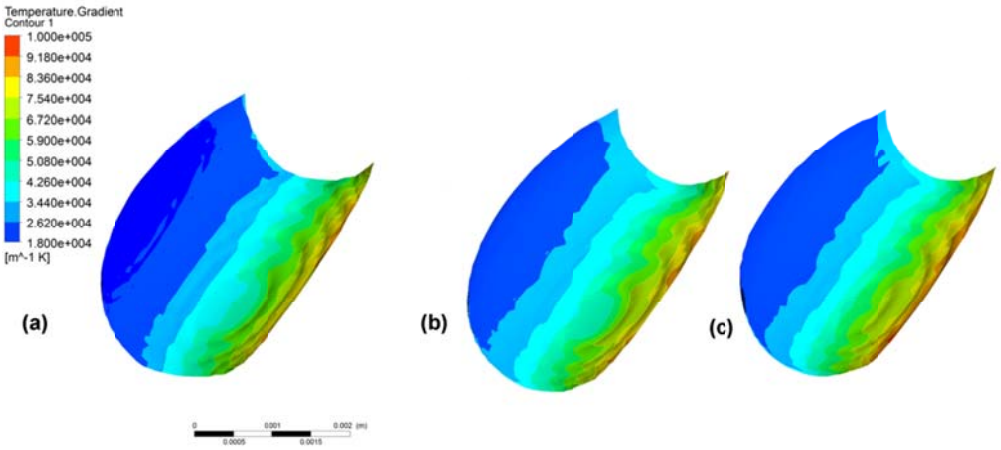

Figure 101. Representative contours of temperature gradient at the solid liquid interface (a) without convection and (b) with convection and (c) with natural and Marangoni convection.

The velocity field generated due to the moving heat source is important for understanding how loose powders are drawn into the melt pool. As shown in Figure 102, the flow field consists of two vortices, with the center of the vortices at lower velocity. The center is located at the middle of the melt pool, and the flow field draws loose powder at the top while the melt pool expands at the bottom and sideways. The moving heat source also results in an outgoing high temperature current at lower velocity, as shown in Figure 102(b). However, in cases that omitted the Marangoni convection the low-temperature particles were drawn right at the top surface, which is unrealistic. A more comprehensive result is found in the cases that include the Marangoni convection in Figure 102(d), which shows low-temperature powder particles falling down and being sucked to the bottom of the melt pool. Video microscopy of the process also suggested that during the preheat scans, the melt pool establishes itself, and, as the scan source progresses, preheated loose powder gradually falls into the melt pool. Then the melt pool elongates laterally. Figure 102(e) shows the resultant effect of Marangoni effect and natural convection on the y-

component of velocity when considered from the transverse direction. As shown, the velocity component flips direction near the middle of the melt pool and at the center of the vortices, and it exhibits high velocity at the top surface. Marangoni convection also results in an increased convection current. The velocity range increases by an order of magnitude, with pure convection showing velocity of order of 10^{-4} m/s, while the Marangoni effect drives it to $2x10^{-3}$ m/s. The velocity at which the powder falls into the melt pool is important in maintaining deposit uniformity. Very high powder velocity may create balling in the current position and starvation of powder from the position ahead, thus resulting in surface rippling. Figure 102(f) and (g) show the temperature contours in the melt pool and the surrounding mushy region.

Marangoni convection, thus results in the extension of the melt pool, an increase in the velocity range and greater tendency to disrupt the microstructure at the back of the melt pool. This can be verified from the streamline plot of pure convection, and with the inclusion of Marangoni convection, as shown in Figure 103, with a greater number of stream lines extending to the solidified region.

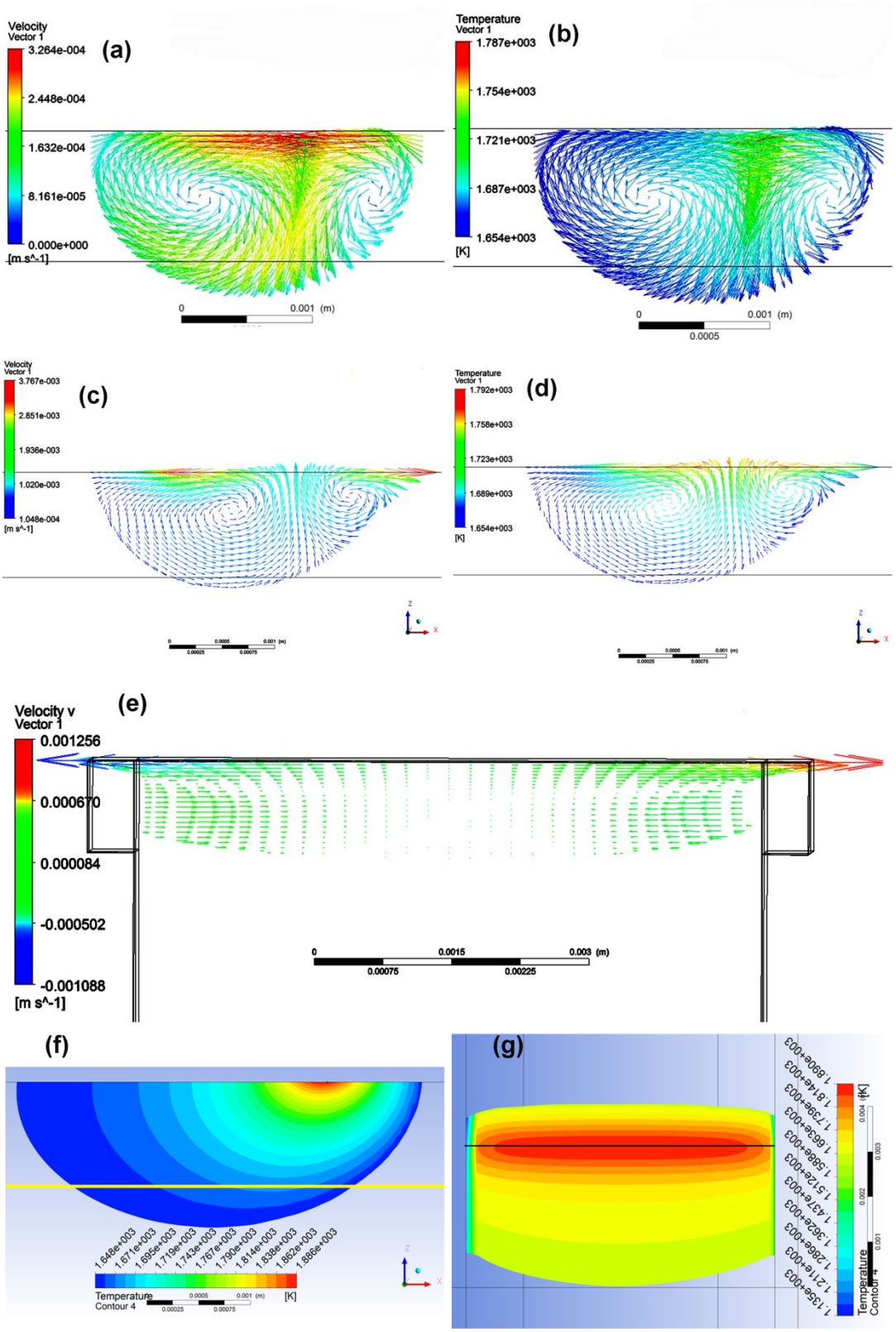

Figure 102. Representative contours of (a) velocity vector observed in the liquid region, (b)

Temperature map of the velocity vector in the melt pool and the effect of Marangoni convection on (c) velocity vector and (d) temperature map (e) transverse cross-section showing the y-component of velocity after inclusion of natural and Marangoni convection, Temperature contour of the melt pool and mushy zone with liquid fraction>0.8 (f) along the longitudinal cross section and (g) at the top surface of deposit.

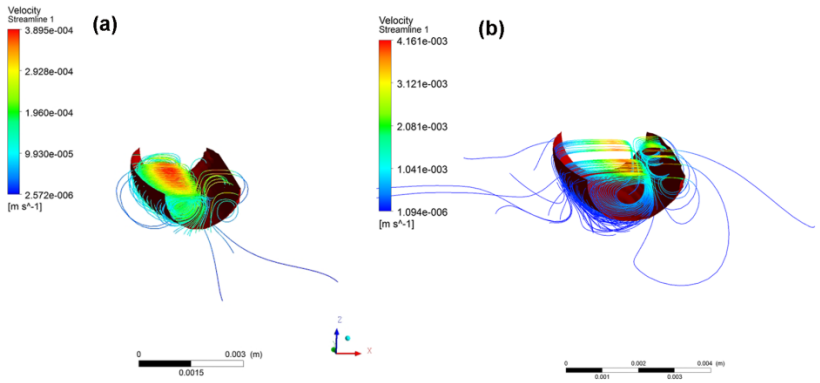

Figure 103. Representative contours showing (a) Velocity Streamlines in the melt zone with convection showing rotational vortices and (b) Effect on streamlines after including Marangoni convection.

5.3 2D domain CFD modeling

The Gaussian beam diameter of the fiber laser at the focal plane was found to be 40 µm, and the raster scan spacing utilized was 12.5-25 µm. A complete 3D numerical model of the system is computationally very expensive. In order to reduce the computational cost, the geometry was simplified to a one element thick pseudo-2D model in CFX. This reduced the computational burden significantly without sacrificing the accuracy in the model. The polynomial used for the laser heat source intensity in the y-direction was found to be flat in the

middle region with some reduction of intensity near the edges of the sample, as shown in Figure 104. Hence, this small variation in y-direction was neglected to model the problem physics in 2D.

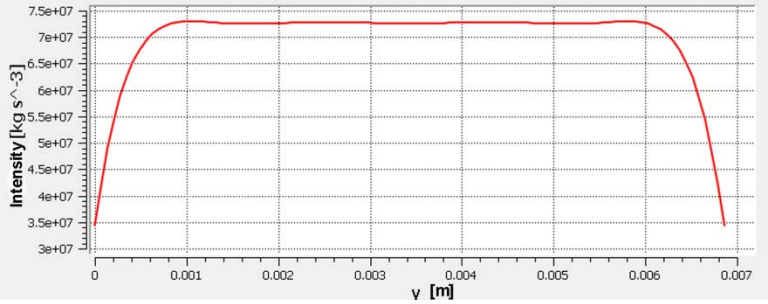

Figure 104. Representative laser heat source intensity variation in y-direction for 3D model.

5.3.1 Geometry and mesh generation

The simplified 2D model excludes the excess powder domain and consists primarily of two domains. The superalloy substrate and powder are coupled into a deposit domain, and the Inconel baseplate was kept separate in a different domain. Figure 105 shows the geometry setup of the problem and the square/hex mesh generated. The grid of the deposit domain was refined to accommodate the fine laser heat source. The total node count of the setup was close to 137k and the skewness was kept below 0.02. The element size of the grid at the top surface was kept close to 10 µm in the x-direction and around 50 µm in the z-direction. The geometry and grid were generated in the ANSYS Workbench platform.

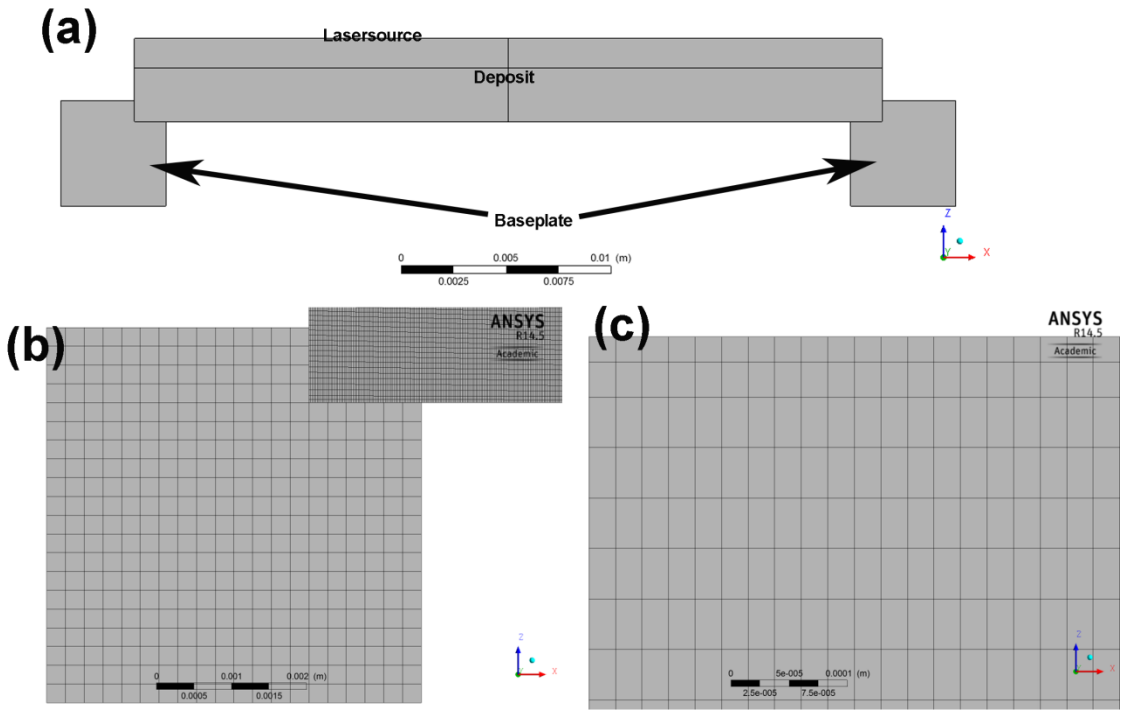

Figure 105. (a) Geometry of the 2D model, (b) Coarse mesh in the Baseplate domain and (c) refined mesh in the Deposit domain.

5.3.2 Physics definition

a) Heat source

The fiber laser heat source has a Gaussian beam radius of 20 μm. The spatial profile in the y-direction is assumed to be of uniform intensity. This particular intensity was used as a line source with a Gaussian distribution applied in the x-direction. The width of the coupon was used in calculating the residence time of the line heat source in any given position, and after that time the line heat source was moved forward by the scan spacing.

b) Domain physics and boundary definition

The other setup for the 3D domain explained in section 5.2.3 was preserved in the 2D model. Hence, the energy equation, melting and solidification, and the Marangoni effect were modeled using identical sets of equations. The excess powder domain was eliminated, and equation 23 was used to solve the solid conduction in the baseplate domain.

The front and back surfaces were modeled with symmetry boundary conditions. All the boundary surfaces of the connected solid domains that are not interfaced with the deposit were treated as adiabatic walls. The top surface of the deposit domain was modeled as a wall with a specified shear value determined by the Marangoni effect. The side surfaces of the deposit domain were modeled as openings that allow both inflow and outflow and provide solver stability. SLE starts from ambient condition and hence, 300K was used as the initial temperature.

c) Grid dependence

The flow physics and temperature dependent property database restricts use of very coarse mesh in the domain. Hence, in order to study the grid dependence, two grids were chosen. Grid I (Fine mesh) contained approximately 272k nodes and 132k elements, while Grid II (Coarse mesh) contained 135k nodes and 66k elements. The grid was altered by changing the number of the element in the powder layer itself and the effect of grid on the maximum velocity on the top surface was studied. As seen in Figure 106, The average value of both the grids are in close match, however, the fine mesh or Grid I showed a much smoother evolution of the velocity. However, since the computational requirement of the Grid I is much higher and the basic flow physics are not altered, for the later modeling effort, Grid II was chosen.

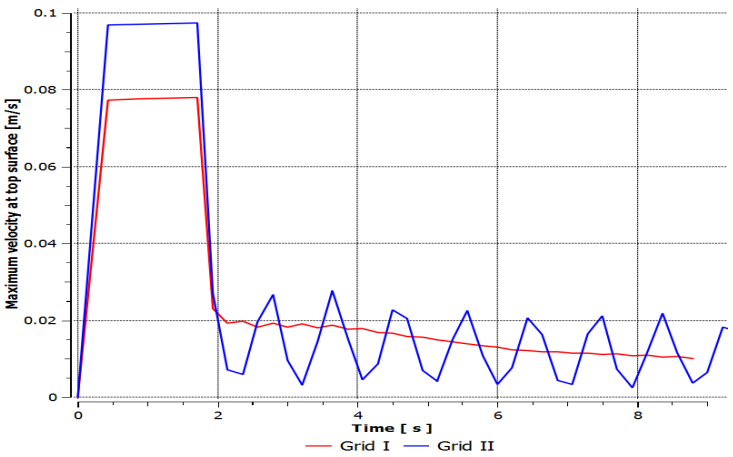

Figure 106. Effect of grid spacing on the maximum velocity observed.

d) Solution and post-processing

The conservation of H-energy was assured at all connecting interfaces between the deposit and the baseplate domain. The convection heat loss was modeled using Newton's law of cooling as a surface sink term applied at all boundaries open to surroundings. Radiation loss was also modeled from open surfaces using a sink term. The use of 2D geometry enabled larger time step values to be used during the preheat scan. The time step was set to be equal to one hundredth of preheat time. During the raster scan the residence time of the laser beam at any x-position was used to calculate the time step. The imbalance in the system was kept within 1%, and the convergence ensured that the RMS value of the residual would remain below $1x10^{-4}$.

Once solved, the result was post-processed in CFD-post to analyze the melt pool nature, the melt depth profile and the temperature distribution. The model was validated by comparing the temperature of the top surface of the moving melt pool and the temperature measured by the IR camera. The melt depth obtained from the micrograph was also used to validate the models.

e) Process parameters

Table 14 and Table 15 list the process parameter ranges used for CMSX-4 and IN 100 respectively for 2-D domain simulations. The scan spacing of 25.4 μm required a very fine mesh to be generated for all the simulation. The powder height was kept fixed at 1.4 mm for all the simulations and other process parameters were varied.

Table 14. Process parameter ranges used for 2-D simulation of SLE process for CMSX-4.

Process Parameter	Range/Value
Powder Thickness	1.4 mm
Laser Power	450 – 600 W
Scan Speed	400 – 600 mm/sec
Initial Repeat Scans	300 – 500
Scan spacing	25.4 μm

Table 15.Process parameter ranges used for 2-D simulation of SLE process for IN 100.

Process Parameter	Range/Value
Powder Thickness	1.4 mm
Laser Power	250 – 500 W
Scan Speed	300 – 600 mm/sec
Initial Repeat Scans	75 – 125
Scan spacing	25.4 μm

5.3.3 Material properties

Thermo-physical property data for CMSX-4 and IN 100 were accurately modeled using tabular data [9, 19, 145]. The properties for Inconel 625 were also modeled using tabular data [9]. The thermo-physical properties that were modeled as temperature-dependent are: specific heat, viscosity and thermal conductivity for the liquid and solid phase. The modeling of density is similar to the 3D model previously presented.

The absorptance of laser energy was modeled using the Hagen-Rubens relationship, which predicts the absorptance (α) as a function of temperature varying electrical resistivity (ρ_e) [149, 150]. The relationship can be expressed as,

$$\alpha = \left[8\varepsilon_0 \omega \rho_e(T)\right]^{1/2} \tag{27}$$

Where, ω is the angular frequency of the laser radiation (1.75×10^{15} rad/s for fiber laser radiation with wavelength $\lambda = 1.07 \times 10^{-6}$ m) and ε_0 is the permittivity of free space (8.85×10^{-12} F/m). The temperature dependency of the electrical resistivity of solid phase can be expressed using a polynomial expression of the form [120],

$$\rho_e(T) = \rho_{e,298K} + A(T-298) + B(T-298)^2 + C(T-298)^3 \tag{28}$$

Where A, B, C are functions of the Al content of the Ni-based superalloy. The base resistivity at 298K can be found using equation 29 as,

$$\rho_{e,298K} = 1155 + 33.5 * (mass\%\ of\ Al) \tag{29}$$

The electrical resistivity of the liquid phase can be evaluated using equation 30 as,

$$\rho_{e,l}(T) / \rho_e(T) = 1.04 \tag{30}$$

Table 16 describes the variation of absorptance for CMSX-4 and IN 100 as a function of temperature. These tabular values were used in the simulation.

Table 16. Variation of absorptance as function of temperature for CMSX-4 and IN 100.

T(K)	Absorptance of CMSX-4	Absorptance of IN 100
298	0.411	0.406
400	0.425	0.419
425	0.428	0.422
500	0.435	0.429
600	0.442	0.435
700	0.447	0.439
800	0.449	0.442
900	0.449	0.442

Table 16 (continued).

1100	0.444	0.438
1300	0.435	0.431
1354	0.423	0.428
1594	0.426	0.425
1639	0.422	0.423
1654	0.420	0.422
1800	0.414	0.416
1900	0.410	0.412
2000	0.407	0.411

5.3.4 Results and discussion

a) CMSX-4 modeling results and validation

The 2D model showed melt pool behavior similar to that found by the 3D model. Figure 107 (a) and (b) shows the temperature and velocity contours of the melt pool while processing the alloy CMSX-4. As found before, the maximum temperature is obtained directly below the laser, and the temperature decreases progressively as we move away from the heat source position. The maximum temperature exceeds 2000K, which matches well with the temperature measured with the IR camera. The velocity contour shows the presence of vortices due to the moving heat source as found before, with higher velocity near the top surface due to the Marangoni effect. The highest velocity is in the range of 2.5 mm/s while the bottom region of the melt pool showed velocity ranging from 0.018-0.75 mm/s

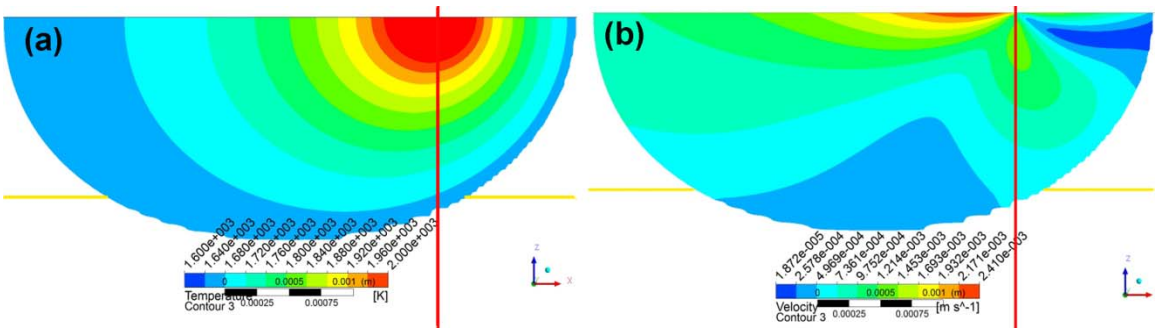

Figure 107. Representative (a) temperature and (b) velocity contours due to the moving heat source for CMSX-4. The yellow line indicates original substrate position before laser processing and the red line indicates the instantaneous position of the laser.

The moving heat source clearly separates the two vortices formed near the leading and trailing edges as found earlier for the 3D model. The vortex formed near the trailing region shows a slightly lower velocity and a dominant Marangoni effect driven velocity pattern with the top layer moving at 2.41 mm/s laterally. Figure 108 shows the velocity vectors in the melt pool. Figure 109 shows the velocity vector map colored by temperature in the melt pool. The effect of natural convection is observed in the melt pool with hot fluid gradually rising to the top and then moving sideways due to Marangoni effect.

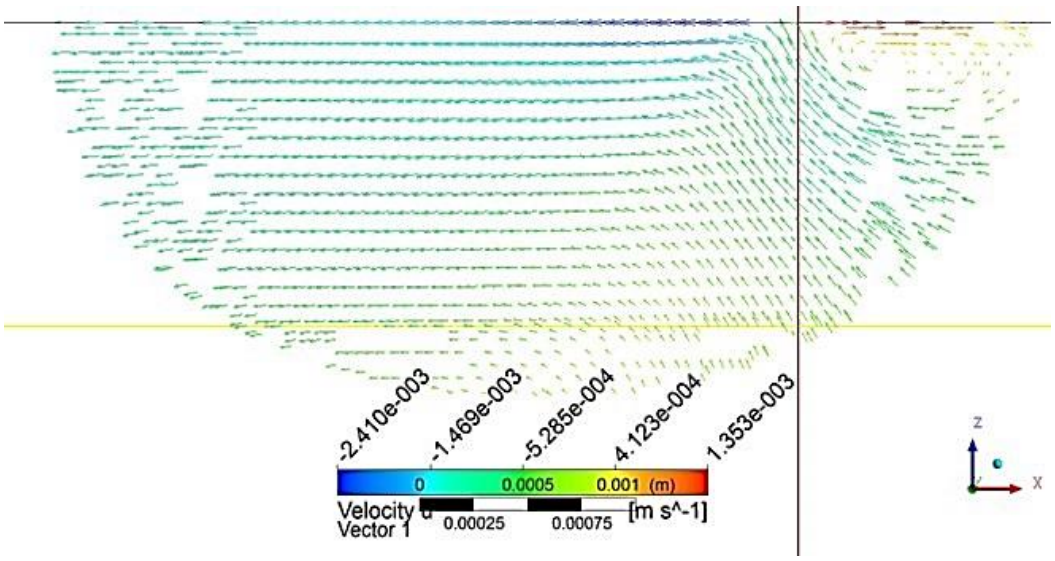

Figure 108. Representative velocity vector map in the CMSX-4 melt pool. The yellow line indicates original substrate position before laser processing and the red line indicates the instantaneous position of the laser.

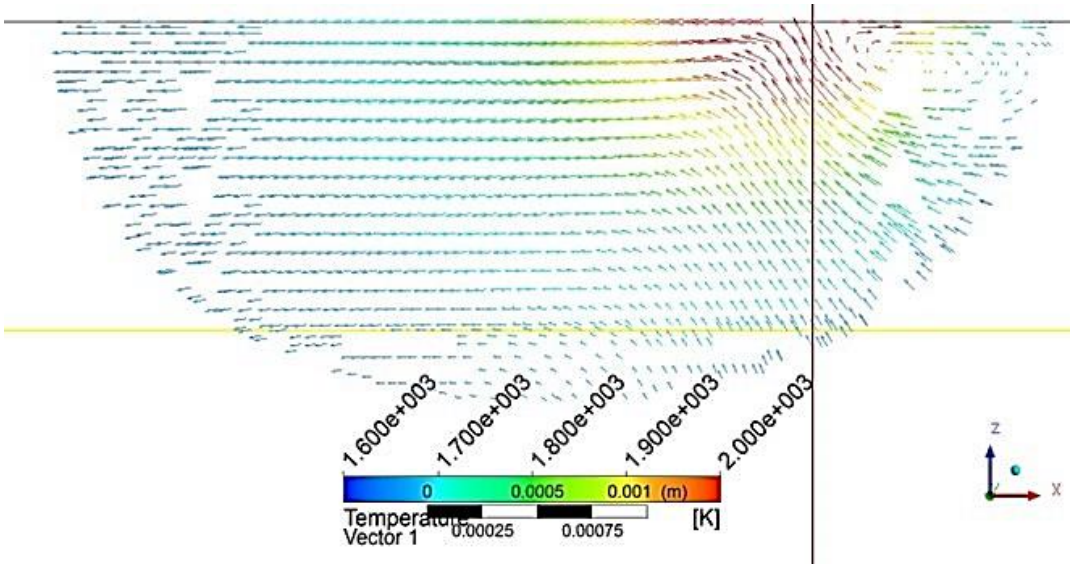

Figure 109. Representative velocity vector map colored by temperature in the CMSX-4 melt pool. The yellow line indicates original substrate position before laser processing and the red line indicates the instantaneous position of the laser.

Figure 110 (a) shows the extent of the mushy region due to the moving heat source which is tracked by the mass fraction of solid CMSX-4 ranging from 0.2 to 0.01. Figure 110 (b) shows the contours of temperature in the mushy region. The characteristics are reasonably similar to the 3D model formed for the ND:YAG laser, with temperature ranging from 1600K to 1648K.

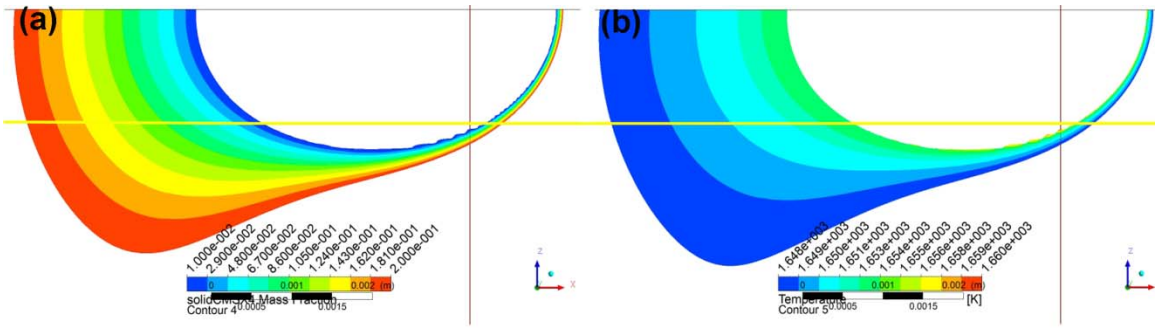

Figure 110. (a) Identification of the mushy region and (b) contours of temperature in the mushy region due to the moving heat source in CMSX-4 melt pool. The yellow line indicates original substrate position before laser processing and the red line indicates the instantaneous position of the laser.

Figure 111 shows the contour of the temperature gradient (G) in the melt pool. The trailing edge showed a lower value of the temperature gradient (~3500 K/m), as found earlier for the 3D model. The leading edge showed a G value on the order of 2.6×10^5 K/m. In this case also, the maximum value of G is observed near the leading edge, which is similar to the 3D model conclusion for ND:YAG laser.

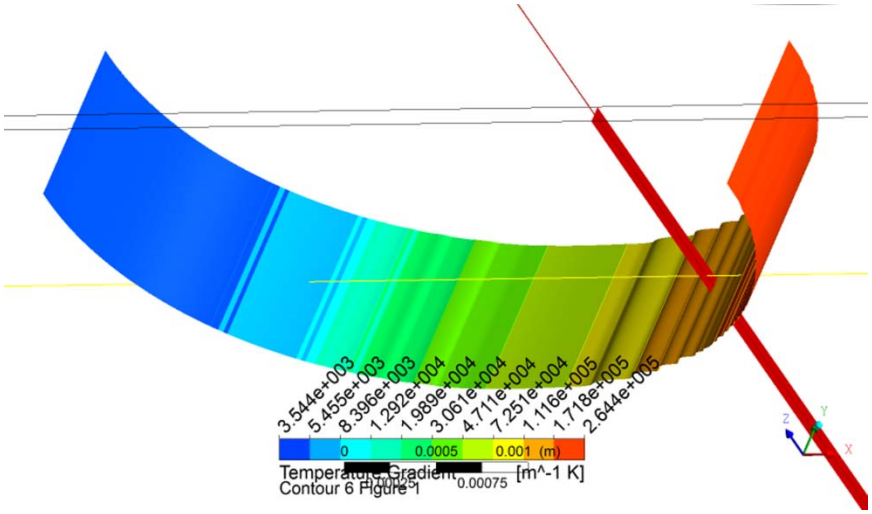

Figure 111. Representative contour of the temperature gradient in the CMSX-4 melt pool. The yellow line indicates original substrate position before laser processing and the red line indicates the instantaneous position of the laser. The parallel black lines indicate the top surface of the powder bed.

Figure 112 compares the experimentally obtained profile of the melt pool size and the averaged temperature with the simulated results for one particular trial with CMSX-4. The simulated melt pool size in the x-direction is multiplied with the sample width (70 pixels) to compute the melt pool size at the top surface. The IR camera also fixes the bounding box of the melt pool to 70 pixels. The melt pool extent in the x-direction obtained by simulation is lower at the beginning and of the order of 0.7 mm or 7 pixels while the experimental value is close to 1.4 mm or 15 pixels. However, these two values gradually come closer as the scan proceeds. In the steady state the value is close to 32 pixels or 3 mm in the x-direction. The simulation identifies the melt pool if the liquid mass fraction is above 0.99. It is possible that the molten powder and mushy region ahead of the actual melt pool gets detected by the IR camera as if it were inside the melt pool. During the preheat scan the anomaly is higher, since in reality the extension of the melt pool

might not be gradual, and it can occur in discrete steps. The simulation predicts a slightly higher average temperature in the range of 1900K to 1800K as function of time than the IR camera, which suggests temperature ranging from 1500 to 1750K. Since the molten powders and mushy region get detected as melt pool by the IR camera, the average temperature value will be reduced. This explains the simulated higher average temperature of the melt pool. Figure 113 shows the simulated melt depth overlayed on the actual micrograph for one representative CMSX-4 sample. The model predicts the melt depth with reasonable accuracy, as before. The absence of excess powder domain may have resulted in some inaccuracy in the simulation.

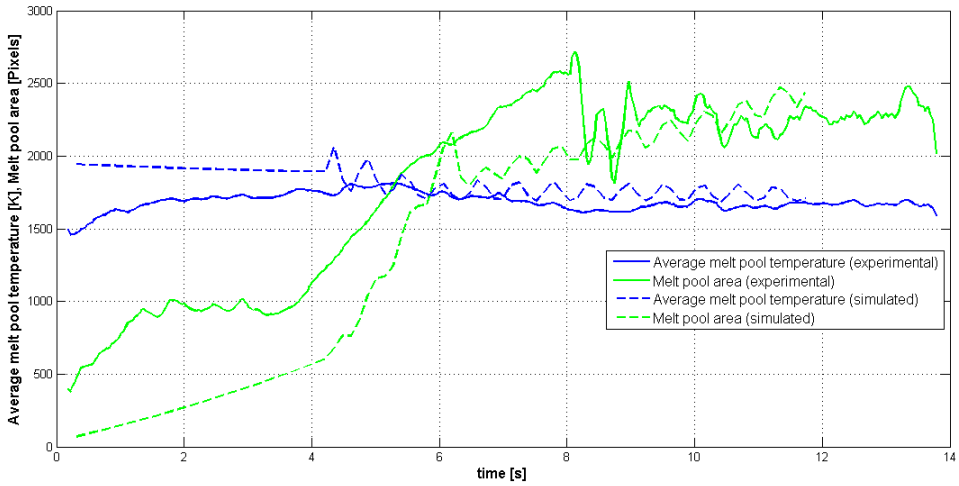

Figure 112. Comparisons of the simulated and experimentally obtained melt pool size and averaged temperature variation with time for the processing of CMSX-4 when observed from the top surface.

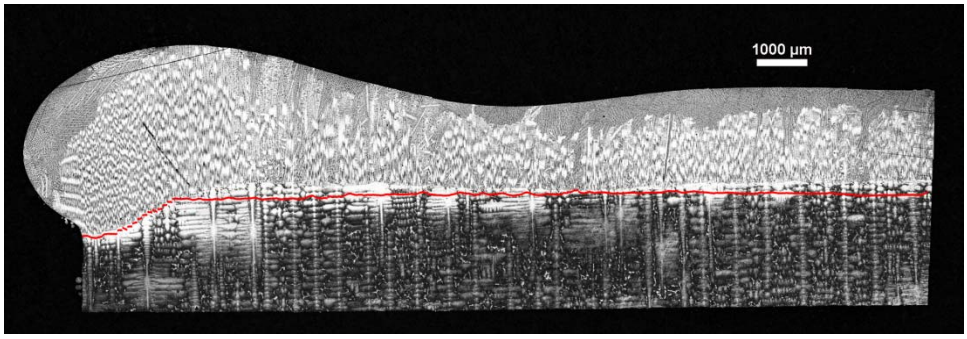

Figure 113. Comparisons of the simulated melt depth (Red line) with actual micrograph for CMSX-4 sample.

b) IN 100 modeling results and validation

The CFD model yielded similar details in the flow field for IN 100 as well. The solidification range for IN 100 is around 290K (from 1350K to 1640K). The solidification range for CMSX-4 is close to 60K (from 1594K to 1654K) CMSX-4. The viscosity value is for IN 100 is lower in the solidification range and of the order of 0.0025 PaS. For CMSX-4 the viscosity value is almost thrice and can range from 0.0068 to 0.0097 PaS. These resulted in some notable differences. The temperature field is similar, as observed in Figure 114 (a). However, the velocity ranges observed for IN 100 are higher, as indicated in Figure 114 (b). The maximum velocity can reach 11.7 mm/s, while the bottom of the melt pool showing velocity in the range of 0.04 to 3 mm/s.

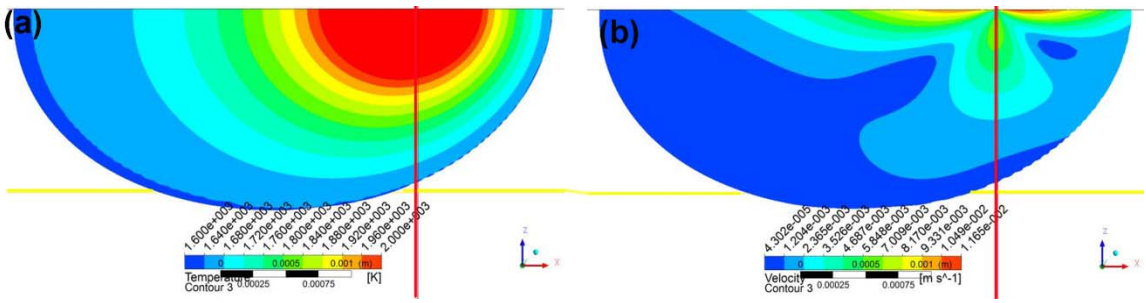

Figure 114. Representative (a) temperature and (b) velocity contours due to the moving heat source for IN 100. The yellow line indicates original substrate position before laser processing and the red line indicates the instantaneous position of the laser.

The lower viscosity also resulted in a fully developed vortex in the trailing edge, as shown in the vector field in Figure 115. For CMSX-4 the higher viscosity resulted in following the surface velocity pattern in the trailing edge. The lower viscosity in IN 100 resulted in a lower shear stress and fully developed vortex. The trends for the flow field indicating Marangoni effect, natural convection and pulling of powder are present as shown in Figure 1Figure 115 and Figure 116.

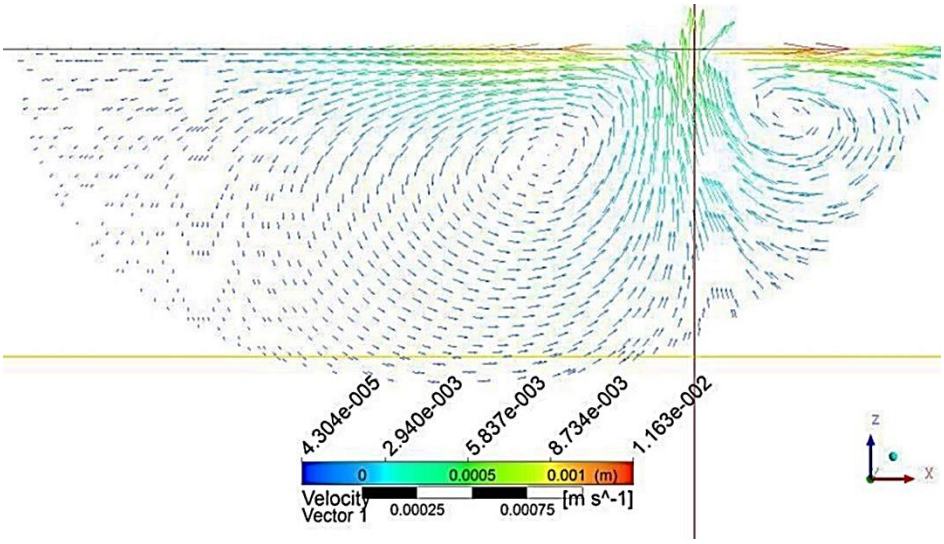

Figure 115. Representative velocity vector map in the IN 100 melt pool. The yellow line indicates original substrate position before laser processing and the red line indicates the instantaneous position of the laser.

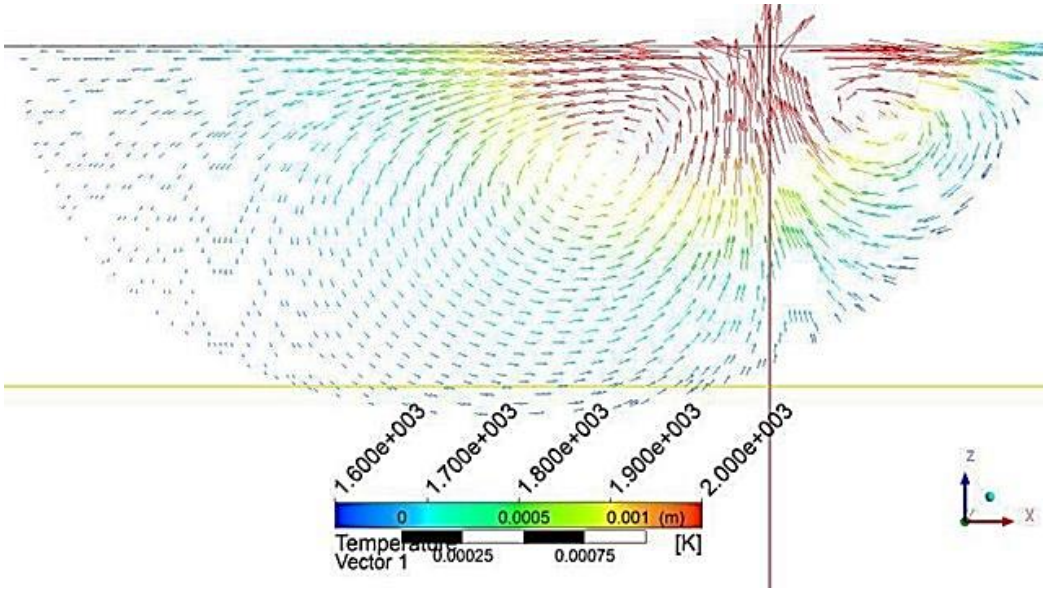

Figure 116. Representative velocity vector map colored by temperature in the IN 100 melt pool. The yellow line indicates original substrate position before laser processing and the red line indicates the instantaneous position of the laser.

Figure 117(a) and (b) identifies the mushy zone and its temperature contour. The features are reasonably similar to those of the CMSX-4 model. The mushy zone showed temperature ranging from 1619K to 1643K in the representative scenario. However, the wide solidification range of the order of 290K may actually cause higher solidification cracking in the mushy region for IN 100. Figure 118 shows the contour of the temperature gradient at the solid-liquid interface. As observed, the temperature gradient again reduces to $1.4x10^4$ K/m in the trailing edge as compared to a value of $4.2x10^5$ K/m at the leading edge.

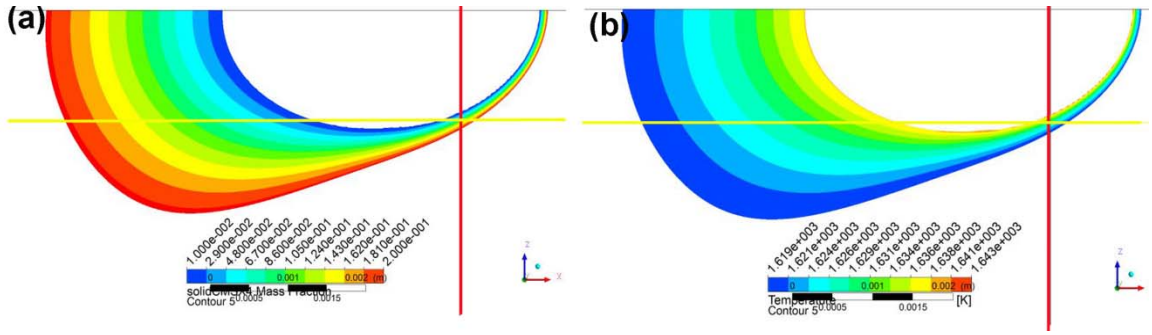

Figure 117. (a) Identification of the mushy region and (b) contours of temperature in the mushy region due to the moving heat source in IN 100 melt pool.

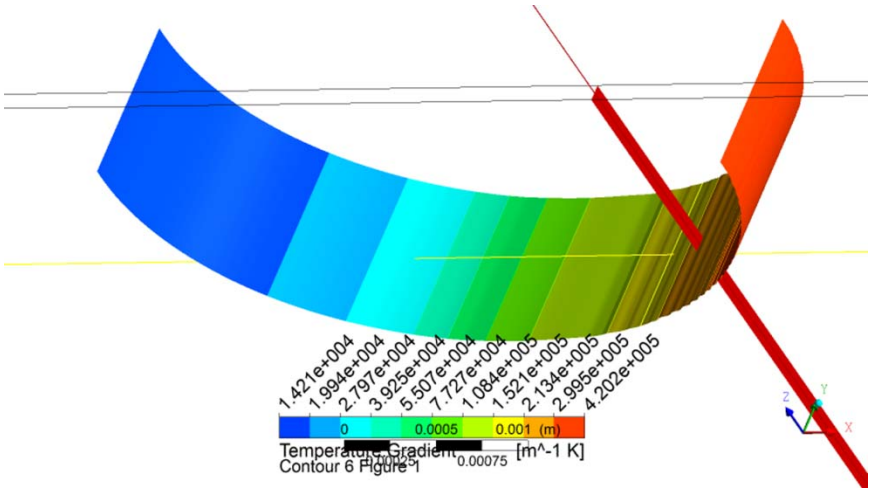

Figure 118. Representative contour of the temperature gradient in the IN 100 melt pool. The yellow line indicates original substrate position before laser processing and the red line indicates the instantaneous position of the laser.

Figure 119 displays the validation of the simulated melt pool size and its averaged temperature data as recorded by the IR camera. IN 100 powders are shown to contain internal porosity, and surface oxidation and internal void formation are known problems for this superalloy. This also causes formation of smoke and sparks during the initial preheat scan and substrate meltback. So, the peak observed for melt pool size during the start of the raster scan actually indicates the presence of sparking. This led to extension of the melt pool to a value close to 60 pixels or 6 mm in the x-direction. The simulation suggests a melt pool size close to 20 pixels or 2 mm in the x-direction. During the later period, the simulated melt pool size matches reasonably well with the experimental data and the melt pool size in x-direction shows a value in the order of 28 pixels or 2.6 mm in the representative scenario. The simulated averaged temperature is slightly higher during the preheat scans and is close to 2100K, since the entrapment of powders makes the melt pool bigger and reduces the experimentally obtained averaged temperature. During the later period of scanning, the area averaged temperature data matches closely and the representative

scenario suggests a temperature close to 1800K. The melt depth found from the experimental micrograph of this particular trial is in harmony with the simulated melt depth as shown in Figure 120.

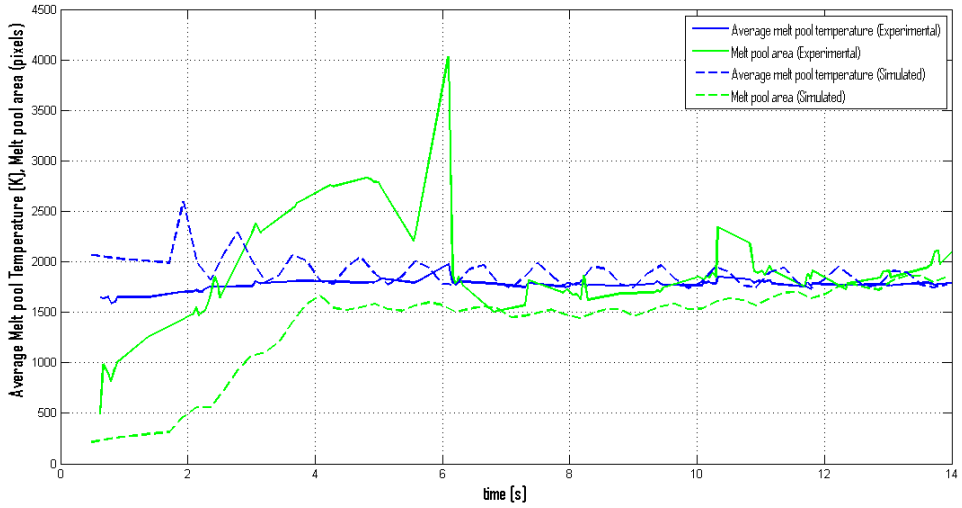

Figure 119. Comparisons of the simulated and experimentally obtained melt pool size and averaged temperature variation with time for the processing of IN 100 when observed from the top surface.

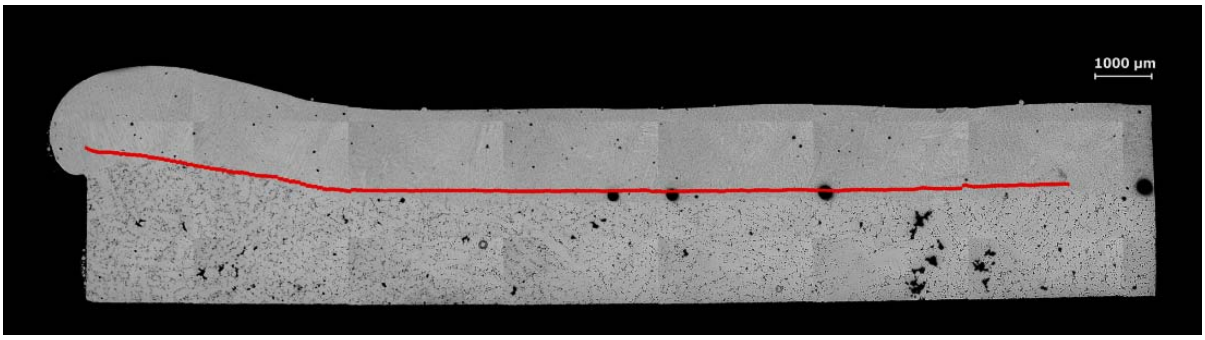

Figure 120. Comparisons of the simulated melt depth (Red line) with actual micrograph for IN 100 sample.

5.4 Empirical microstructural model

The solidification microstructure in the melt pool is a strong function of the temperature gradient (G) and solidification velocity (V) [5, 37, 57, 111]. The higher cooling rate in the SLE process in the range of 3.25 to 9.5 K/s is primarily responsible for the fine microstructure observed in SLE fabricated components. The CFD model enabled G and V to be determined at each point of the melt pool. However, the coupling between CFD and the microstructure evolution models should take account of the rastering beam and the overlap of the melt pools generated by the tightly spaced scan vectors.

In melting and solidification with a raster scanning laser beam, every position in the melt pool is visited twice by the solid-liquid interface as the line heat source progresses. As explained in current research, the temperature gradients at the leading and trailing edge of the melt pool are widely different. The trailing edge is the location at which the final solidification event for any given position of the line source occurs. The temperature history at each position strongly influences the local solidification microstructure. Thus, the current model incorporated time tracking of the solidification history in order to couple the microstructure prediction model with the flow-thermal model. This coupling enables qualitative prediction of the CET.

Optical microscopy provides visual information on the various microstructural characteristics of the deposited material such as melt depth, CET location, OMT location, PDAS etc. A quantitative and consistent investigation of this complex set of characteristics is both challenging and unprecedented. In order to extract microstructural information from the experimentally obtained micrographs, an active contour-based graphical image analysis technique has been developed in MATLAB^{TM} [121] (The MathWorks, Inc., Natick, MA, USA). Active contouring

enables several important characteristics of the micrograph to be tracked, e.g. SX termination contour, meltback contour etc. The image analysis also provides detailed dendrite width data and the termination points of dendrites. These graphically determined points were extracted and then fed into the CFD model to evaluate the thermal and flow data at the corresponding locations. The details of the image analysis will be explored in chapter VI.

The dependence of the primary dendrite arm spacing (PDAS) on the SLE process parameters was considered. Theoretically, it can be shown that for constrained growth, the dendrite tip undercooling is determined by the solute flux at the tip [37]. Assuming the fully developed dendrite to be an ellipsoid of revolution [58] and assuming conditions of marginal stability [59], the PDAS follows the proportional relation $w \sim G^{-0.5}V^{-0.25}$(w = PDAS, G is the temperature gradient at the solid-liquid interface and V is the solidification velocity). Pollock et al. reported the effect of the cooling rate on PDAS for different Ni-based superalloys in the investment casting process [60]. The proportional relation was employed to estimate the temperature gradient in the liquid metal cooling-assisted casting process for René N4 [61]. In SLE, the raster scan pattern of the laser results in a convex hull-shaped melt pool. This work develops the heretofore unexplored dendrite growth relation as a function of the processing parameters for this type of process. The CFD model enabled the computation of the temperature gradient and the solidification velocity at the trailing edge of the melt pool [125]. Statistical data gathered from the image analysis enabled the experimental validation of the proportional relationship for the PDAS found in SLE.

An important solidification phenomenon investigated is the columnar-to-equiaxed transition (CET) near the top surface of the deposit. The CET is known to occur due to an increase in the isotherm velocity near the surface and a decrease in the temperature gradient, which causes the

formation of a constitutionally undercooled zone [5, 14]. This transition parameter was correlated in prior literature to the temperature gradient and the solidification velocity. Hunt was the first to propose the instability criterion for the columnar front and the initiation of the CET as [110] as shown in equation 11.

Hunt simplified the solution by assuming a pseudo-binary alloy composition. Later on, the accuracy was improved by taking into account the composition and associated liquidus temperature profile for the growth of multicomponent dendrites [113]. The Rappaz modification [115], takes into account multi-component dendrites instead of a pseudo-binary alloy composition and the dependence on dendrite orientation. It is applied to predict the CET as follows:

$$G_{hkl}^{n} / V_{hkl} \geq a\left(\sqrt[3]{\frac{-4\pi}{3\ln(1-\phi)}}\sqrt{\frac{N_0}{n+1}}\left(1-\frac{\Delta T_n^{n+1}}{\Delta T_{tip}^{n+1}}\right)\right)^{n} \tag{31}$$

where, <hkl> refers to the direction, n=3.4 for CMSX-4 [5]. The higher the value of G_{hkl}^{n} / V_{hkl}, the lower the value of φ and hence the lower the probability of the CET. Previous literature has suggested a critical value for this criterion (the G_{hkl}^{n} / V_{hkl} value at the SX termination point) that can be applied to predict the CET. Gäumann et al. [5, 14] used a depth-weighted average of $\frac{G^n}{V}$ to characterize a single weld pool. Later, Vitek et al. avoided this simplification in the computation of G by applying the Rosenthal solution to compute G and the melt pool shape [112]. Recent simulations [20] used a complete CFD-based 3D model for a single-bead scan pattern, allowing variation of G and V over the melt pool co-ordinates. The critical value of this parameter governing the CET was shown to be 2.7×10^{24} (in S.I. units) [5, 14]. However, these

efforts did not exclusively consider the effect of the trailing edge of the melt pool in evaluating G and V. The current effort corrects the problem by using time tracking of the solidification history and allows an accurate estimation of this critical parameter by mapping the simulated results onto experimentally obtained micrographs using image analysis. Previous literature also suggested different values for the CET criterion between $5.9x10^{21}$ to $4.7x10^{25}$, based on operating conditions such as laser power, scan speed and preheating temperature [5, 20]. To further explore this issue, the evolution of the CET criterion with time was investigated here. It was found that as the melt pool asymptotically reaches a steady state with time [125], the surface velocity due to Marangoni convection decreases. This phenomenon is found to have a profound influence on the CET criterion.

A second solidification phenomenon known as the oriented-to-misoriented transition (OMT) [7] occurs in the SX deposit. The OMT is caused by a change in the direction of the temperature gradient in the solidifying metal from the <001> to the <100> direction. This occurs as the substrate becomes increasingly hot toward the end of a scan in SLE, resulting in a growth competition between the columnar grains. The current methodology to predict the OMT relies on an estimation of the surface normal of the melt pool for a single bead scan [20, 76]. In this article, the OMT was explored for the raster scan pattern, and a more general formulation of the OMT was formulated based on the temperature gradient in different directions. The height of the OMT was obtained using image analysis from the experimentally obtained micrographs. This data was then mapped back on to the CFD model to accurately compute the temperature gradient in different directions for that co-ordinate. The OMT was shown to take place within a certain band of the ratio of the temperature gradients in the x- and z-directions.

The work presented here explains the interrelation between the coupled thermal-fluid flow-

solidification model and the microstructural model. A customized code based on active contouring was developed to perform quantitative metallography and model validation. Quantitative metallography of the experimental micrographs using active contour-based image analysis allowed development of several transition criteria (CET, OMT) and microstructural parameters (PDAS). These constitutive relations provide a new set of empirical models for the SLE process that can be used to predict the microstructure from the input parameters and can be efficiently used in process control algorithms, enabling the development of controlled microstructure in any given geometry.

5.4.1 Qualitative model

The solidification microstructure was modeled particularly to understand the CET in SX alloys. The CET modeling was carried out in the following manner [20]:

The temperature gradient at the solid-liquid interface (G) was evaluated from the CFD model. Next, the solid-liquid interface orientation (θ_i) was evaluated from, $\theta_i=\cos^{-1}(G_i/G)$ (for i=x, y, z). The growth rate of the solid-liquid interface was given by $V=S\cos\theta$ (S is the scan speed or line source speed). The angle ψ refers to the angle between the normal vector and the possible dendrite growth orientation at the solid-liquid interface; it was evaluated in ANSYS CFD-Post. The temperature gradient parallel to the dendrite growth direction <h k l>, G_{hkl}, was calculated using the equation $G_{hkl} = G/\cos\psi$. The dendrite growth velocity, V_{hkl}, was calculated using the equation $V_{hkl} = S\cos\theta/\cos\psi$. The Rappaz modification [115] was applied to predict the CET as shown in Equation 31.

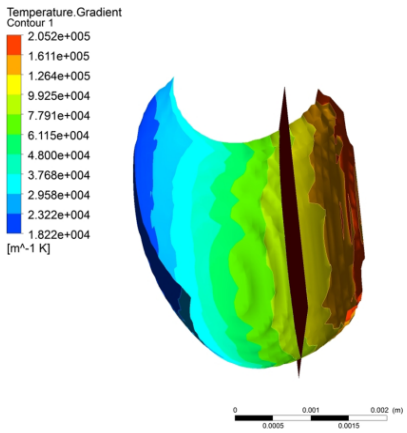

Figure 121. Temperature gradient contour at a given time for a given position of the scan source (designated by intermediate plane).

A lower value of the left hand side increases φ for a given nucleation density. Therefore locations of the melt pool with lower values of the ratio have a greater likelihood for the occurrences of CET. In order to find the critical value of the G_{hkl}^{n}/V_{hkl} ratio, it is essential to understand the importance of time history. Figure 121 shows the temperature gradient contour for a given position of the line heat source that is designated by the intermediate plane. The line heat source is moving to the right. The portion of the interface lying ahead (to the right) of the scan source constitutes the leading edge, and the portion behind the scan source (to the left) constitutes the trailing edge. As can be seen from the picture, the solid-liquid interface has distinct leading and trailing edge characteristics with reference to the scan source and in the scan direction. The leading edge shows a temperature gradient that is much higher than the trailing edge (around 14 times higher in the given contour). As the line heat source progressively passes over a given co-ordinate position, the nearby co-ordinates remain in the solid-liquid interface for a certain time period. If, G_{hkl}^{n}/V_{hkl}, is calculated over the leading edge, it will show a value that is at least 10^3 times higher than that at the trailing edge location. Once the trailing edge of the scan

source leaves a particular position, it will not be remelted again, and thus plays a more important role in dictating the final solidification microstructure. Thus, the time history of G_{hkl}^{n}/V_{hkl} is kept for any given position while it remains in the solid liquid interface, and only the trailing edge value is considered for the critical value of G_{hkl}^{n}/V_{hkl}. The leading edge is important in determining the powder flow characteristics. The temperature obtained at the leading edge is much higher, and this lowers the surface tension coefficient, resulting in Marangoni convection. Any sharp change in temperature over the leading edge position as the line heat source progresses may result in surface rippling.

Figure 122 shows a plot of the G_{hkl}^{n}/V_{hkl} ratio for the same sample at two different positions of the line heat source. In (a) and (b) only the portion of the melt pool lying behind the instantaneous position of the line heat source is compared for the pure conduction model. As seen, the 2nd position shows a large region with a lower value of G_{hkl}^{n}/V_{hkl} ratio. Hence, the model suggests a lower columnar height in the 2nd position. With the inclusion of convection, the G_{hkl}^{n}/V_{hkl} ratio increases near the back region, as verified from the contour provided in Figure 122(c) and (d). Hence, the probability of CET is lower than its probability under pure conduction, if pure convection results are adopted. The two positions also show similar contour ranges, suggesting no change in the columnar height. Inclusion of the Marangoni convection, however, reduces the CET criterion value as shown in Figure 122(e) and (f) for the same positions. However, a lower value of the CET criterion for position 2 indicates a higher probability for CET and lower columnar height in position 2.

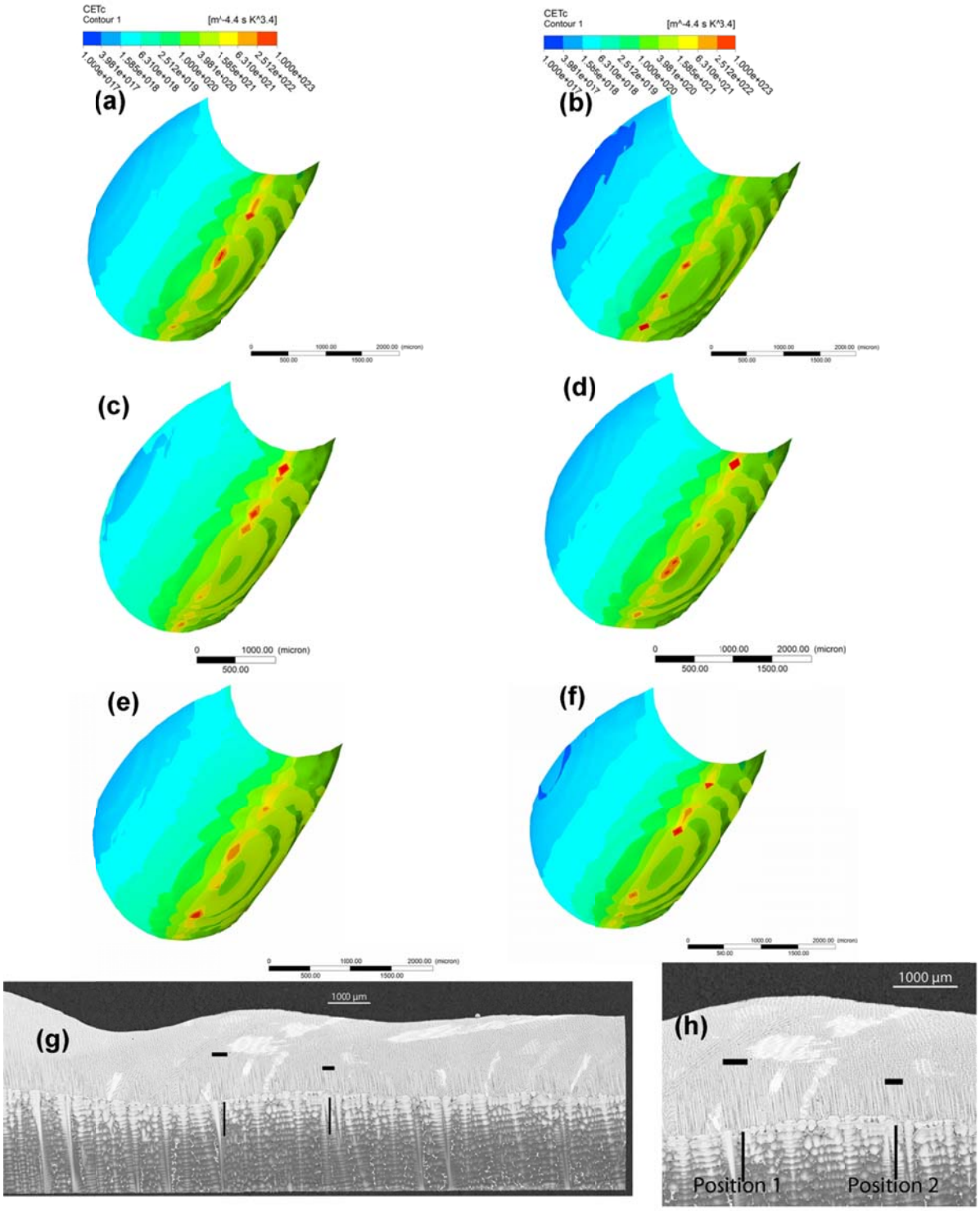

Figure 122. CET criterion plot for same sample at (a) heat source position 1=7.9 mm and (b) heat source position 2=10.1 mm for pure conduction, (c) heat source position 1=7.9 mm

and (d) heat source position 2=10.1 mm for pure convection, (e) heat source position 1==7.9 mm and (f) heat source position 2=10.1 mm with Marangoni convection and (g) experimental micrograph for the given sample showing CET and (h) closer look at the CET for the given position showing larger columnar height for position 1.

Thus, according to the model developed, the CET parameter is lower for the 2nd position, which indicates a probability that CET will be higher for position 2. The experimental micrograph in Figure 122 (g) and (h) also confirms that the CET occurs at a lower height (~700 μm) into the deposit above the substrate for position 2 than for position 1, where the CET occurs at around 1000 μm. This experimental result thus qualitatively validates the microstructure model developed.

5.4.2 Stochastic model

Each CMSX-4 sample was passed through the customized image analysis procedure to extract the following microstructural data: 1) PDAS, 2) primary dendrite start and end location, 3) the OMT initiation and 4) the CET initiation. Several algorithms have been developed to couple this data to the CFD simulation results. They were used to develop empirical relations and criteria to describe the PDAS, the CET and the OMT.

a) <u>PDAS</u>

Figure 123 shows representative primary dendrites tracked across a sample; these dendrites are then used to calculate the PDAS. The calculated temperature gradient and solidification velocity from the CFD model and the dendrite width and position determined from the image

analysis are next used to verify the relation in equation 9 and to find the proportionality constant. This is accomplished through the following steps:

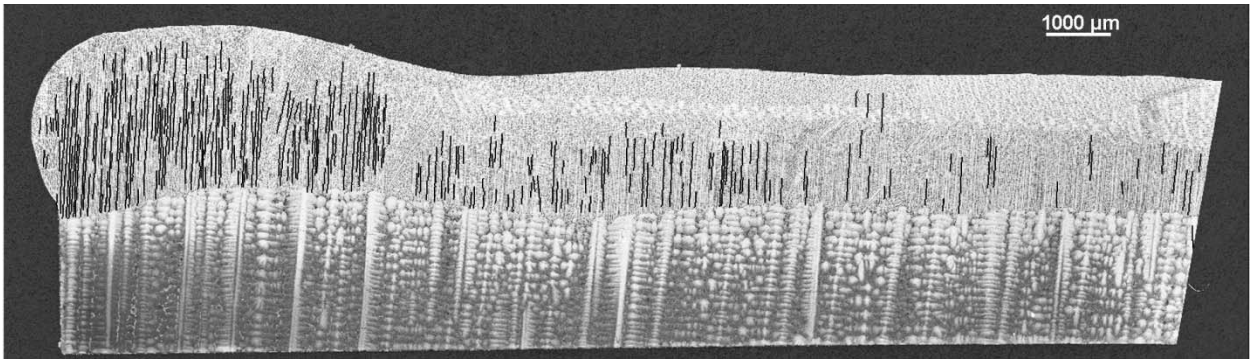

Figure 123. Representative lengthwise cross-section of CMSX-4 sample with the primary dendrites tracked across the length of the sample.

First, the start position of a dendrite was imported in the post-processing environment of the CFD suite (CFD-Post). Next, the transient results were loaded to find the melt pool data and to determine whether the position lies in the trailing edge of the melt pool. A small rectangular area was generated (50 µm x 50 µm) around that point and on the solid-liquid interface. In this stage, a check was performed to determine whether the rectangular area has any points in common with the solid-liquid interface. If a point was found to be on the solid-liquid interface, the average value of the temperature gradient and solidification velocity in the <001> direction was determined for the area. If not, then that data was discarded. The process was repeated for all identified dendrites.

Thus, the image processing algorithm generated the PDAS data, and the CFD results provided corresponding G and V values. The data extracted from the metallographic images of all the samples were then imported into MATLAB and fitted to the polynomial equation,

$$w = c * V^{-0.25} G^{-0.5} \quad (32)$$

b) CET

The SX growth termination contour was found using the active contour-based image analysis program. A representative sample with the SX height data is shown in Figure 124(a).

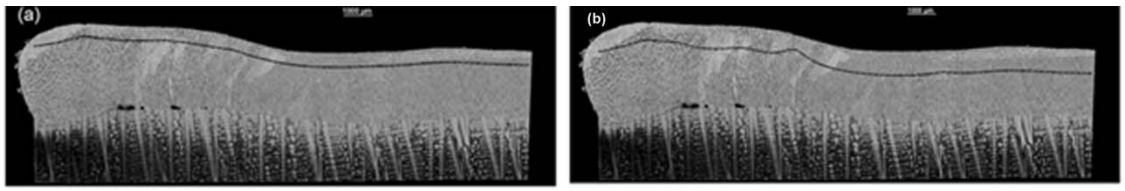

Figure 124. Representative CMSX-4 sample (a) with the CET initiation indicated by the black line and (b) showing termination of <001> growth to <100> growth or OMT.

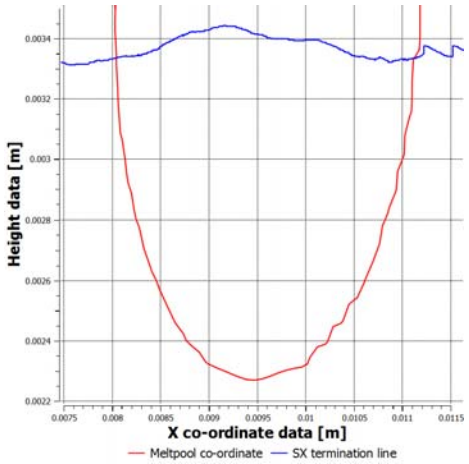

Figure 125. Determination of the intersection point between the trailing edge of the simulated melt pool and the experimentally obtained CET initiation position.

The algorithm to determine the G^n/V value at the transition point was then executed as a customized script in CFD-Post, allowing for the determination of the CET criterion in the following manner:

First, The SX height data was imported as a polyline into CFD-Post. Next, for each time point in the simulation, the trailing edge of the melt pool was determined. The intersection point of the SX height polyline and the trailing edge of the melt pool was determined for each line source position as shown in Figure 125. A small rectangular area (50 μm x 50 μm) was drawn on the solid-liquid interface around this point. Then, the average value of G_{001}^{n}/V_{001} (the CET criterion, n=3.4 for CMSX-4) was determined for the rectangular area. The entire process, when conducted over the simulation duration, enabled the critical value of the CET criterion to be determined as a function of time.

c) OMT

The <100> dendrite growth initiation was first estimated from the experimentally obtained micrographs as shown in Figure 124 (b).

The OMT height data was imported as a polyline in CFD-Post. The CFD solver allowed the estimation of the temperature gradients in the <100> or x-direction and the <001> or z-direction. Next for each line source position, a point was found on the trailing edge of the melt pool that satisfied the criterion, $\frac{G_{100}}{G_{001}} \geq 1$. Another criterion was set to find the upper band of OMT as, $\frac{G_{100}}{G_{001}} \leq 5$. When repeated over all the line source positions, this procedure enabled the determination of the co-ordinates of the points corresponding to the range of G-ratio ($1 \leq \frac{G_{100}}{G_{001}} \leq 5$) in the x- and z-directions within which the OMT occurred.

5.4.3 Results and discussion

a) PDAS

As seen in Figure 123, the deposit region displays a finer microstructure than the substrate region. The value of the PDAS in the deposit region ranges from 10 μm to 30 μm, while it is more than 250 μm for the substrate region, as found from the microstructural image. The PDAS is related to the cooling rate of the metal during solidification and the thermal gradient during processing [37].

In a constrained growth process like SLE, the dendrites are constrained to adapt to the corresponding tip undercooling, which is determined by the solute flux at the tip. The assumption of marginal stability yields the following relation for the PDAS,

$$\boldsymbol{w = 4.3\left(\frac{D\Gamma\Delta T_0}{k}\right)V^{-0.25}G^{-0.5}} \tag{33}$$

where, w is the PDAS, D is the diffusion coefficient in the liquid, Γ is the Gibbs-Thomson coefficient, ΔT_0 is the liquidus-solidus range in the initial alloy concentration, k=equilibrium distribution coefficient, V is the solidification velocity and G is the temperature gradient. A similar relationship can be developed for low Péclet numbers and can be written as [108],

$$\boldsymbol{w = 6(\Delta T_0 kD\Gamma)^{0.25}V^{-0.25}G^{-0.5}\{1-\left(\frac{DG}{V\Delta T_0 k}\right)\}^{0.5}} \tag{34}$$

In the above models, the PDAS essentially follows the proportional relation with powered value of temperature gradient and solidification velocity. However, it has been established that these models cannot provide a precise prediction for PDAS and are only useful in obtaining a qualitative estimate for PDAS [109].

The result of the statistical data fitting for the PDAS conducted in the current study is shown in Figure 126. For the plot shown, the R-squared value, describing the goodness of fit is 0.72. The coefficient 'a' is found to be 0.00039 with 95% confidence bounds at (0.00038, 0.00040).

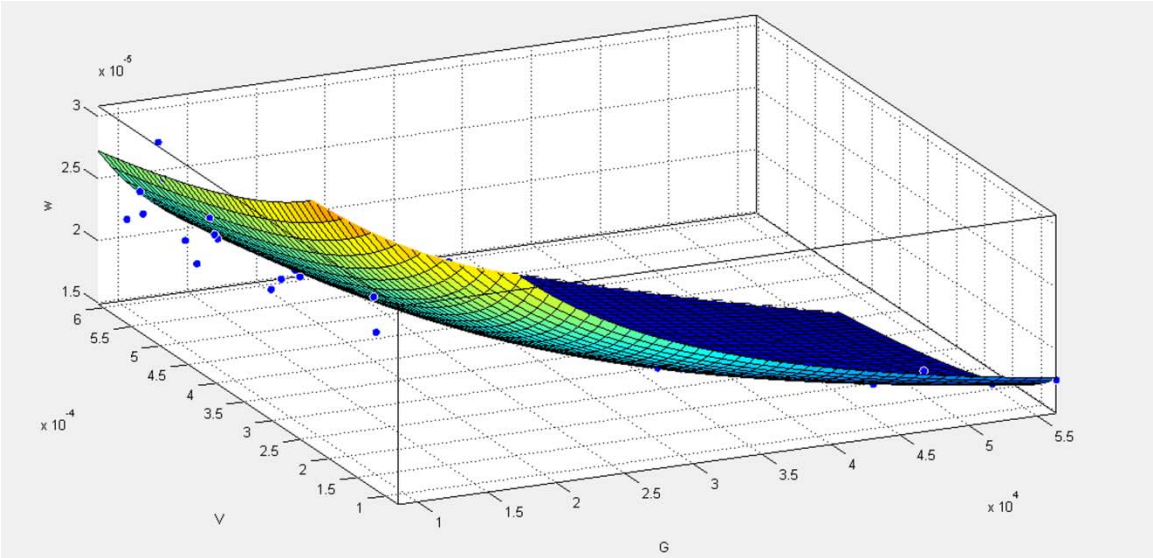

Figure 126. Plot showing dependence of the PDAS on the temperature gradient and solidification velocity and the polynomial fit obtained for the plotted data.

The proportional relation between the PDAS, the temperature gradient and the solidification velocity is thus experimentally verified. The model is based on the raster scan pattern utilized in SLE and the line heat source assumption adopted for the simulation, and it results in the same form of the growth relation as that developed for marginal stability under constrained growth. Based on the proportionality constant found for the operating parameter ranges investigated, equation 35 was used to determine the approximate PDAS in the deposit region of an SLE processed sample as follows:

$$\boldsymbol{w = 0.00039 V^{-0.25} G^{-0.5}} \tag{35}$$

b) CET

In the CFD modeling analysis the roles of the temperature gradient and the solidification velocity in the CET are discussed in detail. A contour plot of the G^n/V value over the trailing edge of the melt pool enables the CET probability to be qualitatively predicted. Since the temperature gradient is much higher in the leading edge region of the melt pool, and since the leading edge will not have any role in solidification, only the trailing edge of the melt pool should be considered for solidification analysis. Thus, time tracking of solidification history was developed to address the solidification conditions based on thermal conditions exclusively at the melt pool trailing edge. A representative contour of the melt pool trailing edge with $\frac{G_{001}^{3.4}}{V_{001}}$ plotted over it is shown in Figure 127. As shown, at the trailing edge, the CET criterion displays a minimum value of 3.695×10^{16} near the top and a maximum value of 1.559×10^{23} at the bottom of the melt pool.

The plots of the CET criterion value with time for three different samples are shown in Figure 128, with the standard error bar value set equal to standard error for the population. Previous literature suggested an optimal value of 2.7×10^{24} (SI units) [5, 14, 20]. In contrast, the maximum value found in the present study is close to 5×10^{18}, which is considerably lower. This might be due to the raster scan pattern used in the SLE process, which is different from a single bead melt pool process investigated previously. The exclusive use of the melt pool trailing edge value for this analysis could also lower this critical value and provide a more accurate estimate of the CET criterion. The reason, as explained earlier, is that the trailing edge is responsible for the final solidification microstructure; hence the CET criterion based only on the trailing edge solidification conditions, rather than an average value over entire melt pool, should provide a more accurate representation of final solidification microstructure.

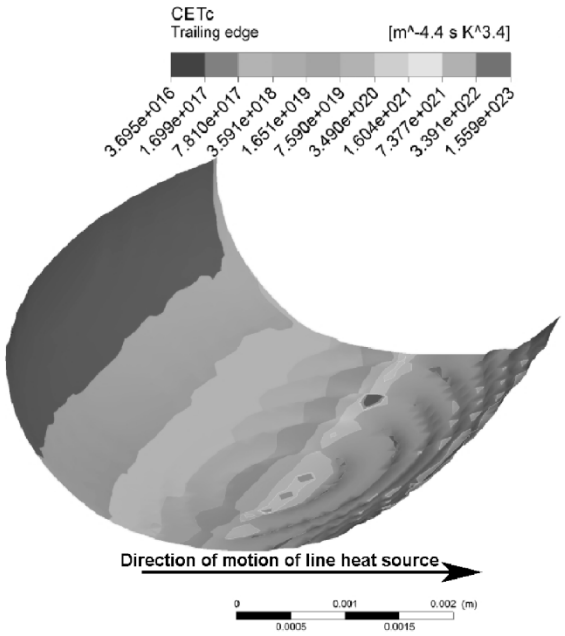

Figure 127. Representative contour of the CET criterion on the trailing edge of the melt pool.

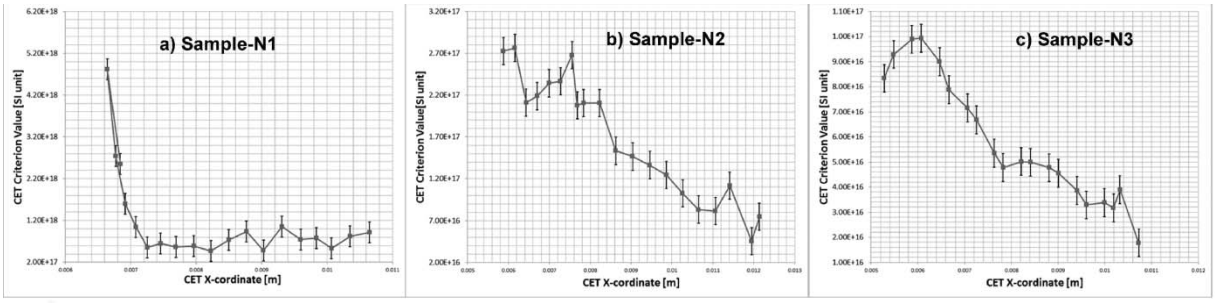

Figure 128. Evolution of the CET criterion for (a) Sample-N1, (b) Sample-N2 and (c) Sample-N3.

Another important feature observed across the samples is the higher value of the CET criterion at the beginning of the scan. The CET criterion decreases as the scan progresses over time. If two different line source positions (e.g. position 1 and position 2) with similar SX heights (and with line source movement in the positive x-direction) are compared, then the position with the higher

x co-ordinate value will experience a lower temperature gradient in the z-direction. Since the substrate gets progressively hotter as the scan progresses, G_{001} decreases and the $G_{001}^{3.4}/V_{001}$ value for position 2 is lower than that for position 1. For a steady state and ideal conditions, this should lower the SX height for position 2. However, since position 1 shows a higher value of the CET criterion for the same height of SX as for position 2, this suggests higher unsteadiness for lower x-values in the scanned region. This conclusion is similar to that described in the CFD modeling discussion, where the melt pool dimensions approached a steady state as the scan progressed. As the scan progresses over time, the CET also occurs at lower values of the CET criterion because of the lower unsteadiness.

The flow simulation developed earlier can be used to explain the unsteadiness in the system. Marangoni convection is known to be responsible for making the melt pool shallower and wider [93, 148]. However, it was also postulated in previous literature that Marangoni convection can drive broken dendrites to prior-scanned regions [5]. The convected dendrites may result in termination of the SX growth at lower SX heights (or at greater depths in the melt pool) and consequently at higher values of the CET criterion. According to the CFD model, the Marangoni convection driven streamlines are shown to extend into prior scanned regions that may disrupt the nascent microstructure in the mushy zone. For the three samples analyzed, the absolute value of the surface velocity at the laser scanned surface is shown in Figure 129. It can be clearly seen that this velocity decreases as the scan progresses. For the given cases, the velocity is reduced by 10-30% near the end of the scanned region. This brings down the rate of convection of the dendrites and allows the CET criterion value to reach an ideal value, which is the lowest value found for the CET criterion (around 5.0×10^{17} for sample-N1, 7.0×10^{16} for sample-N2 and 2.0×10^{16} for sample-N3).

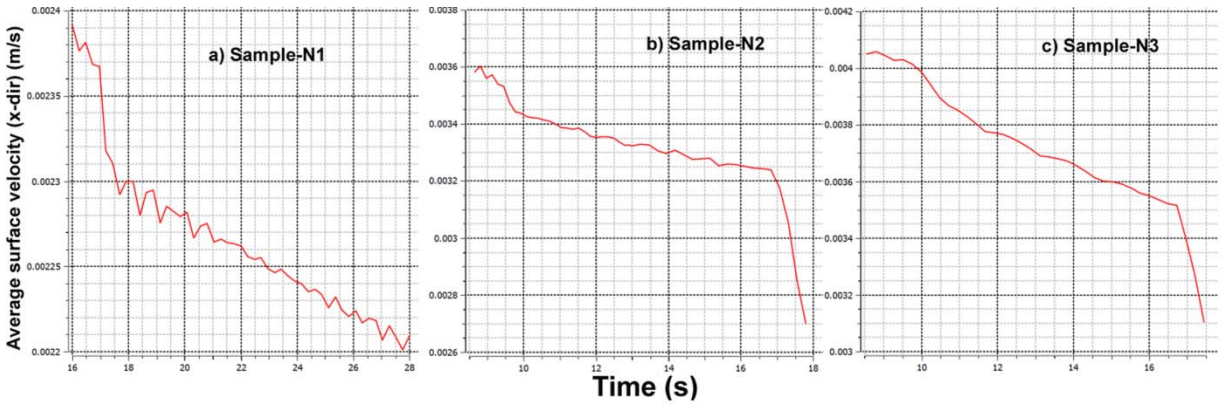

Figure 129. . Plot of average surface velocity in x-direction with time for (a) Sample-N1, (b) Sample-N2 and (c) Sample-N3.

c) OMT

The present methodology employed to understand the OMT phenomenon is based on finding the minimum dendrite growth velocity [7, 76, 111]. This leads to minimum undercooling at the dendrite tip [113]. This process thus essentially relies on finding the direction that is most closely aligned to the heat flux direction. For a single bead scan pattern, the direction cosine can be found analytically [77].

An important variation of this methodology is to consider the temperature gradient in different directions for possible dendrite orientations. In the present case, the line heat source is moving in the <100> or x-direction and the desired SX growth orientation is in the <001> or z-direction. Hence, intuitively the growing dendrite will follow the largest temperature gradient direction, and the direction cosine thus obtained would be the same as that for the Rappaz model [77]. The substrate gets progressively hotter as the scan progresses, thus reducing the temperature gradient in the <001> direction and allowing the <100> direction to become the dominant dendrite growth direction.

However, the raster scan is found to introduce some modifications in the available model. The temperature gradient, when plotted on the trailing edge of the solid-liquid interface, suggests the occurrence of OMT at a much lower height for both the velocity-based and temperature gradient-based approaches. This anomaly can be explained by introducing a band of G-ratio in different directions over which OMT takes place. The vertical growth of the dendrites starts from the bottom of the melt pool and is prevalent. The tilting of the temperature gradient initiates a competition between differently oriented columnar dendrites and finally leads to OMT when the temperature gradient in the <100> direction (G_{100}) is significantly higher than the temperature gradient in the <001> direction (G_{001}). The results from the CFD model allow us to plot the distribution of the $\frac{G_{100}}{G_{001}}$ ratio across the solid-liquid interface. Figure 130 shows the misoriented region in the lighter shade that is found by applying the criterion, $\frac{G_{100}}{G_{001}} \geq 5$.

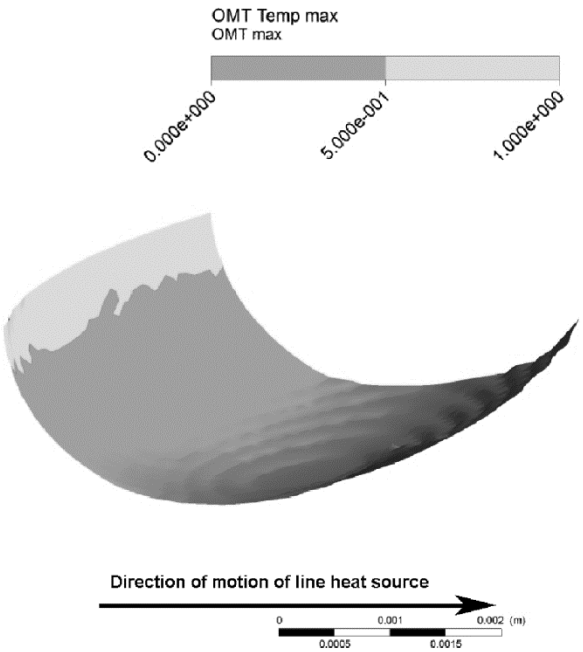

Figure 130. Representative contour indicating G_{100}/G_{001} at the trailing edge of the melt pool with the lighter region indicating $G_{100}/G_{001} \geq 5$.

In Figure 131, a comparison is presented for three different samples along with the experimentally obtained height values for the OMT. As can be seen, the experimentally obtained heights for the OMT lie in the range $1 < \frac{G_{100}}{G_{001}} \leq 5$. As shown, for the sample-N4, the experimentally determined OMT lies between 0.0034 m and 0.0038 m. G_{100} becomes more than G_{001} within the 0.0026m to 0.0028m range. The same values are obtained using the approach based on minimization of the angle between the surface normal of solid-liquid interface and the possible dendrite directions. Using the $G_{100}/G_{001} \geq 5$ criterion allows determination of the zone in which the OMT occurred in the samples investigated.

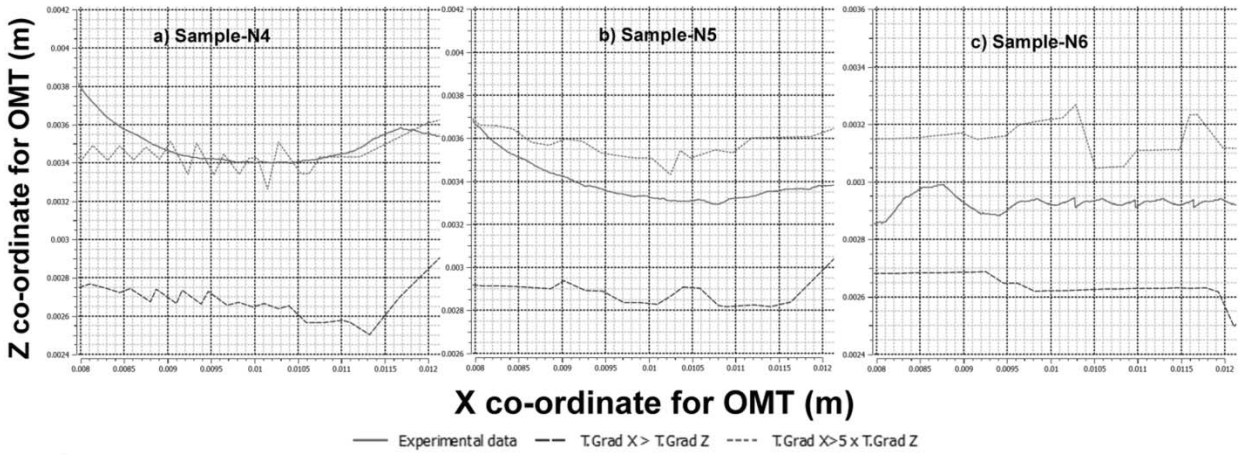

Figure 131. Simulated result with the OMT initiation determined by the temperature gradient ratios along with the experimentally obtained OMT initiation data for (a) Sample-N4, (b) Sample-N5 and (c) Sample-N6.

The work presented here explains the relationship between the coupled thermal-fluid flow-solidification model and the microstructural model. A customized code based on active contouring was developed to perform quantitative metallography and model validation. Quantitative metallography of the experimental micrographs using active contour-based image

analysis enabled development of several transition criteria (CET, OMT) and microstructural parameters (PDAS). These constitutive relations provide a new set of empirical models for the SLE process. These can be used to predict the microstructure from the input parameters and can be efficiently used in process control algorithms, enabling the development of controlled microstructure in any given geometry.

5.5 Summary

This chapter studies the fundamentals of SLE process to gather insight into the flow fields as well as to understand the microstructural evolution and transitions. The findings of this chapter can be used to add more predictive capability in the feedback control system previously developed.

5.5.1 CFD model

A CFD-based modeling scheme has been implemented to simulate the SLE process using a single platform. The model can predict the complete temperature distribution and melt pool behavior. Including convection in the model provides insights into the flow field established in the melt pool and into the way the loose powders are drawn inside melt pool. It is shown that the flow field comprises two rotational vortices. The inclusion of Marangoni convection in the study provides a more realistic description of flow and also shows the disruptive effect it might have on the existing microstructure besides making the melt pool shallower and wider.

The same platform also allows prediction of the CET by modeling the solidification microstructure. Time tracking of solidification history and generalization of geometry is implemented to account for the raster scan pattern. The final aim would be to predict the

microstructure beforehand by developing a processing map based on the CET. However, the current simulation still allows us to estimate the possibility of CET as well as the most likely locations of their occurrence. The simulation shows reasonable qualitative agreement with the experimental data in predicting the CET. However, it is necessary to determine the CET criteria experimentally in order to obtain quantitative data for microstructural investigation e.g. columnar-to-equiaxed ratio. The thermal stresses in HAZ and the transient mushy zone volume data can also provide important information about solidification cracking and thermal deformation.

The 2D model built for the fiber laser allowed the flow field to be explored in shorter computation time, and it enabled the CFD model to be validated using the thermal imaging camera data and the experimentally obtained melt depth. This work proved that simplifying the domain does not necessarily reduce accuracy. The average melt pool temperature profile and melt pool size agree with the simulated profile for both the superalloys explored. Due to different thermophysical properties some variations are found for IN 100 and CMSX-4. However, the basic properties of different temperature gradients in leading and trailing edges, the formation of two rotational vortices and the presence of higher velocity at the top surface are retained.

However, there are sources of uncertainty or error in both experimental and simulation approach. The thermal camera was calibrated to display temperature within an accuracy of 0.5%±1^{o}C. The fixed emissivity adopted for the thermal imaging camera also changes with the temperature of the sample and introduces additional sources of error. Additional refinement of the grid near the top surface of the powder bed is recommended to resolve the flow feature due to Marangoni convection with higher accuracy.

5.5.2 Microstructural model

The current work investigates the SLE process for SX alloy CMSX-4; it describes a detailed microstructure evolution model and the methodology employed to couple that model to actual experimental data obtained from micrographs. This methodology is broadly applicable to other SX alloys, provided that reliable thermo-physical properties are available. A novel active contour-based image processing technique has been developed for quantitative metallography [121]. This has enabled key microstructural data to be extracted. This data is then used to combine the CFD model with the microstructural evolution model in order to obtain fully coupled and experimentally validated flow-thermal-microstructural evolution models. The following conclusions can be drawn:

- The image analysis suggests a PDAS of 10 to 30 μm in the deposit region as compared to more than 250 μm in the substrate region. The data fitting obtained from the above empirical approach allows for experimental verification of the proportional model for the PDAS in constrained growth under marginal stability. The proportionality constant (~0.0004) found can be used to determine the approximate dendrite width from the simulated data of temperature gradient and solidification velocity.
- The CET phenomenon is investigated in great detail, and the evolution of the CET criterion for the raster scan pattern is presented. Time tracking of the solidification history and the availability of an accurate property database allows for improved accuracy in the present approach. The unsteadiness of the CET criterion value is found to be related to the Marangoni effect-driven velocity and resulting convection of dendrites.

The reduction of this surface velocity also lowers the value of the CET criterion to the ideal condition.

- An alternate approach to predict the OMT phenomenon, based on the temperature gradient, is presented here. The competition of differently oriented dendrites in the raster scan pattern, and the subsequent flip in the direction of the columnar orientation, occurs over a range of the ratio of the temperature gradient in the <100> to the <001> directions. For the investigation of CMSX-4 processing by SLE presented here, the band over which this transition takes place is shown to be $1<\frac{G_{100}}{G_{001}} \leq 5$.

With knowledge of alloy-specific properties, the experimentally validated models for the PDAS, the CET and OMT criterion can be developed to predict microstructural parameters (PDAS) and microstructural transitions in SLE of SX alloys as functions of SLE processing parameters. This predictive capability enables control of the solidification microstructure in laser-based additive manufacturing of SX superalloys.

Chapter VI

Statistical Design of Experiments and Multivariate Analysis

6.1 Introduction

The aim of this chapter is to describe studies aimed at the optimization of SLE processing parameters. Design of experiments (DoE) studies were conducted on 'non-weldable' superalloys to identify the parameter ranges that yielded the best possible deposits in SLE trials. The quantification of the deposit quality was performed through a novel image analysis-based quantitative metallography technique. The datasets from these analyses were further utilized in developing multivariate statistics-based control charts for the SLE process for different superalloys.

Control charts provide an effective methodology for detecting any anomalies in industrial processes where the variation from the normal output or any special cause of variation can be detected in an efficient and timely manner. An efficient control chart allows detection of anomalies as quickly as possible while not being influenced by false alarms or false out-of-control signals. The first kind of error associated with no detection even if the system is out-of-control is known as type I error. The second kind of error where an out-of-control signal is generated even though the system is actually in-control is known as type II error. If simultaneous monitoring of two or more related quality characteristics is required, multivariate detection tools become essential. If several univariate controls are still utilized for a multivariate situation, the type I error probability gets inflated. Similarly, another decision rule that is often considered is as

follows: only if all variables are out-of-control, then the system is to be concluded out of control. This leads to inflated type II error. Also, for dependent variables there is no easy way to measure the distortion in the joint control rules. Hence, the development of multivariate detection methods for SLE-repaired or fabricated components is of immense interest for the successful commercialization of this additive manufacturing process.

This chapter begins by describing the quantitative metallography techniques developed [121, 151] and extended in the present work to identify deposit characteristics from optical micrographs. The DoE results of EQ superalloy IN 100 are presented later. Multivariate statistics are introduced for the DoE conducted on IN 100. Finally, a DoE study and a control chart developed for one SX superalloy (CMSX-4) is presented.

6.2 Quantitative metallography

Figure 132(a) shows a typical cross-sectional optical micrograph obtained from a SLE-processed CMSX-4 sample. Here, the initial substrate top surface is demarcated by the superimposed dark line. However, in practice, even identifying this surface is difficult. The sample when imaged in the optical microscope might be oriented in a different direction or might be in a non-horizontal position during the mounting procedure. Further problems may arise if the sample is bent due to excessive heating. However, the accuracy and consistency of results obtained from the image analysis need to be ensured across these scenarios. The sample needs to be isolated from the mounting material and the melt depth needs to be determined. After these initial steps, the microstructural and transitional information need to be obtained. As can be seen from Figure 132(a) the dendrites are much finer in the deposit than in the substrate, and hence the PDAS would also be difficult to measure accurately. Furthermore, the starting and

termination points of each dendrite are required. The next step would be to identify the CET and the OMT positions precisely. Figure 132(b) and (c) illustrates these two types of transitions typically seen in SLE of SX superalloys.

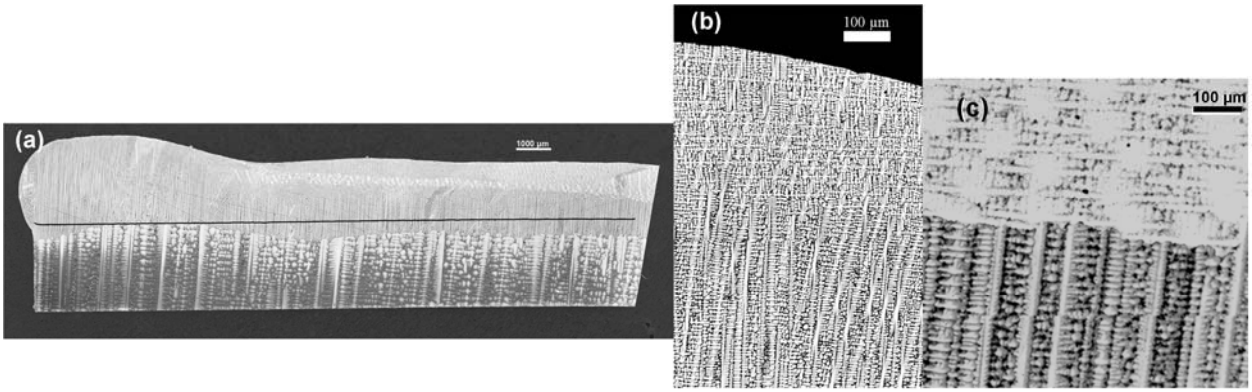

Figure 132. (a) SLE deposited sample with initial substrate location highlighted with black line and microstructural transitions showing (b) the CET and (c) the OMT.

The microstructural image of a SLE processed sample typically contains the information on the melt depth, the PDAS, the dendrite locations, the dendrite orientations, the OMT, the CET and also sometimes bending of the sample (if any). Consistent manual calculation of all of these parameters for a larger batch of samples can be very tedious, thus an efficient image-analysis code to perform this task automatically and consistently is highly desirable. However, most image analysis software tools (e.g. Image tools [127]) are semi-quantitative and based on scanning electron microscopy. To address this need, a customized, active contour-based image analysis code is written in MATLAB to extract all the microstructural parameters that are essential for coupling the CFD model to the microstructural evolution model. The key steps in the customized image analysis are discussed below.

Typically, the microstructural image first passes through the Canny edge detection technique which can preserve important structural data while filtering out a vast majority of the image information [152, 153]. Active contours are splines (also known as snake lines) that move due to external energies being applied to them through a map, while maintaining a shape through the use of an internal energy. The total energy of the snake line is given as [154-156],

$$E_{snake} = \int_0^1 (F_{int} + F_{image} + F_{con}).ds \quad (36)$$

F_{int} is the internal force that is used to hold the shape of the spline, F_{image} is the force applied on the spline by the image and F_{con} is the force used to apply constraints on the contour. The combination of these forces allows the movement of the snake line to a desired contour location,

The energy terms for the snake line are calculated first. The internal force term can be expressed as the summation of a first order (provides membrane-like behavior) and second order (provides thin plate-like behavior) terms [155]. The image force in equation 36 controls how the active contour will behave with respect to lines, edges and terminations. This can be expressed as [155, 156],

$$F_{image} = f_{line}F_{line} + f_{edge}F_{edge} + f_{term}F_{term} \quad (37)$$

Where, f_i is the corresponding coefficient. F_{line} is the intensity of the filtered image from Canny output. This applies a downward force on each spline knot and pushes the spline away from the top of the substrate to the meltback transition. The termination force F_{term} allows the contour to be attracted to the corners of the image. The edge force term F_{edge} attracts the contour to large image gradients and is given as,

$$F_{edge} = -|\nabla I(x,y)|^2 \quad (38)$$

The experimentally obtained micrographs of CMSX-4 samples are passed through a number of steps based on the active contour as follows:

The first step is to consider the bottom left corner of the image (50 pixels high and wide) to estimate the average intensity value of the mounting material. This allows the sample to be isolated with relative ease. Then five active contouring steps are performed to isolate the sample along the bottom, top, left and right sides. First, an active contour is generated at the bottom of the image which is pushed upward by the intensity difference between the sample intensity and average intensity of the mounting material, bakelite in this case. This allows the bottom line to be generated for 80% of the sample (i.e. barring the left and right edges). A similar procedure gives the left and right edges. The corner location is determined by locating rapid changes in the vertical direction. A second active contour is now run at the bottom of the sample and within the bounds of the left and right corners to accurately determine the bottom edge. Finally an active contour is generated at the top of the sample, between the bounds of the left and right edges and then it is propagated downwards. This generates the top edge for the sample. Figure 133(a) shows the top edge demarcated by red line for one representative CMSX-4 sample.

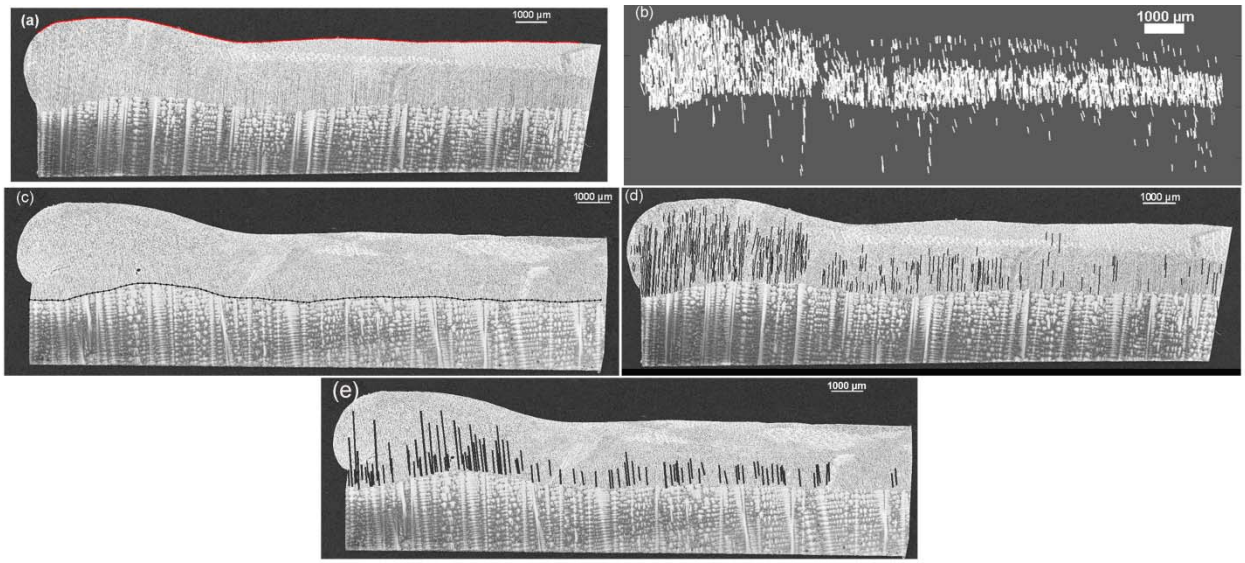

Figure 133. Representative lengthwise cross-section of CMSX-4 sample (a) with the top edge indicated by the red line determined from image processing, (b) with heat map, (c) with final snake line location for melt depth indicated in black line, (d) with the dendrites across the length of the sample and (e) with the primary dendrites tracked across length.

The second step is to identify primary dendrites and to isolate them from the shorter offshoots or secondary dendrites. The microstructure image is first differentiated in the x-direction to highlight prevalent changes surrounding both sides of SX primary dendrites. The Canny edge detection algorithm is then used to return an image with the lines. Following this step, a hysteresis map is used to mark already-searched pixels and to make sure that the search is not repeated over any location. The Canny output is then used to find long vertical growths that denote primary dendrites. The search is kept limited to ±45 degrees from the vertical so that horizontal lines are not traced. Figure 134(a) and (b) show the Canny detection output and the edges found using the Canny output respectively.

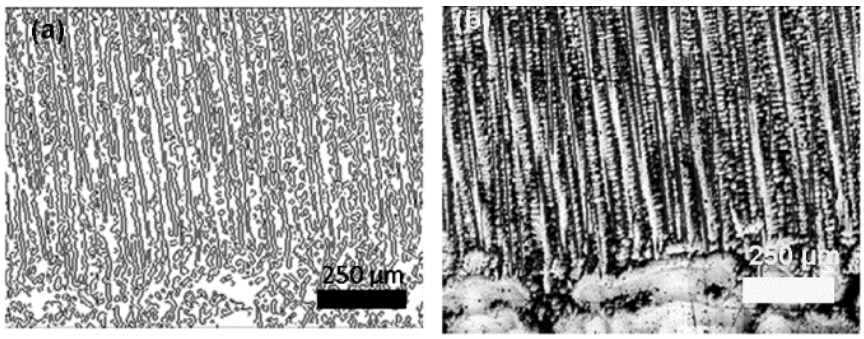

Figure 134. Representative section showing (a) Canny detection output and (b) edges found using Canny output.

In the third step, a heat map based on the dendrite edge data is created. This map allows the determination of the transition between the coarser dendrites in the substrate and the finer dendrites in the deposit. Bresenhams line algorithm [157, 158] is used for this purpose. Figure 133(b) shows one such representative heat map.

The heat map is used as the external force and the initial active contour is placed at the original top surface of the substrate on which the new deposit was created. An upward force is also included to better represent lack of fusion in some samples. Once the total energy of the active contour remains near constant between two subsequent iterations, the melt line is recognized, as shown in Figure 133(c). The dark line is the final output indicating the contour of meltback into the substrate.

In the fourth step, a more detailed analysis is carried out to track the PDAS. The secondary dendrite effects are mitigated by blurring in that direction for close proximity of any tracked primary dendrite line. Keeping each blurring effect localized also stops the propagation of error

by a poorly tracked dendrite from the earlier attempt. Figure 135 shows the effect of blurring and how the primary dendrite shapes remain largely unaffected by this operation.

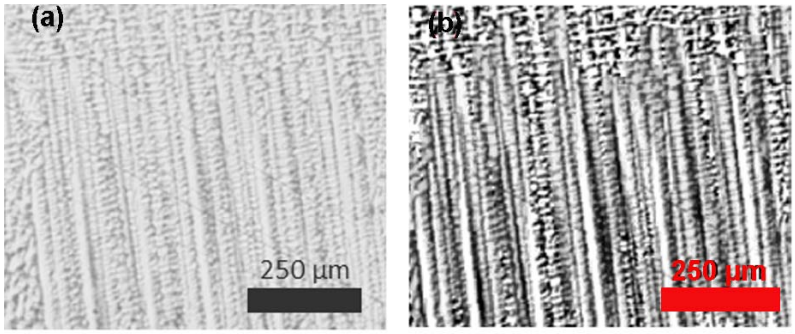

Figure 135. Representative images comparing microstructural cross-section (a) before blurring and (b) after blurring.

A closing operation (use of dilation followed by erosion) is performed to highlight the trunk of each dendrite. The starting point of each edge detected by the Canny output is recalled. These points serve as the probable locations of the primary dendrites. Next, by searching in the heat map the highest intensity is located in the surrounding area (within 5 pixels). This allows the generation of new points within a tolerance. These two points are now joined and a threshold intensity is maintained along the line to stop the line from jumping between two closely aligned dendrites. The final result of these operations is lines representing dendrites across the length of the sample, as shown in Figure 133(d).

Next, another heat map is generated using the start and end points of the accurately tracked dendrites. An active contour is established at the top of the sample and it propagates downwards until it reaches the SX termination points. Figure 136 shows a close-up of the calculated SX termination contour.

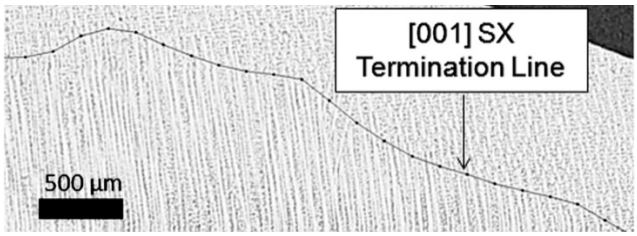

Figure 136. Representative image showing the termination of <001> SX growth.

The PDAS is determined in the final step. The heat map from the previous step is differentiated in the x-direction. This allows the transition from the dendrite trunk to the secondary growth to be highlighted. An assumption is made that the center dendrite trunk area is clipped, or close to it, in the image. This assumption can be represented mathematically as,

$$\frac{dy}{dx} = 0, \quad \frac{d^2y}{dx^2} = 0 \tag{39}$$

A search is then conducted to the left and right of the point to find a non-zero value of the first derivative. As the search continues, if a pixel in question exceeds a certain threshold value, it is assumed to be the edge of the trunk. To find the dendrite termination point, the second derivative is calculated. This allows the determination of whether the termination point is on the left or right side of the trunk. This criterion can be represented as,

$$\frac{d^2y}{dx^2} < 0 \quad \Rightarrow \text{Right side termination} \tag{40}$$

$$\frac{d^2y}{dx^2} > 0 \quad \Rightarrow \text{Left side termination} \tag{41}$$

If both the right side and left side termination points cannot be located, the data is error prone and discarded from further analysis. After completing this analysis for every point the average width for each dendrite is found and saved relative to its location along the sample length. Figure

6 uses the starting and ending points for the tracked primary dendrites to draw a straight line near the center of the primary dendrite trunk, as shown by the black line. The two light gray lines are created at an offset to represent the average width along the dendrite length.

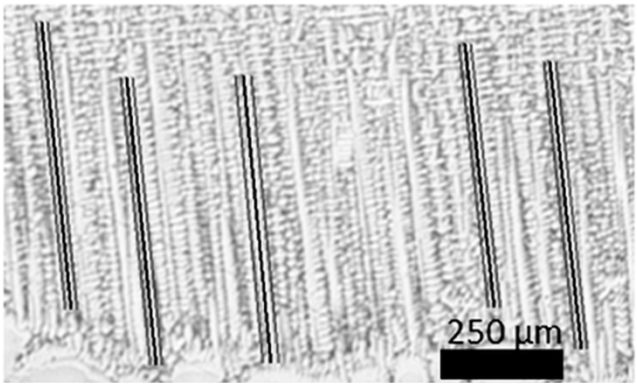

Figure 137. Representative image showing the PDAS tracked using image processing.

Equiaxed superalloys do not have as clear of a transition from the substrate to the re-melted region denoting the meltback line. Hence, the contrast is created by several steps. The first step is to average each pixel of the image using an 11x11 kernel. The deposit section tends to be slightly lower in intensity than the cast section. Searching along the bottom of the substrate and the top of the sample, using the top and bottom lines found while isolating the sample, average pixel values for the two regions can be determined. Using an intensity value between the upper and lower numbers and subtracting that amount from the image intensity gives a starker contrast between the substrate and remelted region by making a majority of the substrate positive while the newly deposited region becomes negative. An opening algorithm and distance transform is then used on the image to better connect separate features and fill holes found in high intensity locations. For polycrystalline samples, the melt line is tracked, again using active contouring, as shown in Figure 138.

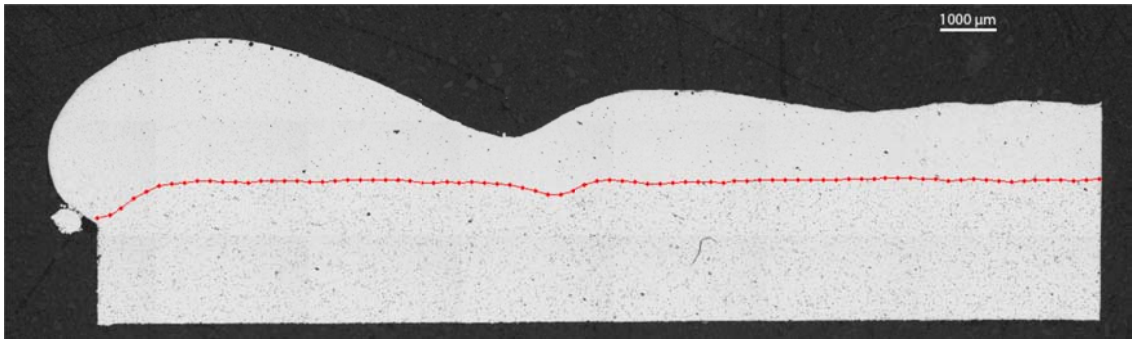

Figure 138. Melt line tracked for René-80 sample across the length [121].

The algorithm also detects cracks and porosity in the deposits as illustrated in Figure 139. This is done by checking with a threshold value of the intensity found for the images and then separating the cavities by the lower value. Defects found with high circularity values are labeled as pores and those found with low circularity values are labeled as cracks.

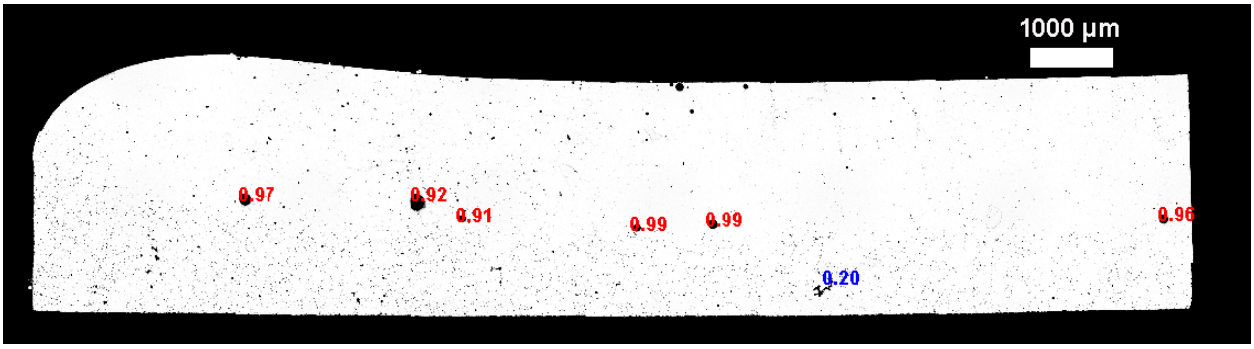

Figure 139. Pores and cracks detected for EQ sample.

6.2.1 SX material analysis metrics

The microstructural information derived from the image analysis and used in DoE-based investigations are reported in Table 17. It was of particular interest to see how volumetric energy density relates to the percentage of the sample that was fused, the overall average deposit height, the average columnar height, the average melt-back depth, the amount of deformation, and the

number of stray grains present in the deposit. The derived parameters chosen to represent the quality of CMSX-4 deposits were columnar to total height ratio, deposit uniformity, lack of deformation and number of stray grains. The deposit uniformity was calculated by taking the deposit height of the sample, developing a linear fit for the height and then calculating the average R^2 residual between the height and the linear fit. The higher the R^2 value, the more uniform was the deposit. Similarly, the deformation of the sample was found from the bottom line of the substrate. A similar procedure is adopted to compute the lack of deformation. Higher the value of this parameter, lower is the amount of deformation of the substrate region.

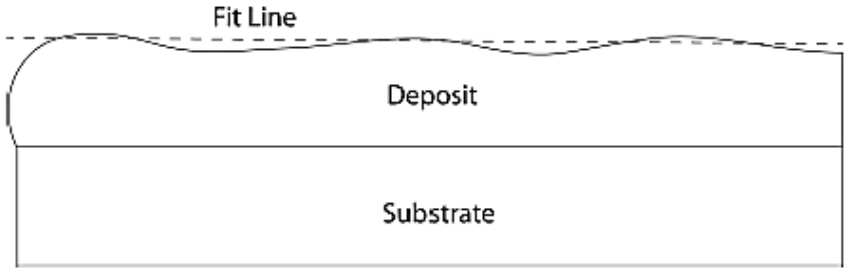

Figure 140. Linear fit to represent the deposit uniformity in samples.

Table 17. CMSX-4 image analysis outputs and analysis metrics

Image analysis output	Analysis metrics
Total deposit height	Columnar to total height ratio
Melt line	Deposit uniformity
Melt depth	Number of stray grains
SX deposit height	Lack of deformation
SX angle information	
Substrate angle information	
PDAS	
Substrate deformation	

6.2.2 EQ material analysis metrics

The set of metrics used to develop process maps for the EQ samples included the average deposit height, average melt back depth, number of pores and deposit uniformity. The image analysis output and analysis metrics are listed in Table 18. In EQ samples investigated (IN 100 and René 80), the combination of scan speed and power results in high surface tension and instability at the front of the melt pool, adversely affecting smooth flow of molten powder into the melt pool front. The scan proceeds so quickly that a large amount of powder will fall into the melt pool and resulting in balling. This will create a starvation of powder slightly later in the scan, resulting in the humps, generating non-uniformity in the deposit.

Table 18. EQ material image analysis output and analysis metrics

Image analysis output	Analysis metrics
Total deposit height	Average deposit height
Melt line	Average melt depth
Melt depth	Deposit uniformity
Pore list	Lack of deformation
Crack list	
Deposit top line	
Substrate deformation	

6.3 Study on IN 100

As mentioned in section 4.4.1, IN 100 powder contained internal porosity and the powder particle size distribution was bimodal. The use of a scan spacing of 25.4 μm thus sometimes caused partial melting and consequently, a large number of porosities in the deposit region as shown in Figure 141. Use of a lower scan spacing of 12.7 micron typically resolved this problem by completely melting the powder, however, this often led to excessive or complete melt-through

in the substrate region. One such example is shown in Figure 142. Hence, a careful balance of the scan spacing and the other scan parameters had to be accomplished in the DoE to minimize the number of pores and to avoid excessive melting of the substrate region.

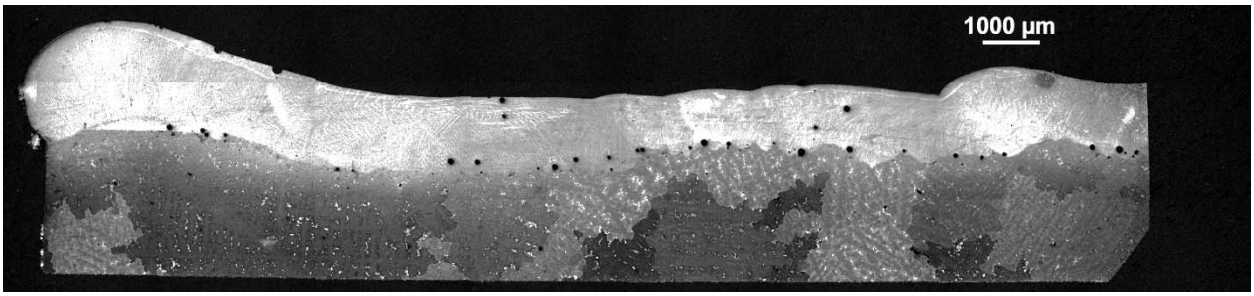

Figure 141. IN 100 sample containing excessive number of pores in the deposit region.

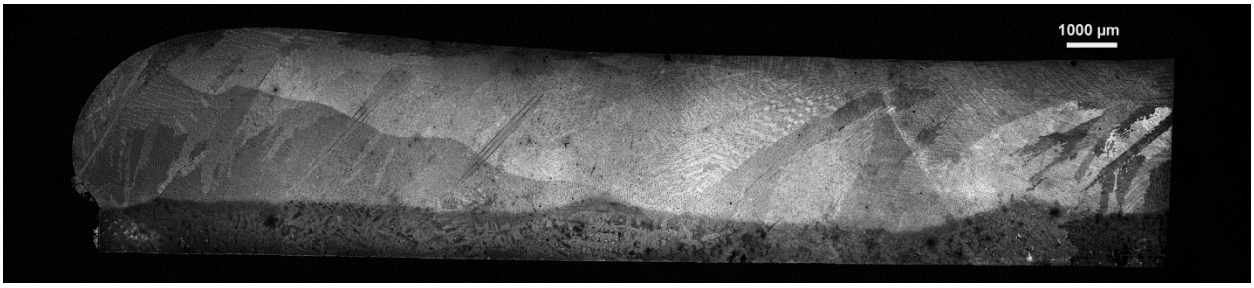

Figure 142. IN 100 sample showing excessive melt depth in the substrate region.

During the DoE-based study on IN 100, two sets of screening experiments were conducted to develop a feasible operating range in which samples exhibited consistent bonding across the sample length while also not melting through the substrate. Several DoEs were conducted to drill down on an optimal set of parameters for producing high quality IN 100 deposits. The parameter ranges explored included 75-125 preheat scans, scan speeds of 300-600mm/sec, laser powers of 250-500W. The samples were run with a scan spacing of 12.7-25.4 µm to account for the smaller beam diameter on the fiber laser and each substrate coupon had dimensions of 35.6 x 6.9 x 2.54mm. Additionally, all trials were run at a fixed powder height of 1.4mm. The DoEs

conducted were phase one ascent DoEs based on a fractional factorial design meant to quickly identify the proper parameter range and identify the main factor effects on the chosen quality metrics of melt depth, melt uniformity, deposit height, and deposit uniformity. The sets of DoEs that were conducted are listed in Table 19.

Table 19. Samples used for IN 100 process map development.

Repeats	Energy Density (J/mm^3)	Powder thickness (mm)
100	28.12	1.4
125	15.23	1.4
100	18.28	1.4
75	22.85	1.4
125	22.85	1.4
100	17.58	1.4
125	22.50	1.4
75	22.50	1.4
75	28.12	1.4
75	24.10	1.4
75	24.61	1.4
75	21.09	1.4
75	23.43	1.4
100	56.24	1.4
100	46.87	1.4
100	49.99	1.4
100	56.24	1.4
100	50.62	1.4
100	56.24	1.4
100	56.24	1.4
100	51.13	1.4
100	49.99	1.4
100	60.93	1.4
100	54.24	1.4
100	56.24	1.4
100	49.48	1.4
100	28.12	1.4
100	24.37	1.4
100	28.12	1.4

Table 19 (continued).

100	32.45	1.4
100	28.12	1.4
100	25.16	1.4
100	31.43	1.4
100	28.12	1.4

6.3.1 Design of experiments study

Figure 143 provides an overview of the effect of process parameters on the different quality metrics. The average melt depth along the length of the deposit, the deformation of the substrate region and the number of pores found in the deposit region were studied as functions of process parameters. As seen, scan power and scan spacing are most influential in controlling the melt depth. Increasing the scan power and reducing the scan spacing resulted in more melt depth, which is intuitive since the volumetric energy density increases and the melt pool size increases due to increase in power and reduction of scan spacing. Number of preheat scans (Repeats) and raster scan speed is more influential in the deformation of the substrate. Higher preheat scans typically results in an increase in the average temperature of the deposit region. The increase in the amount of energy being dumped into the substrate due to higher number of preheat scans caused bending of the substrate region. The raster scan speed controls the thermal lag between the deposit and substrate region. With higher scan speeds, the thermal mismatch between the substrate and the deposit region caused the substrate to deform more. As suggested earlier, the pore count can be reduced by reducing the scan spacing. Increasing the power and reducing the raster scan speed caused higher volumetric energy density, thus allowing complete melting of the powder, and resulting in reduced pore counts.

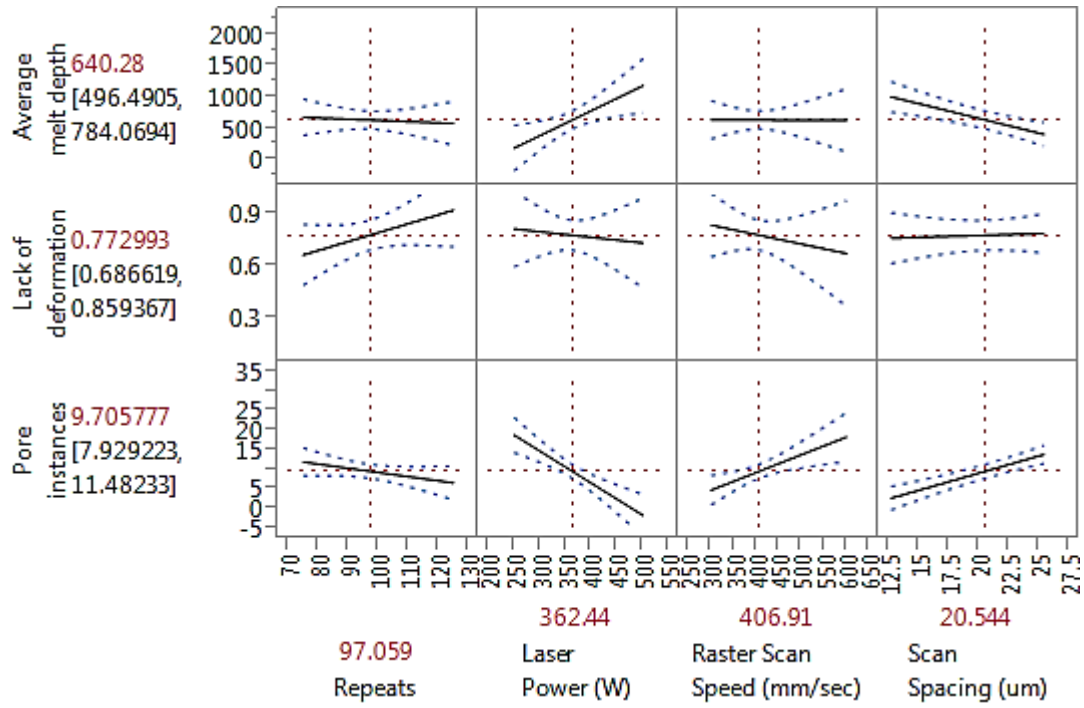

Figure 143. Overview of the effects of each process parameter on the various quality metrics for IN 100 deposits.

Figure 144 shows the fit model generated in JMP-10 software package to predict different analysis metrics as a function of operational paramaters. Figure 144 (a), (b) and (c) show the fits obtained for average melt depth, pore counts and average deposit height as functions of volumetric energy density and number of preheat scans. Figure 144 (d), (e) and (f) show the prediction fit for deposit height uniformity, average melt depth and pore counts as functions of scan power and rater scan speed. These prediction formulas were later used in developing the process map and to identify the optimized parameter ranges.

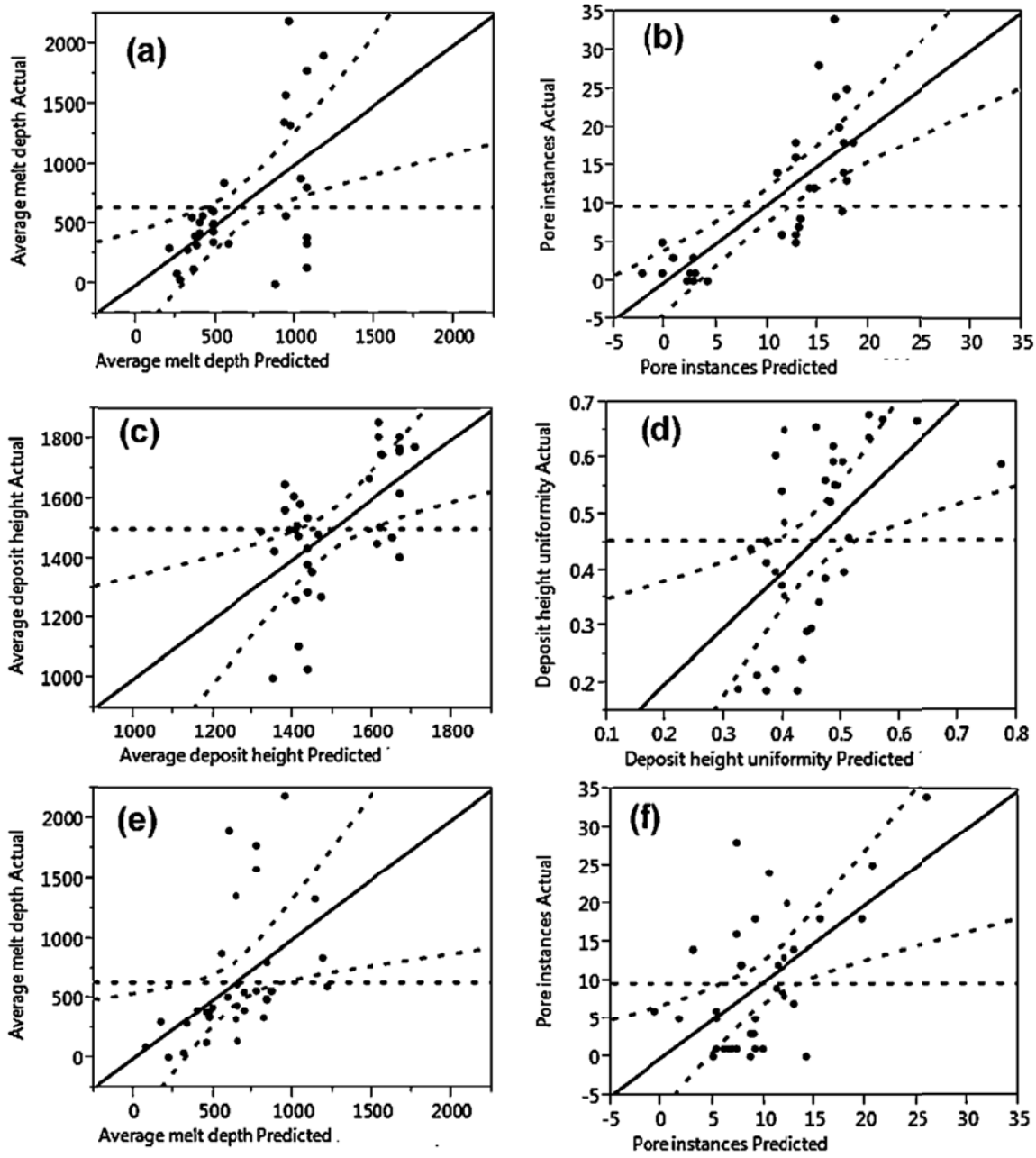

Figure 144. Prediction fit of (a) Average melt depth, (b) Pore count, (c) Average deposit height as function of volumetric energy density and number of preheat scans, (d) Deposit height.R^2, (e) Average melt depth and (f) Pore counts as function of laser power and raster scan speed.

The prediction quality of the fit models can be quantified by the P-value. P-value represents the likelihood that a measured value would have been observed in the absence of variation of the considered process parameters. It helps to indicate the level of statistical significance of each model. P-values below 0.05 or 5% indicate that the observed result would be highly unlikely if the process parameters considered were not varied, indicating that it may be a statistically significant model. Table 20 describes the P-value for each of the fit model generated as function of contributing factors.

Table 20. Prediction quality of the fit models generated for IN 100.

Variable	Contributing factors	P-value
Average melt depth	Volumetric energy density, Number of preheat scans	0.0019
Pore instances	Volumetric energy density, Number of preheat scans	0.0001
Average deposit height	Volumetric energy density, Number of preheat scans	0.0025
Deposit height uniformity	Laser power, Raster scan speed	0.0033
Average melt depth	Laser power, Raster scan speed	0.0001
Pore instances	Laser power, Raster scan speed	0.0018

Figure 145 demonstrates the development of a process map as a function of the volumetric energy density and the number of preheat scans. The lower limit of 200 µm average melt back depth is demarcated by the red line on the left side and upper limit of 500 µm average melt back depth is similarly demarcated by the red line on the right. Thus the region of 200-500 µm average melt back depth is bounded by these two lines and shaded in red. The region shaded in green to the right side of the green line indicates a deposit height above 1.4 mm. The region shaded in blue to the right side of the blue line indicates number of pore count below 20. The black dots indicate the data points. As can be seen, the optimal processing zone that produces an

'acceptable deposit' with the abovementioned criteria is the overlap of all the above regions, with volumetric energy density 15-30 J/mm^3 and number of preheat scans ranging 80-120. A similar process map can also be developed as function of scan power and raster scan velocity as shown in Figure 146. The optimal parameters here are: power value ranging from 275 to 375 W and raster scan speed ranging from 300 to 500 mm/s.

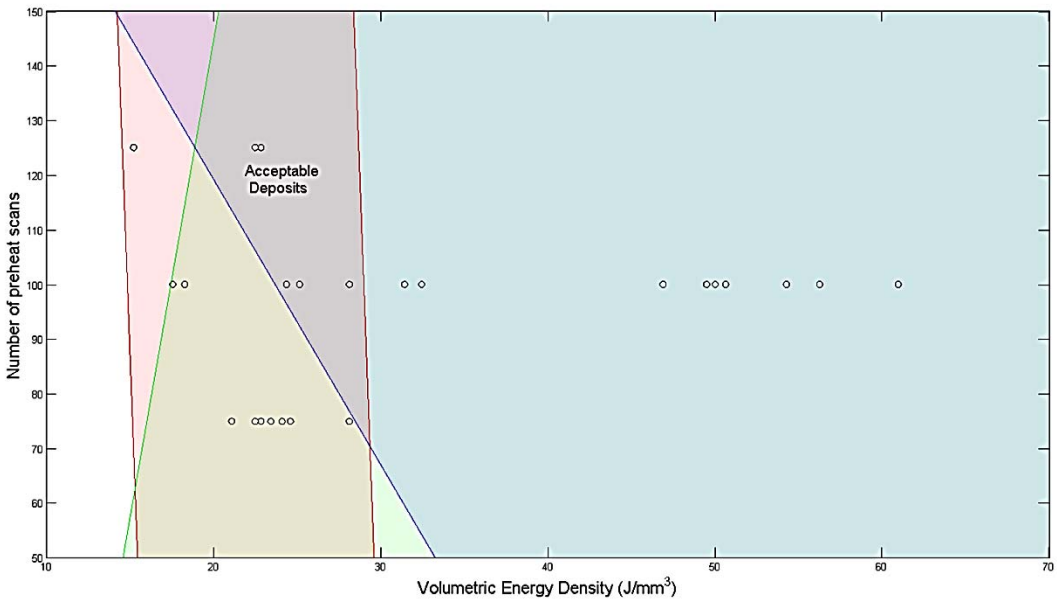

Figure 145. Process map relating number of preheat scans and volumetric energy density to high quality deposit formation. The lower limit of 200 µm average melt back depth is demarcated by red line on the left side and upper limit of 500 µm average melt back depth is demarcated similarly on the right. The green shaded region indicates deposit height above 1.4 mm. The blue shaded region indicates number of pore count below 20. The black dots indicate the data points.

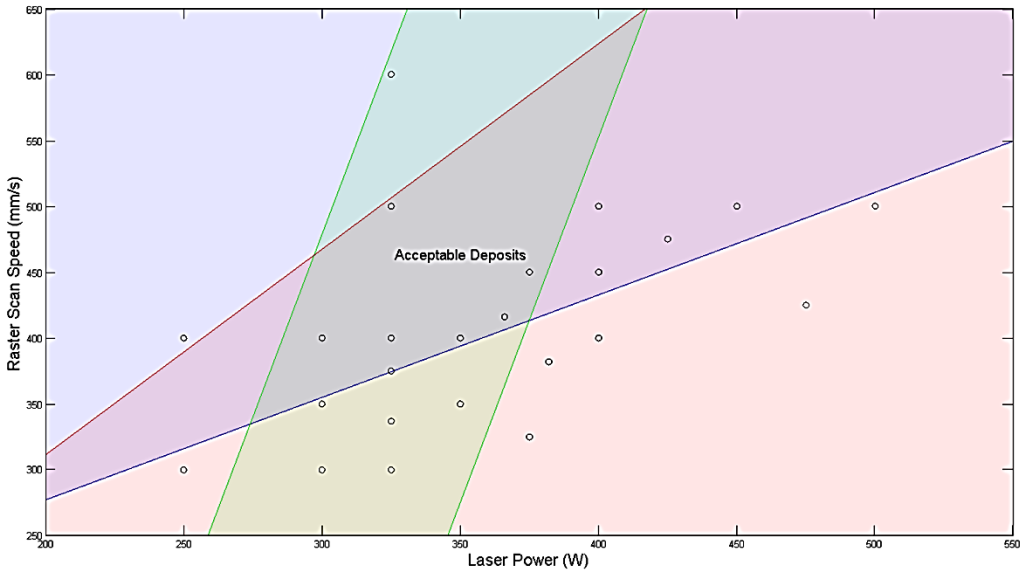

Figure 146. Process map relating laser power and raster scan speed to high quality deposit formation. The lower limit of 200 µm average melt back depth is demarcated by the green line on the left side and upper limit of 500 µm average melt back depth is demarcated similarly on the right side. The blue shaded region indicates deposit height uniformity above 0.45. The red shaded region indicates number of pore count below 20. The black dots indicate the data points.

6.3.2 Multivariate statistics

Hotelling T^2 method was utilized for multivariate detection in the present scenario. The initial or phase I goal of the process is to evaluate the mean and co-variance matrix of the in-control data. Since, the aim was to screen the out-of-control data points as well, Hotelling T^2 method was utilized for sample size =1. The monitoring and detection process is divided into two phases. Phase I identifies the in-control training data (which are used to estimate the distribution parameters). Typically, a chart is applied to the training data to see if the training data are really in control. All out-of-control data is removed and iterated until all training data are in control.

The sample mean and covariance matrix were evaluated first. The sample mean or $\bar{x}$ and the sample covariance S was calculated as,

$$\bar{x} = \frac{1}{n}\sum_{j=1}^{n} x_j \tag{42}$$

$$s = \frac{1}{n-1}\sum_{j=1}^{n}\left(x_j - \bar{x}\right)\left(x_j - \bar{x}\right)^T \tag{43}$$

The T^2 statistic was calculated as,

$$T^2 = \left(x_j - \bar{x}\right)^T S^{-1}\left(x_j - \bar{x}\right) \tag{44}$$

T^2 closely follows a chi-square distribution instead of an F-distribution. So, the upper control limit (UCL) can be found using the $\chi^2(p)$ distribution, where p is number of variables.

Hence, $T^2 \sim \chi^2(p)$ and $UCL = \chi^2_\alpha(p)$ (45)

In Phase II, the control charts established from the in-control training data are applied to future observations. This Phase I & II analysis should also be performed in the univariate detection. In the present analysis, a value of 0.1 is used for α. So, the UCL was equal to 4.6052. The univariate control limit was also determined using the same α value and the variance. The average melt depth and the standard deviation of deposit height value were chosen as the variables. The correlation coefficient between the variables were calculated as,

$$\rho_C = Correl(X,Y) = \frac{Cov(X,Y)}{\sqrt{Var(X)Var(Y)}} \tag{46}$$

The correlation coefficient between the average melt depth data and number of pores is calculated and found as, ρ_c = - 0.24, so there is negative correlation between these two set of variables.

Data point 15 revealed lack of fusion along the length and a zero value of average melt depth. That point was removed during inspection. Figure 147 (a) shows that data points 18 and 23 have

T^2 value more than the UCL. This can be either due to the higher value of the standard deviation of deposit height value as shown in Figure 147(b) or the higher value of the melt depth as shown in Figure 147(c). Hence, in the 1st pass these data points are removed and the process was repeated. Figure 148 shows an intermediate pass. Here data points 22 and 25 are out-of-control and are removed due to higher value of the melt as shown in Figure 148(c). Finally, Figure 149 shows the final pass where all the data points are in-control. The univariate control chart for standard deviation of the deposit height in Figure 149 (b) and univariate control chart for melt depth in Figure 149(c) are also in-control. Hence, the mean and covariance matrix at this step can be used as in-control mean and covariance value for Phase II analysis.

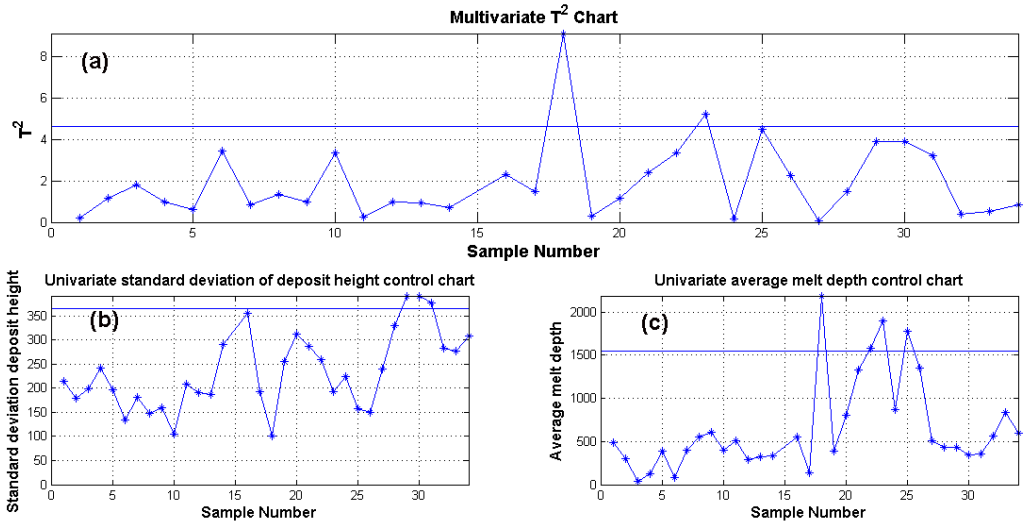

Figure 147. (a) Multivariate T^2 chart and univariate control chart for (b) standard deviation of deposit height and (c) melt depth (1st pass).

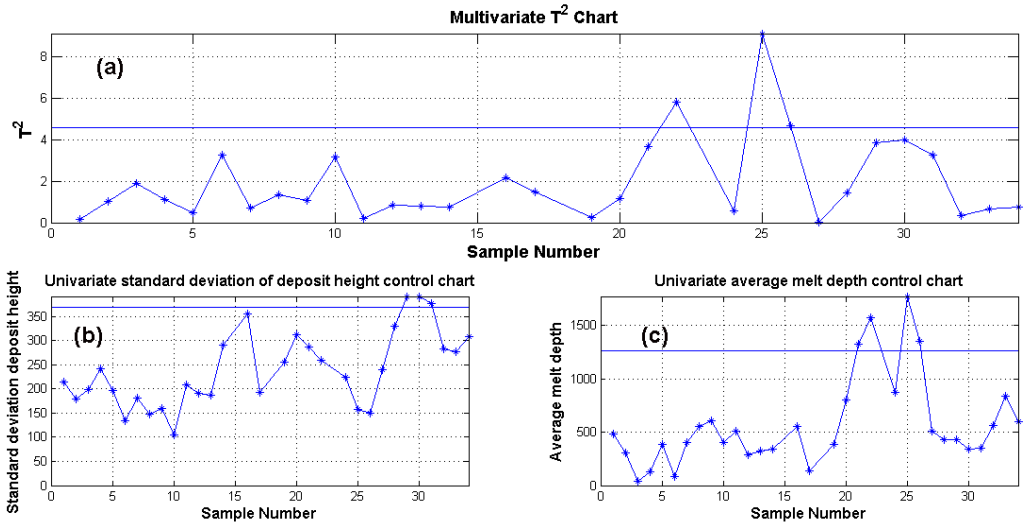

Figure 148. Multivariate T^2 chart and univariate control chart for (b) standard deviation of deposit height and (c) melt depth (Intermediate pass).

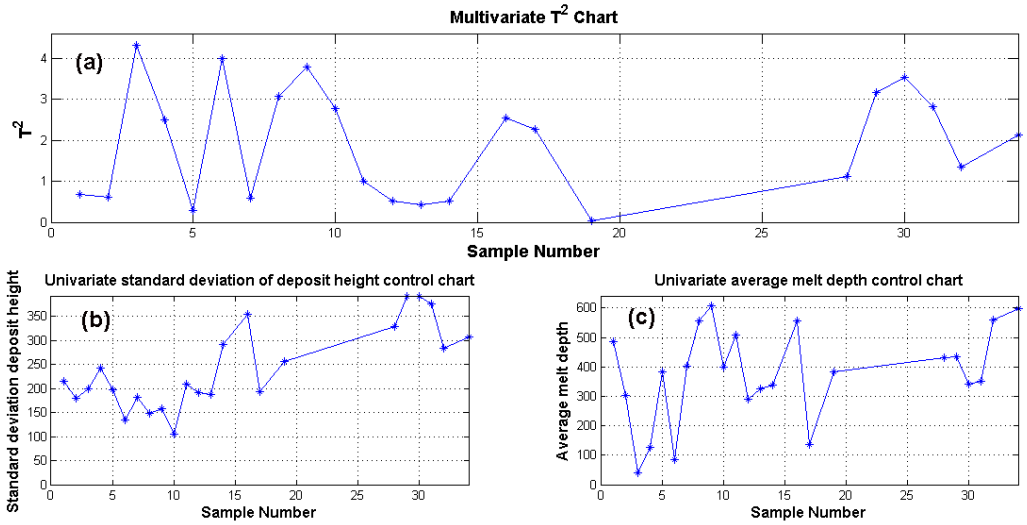

Figure 149. Multivariate T^2 chart and univariate control chart for (b) standard deviation of deposit height and (c) melt depth (final pass).

The iterative removal of out-of-control data points is illustrated in Table 21. The rows marked in one color are removed in the same iteration and the unshaded rows are the finally calculated in-control data. The mean data are found as = (375.8913 239.8114) and the covariance is calculated

as, ($2.6077x10^4$ $3.0093x10^3$; $3.0093x10^3$ $7.2362x10^3$). The correlation coefficient of the in-control data points is calculated and is equal to $\rho_c = 0.216$. So, the multivariate analysis gradually optimized the dataset and selected those samples where average melt depth and standard deviation of the deposit height are both minimized simultaneously.

Table 21. Multivariate detection table showing the removal of out-of-control data points for IN 100 samples. The shaded rows are the out-of-control data points and rows shaded by similar colors are removed in the same pass.

Repeats	Powder Thickness (mm)	Energy density (J/mm^3)	Deposit height standard deviation (µm)	Average melt depth (µm)
100	1.4	28.12	214.1952	486.2
125	1.4	15.23	179.262	302.3
100	1.4	18.27	198.3657	40.7
75	1.4	22.85	241.6902	127.4
125	1.4	22.85	197.2835	384.2
100	1.4	17.58	133.4698	86.4
125	1.4	22.50	181.5143	403.2
75	1.4	22.50	148.091	555.7
75	1.4	28.12	158.6185	609
75	1.4	24.10	104.7545	400.4
75	1.4	24.61	208.2525	509
75	1.4	21.09	190.7147	289.5
75	1.4	23.43	186.5668	324.8
100	1.4	56.24	291.3566	337.4
100	1.4	46.87	311.3232	0
100	1.4	49.99	354.5206	557.4
100	1.4	56.24	192.4888	135.7
100	1.4	50.62	101.6827	2186.4
100	1.4	56.24	255.9674	384.4
100	1.4	56.24	311.1997	804.9
100	1.4	51.13	286.0866	1326.2
100	1.4	49.99	260.0997	1575.4
100	1.4	60.93	192.06	1897.3
100	1.4	54.24	223.5214	872.9

Table 21 (Continued).

100	1.4	56.24	157.6436	1772
100	1.4	49.48	148.9442	1347.9
100	1.4	28.12	240.3227	505.2
100	1.4	24.37	329.4664	430.1
100	1.4	28.12	391.2836	433.1
100	1.4	32.45	390.9138	340.9
100	1.4	28.12	376.0255	352.4
100	1.4	25.16	283.6203	558.4
100	1.4	31.43	277.7506	835.8
100	1.4	28.12	307.2413	596.9

6.4 Study on CMSX-4

The metallographic features of CMSX-4 deposits were described in detail in section 4.3. From an application point of view, the goals were to increase the <001> SX height and to delay the equiaxed grain nucleation. This required careful balancing of the scanning parameters to select a proper volumetric energy density. Excessive raster scan speed or lower power may also cause distortion of the substrate and can promote stray grain formation. Figure 150 shows a sample with a very low SX<001> growth due to lower scan spacing resulting in a higher volumetric energy. This expanded the melt pool and reduced the temperature gradient, thus expediting equiaxed grain formation [5]. Figure 151 shows evidence of stray grain formation and distortion of the substrate due to higher raster scan speed. The higher number of preheat scans also caused excessive melt depth near the starting edge.

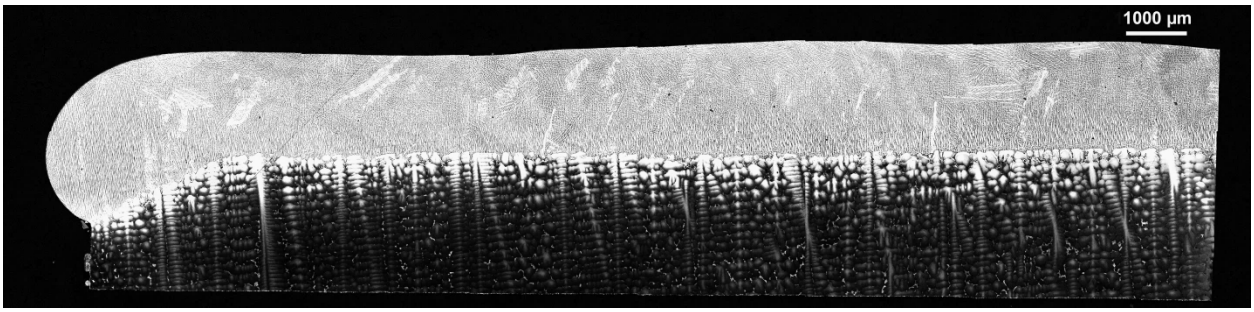

Figure 150. CMSX-4 deposit with lower <001> SX height.

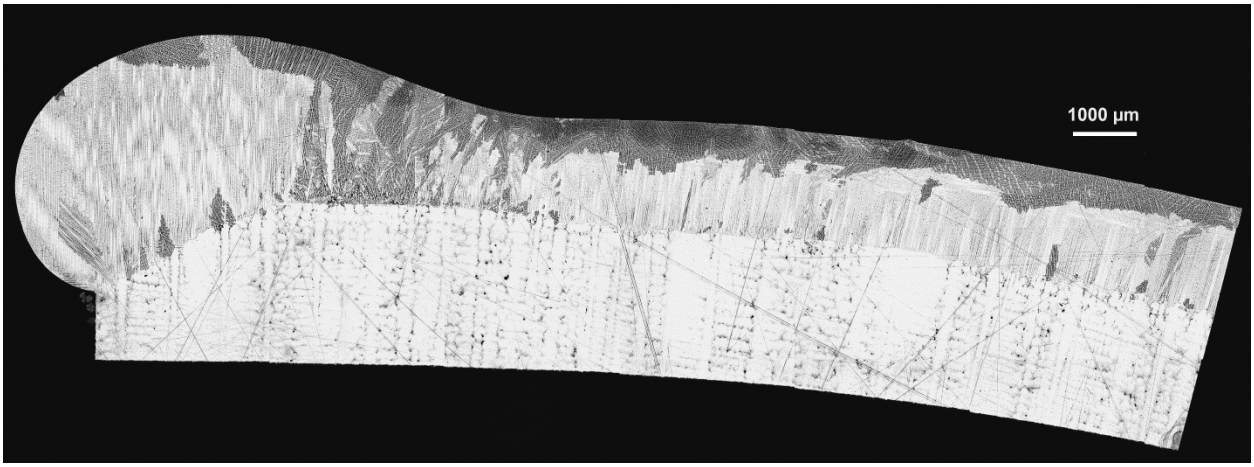

Figure 151. CMSX-4 deposit showing evidence of deformation, stray grain formation and higher melt depth near starting edge.

The DoE methodology used for CMSX-4 was similar to that adopted for IN 100. The sample space explored is listed in Table 22.

Table 22. Sample space used for CMSX-4 process parameter development.

Repeat	Energy density (J/mm^3)	Powder thickness (mm)
400	31.64	1.4
400	25.78	1.4
300	30.93	1.4
500	38.67	1.4
400	52.23	1.4

Table 22 (continued).

450	52.73	1.4
350	38.67	1.4
450	51.56	1.4
450	38.67	1.4
350	52.73	1.4
450	70.30	1.4
350	70.30	1.4
350	51.56	1.4
400	25.96	1.4
400	18.75	1.4
450	22.50	1.4
350	22.50	1.4
400	35.79	1.4
350	21.63	1.4
350	30.68	1.4
450	30.28	1.4
450	21.63	1.4
400	25.56	1.4
450	30.68	1.4
400	26.25	1.4
350	30.28	1.4

6.4.1 Design of experiments study

Figure 152 shows the effect of process parameters on the analysis metrics. The SX ratio or the ratio of the columnar height to the total deposit height is of immense interest. As seen, the SX ratio decreases as laser power is increased, the scan speed is reduced and scan spacing is decreased. All of these changes increase the volumetric energy density and expand the melt pool, thus reducing the vertical temperature gradient and causing nucleation of new grains. The SX ratio also decreases as the number of preheat scans is increased. A higher number of preheat scans increase the average substrate temperature and decreases the vertical temperature gradient, thus lowering the SX height [5]. The lack of deformation is found to be dependent on the scan

speed since it is responsible for the thermal lag between the deposit and substrate region. The average melt depth increases with increase in laser power and reduction of scan speed, since both changes result in more energy being provided to the substrate region.

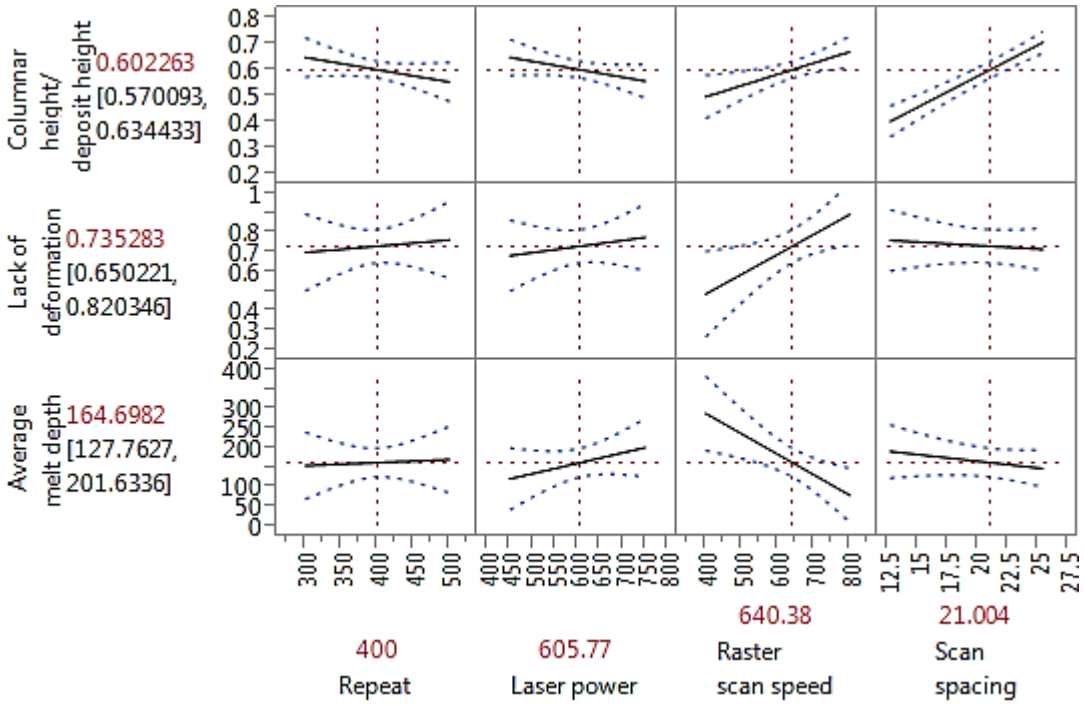

Figure 152. Overview of the effects of each process parameter on the various quality metrics for CMSX-4 deposits.

The volumetric energy density is an metric for to combining several process parameters into a single parameter, and it is known to be influential for SX deposits in terms of SX height, stray grains, deformation etc. [20, 80]. Figure 153 shows the effect of volumetric energy density on the average deposit height. A higher volumetric energy density expands the melt pool, drawing more powder from the side of the melt pool, thereby increasing the average deposit height.

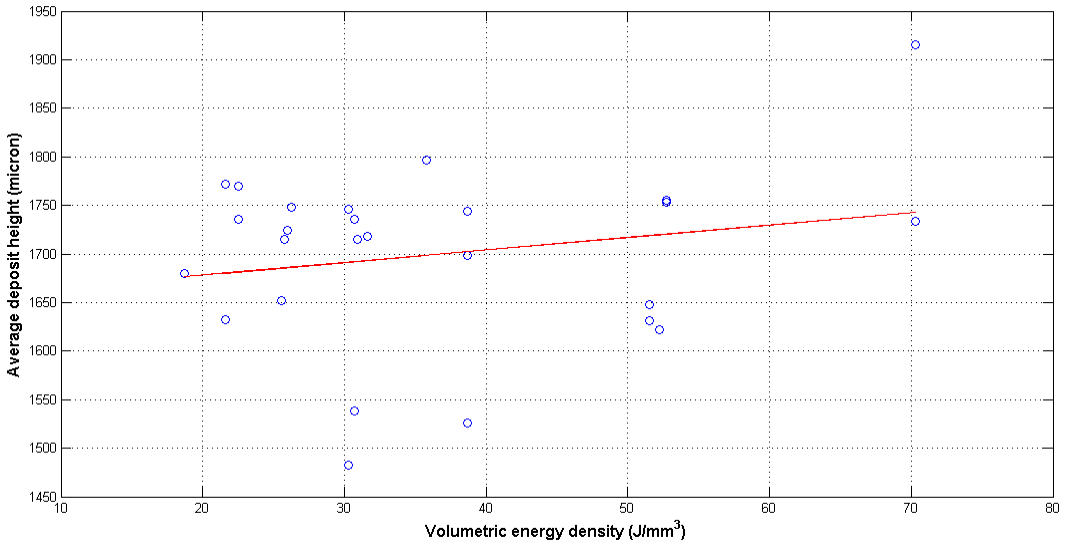

Figure 153. Effect of volumetric energy density on average deposit height for CMSX-4 deposit.

Figure 154 shows the effect of the volumetric energy density on deposit uniformity. It can be noted that a higher volumetric energy density reduces the surface rippling and improves deposit uniformity. Higher volumetric energy density is associated with higher power and/or lower scan speed. Together they cause smoother flow of powder due to removal of surface instabilities.

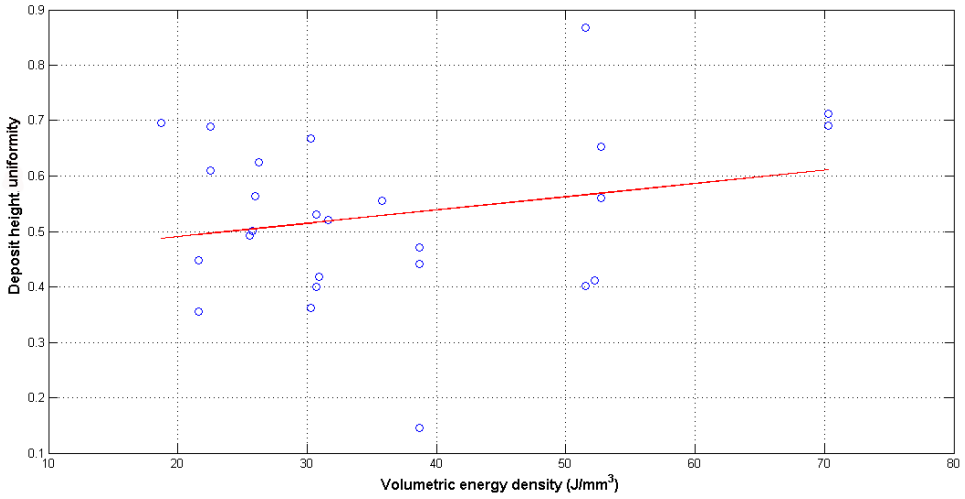

Figure 154. Effect of volumetric energy density on deposit height uniformity for CMSX-4 deposit.

Figure 155 shows the effect of volumetric energy density on the lack of deformation. The higher the value of the lack of deformation parameter, the lower is the deformation amount. Higher energy densities associated with lower scan speeds result in lower thermal lag; lower energy densities associated with higher scan speeds promote thermal lag between the melt pool and the bulk substrate. Thus lower energy density causes more deformation and consequently, lower value of the lack of deformation parameter in the substrate region.

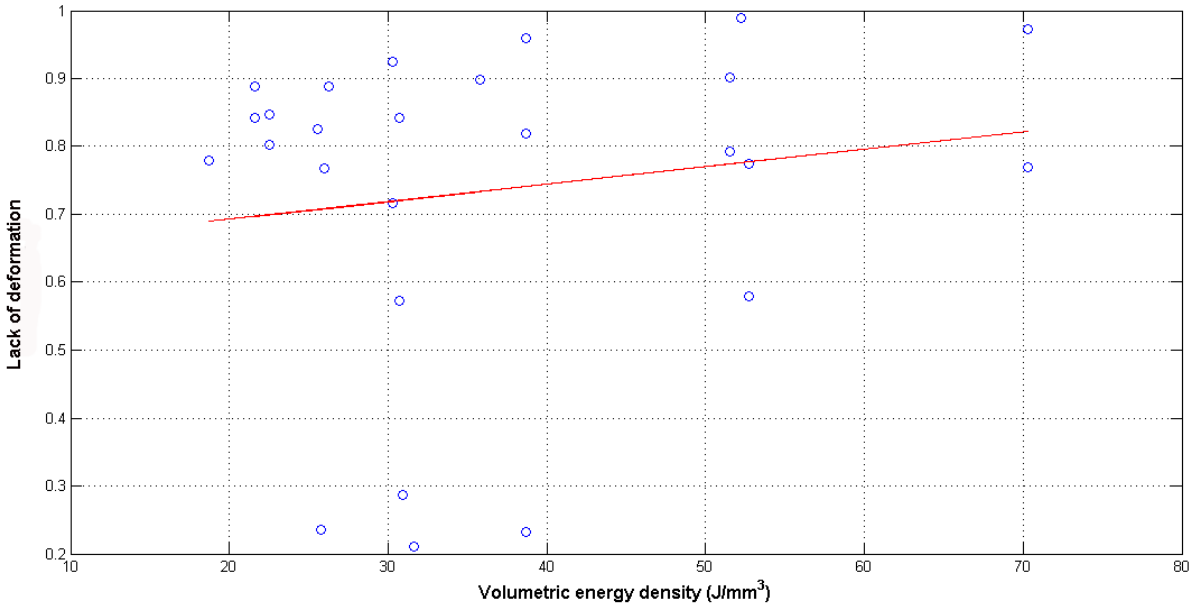

Figure 155. Effect of volumetric energy density on deformation amount for CMSX-4 deposit.

It is also observed that higher volumetric energy densities decrease the amount of stray grains from an average of 6 to 2 as the energy density is increased from 20 to 70 J/mm^3. The lower scan speeds and higher laser powers cause smoother flow of powder and lower Marangoni velocity at the top surface of the melt pool, thus decreasing the convection of broken dendrites [5, 92, 159]. This reduces stray grain formation significantly.

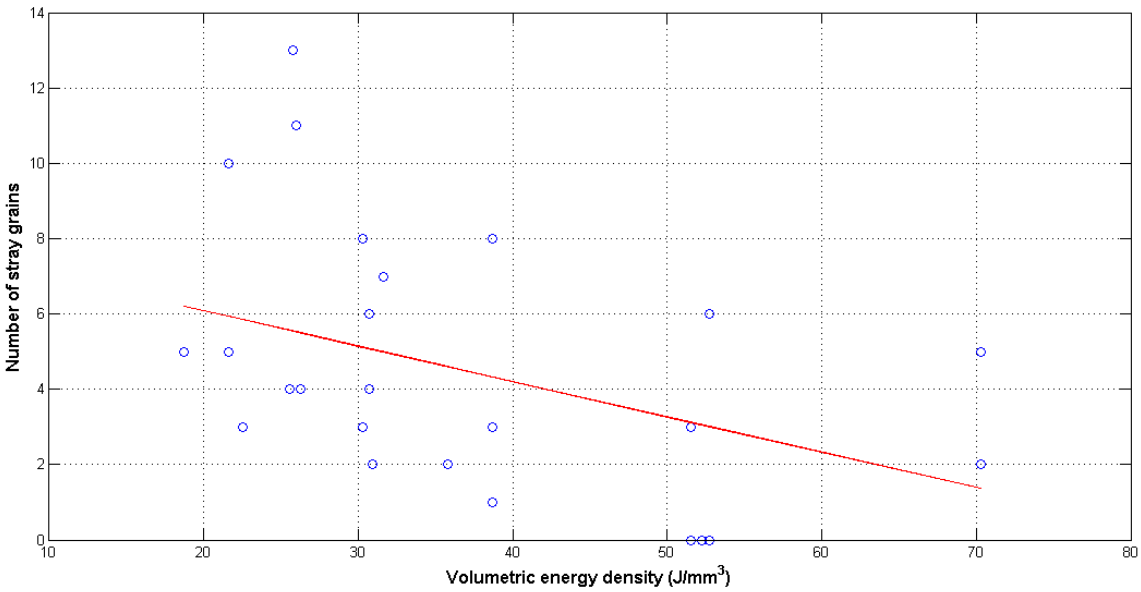

Figure 156. Effect of volumetric energy density on number of tray grains for CMSX-4 deposit.

Even though higher values of the volumetric energy density reduce the number of stray grains and improve deposit uniformity, they impair the deposit quality significantly by reducing the columnar ratio from 0.8 to 0.3 as the energy density is increased from 20 to 70 J/mm^3. This can be observed in Figure 157. The higher laser powers and lower scan speeds utilized expand the melt pool, thus reducing the temperature gradient in the vertical direction. This forces nucleation of new grains due to constitutional undercooling [14, 160] and the SX height decreases, resulting in lower columnar ratio at higher volumetric energy densities.

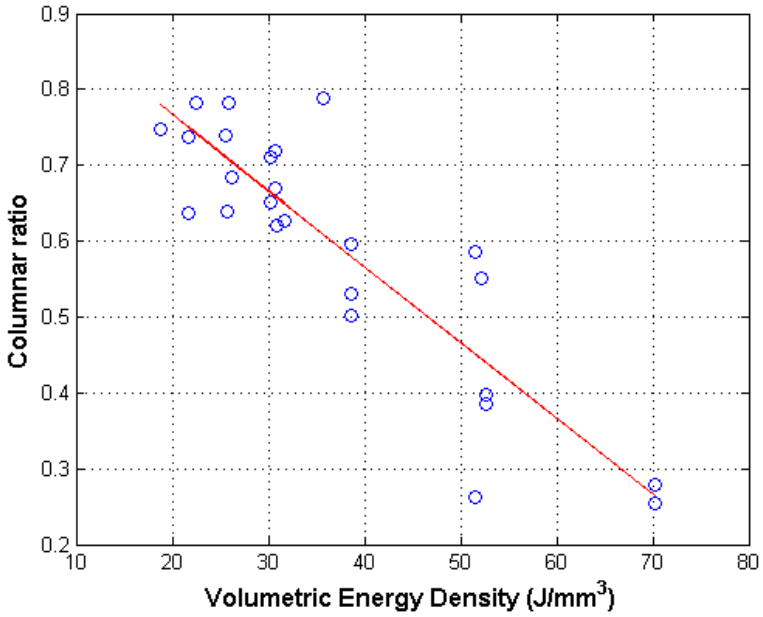

Figure 157. Effect of volumetric energy density on SX ratio for CMSX-4 deposit.

The volumetric energy density and the number of preheat scans are significant in determining the deposit quality. Lowering of the volumetric energy density increases the SX ratio, but it also increases stray grain formation and reduces deposit uniformity. The preheats scans are important in initiating the melt pool, however too high a value of repeat scan causes balling at the starting edge and a ridge after. Excessive repeat scans can also cause penetration of melt pool in to the substrate, causing deformation. Prediction fit models are generated for SX ratio, average melt depth and stray grain count in JMP as shown in Figure 158. These models are then used to develop a process map for CMSX-4 and to identify the optimal parameter range for 'acceptable deposit' as shown in Figure 159. The lower limit of 100 µm average melt back depth is demarcated by the red line on the left side and upper limit of 200 µm average melt back depth is demarcated on the right similarly. Thus the region of 100-200 µm average melt back depth is bounded by these two lines and shaded in red. The green shaded region on the left of the green line indicates SX ratio above 0.5. The blue shaded region on the right of the blue line indicates

deposits with the number of stray grains below 5. As can be seen, the optimal processing zone that produces 'acceptable deposit' with the above mentioned criteria is the overlap of all the above regions, with 35-50 J/mm^3 energy density and 300-600 numbers of preheats scans.

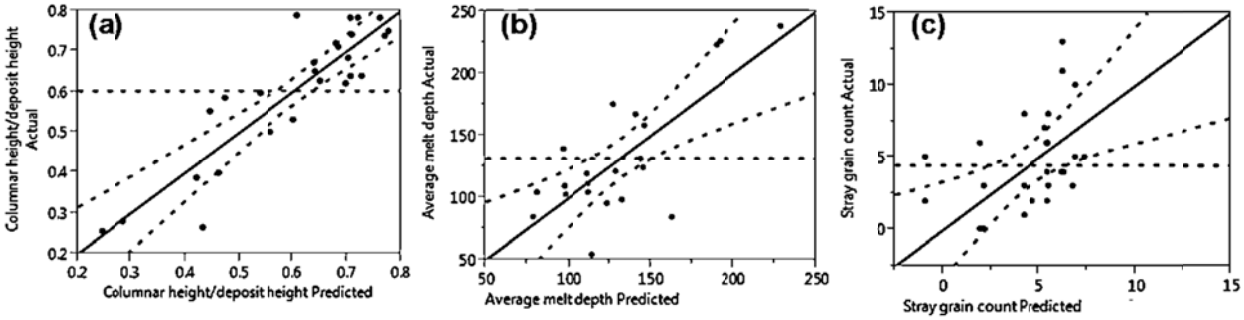

Figure 158. Prediction fit of (a) SX ratio, (b) Average melt depth, and (c) Stray grain count as function of volumetric energy density and number of preheat scans.

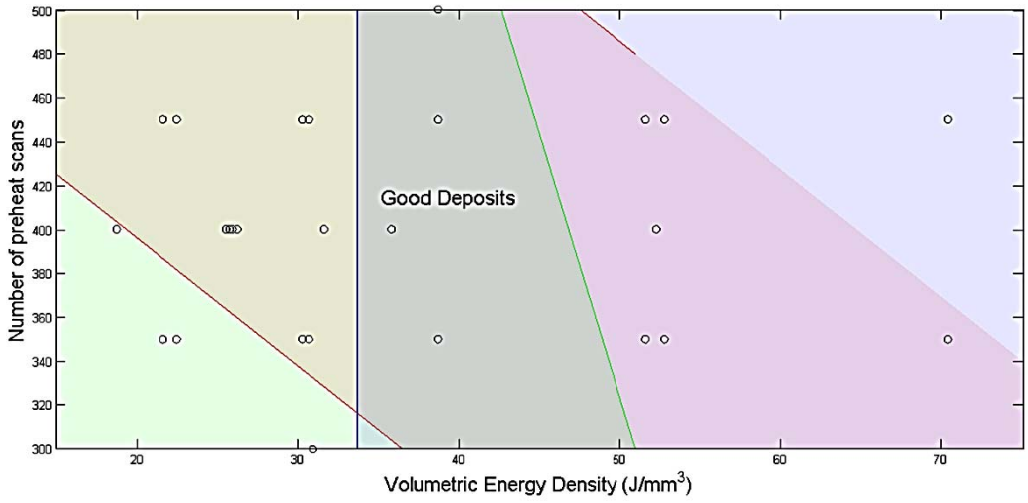

Figure 159. Process map relating number of preheat scans and volumetric energy density to high quality deposit formation. The lower limit of 100 µm average melt back depth is demarcated in red on the left side and upper limit of 200 µm average melt back depth is demarcated similarly on the right. The green shaded region indicates SX ratio above 0.5.

The blue shaded region indicates number of stray grains below 5. The black dots indicate the data points.

6.4.2 Multivariate statistics

A phase I Hotelling T^2 method was utilized for CMSX-4 deposits and an iterative procedure was again utilized to remove out-of-control data points. The sample mean or $\bar{x}$, the sample covariance S and T^2 were calculated using equations 42, 43 and 44. Figure 160 (a) shows the 1st pass ran on the DoE set for CMSX-4. Two response variables, SX ratio and deposit uniformity (R^2) were chosen as monitoring parameters. The correlation coefficient is calculated using equation 46 and is found as, ρ_c =-0.285. Hence, the SX ratio and deposit uniformity are negatively correlated and it can be stated that increase of one of the variable may lead to reduction in other one. Since the method works on minimization, (1-SX ratio) and ($1-R^2$) were used as response parameters. As can be seen, the 1st pass removes data points 8, 9, 11, 12 and 17. Data point 17 is triggered by the covariance matrix while the others can be described using the univariate chart presented in Figure 160(b) and (c).

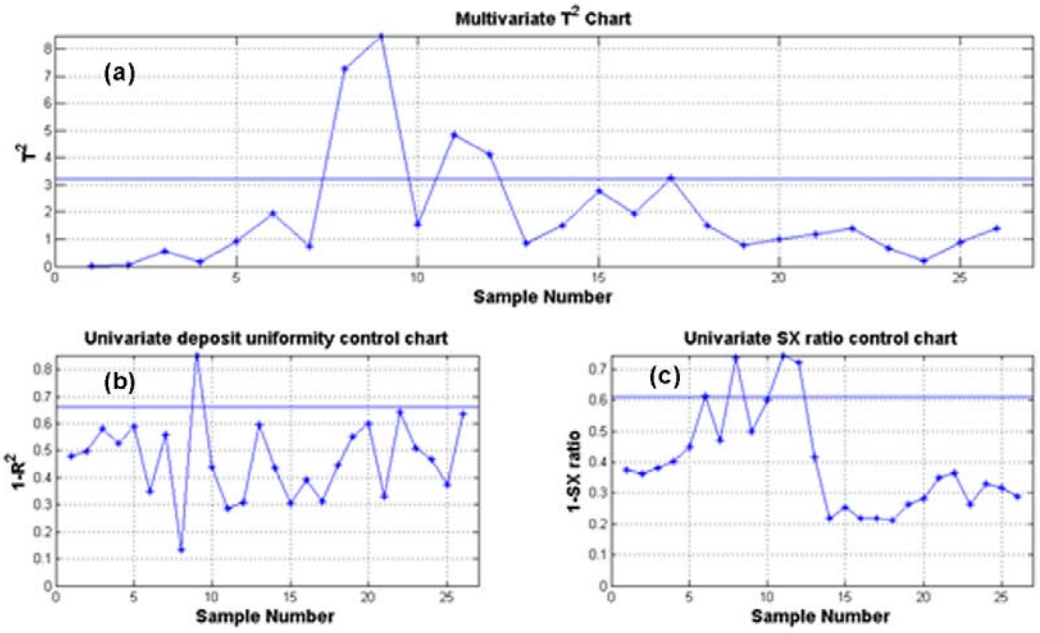

Figure 160. (a) Multivariate T^2 chart and univariate control chart for (b) (1-SX ratio) and (c) deposit uniformity (1^{st} pass).

Figure 161 shows an intermediate pass of the multivariate detection process with the univariate control charts and Figure 162 shows the final pass.

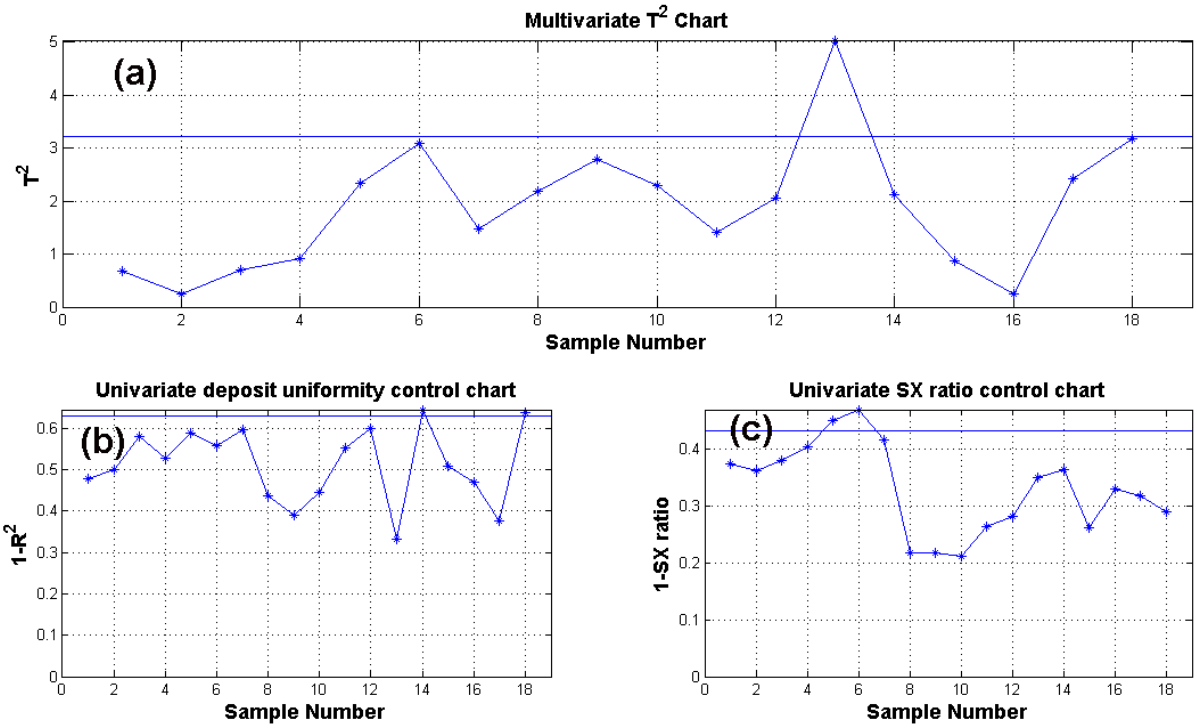

Figure 161. (a) Multivariate T^2 chart and univariate control chart for (b) (1-SX ratio) and (c) deposit uniformity ($1-R^2$) (Intermediate 3rd pass).

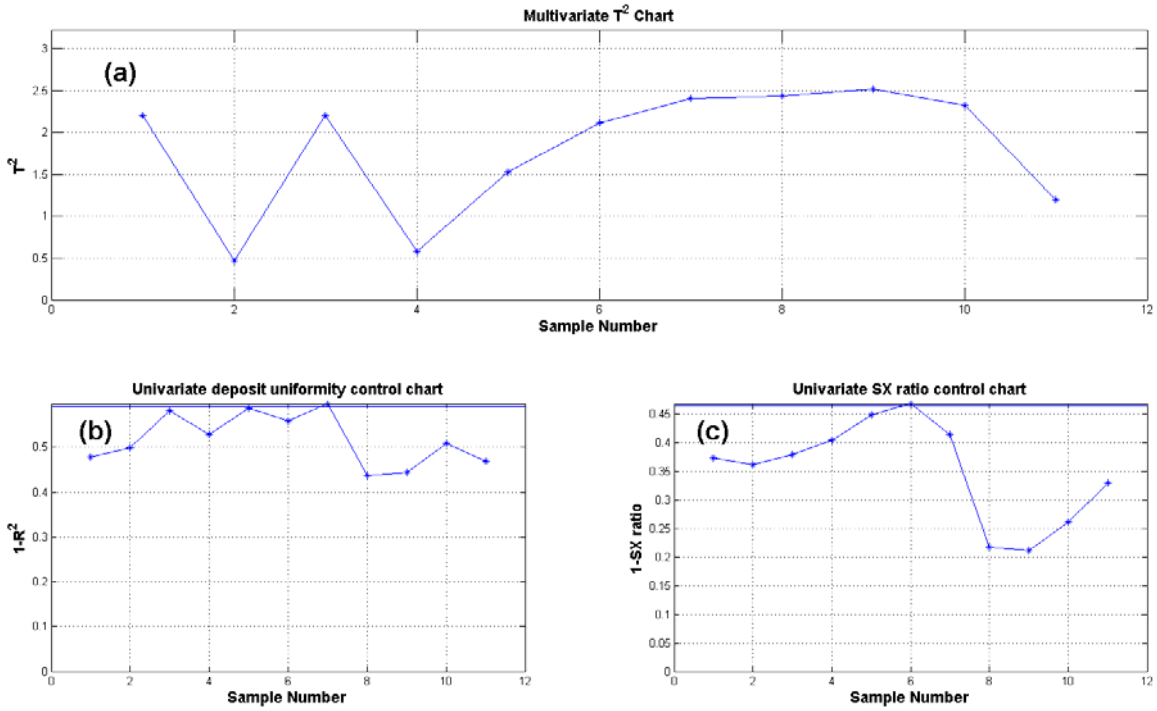

Figure 162. (a) Multivariate T^2 chart and univariate control chart for (b) (1-SX ratio) and (c) deposit uniformity (final pass).

Table 23 shows the iterative removal of the out-of-control data points for CMSX-4 with identical colored row suggesting removal in the same iteration. The unshaded rows are the in-control data set.

Table 23. Multivariate detection table showing the removal of out-of-control data points for CMSX-4 samples. The shaded rows are the out-of-control data points and rows shaded by similar colors are removed in the same pass.

Repeat	Powder thickness (mm)	Energy density (J/mm^3)	Columnar height/deposit height	Deposit height uniformity (R^2)
400	1.4	31.64	0.6261	0.5209
400	1.4	25.78	0.6382	0.5005
300	1.4	30.93	0.6205	0.4186

Table 23 (continued).

500	1.4	38.67	0.5954	0.4712
400	1.4	52.23	0.5507	0.4123
450	1.4	52.73	0.3857	0.6523
350	1.4	38.67	0.5311	0.4414
450	1.4	51.56	0.2621	0.8685
450	1.4	38.67	0.501	0.1461
350	1.4	52.73	0.3984	0.5601
450	1.4	70.30	0.2543	0.7118
350	1.4	70.30	0.2793	0.6907
350	1.4	51.56	0.5849	0.4024
400	1.4	25.96	0.7832	0.5631
400	1.4	18.77	0.7481	0.6957
450	1.4	22.50	0.7821	0.6095
350	1.4	22.50	0.7833	0.6889
400	1.4	35.79	0.7877	0.5547
350	1.4	21.63	0.7371	0.4481
350	1.4	30.68	0.7192	0.4005
450	1.4	30.28	0.6504	0.6682
450	1.4	21.63	0.6367	0.3547
400	1.4	25.56	0.7386	0.4919
450	1.4	30.68	0.6701	0.5304
400	1.4	26.25	0.6832	0.6243
350	1.4	30.28	0.7114	0.3618

The final sample mean and the co-variance matrix can be formulated as, in-control sample mean= (0.3521 0.5175) and in-control sample variance = (0.0078 0.0041; 0.0041 0.0033). This can further be refined by incorporating new data and through continuous improvement. The correlation value of the in-control data set is found as, ρ_c= 0.806. So, the multivariate analysis gradually optimized the dataset and selected those samples where the SX ratio and deposit uniformity both displayed higher value simultaneously.

6.5 Summary

This chapter presented a DoE-based optimization of the SLE process parameters enabling the fabrication of good quality deposits. The quality factors are identified and calculated using a

novel active contour-based image analysis technique. The image analysis took the digital optical micrographs as input and produced several analysis metrics representing deformation, porosity, cracks, surface uniformity, SX height for SX deposit, melt depth and variation of melt depth along the length of sample. The overall quantitative metallography is coupled with the DoE-based investigation and sample spaces are refined based on analysis metrics.

Multivariate statistics tools are also used to develop control charts based on two parameters for EQ (IN 100) and SX (CMSX-4) deposits. The limit of using two parameter-based Hotelling T^2 method is due to sample size limitation and can be removed as more samples are incorporated in the subsequent study.

For IN 100 the multivariate statistics showed in-control data for a wide range of energy density (from 15-56 J/mm^3), however, the power and scan speed should be controlled in order to reduce the pores and obtain reasonable melt depth and deposit uniformity. Scan spacing also becomes significant particularly due to internal porosity and bimodal distribution in the powder particle diameter. The optimal processing zone for 'acceptable deposit' can be identified by Figure 145 and Figure 146 together.

Parameter optimization for CMSX-4 is further complicated due to dependency of SX ratio and stray grain formation on volumetric energy density. A careful balancing of process parameter with energy density ranging from 25 to 52 J/mm^3 produced the best possible results. However, the optimal processing zone can be best identified from Figure 159 and more response variables should be incorporated to obtain a better multivariate detection tools.

Chapter VII

Summary and Conclusions

This chapter serves to present a summary of the research work performed in this dissertation and the conclusions that can be drawn. The chapter begins with a brief description and objectives of this dissertation. The conclusions drawn from the research are presented and the unique contributions of this dissertation are highlighted. Finally some potential avenues for future research in this area are suggested.

7.1 Summary

This doctoral research is aimed at advancing the development a new laser-based additive manufacturing technique, SLE, which allows epitaxial growth of Ni-based superalloys over like-chemistry substrates. The key components of this research are:

1) Development of the SLE process and demonstration of its ability to produce crack-free, dense deposits of 'non-weldable' superalloys from laser-consolidated constituent powders.

2) Detailed microstructural and microindentation hardness investigations of SLE-fabricated deposits demonstrating the epitaxial nature of such deposits for SX, DS and EQ superalloys. The quantitative metallography techniques developed to extract microstructural data [121, 125] for all samples were expanded further to obtain additional statistics.

3) Creation of a fundamental multiphysics model of the laser-material interaction in the SLE process and coupling the model to results from the quantitative metallography. The results were further validated with the temperature measurement data obtained from a thermal imaging camera with accurate emissivity estimation and correction, and melt pool detection algorithms.

4) Design-of-experiments and multivariate statistics-based investigation of the SLE process to understand the effect of input parameters on microstructural responses and to further optimize the process parameter iteratively.

The immediate application regime of the SLE process is in hot-section gas flow path components in turbine engines. The high-temperature environment inside these regions restricts the use of Ti- or Co-based superalloys. Ni-based superalloys are capable of withstanding the severe environment due to secondary phase precipitates and higher creep strength. The state-of-the-art methods of welding and additive manufacturing are not capable of restoring the original or proximate alloy chemistry and microstructure, or of fabricating entirely new, defect-free, hot-section superalloy components from the ground-up in desired microstructural configurations. Hence, the research in this dissertation is aimed at overcoming the limitations of the available processes and further advancing the SLE process for several 'non-weldable' superalloys. The experimental component of this research was conducted with an aim towards developing the process to obtain crack-free and dense deposits for EQ (René 80, IN 100), SX (CMSX-4) and DS (René 142) superalloys. Detailed microstructural investigations were carried out to understand the grain structure and morphology of the fabricated structures.

The microstructural responses were used in a quantitative metallography technique based on an active contour method. This method enabled extraction of microstructural responses for each process parameter and provided the framework for DoE-based statistical investigations for each of the superalloys investigated. Thus, the DoE was able to capture microstructural features as output parameters and subsequent optimizations of process parameters were carried out. A Hotelling T^2 based multivariate Phase I detection method was developed to detect anomalies in the process. This scheme was applied to one SX (CMSX-4) and one EQ (IN 100) alloy, and in-control statistics were calculated for use on further studies.

To gain insights into the fundamental physics of the SLE process, a CFD-based multiphysics model was developed and further coupled with an empirical microstructural model through measurements obtained from a custom-built and automated quantitative metallography technique. The flow inside the laser melt pool, the rotational vortices and the evolution of temperature gradients with time were studied in detail. The effect of Marangoni convection on disrupting the stability of nascent single-crystal dendritic microstructure was studied and correlated with experimental identification of the columnar-to-equiaxed transition. A particle tracking method was further coupled with the line heat source-based model to obtain a visualization of the flow field and to understand the effect of the wide melt pool formed during the SLE process. The real-time measurement and archival of the evolving temperature field by a thermal imaging camera enabled computation of the melt pool size and the area-averaged temperature, while also enabling model calibration and validation. Additionally, the model was validated with the experimentally obtained melt depth data from the quantitative metallographic microstructural analysis.

7.2 Conclusions

The new scientific knowledge generated from the research carried out during this dissertation leads to the following conclusions in the areas of the multiphysics modeling, microstructural investigation, and statistical analysis.

7.2.1 Multiphysics modeling

1) A CFD-based modeling scheme has been implemented to simulate the SLE process using a single computational platform. The model is able to predict the complete temperature distribution and melt pool behavior.

2) Inclusion of convection in the model provides insights on the flow field established in the melt pool and how the loose powders are drawn inside melt pool. It is shown that the flow field comprises of two rotational vortices.

3) The inclusion of Marangoni convection in the study provides a more realistic description of flow and also shows the disruptive effect it might have on the existing microstructure besides making the melt pool shallower and wider.

4) The temperature field data gathered from the thermal imaging camera enabled validation of the model developed. Reasonable agreement was obtained for melt pool size and the average melt pool temperature.

5) The empirical microstructural model enabled qualitative and quantitative prediction of microstructural transitions such as OMT and CET and allowed estimation of the PDAS from temperature gradient and solidification velocity.

7.2.2 Microstructural Investigation

1) The high resolution scan spacing used in the SLE process causes each subsequent raster scan to overlap a portion of both the prior and the subsequent raster scans, resulting in a pre-heat and post-heat treatment during the scanning operation, eliminating any hot tearing as seen in other processes. The high resolution scan spacing also results in the development of finer grain structures in the deposits made via SLE.

2) The SLE process is thus able to provide crack free, dense deposits for "non-weldable" superalloys such as René 80, IN 100, CMSX-4 and René 142.

3) Advanced microstructural investigations such as SEM and TEM showed the formation of γ-γ′ structure in the superalloy deposit and refinement of the microstructure as a function of operational parameters. The presence of MC carbides and secondary γ′ was validated using these techniques.

4) EBSD analysis enabled the study of the morphology and the grain size for SX deposits. The traditionally DS material René 142 showed SX morphology when deposited on top of SX René N5. The higher SX height in the deposit proves the capability of SLE in minimizing melt pool disturbances and retaining epitaxy for majority of the deposit length and thickness.

7.2.3 Statistical data analysis

1) Design of experiments-based studies were conducted on EQ (IN 100) and SX (CMSX-4) superalloys to understand the effect of process parameters on the microstructural properties.

2) The volumetric energy density was verified to be of prime importance in controlling the SX height for CMSX-4. Higher volumetric energy density increases the melt pool area and causes a smoother flow of powder, thus increasing the deposit uniformity. The higher energy density also draws more powder from the surrounding powder region and increases the average deposit height. However, the expanded melt pool results in a reduced vertical temperature gradient and consequently lowers SX height.

3) The optimization of laser power, raster scan speed and scan spacing was shown to produce acceptable crack-free deposits in EQ IN 100. Lowering the raster scan spacing can reduce the entrapment of gas porosity in the deposit, however, it can also deliver higher levels of energy in the deposit region, causing excessive melt depth and bending in the substrate region. A higher raster scan speed can also cause higher degree of deformation in the deposit region. Hence, a careful optimization of the process parameters enables development of an ideal processing widow for IN 100.

4) Multivariate detection techniques were explored as a method to detect anomalies in the SLE process. A Hotelling T^2-based phase I detection scheme was utilized to compute the control limit and the covariance matrix. The computation was based on the SX ratio and the deposit uniformity for SX CMSX-4. For EQ superalloy IN 100 the computation was based on the average melt depth and the deposit uniformity.

7.3 Intellectual contributions

The research performed as part of this dissertation demonstrated the capability of SLE in producing crack-free, dense and epitaxial deposits on like-chemistry substrates for SX and DS

superalloys. The key intellectual contributions of this research are presented in the following subsections.

7.3.1 Multiphysics modeling

1) A single computational platform was used to develop and execute a coupled flow-thermal-microstructural model, and the model was validated with experimentally obtained detailed microstructural data. This also enables greater traceability in the overall process, since the model allows estimation of microstructural parameters at any time instant and at any spatial co-ordinate.

2) In contrast with the existing models based on a laser beam describing a single bead on top of constant property materials, a raster scanning laser beam and temperature dependent property database were explored. This generalization also results in a change of melt pool shape from an ellipsoid to a convex hull, and increased solver instability due to rapid change in thermophysical properties.

3) The CFD-based model showed reasonable agreement with the experimentally obtained melt depth contours from cross-sectional micrographs of actual samles. In addition, temperature data from the thermal imaging camera was used to calculate the transient average melt pool temperature and transient melt pool area at the top surface. These data were used to validate the CFD model as well and showed reasonable agreement.

4) Time tracking of the solidification history and generalization of geometry was implemented to account for the raster scan pattern. Since, the trailing edge of the melt pool does not undergo further melting, it is solely responsible for the final solidification microstructure and hence was

given priority while evaluating the transition events. The rotational vortex in the leading edge controls the powder flow characteristics and can cause surface rippling.

5) The dendrite width data gathered for the operational range was extracted and the simulated data for the temperature gradient and the solidification velocity was calculated at the dendrite start location on the trailing edge of the melt pool. The image analysis suggested a PDAS of 10 to 30 μm in the deposit region as compared to more than 250 μm in the substrate region. The data fitting obtained from the above empirical approach enabled experimental verification of the proportional model for the PDAS in constrained growth under marginal stability. The proportional constant (~0.0004) found can be used to determine the approximate dendrite width from the simulated data of the temperature gradient and the solidification velocity.

6) The CET phenomenon was investigated in great detail and the evolution of the CET criterion for the raster scan pattern is presented. Time tracking of the solidification history and an accurate property database allows for improvement of the accuracy of the present approach. The unsteadiness of the CET criterion value is found to be related with the Marangoni effect-driven velocity and resulting convection of dendrites. The decline of this surface velocity value also lowers the value of the CET criterion to the ideal condition.

7) An alternate approach to predict the OMT phenomenon based on the temperature gradient is presented here. The competition of differently oriented dendrites in the raster scan pattern and subsequent flip in the direction of columnar orientation seems to occur over a range of ratios of the temperature gradient in the <100> to the <001> direction. For the investigation of CMSX-4 processing by SLE presented here, the band over which this transition takes place can be shown as, $1<\frac{G_{100}}{G_{001}} \leq 5$, where G_{ijk} is temperature gradient in <ijk> orientation.

8) A lagrangian particle tracking model is used to understand the flow of powder particles and resultant velocities within the laser melt pool. The wider melt pool and larger trailing edge provides significant damping on the particle velocity, causing negligible shear of the dendrites at the trailing edge, thus facilitating SX growth.

7.3.2 Microstructural investigation

1) A novel active contour-based image analysis technique has been developed and employed to obtain the melt depth, SX height, dendrite start and end position, dendrite width and OMT initiation. This allowed extraction of microstructural information and its use as an input to couple the CFD model with the microstructural model.

2) A novel method was developed to compute the emissivity of Ni-based superalloys by observing the change of slope in the temperature curve at solidus and liquidus temperature. For all the superalloys investigated, the determination of emissivity was done systematically to ensure calibration of the thermal imaging camera and accurate estimation of temperature during SLE process.

3) SLE is capable of delivering unparalleled performance in the additive manufacturing of components in SX superalloys. The absence of a powder blowing mechanism reduces unwanted melt pool convection and consequent breaking of dendrites, thus reducing stray grains and maintaining SX microstructure. CMSX-4 and René 142 deposits showed more than 1000 μm of columnar growth, which is desirable for repair or restoration operations on worn or damaged SX hot-section components.

4) The finer microstructure is partially responsible for the improved microindentation hardness in all the alloys investigated. The deposit region showed around 10-20% higher hardness compared to the investment cast substrate and significantly higher hardness than the available hardness data on these alloys.

7.3.3 Statistical data analysis

1) A quantitative metallography technique was developed and extended in the present research to extract microstructural responses from experimental micrographs and to provide feedback into DoE-based studies. The statistical database generated from this approach enabled the coupling between the microstructural response estimation and process parameter optimization. This step is automated and is of significant commercial interest.

2) Multivariate detection based on Hotelling T^2 method was used on test data to obtain control charts and to detect anomalies in the SLE process. These control charts and estimation of mean and co-variance of sample statistics enables better monitoring and commercial viability for SLE.

7.4 Commercial relevance

The SLE process is shown to be capable of producing fully dense, crack free and porosity free deposits of conventionally “non-weldable” superalloys while maintaining the desired microstructure. The potential technological and commercial impacts of SLE are as follows:

1) The alloys investigated in the present research are all considered to be "non-weldable" and state-of-the-art repair techniques are incapable of performing weld-repair on these alloys. Hence,

the development of SLE will be beneficial in restoring worn-out or damaged superalloy components back to service conditions.

2) Due to tighter thermal control, finely focused beam and no mechanical tool movement, SLE can easily be extended to complex geometry, allowing repair of turbine blades, vanes and shrouds.

3) As a repair process, SLE is capable of depositing more than 1000 μm SX deposit in a single pass, whereas other processes are limited to 200 μm.

4) SLE can easily be extended to a multi-layer process, allowing complete 3-D fabrication of complex geometry superalloy components.

5) The research approach presented in this thesis has great importance in feedback control algorithms for commercially viable SLE. Thermocouples mounted over different regions and IR cameras can be used to calculate the temperatures and the temperature gradients in different directions. With knowledge of alloy specific properties, the experimentally validated models for the PDAS, the CET and OMT criterion can be developed to predict microstructural parameters (PDAS) and microstructural transitions in SLE of SX alloys. This predictive capability can be powerful in real-time control of solidification microstructure in laser-based additive manufacturing of superalloys. Thus, the control algorithm based on the empirical relations developed, can be used to control the laser power or the scan velocity to alter the temperature gradient in a beneficial manner and to obtain locally controlled microstructures with desired PDAS, higher SX height and lower occurrences of OMT.

7.5 Suggestions for future work

7.5.1 Process improvement

There is ample scope for further optimization of the processing parameters for the superalloy materials investigated thus far. The process needs to be studied for shallow melt pool generation and for complex geometries where wide melt pools cannot be maintained.

7.5.2 Coupling with Finite Element (FE) model

The transient thermal data can be used as a thermal load for thermal stress simulation using FEM. The condition that the stress is zero in the weld pool means that the pool walls become distorted by the compression ahead of the weld. This produces a region of tensile transverse stress adjacent to the weld pool and in turn a region of compressive transverse stress directly behind it. A regeneration model with negligible stiffness inside the melt pool is a viable way to solve for the deformation and stress near the melt pool and the mushy zone. However, this requires accurate mechanical property databases for the superalloys.

7.5.3 Coupling with Cellular Automata (CA) model

The CFD model can further be coupled with CA model to simulate the solidification grain structure. This requires careful consideration of nucleation and grain growth models and significant computational cost due to requirement of finer mesh in the CA domain. The CA elements are typically activated or deactivated based on the local temperature data.

7.5.4 Coupling with Lattice-Boltzmann model (LBM)

The current model assumes a porous domain model for the mushy zone and does not consider effect of powder particles in great detail. LBM coupled with the CFD flow will allow modeling the flow of powder in a more realistic way. The particle tracking method currently used in conjunction with the CFD model can be validated as well using the LBM.

7.5.5 Implementation of multivariate statistical control

Multivariate statistical process control has been implemented for IN 100 and CMSX-4. This needs to be extended for all the additional alloys to be investigated. Also, a greater number of response variables (degrees of freedom) require more sample data, hence further experimentation is needed to improve the multivariate detection.

7.5.6 Quantitative metallographic study

The quantitative metallographic study needs to be validated further using advanced microstructural techniques such as TEM and EBSD. SEM is conducted on René 80, CMSX-4 and IN 100 samples to investigate the γ' formation. However, these need to be explored further using TEM and the interfacial structure needs to be studied in more detail.

7.5.7 Mechanical property estimation

The quality of the deposit needs to be verified from mechanical tests. For this purpose microindentation hardness was used so far. To further evaluate the mechanical properties of the deposit under severe conditions, elevated temperature tensile and shear tests need to be performed to understand the benefit of microstructural refinement during SLE.

References

1. Donachie, M.J., *Superalloys- Source book.* Metals Park, OH, American Society for Metals, 1984, 424 p, 1984.

2. Balsone, S., *Buckets, and Nozzles.* The Gas Turbine Handbook, Section, 2004. **4**(1).

3. Takeuchi, S. and E. Kuramoto, *Temperature and orientation dependence of the yield stress in Ni_3Ga single crystals.* Acta Metallurgica, 1973. **21**(4): p. 415-425.

4. Yoo, M., *On the theory of anomalous yield behavior of Ni_3Al—Effect of elastic anisotropy.* Scripta metallurgica, 1986. **20**(6): p. 915-920.

5. Gaumann, M., *Epitaxial Laser Metal Forming of a Single Crystal Superalloy*. PhD Thesis in 1999, EPFL Lausanne, Lausanne.

6. Glavicic, M.G., et al., *The Repair of Single Crystal Nickel Superalloy Turbine Blades Using Laser Engineered Net Shape (LENS) Technology*. 2003, DTIC Document.

7. Mokadem, S., et al., *Laser Repair of Superalloy Single Crystals with Varying Substrate Orientations.* Metallurgical and Materials Transactions A, 2007. **38**(7): p. 1500-1510.

8. Zhao, J., et al., *Research on laser engineered net shaping of thick-wall nickel-based alloy parts.* Rapid Prototyping Journal, 2009. **15**(1): p. 24-28.

9. Matthew J. Donachie, *Superalloys, A Technical Guide*. 2003: ASM International.

10. Henderson, M., et al., *Nickel based superalloy welding practices for industrial gas turbine applications.* Science and Technology of Welding & Joining, 2004. **9**(1): p. 13-21.

11. Rappaz, M. and C.A. Gandin, *Probabilistic modelling of microstructure formation in solidification processes.* Acta Metallurgica et Materialia, 1993. **41**(2): p. 345-360.

12. Bansal, R., *Analysis and feedback control of the scanning laser epitaxy process applied to nickel-base superalloys*, PhD Thesis in *Mechanical Engineering*. 2013, Georgia University of Technology, Atlanta.

13. Mokadem, S., *Epitaxial Laser Treatment of Single Crystal Nickel-Base Superalloys*. PhD thesis in 2004., EPFL Lausanne, Lausanne

14. Gäumann, M., et al., *Single-crystal laser deposition of superalloys: processing–microstructure maps.* Acta Materialia, 2001. **49**(6): p. 1051-1062.

15. Gäumann, M., R. Trivedi, and W. Kurz, *Nucleation ahead of the advancing interface in directional solidification.* Materials Science and Engineering: A, 1997. **226**: p. 763-769.

16. Ross Earl W., O'Hara Kevin S., *Rene' l42: A High strength, oxidation resistant DS turbine airfoil alloy,* in *Superalloys*. 1992.

17. Sexton, L., et al., *Laser cladding of aerospace materials.* Journal of Materials Processing Technology, 2002. **122**(1): p. 63-68.

18. Murr, L.E., et al., *Microstructures of Rene 142 nickel-based superalloy fabricated by electron beam melting.* Acta Materialia, 2013. **61**(11): p. 4289-4296.

19. Quested, P., et al., *Measurement and estimation of thermophysical properties of nickel based superalloys.* Materials Science and Technology, 2009. **25**(2): p. 154-162.

20. Anderson, T.D., J.N. DuPont, and T. DebRoy, *Origin of stray grain formation in single-crystal superalloy weld pools from heat transfer and fluid flow modeling.* Acta Materialia, 2010. **58**(4): p. 1441-1454.

21. Das, S., *Direct selective laser sintering of high performance metals: Machine design, process development and process control*. PhD Thesis in Mechanical Engineering. 1998, University of Texas at Austin.

22. Langston, L.S., *Gems of turbine efficiency*, in *ASME*. Mechanical Engineering Magazine 2014. p. 76-81.

23. Spittle, P., *Gas turbine technology.* Physics education, 2003. **38**(6): p. 504.

24. Seth, B.B., *Superalloys - the utility gas turbine perspective.* Minerals, Metals and Materials Society/AIME, Superalloys 2000(USA), 2000: p. 3-16.

25. PCC. *Gas turbine components*. 2013 [cited 2014; Available from: http://www.pccforgedproducts.com/products/.

26. Wang, S., et al., *Effect of long-term aging on the fatigue crack growth rate of a nickel-based superalloy.* Materials Science and Engineering: A, 2011. **528**(4): p. 2110-2117.

27. Kim, D.K., et al., *Application of nimonic 80A to the hot forging of an exhaust valve head.* Journal of Materials Processing Technology, 2001. **113**(1): p. 148-152.

28. Pyczak, F., et al., *The influence of different alloying elements on the development of the γ/γ′ microstructure of nickel-base superalloys during high-temperature annealing and deformation.* Acta materialia, 2005. **53**(14): p. 3879-3891.

29. Sharma, K., D. Banerjee, and S. Tewari, *Effect of reverse-aging treatment on the microstructure and mechanical properties of Nimonic alloys.* Materials Science and Engineering: A, 1988. **104**: p. 131-140.

30. Xu, Y., et al., *Relationship between Ti/Al ratio and stress-rupture properties in nickel-based superalloy.* Materials Science and Engineering: A, 2012. **544**(0): p. 48-53.

31. Ross, E.W. and K.S. O'hara, *Rene'142- A high strength, oxidation resistant DS turbine alloy* Superalloys, 1992: p. 257-265.

32. Yang, Y.H., et al., *Investigation of impact toughness of a Ni-based superalloy at elevated temperature.* Materials & Design, 2012. **36**(0): p. 699-704.

33. Larson, F. and J. Miller, *A time-temperature relationship for rupture and creep stresses*. ASME, 1952: 765-775.

34. Garofalo, F., *Fundamentals of creep and creep-rupture in metals*. 1965: Macmillan.

35. Scholz, A., et al., *Modeling of mechanical properties of alloy CMSX-4.* Materials Science and Engineering: A, 2009. **510–511**(0): p. 278-283.

36. Egly, T.A., K.H. Lang, and D. Löhe, *Influence of phase shift and strain path on the thermomechanical fatigue behavior of CMSX-4 specimens.* International Journal of Fatigue, 2008. **30**(2): p. 249-256.

37. Fisher, K. and W. Kurz, *Fundamentals of solidification.* Trans Tech Publications, 1986.

38. Reed, R., *The Superalloys: Fundamentals and Applications. 2006*. Cambridge: Cambridge University Press.

39. ALD Vacuum Technologies, L*iquid Metal Cooling for DS/SC Solidification*. 2013 [cited 2014; Available from: http://www.ald-vt.com/cms/en/vacuum-technology/applications/lmc-for-dssc-solidification/.

40. Nabarro, F., *Solution hardening.* Dislocations and Properties of Real Materials, 1984: p. 152-169.

41. Decker, R. and J. Mihalisin, *Coherency strains in gamma prime hardened nickel alloys.* Asm trans. quart., 1969. **62**(2): p. 481-489.

42. Gregori, A., *A survey of welding and repairing of nickel superalloys for gas turbines. TWI*. 2003, Report.

43. Betteridge, W. and S. Shaw, *Development of superalloys.* Materials science and technology, 1987. **3**(9): p. 682-694.

44. Swaminathan, V. and N. Cheruvu, *Advanced materials and coatings for combustion turbines: proceedings of ASM 1993 Materials Congress Materials Week:93, October 17-21, 1993, Pittsburgh, Pennsylvania*. 1994: Asm Intl.

45. Erickson, G. and K. Harris, *DS and SX superalloys for industrial gas turbines.* Proceedings Materials for Advanced Power Engineering, Kluwer Academic Publishers, Belgium, Liege, 1994: p. 1055-1074.

46. Schilke, P., A. Foster, and J. Pepe, *Advanced gas turbine materials and coatings*. 1991: General Electric Company.

47. Schilke, P., *Advanced gas turbine materials and coatings*. 2004, General Electric Company. p. 30.

48. Buchakjian Jr, L., T. Tom, and C.S. Wukusick, *Cast nickel-base alloy article*. 1979, US Patent 4,169,742.

49. O. Hunziker, D. Dye, S.M. Roberts, R.C. Reed., *A coupled approach for the prediction of solidification cracking during the welding of superalloys*, in *Mathematical modelling of weld phenomena 5*. 2001, IOM Communications: London. p. 299-320.

50. Yaman, Y. and M. Kuşhan, *Hot Cracking Susceptibilities in the Heat-affected Zone of Electron Beam–welded Inconel 718.* Journal of materials science letters, 1998. **17**(14): p. 1231-1234.

51. Çam, G. and M. Koçak, *Progress in joining of advanced materials.* International Materials Reviews, 1998. **43**(1): p. 1-44.

52. Rush, M.T., et al., *Liquation and post-weld heat treatment cracking in Rene 80 laser repair welds.* Journal of materials processing technology, 2012. **212**(1): p. 188-197.

53. Osoba, L., R. Sidhu, and O. Ojo, *On preventing HAZ cracking in laser welded DS Rene 80 superalloy.* Materials Science and Technology, 2011. **27**(5): p. 897-902.

54. Rush, M.T., et al., *An investigation into cracking in nickel-base superalloy repair welds.* Advanced Materials Research, 2010. **89**: p. 467-472.

55. Shahsavari, H., A. Kokabi, and S. Nategh, *Effect of preweld microstructure on HAZ liquation cracking of Rene 80 superalloy.* Materials Science and Technology, 2007. **23**(5): p. 547-555.

56. Lee, P.D. and J. Wang, *Formation of Microstructures, Grain Textures, and Defects during Solidification.* ASM Handbook, Volume 22B: Metals Process Simulation, 2010: p. 256-263.

57. Asta, M., et al., *Solidification microstructures and solid-state parallels: Recent developments, future directions.* Acta Materialia, 2009. **57**(4): p. 941-971.

58. Kurz, W. and D. Fisher, *Dendrite growth at the limit of stability: tip radius and spacing.* Acta Metallurgica, 1981. **29**(1): p. 11-20.

59. Langer, J. and J. Müller-Krumbhaar, *Stability effects in dendritic crystal growth.* Journal of Crystal Growth, 1977. **42**: p. 11-14.

60. Pollock, T.M. and S. Tin, *Nickel-based superalloys for advanced turbine engines: chemistry, microstructure and properties.* Journal of propulsion and power, 2006. **22**(2): p. 361-374.

61. Elliott, A. and T. Pollock, *Thermal analysis of the Bridgman and Liquid-Metal-Cooled directional solidification investment casting processes.* Metallurgical and Materials Transactions A, 2007. **38**(4): p. 871-882.

62. Hoppin, G. and T. Berry, *Activated diffusion bonding: a new joining process produces high-strength joints in difficult-to-weld superalloys, including René 80.* Weld. J, 1970. **11**: p. 505s-509s.

63. Milidantri, T., R.J. Stueber, and M. Tadayon, *Welding high-strength nickel base superalloys*. 1992, US patent 2,052,346.

64. Ojo, O. and M. Chaturvedi, *On the role of liquated γ' precipitates in weld microfissuring of a nickel-based superalloy.* Materials Science and Engineering: A, 2005. **403**(1): p. 77-86.

65. Babu, S., et al., *Joining of nickel base superalloy single crystals.* Science and Technology of Welding & Joining, 2004. **9**(1): p. 1-12.

66. Abbott, D.H., et al., *Method of repairing metallic articles by energy beam deposition with reduced power density*. 1999, US Patent 5,914,059.

67. Mah, R., *Directed light fabrication.* Advanced materials & processes, 1997. **151**(3): p. 31-33.

68. Kathuria, Y. *Laser surface cladding: a unique application to the turbine industry*. in *Proceedings of the Laser Assisted Net Shape Engineering*. 1997.

69. Kreutz, E.W., *Pulsed laser deposition of ceramics – fundamentals and applications.* Applied Surface Science, 1998. **127–129**(0): p. 606-613.

70. Hofmeister, W., et al., *Investigation of solidification in the laser engineered net shaping (LENS^{TM}) process.* JOM, 1999. **51**(7): p. 1-6.

71. Lewis, G.K. and E. Schlienger, *Practical considerations and capabilities for laser assisted direct metal deposition.* Materials & Design, 2000. **21**(4): p. 417-423.

72. Breinan, E.M., C.O. Brown, and B.H. Kear, *Method for fabricating articles by sequential layer deposition*. 1982, US patent U.S. Patent 4,323,756.

73. Griffith, M., et al., *Understanding thermal behavior in the LENS process.* Materials & design, 1999. **20**(2): p. 107-113.

74. Hofmeister, W. and M. Griffith, *Solidification in direct metal deposition by LENS processing.* JOM, 2001. **53**(9): p. 30-34.

75. Gremaud, M., et al., *Laser metal forming: process fundamentals.* Surface Engineering, 1996. **12**(3): p. 251-259.

76. Liu, W. and J.N. DuPont, *Effects of substrate crystallographic orientations on crystal growth and microstructure development in laser surface-melted superalloy single crystals. Mathematical modeling of single-crystal growth in a melt pool (Part II).* Acta Materialia, 2005. **53**(5): p. 1545-1558.

77. Liu, W. and J.N. DuPont, *Effects of melt-pool geometry on crystal growth and microstructure development in laser surface-melted superalloy single crystals: Mathematical modeling of single-crystal growth in a melt pool (part I).* Acta Materialia, 2004. **52**(16): p. 4833-4847.

78. Park, J.-W., et al., *Stray grain formation in single crystal Ni-base superalloy welds.* Journal of Applied Physics, 2003. **94**(6): p. 4203-4209.

79. Lippold, J.C., S.D. Kiser, and J.N. DuPont, *Welding metallurgy and weldability of nickel-base alloys*. 2011: John Wiley & Sons.

80. Anderson, T., J. DuPont, and T. DebRoy, *Stray grain formation in welds of single-crystal Ni-base superalloy CMSX-4.* Metallurgical and Materials Transactions A, 2010. **41**(1): p. 181-193.

81. Rosenthal, D. *The theory of moving sources of heat and its application to metal treatments*. ASME Trans.,1946.849-866.

82. Eagar, T. and N. Tsai, *Temperature fields produced by traveling distributed heat sources.* Welding Journal, 1983. **62**(12): p. 346-355.

83. Cline, H. and T. Anthony, *Heat treating and melting material with a scanning laser or electron beam.* Journal of Applied Physics, 1977. **48**(9): p. 3895-3900.

84. Christensen, N., V.d.L. Davies, and K. Gjermundsen, *Distribution of temperatures in arc welding.* British Welding Journal, 1965. **12**(2): p. 54-75.

85. Goldak, J., A. Chakravarti, and M. Bibby, *A new finite element model for welding heat sources.* Metallurgical transactions B, 1984. **15**(2): p. 299-305.

86. Childs, T.H. and A. Tontowi, *Selective laser sintering of a crystalline and a glass-filled crystalline polymer: experiments and simulations.* Proceedings of the Institution of Mechanical Engineers, Part B: Journal of Engineering Manufacture, 2001. **215**(11): p. 1481-1495.

87. Childs, T.H.C., C. Hauser, and M. Badrossamay, *Mapping and Modelling Single Scan Track Formation in Direct Metal Selective Laser Melting.* CIRP Annals - Manufacturing Technology, 2004. **53**(1): p. 191-194.

88. Hauser, C. and T.H.C. Childs, *Raster scan selective laser melting of the surface layer of a tool steel powder bed.* Proceedings of the Institution of Mechanical Engineers, Part B: Journal of Engineering Manufacture, 2005. **219**(4): p. 379-384.

89. Mundra, K., T. DebRoy, and K.M. Kelkar, *Numerical prediction of fluid flow and heat transfer in welding with a moving heat source.* Numerical Heat Transfer, Part A: Applications, 1996. **29**(2): p. 115-129.

90. Zhang, W., C.H. Kim, and T. DebRoy, *Heat and fluid flow in complex joints during gas metal arc welding (Part I): Numerical model of fillet welding.* Journal of Applied Physics, 2004. **95**(9): p. 5210-5219.

91. Houldcroft, R., *Dilution and uniformity in aluminum alloy weld beads.* British Welding Journal, 1954. **1**: p. 468-472.

92. Acharya, R., et al., *CFD Modeling of Microstructural Development in the Scanning Laser Epitaxy Process.* CFD Modeling and Simulation in Materials Processing, 2012: p. 197-204.

93. Chan, C.L., J. Mazumder, and M.M. Chen, *Effect of surface tension gradient driven convection in a laser melt pool: Three-dimensional perturbation model.* Journal of Applied Physics, 1988. **64**(11): p. 6166.

94. Chande, T. and J. Mazumder, *Mass transport in laser surface alloying: Iron-nickel system.* Applied Physics Letters, 1982. **41**(1): p. 42-43.

95. Copley, S. and D. Beck. *O. Esquivel, and M. Bass (1981)*. in *Proc. Conf. of Laser in Metallurgy, Chicago, IL, K. Mukerji and J. Mazumder, Eds., TMS-AIME, Warrendale, PA*.

96. Oreper, G., T. Eagar, and J. Szekely, *Convection in arc weld pools.* Welding Journal, 1983. **62**(11): p. 307s-312s.

97. Mazumder, J., *Overview of melt dynamics in laser processing.* Optical Engineering, 1991. **30**(8): p. 1208-1219.

98. Paul, A. and T. DebRoy, *Free surface flow and heat transfer in conduction mode laser welding.* Metallurgical Transactions B, 1988. **19**(6): p. 851-858.

99. Bedenko, D.V. and O.B. Kovalev, *Modelling of heat and mass transfer in the laser cladding during direct metal deposition.* Thermophysics and Aeromechanics, 2013. **20**(2): p. 251-261.

100. Liu, Z. and H. Qi, *Numerical Simulation of Transport Phenomena for a Double-Layer Laser Powder Deposition of Single-Crystal Superalloy.* Metallurgical and Materials Transactions A, 2014. **45**(4): p. 1903-1915.

101. German, R., *Powder Metallurgy Science*. 2nd ed. 1994: Matal Powder Industries Federation. 472.

102. Gusarov, A.V., et al., *Contact thermal conductivity of a powder bed in selective laser sintering.* International Journal of Heat and Mass Transfer, 2003. **46**(6): p. 1103-1109.

103. Wang, X.C., et al., *Direct Selective Laser Sintering of Hard Metal Powders: Experimental Study and Simulation.* The International Journal of Advanced Manufacturing Technology, 2002. **19**(5): p. 351-357.

104. Gusarov, A. and I. Smurov, *Modeling the interaction of laser radiation with powder bed at selective laser melting.* Physics Procedia, 2010. **5**: p. 381-394.

105. Wang, W., P. Lee, and M. McLean, *A model of solidification microstructures in nickel-based superalloys: predicting primary dendrite spacing selection.* Acta Materialia, 2003. **51**(10): p. 2971-2987.

106. Matsumoto, M., et al., *Finite element analysis of single layer forming on metallic powder bed in rapid prototyping by selective laser processing.* International Journal of Machine Tools and Manufacture, 2002. **42**(1): p. 61-67.

107. Lim, L.C., J.-Z. Yi, and N. Liu, *Mechanism of post-weld heat treatment cracking in Rene 80 nickel based superalloy.* Materials Science and Technology, 2002. **18**(4): p. 407-412.

108. Trivedi, R., *Interdendritic Spacing: Part II. A Comparison of Theory and Experiment.* Metallurgical Transactions A, 1984. **15**(6): p. 977-982.

109. Esaka, H., W. Kurz, and R. Trivedi. in *Solidification Processing* 1988. The Institute of Metals, London.

110. Hunt, J., *Steady state columnar and equiaxed growth of dendrites and eutectic.* Materials Science and Engineering, 1984. **65**(1): p. 75-83.

111. Rappaz, M., et al., *Development of microstructures in Fe−15Ni−15Cr single crystal electron beam welds.* Metallurgical Transactions A, 1989. **20**(6): p. 1125-1138.

112. Vitek, J., *The effect of welding conditions on stray grain formation in single crystal welds–theoretical analysis.* Acta Materialia, 2005. **53**(1): p. 53-67.

113. Rappaz, M., et al., *Analysis of solidification microstructures in Fe-Ni-Cr single-crystal welds.* Metallurgical Transactions A, 1990. **21**(6): p. 1767-1782.

114. Chopard, B. and A. Masselot, *Cellular automata and lattice Boltzmann methods: a new approach to computational fluid dynamics and particle transport.* Future Generation Computer Systems, 1999. **16**(2): p. 249-257.

115. Rappaz, M. and C.-A. Gandin, *Probabilistic modelling of microstructure formation in solidification processes.* Acta metallurgica et materialia, 1993. **41**(2): p. 345-360.

116. Chen, S., G. Guillemot, and C.-A. Gandin, *3D Coupled Cellular Automaton (CA)–Finite Element (FE) Modeling for Solidification Grain Structures in Gas Tungsten Arc Welding (GTAW).* ISIJ International, 2014. **54**(2): p. 401-407.

117. Wang, N., et al., *Simulation of grain selection during single crystal casting of a Ni-base superalloy.* Journal of Alloys and Compounds, 2014. **586**: p. 220-229.

118. Athreya, S.R., *Processing and characterization of carbon black-filled electrically conductive nylon-12 nanocomposites produced by selective laser sintering*,PhD Thesis in *ME*. 2010, Georgia Institute of Technology: Atlanta.

119. Ghaemi, A., *Freezing-point-blackbody radiation sources for the 29.78–1084.62° C temperature range.* Applied Optics, 1996. **35**(13): p. 2211-2215.

120. Mills, K.C., et al., *Calculation of Thermophysical Properties of Ni-based Superalloys.* ISIJ International, 2006. **46**(5): p. 623-632.

121. Gambone, J.J., *Quantitative Metallography Tracking and Analysis for the Scanning Laser Epitaxy Process*, M.S. Thesis in *Mechanical Engineering*. 2012, Georgia Institute of Technology: Atlanta.

122. Vander Voort, G.F., E.P. Manilova, and G.M. Lucas, *Metallographic Techniques for Superalloys.* Microscopy and Microanalysis, 2004. **10**(S02): p. 690-691.

123. Vander Voort, G.F. and G.M. Lucas, *Microindentation hardness testing.* Advanced Materials & Processes, 1998. **154**(3): p. 21-25.

124. Mathey, G.F., *Method of making superalloy turbine disks having graded coarse and fine grains*. 1994, US Patent 5,312,497.

125. Acharya, R., et al., *A Coupled Thermal, Fluid Flow, and Solidification Model for the Processing of Single-Crystal Alloy CMSX-4 Through Scanning Laser Epitaxy for Turbine Engine Hot-Section Component Repair (Part I).* Metallurgical and Materials Transactions B, 2014: p. 1-15.

126. Suciu, S., *High Temperature Turbine Design Considerations: A discussion of the major technological developments which have led to the trend of using higher temperatures in modern gas turbine aero engines from a paper first presented at an AGARD conference in September.* Aircraft Engineering and Aerospace Technology, 1970. **42**(12): p. 10-17.

127. Safari, J. and S. Nategh, *On the heat treatment of Rene-80 nickel-base superalloy.* Journal of materials processing technology, 2006. **176**(1): p. 240-250.

128. Yang, C., et al., *Effects of heat treatments on the microstructure and mechanical properties of Rene 80.* Materials & Design, 2013. **43**(0): p. 66-73.

129. Gayda, J. and R. Miner, *Fatigue crack initiation and propagation in several nickel-base superalloys at 650 C.* International journal of fatigue, 1983. **5**(3): p. 135-143.

130. Murata, Y., K. Suga, and N. Yukawa, *Effect of transition elements on the properties of MC carbides in IN-100 nickel-based superalloy.* Journal of materials science, 1986. **21**(10): p. 3653-3660.

131. Wusatowska-Sarnek, A.M., et al., *Characterization of the microstructure and phase equilibria calculations for the powder metallurgy superalloy IN100.* Journal of materials research, 2003. **18**(11): p. 2653-2663.

132. Yukawa, N., Y. Murata, and T. Noda. *Analysis of solidification behavior and alloy design of a nickel-base superalloy, IN 100*. in *Superalloys 1984: proceedings of the Fifth International Symposium on Superalloys sponsored by the High Temperature Alloys Committee of the Metallurgical Society of AIME, held October 7-11, 1984, Seven Springs Mountain Resort, Champion, Pennsylvania*. 1984. TMS.

133. Ojo, O.A., N.L. Richards, and M.C. Chaturvedi, *Microstructural study of weld fusion zone of TIG welded IN 738LC nickel-based superalloy.* Scripta Materialia, 2004. **51**(7): p. 683-688.

134. Owczarski, W., D. Duvall, and C. Sullivan, *A model for cracking in nickel-base superalloys.* WELD J, 1966. **45**(4): p. 145.

135. Cam, G. and M. Koçak, *Progress in joining of advanced materials*. International Materials Reviews, 1998. **43**: p. 1-39.

136. Murr, L., et al., *Microstructures of Rene 142 nickel-based superalloy fabricated by electron beam melting.* Acta Materialia, 2013. **61**(11): p. 4289-4296.

137. Ekrami, A., S. Moeinifar, and A.H. Kokabi, *Effect of transient liquid phase diffusion bonding on microstructure and properties of a nickel base superalloy Rene 80.* Materials Science and Engineering: A, 2007. **456**(1–2): p. 93-98.

138. Sidhu, R.K., O.A. Ojo, and M.C. Chaturvedi, *Microstructural Response of Directionally Solidified René 80 Superalloy to Gas-Tungsten Arc Welding.* Metallurgical and Materials Transactions A, 2009. **40**(1): p. 150-162.

139. Flemings, M.C., *Solidification processing.* Metallurgical Transactions, 1974. **5**(10): p. 2121-2134.

140. Rae, C.M.F., M.S. Hook, and R.C. Reed, *The effect of TCP morphology on the development of aluminide coated superalloys.* Materials Science and Engineering: A, 2005. **396**(1–2): p. 231-239.

141. Tan, X.P., et al., *Characterization of topologically close-packed phases in secondary reaction zone in a coated CMSX-4 single crystal Ni-based superalloy.* Journal of Materials Science, 2013. **48**(3): p. 1085-1089.

142. Aluru, R., et al., *Transient liquid phase bonding of dissimilar nickel base superalloys—wettability, microstructure and mechanical properties.* Materials Science and Technology, 2008. **24**(5): p. 517-528.

143. Lapin, J., T. Pelachova, and O. Bajana, *The effect of microstructure on mechanical properties of single cruystal alloy CMSX-4 superalloy. in Metal:2013, Brno, Czech repubic, EU.*

144. Haafkens, M. and J. Matthey, *A new approach to the weldability of nickel-base As-cast and power metallurgy superalloys.* Weld. J.(Miami);(United States), 1982. **61**(11).

145. Matsushita, T., et al., *Studies of the Thermophysical Properties of Commercial CMSX-4 Alloy.* J. Chem. Eng. Data, 2011. **54**(9): p. 2584-2592.

146. Hamill, I., *Implementation of a Solidification Model in CFX-5*. 2003, CFX Ltd. p. 1-28.

147. McCabe, W.L.S., Julian C.; Harriot, Peter, *Unit Operations of Chemical Engineering*. 7 ed. (2005), New York: McGraw-Hill.

148. Yang, L.X., X.F. Peng, and B.X. Wang, *Numerical modeling and experimental investigation on the characteristics of molten pool during laser processing.* International Journal of Heat and Mass Transfer, 2001. **44**(23): p. 4465-4473.

149. Lee Y., et al., *Influence of Fluid Convection on Weld Pool Formation in Laser Cladding.* Welding Journal, 2014.

150. Xie, J., et al., *Temperature-dependent absorptivity and cutting capability of CO_2, Nd:YAG and chemical oxygen–iodine lasers.* Journal of Laser Applications, 1997. **9**(2): p. 77-85.

151. Acharya, R., et al., *A Microstructure Evolution Model for the Processing of Single-Crystal Alloy CMSX-4 Through Scanning Laser Epitaxy for Turbine Engine Hot-Section Component Repair (Part II).* Metallurgical and Materials Transactions B, 2014: p. 1-12.

152. Canny, J., *A computational approach to edge detection.* Pattern Analysis and Machine Intelligence, IEEE Transactions on, 1986(6): p. 679-698.

153. Marr, D. and E. Hildreth, *Theory of edge detection.* Proceedings of the Royal Society of London. Series B. Biological Sciences, 1980. **207**(1167): p. 187-217.

154. Blake, A., M. Isard, and D. Reynard, *Learning to track the visual motion of contours.* Artificial Intelligence, 1995. **78**(1): p. 179-212.

155. Kass, M., A. Witkin, and D. Terzopoulos, *Snakes: Active contour models.* International journal of computer vision, 1988. **1**(4): p. 321-331.

156. Kichenassamy, S., et al. *Gradient flows and geometric active contour models*. in *Computer Vision, 1995. Proceedings., Fifth International Conference on*. 1995. IEEE.

157. Pitteway, M.L., *Algorithm for drawing ellipses or hyperbolae with a digital plotter.* The Computer Journal, 1967. **10**(3): p. 282-289.

158. Flanagan, C. *The Bresenham line-drawing algorithm*. 2009 [cited 2012; Available from: http://www.cs.helsinki.fi/group/goa/mallinnus/lines/bresenh.html.

VITA

Ranadip Acharya was born in Kolkata, West Bengal, India in 1983 and raised in Kolkata and Haldia, West Bengal. He graduated from Laban Hrad Vidyapith in 2002 and went on to pursue undergraduate study in Mechanical Engineering at Jadavpur University, Kolkata. After completing undergraduate studies in 2006, he enrolled at the Indian Institute of Technology Kharagpur to pursue a Masters in Manufacturinng Science and Enginerring. He was awarded the prestigious Institute Silver Medal for holding highest grades during his Masters in the Mechanical Engineering department. He joined Ansys, Inc. as an application engineer after that. In 2011, he enrolled in the graduate program at Georgia Tech to pursue a PhD. During graduate school, he joined the Direct Digital Manufacturing lab and worked on development of the Scanning Laser Epitaxy (SLE) additive manufacturing process under the advisement of Dr. Suman Das. He completed his Masters of Science in Material Science in 2014 and received his Doctor of Philosophy in Mechanical Engineering in 2014 for his dissertation entitled *Multiphysics Modeling and Statistical Process Optimization of the Scanning Laser Epitaxy Process Applied to Additive Manufacturing of Turbine Engine Hot-Section Superalloy Components*. He will be joining United Technologies Research Center at Hartford, CT as a senior research engineer after leaving Georgia Tech.